Spring 2-15-2022

Analytical, Simulation, and Experimental Study of the Generation of Multiple Beams for Application to a Traveling Wave Tube(TWT)

Khandakar Nusrat Islam
University of New Mexico

Khandakar Nusrat Islam

Candidate

Electrical and Computer Engineering

Department

This dissertation is approved, and it is acceptable in quality and form for publication:

Approved by the Dissertation Committee:

Dr. Edl Schamiloglu,	Chairperson
Dr. Mark Gilmore,	Member
Dr. Ylva Pihlström,	Member
Dr. Salvador Portillo,	Member
Dr. Larry Ludeking,	Member

ANALYTICAL, SIMULATION, AND EXPERIMENTAL STUDY OF THE GENERATION OF MULTIPLE BEAMS FOR APPLICATION TO A TRAVELING WAVE TUBE (TWT)

by

KHANDAKAR NUSRAT ISLAM

B.Sc., Electrical and Electronic Engineering, Eastern University,
Dhaka, Bangladesh, 2010

M.S., Electrical Engineering, University of New Mexico,
Albuquerque, NM, 2017

DISSERTATION

Submitted in Partial Fulfillment of the
Requirements for the Degree of
Doctor of Philosophy

Engineering

The University of New Mexico
Albuquerque, New Mexico

May, 2022

DEDICATION

I dedicate this dissertation to

my mother Noor Alam Mortuza Begum,

my father late Khandakar Nural Islam, MD,

my five sisters, Nice, Nasrin, Nilufa, Noushad, Nuzhat, and my brother, Life for their unconditional love, support and encouragement,

and my undergraduate research mentor late Dr. Zahid Hasan Mahmood who taught me to follow my true passion.

ACKNOWLEDGMENTS

I would like to acknowledge and extend my deepest gratitude to my committee chair and advisor Professor Edl Schamiloglu for all of his support, invaluable supervision, and encouragement during these past five years, but most of all, for his patience with me during the entire process of completing this dissertation. Dr. Schamiloglu is one of the most thoughtful, understanding, and smartest people I know and I hope I can be as lively and energetic as him. I'm also deeply indebted to Dr. Schamiloglu for the incredible opportunity to work on this project and for giving me the freedom to pursue my Ph.D. on this topic of interest. The completion of my dissertation would not have been possible without his guidance and persistent help.

I would like to express my deepest appreciation to the members of my Ph.D. committee, Professors Mark Gilmore, Salvador Portillo, Ylva Pihlström, and Dr. Larry Ludeking, for agreeing to serve on my committee. I will forever be thankful to my MS thesis advisor, Dr. Gilmore, for all of his support and the opportunity to start research in his lab at UNM during my master's and for providing advice many times during my graduate school career. I'm extremely grateful to Dr. Ludeking for his valuable advice, practical suggestions, and answering many simulation questions. I would also like to extend my gratitude to Dr. Portillo for his profound belief in my abilities and always encouraging me to be confident and the best in my endeavor.

This work wouldn't have been possible without the expertise of Dr. Andrey Andreev and Dr. Ahmed Elfrgani for their countless hours of valuable discussions and suggestions during group meetings. I very much appreciate Dr. Andreev, who extended a great amount of assistance from the day I started my Ph.D. project. His constructive criticism, insightful suggestions, and extensive knowledge were helpful to me throughout this project. I would also like to thank Professor Alexander Figotin,

Department of Mathematics, the University of California at Irvine, Irvine, CA, for his suggestions and valuable comments during joint group meetings.

For all the financial support needed throughout my Ph.D. journey, my gratitude extends to my advisor, Dr. Schamiloglu, as well as to AFSOR, AFSOR MURI Grant, and LANL Accelerator Science and Technology Graduate and Undergraduate Research Program.

My sincere thanks also go to my labmate Dmitri Andreev for providing motion into lab experiment. I also had the great pleasure of working with Christopher Rodriguez, Alexander Glick, and John Rose in the lab. Thanks also goes to my colleagues, Justin Smith and Seth Miller, for providing apparatus for my dissertation work. I extend my thanks to the wonderful staff members Cornelia Platero, Yvone' Nelson, and Carol Jimerson in the department of Electrical and Computer Engineering for always being so helpful, friendly, and for their administrative support throughout my degree program.

I cannot begin to express my thanks to my friends (too many to list here, but you know who you are!) who never let me down and helped me to complete this work whenever I found myself struggling with problems. I also very much appreciate my host family, Schea and Peter Freimanis, for their love, encouragement and patience with me throughout the past few years.

I especially thank my mom, who has sacrificed her life for my six siblings and myself with unconditional love and care. My hard-working mom was only 44 years when my dad passed on, and she has raised all seven kids as a single mom afterward. I also thank my six siblings for their love, encouragement, and support throughout my studies. Without their inspiration, I would not be where I am today.

ANALYTICAL, SIMULATION, AND EXPERIMENTAL STUDY OF THE GENERATION OF MULTIPLE BEAMS FOR APPLICATION TO A TRAVELING WAVE TUBE(TWT)

by

Khandakar Nusrat Islam

B.Sc., Electrical and Electronic Engineering, Eastern University,

Dhaka, Bangladesh, 2010

M.S., Electrical Engineering, University of New Mexico,

Albuquerque, NM, 2017

Ph.D. Engineering, University of New Mexico,

Albuquerque, NM, 2022

ABSTRACT

The traveling wave tube (TWT) has been a reliable conventional vacuum electron device (VED) since the 1940s. Researchers, beginning in the late 1980s, extended the TWT to the relativistic electron beam regime to generate 100s MW power in X-band. Since the mid-1990s there has been little advancement in the field. Recently, the linear theory of a multi-stream TWT was published that showed super-exponential amplification properties. This study describes a novel technique for producing multiple electron beams with energy difference of about 4-31% with comparable currents from a single cathode at a single potential for a multi-stream TWT. This work presents a new model of two nested cathodes where two annular electron beams are generated and propagate in a smooth cylindrical pipe immersed in a strong magnetic field. The two nested cathodes are magnetically insulated coaxial diodes (MICDs). The

simulation results are obtained using the MAGIC particle-in-cell (PIC) code for the experimental vacuum diode geometry of the SINUS-6 high-current electron beam accelerator at the University of New Mexico (UNM). Results are obtained which are then (i) compared with earlier experimental results for a single beam, (ii) study the current-voltage characteristics of two electron beams powered by a single cathode at a single potential immersed in a strong magnetic field, and (iii) show 4-31% energy difference with comparable currents between two beams.

The analytically derived results are obtained by extending Fedosov's solution for generating a hollow electron beam from an MICD on a cathode stalk in an infinite magnetic field. Two electron beams are generated and accelerated downstream assuming zero initial kinetic energy of the electrons from the cathodes. Results show both electron beam currents ranging from 66 A – 2.8 kA with an energy difference ranging from 4-31% depending on voltages applied from 100 – 600 kV and the geometry of the two MICDs. An optimal geometry is a crucial factor in achieving the maximum energy difference between the electron beams for comparable currents. The analytical and numerical simulation results show good agreement. Preliminary experimental results using the SINUS-6 electron beam accelerator to validate the analytical and simulation results will be presented. This technique is viable for pulsed power-driven, relativistic electron beams for a relativistic multi-stream TWT.

Contents

List of Figures

List of Tables

Nomenclature

ϵ_0 $[F/m]$	Permittivity of free space
η	e_0/m_e
ρ $[C/m^3]$	Charge density
E $[V/m]$	Electric field intensity
h $[m]$	Thickness of both cathodes
I $[A]$	Current
j $[A/m^2]$	Current density
n_e $[1/m^3]$	Electron density
p $[kg-m/s]$	Momentum
r_a $[m]$	Radius of anode
r_{ic} $[m]$	Inner radius of not infinitesimally thin cathode
r_{oc} $[m]$	Outer radius of not infinitesimally thin cathode
β	v/c
$\gamma = \frac{1}{\sqrt{1-\beta^2}}$	Relativistic factor

φ_a [volt]	Anode potential
φ_c [volt]	Cathode potential
c $[m/s]$	Speed of light
e_0 [Coulomb]	Electron Charge
m_e [kg]	Electron Mass
v $[m/s]$	Velocity

CHAPTER 1

INTRODUCTION

1.1 Introduction and significance of research

Multi-stream electron beam generation has recently been of great interest in high power microwave (HPM) sources [1–3], especially for a traveling wave tube amplifier (TWTA) with a slow wave structure (SWS) for efficiency enhancement. Recently, the linear theory of a multi-stream TWT was published that showed super-exponential amplification properties [4]. Over the last four decades, the need for high-efficiency-based TWTs, especially in the THz regime [5], has significantly increased for the application of high power devices specifically for satellite communication systems [6] [7]. In addition, achieving electron beam energy, possibly greater than 200 keV, is becoming crucial and a necessity in today's accelerator technology [8]. This study presents a technique for generating multiple electron beams with different energies and comparable currents from a single cathode at a single potential with application to relativistic TWTs [9], [10].

The TWT came to the limelight at the end of World War II, introduced by Dr.

Rudolph Kompfner, an Austrian refugee who was involved with British Admiralty at the time [11]. The very first TWT (helix prototype) was introduced by J.R Pierce at Bell Laboratories in the USA in 1945 [12]. Figure 1.1 shows a photograph of an early TWT being held by J.R. Pierce [13]. The application of these types of helix prototype TWTs was mainly for communications (i.e., satellite relays) [14]. Later, different types of TWTs (e.g., broadband, narrowband, coupled-cavity TWTs (CCTWTs), etc.) were developed [15]. The helix TWT started being widely used for broadband 'Electronic Counter Measures' (ECM) and multi-beam ECM transmitters [16].

Figure 1.1: J.R. Pierce holding an early TWT. The photograph is taken from 'My Work With Vacuum Tubes At Bell Laboratories,' by J.R. Pierce [13].

Narrowband helix TWTs are primarily used for satellite communications and broadcasting systems [17]. High efficiency and long-life time-based TWT transmitters are highly crucial to satellite communications [18]. CCTWTs were developed (at Stanford University) to produce high power, which later replaced the magnetron in

airborne radar systems [19]. In the modern age, pulsed klystron amplifiers of linear beam tubes are being used as a substitute for CCTWTs for the application of radar and uplink transmitters [20]. Cross-field amplifiers (CFAs) are also used in similar applications [21–24]. On the other hand, large-bandwidth gyro-TWTs are of great interest for use in radar systems at higher frequencies [25].

Solid-state devices are commonly used for low-frequency applications [26]. For high power, high frequency applications (typically >3 GHz), conventional tubes (i.e., TWTs [27], klystrons [28], magnetrons [29], CFAs [30]) are widely used in radar communications [31] [32]. These conventional devices include helix or coupled cavity SWSs, and the velocity of the electron beam is less than the speed of the light in these types of devices. Therefore, an SWS in these devices is used to slow down the phase velocity of the RF wave to slightly lower than the electron beam velocity [33]. Thus, energy transfers from electrons to the RF waves, and this transfer process takes place whenever the electrons are synchronous with the retarding RF fields [34]. On the other hand, fast wave tubes, such as high power millimeter-wavelength vacuum electron devices (HPmmWVEDs), do not slow down RF waves but instead use very high electron velocities [35]. A brief overview of the applications of high power microwave (HPM) tubes is shown in Table 1.1.

Figure 1.2 shows an overview of the present state of HPM devices of average peak power as a function of energy. These devices cover a wide range of applications needing low or high power, especially for a TWTA. This dissertation work is limited to the subject of non-conventional TWTs, focusing on understanding the beam dynamics of multiple electron beam TWTs rather than a single beam TWT. In conventional linear beam tubes, the electron beam propagates along a straight pipe focused by an axial magnetic field. In this case, one of the significant physics is that both electric field and magnetic fields are parallel to the beam axis and electron beam motion

Table 1.1: Overview of the applications high power tubes [11].

	Installation		
Application	*Surface*	*Airborne*	*Spaceborne*
1. Radar			
• search and surveillance[a]	TWT/CFA chain klystron CCTWT/twystron[b] magnetron	TWT	TWT or klystron
• fire control	TWT/CFA TWT	TWT magnetron	
• weather radar		TWT magnetron	
• missile homing		TWT	
2. Navigation beacons	magnetron (mostly replaced by solid-state)		
3. ECM	TWT	TWT	
4. Communications[c,d]			
• point-to-pont and mobile	TWTs replaced by solid-state	solid-state	
• Satellite uplink	TWT or klystron		
• Satellite down-link (transponders)			TWT (above the S band)
5. Broadcast	klystron (UHF TV) TWT/EIA (millimeter wave TV distribution)		TWT for TV
6. Scientific and industrial			
• Linear accelerator	klystron		
• Microwave heating	magnetron klystron		
• Instrumentation amplifiers	TWT		

a Phased array search radars at frequencies up to to the C band use solid-state transmitters.

b Twystron is a Varian tradename.

c Radar communications.

d Satcom and satellite TV broadcast bands.

becomes 1D. The significance of the parallel magnetic field, uniform in this case, will be discussed later in this chapter, which plays an important role in this study.

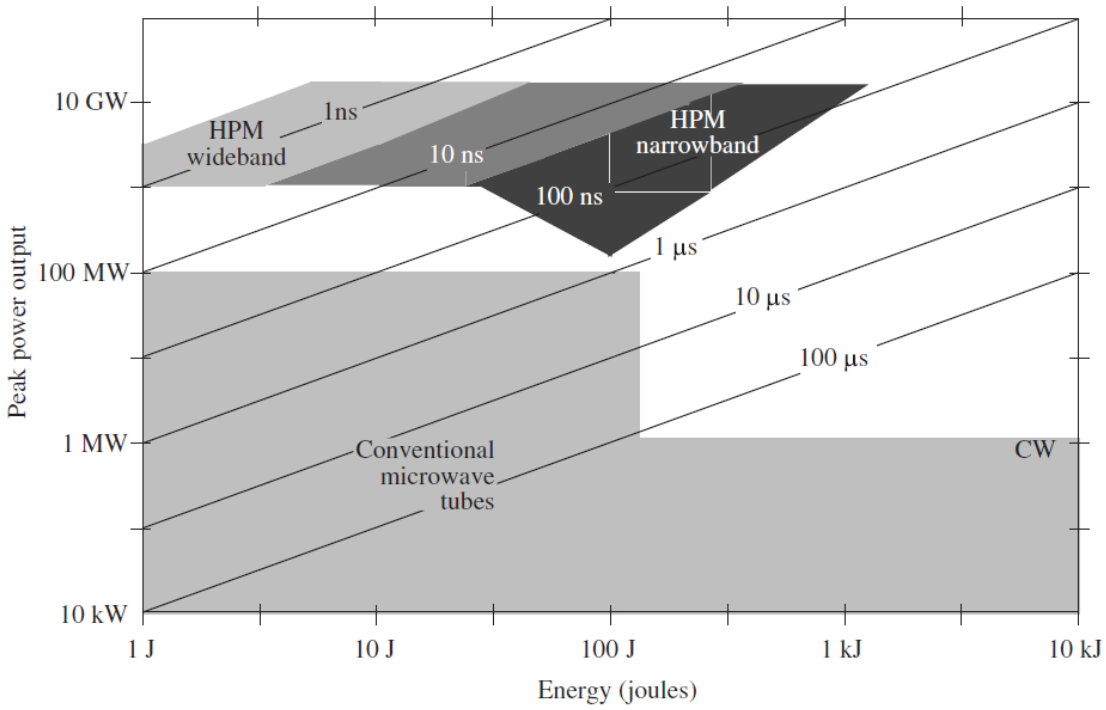

Figure 1.2: High power microwave source's peak power vs. energy [2].

Figotin has shown [4] using a linear theory that amplification in a TWT can be enhanced if it is driven by two or more electron beams with comparable currents and 10-20% energy difference. For multiple-stream electron beam generation in HPM sources [36], particularly TWTs, the first challenge is how to generate multiple beams with different energies and comparable currents from a single cathode stalk at a single potential driven by a pulsed power generator.

There has been some work done in the past (Chapter 2) that used multiple cathode sources to produce multiple electron beams in low power microwave sources where each cathode is powered using a separate power supply at different voltages. However, for HPM generation using a pulsed power generator [37], it is not practical to use separate power supplies to individually power separate cathodes. Therefore, we need

to identify a technique to generate multiple electron beams with different energies and comparable currents from a single cathode stalk at a single potential. The goal is to achieve a 10%-20% difference in energies from the two beams with comparable currents.

The concept of a two-beam amplifier was first proposed by Pierce [38] and Haeff [39], [40]. But both designs were for low voltages and used separate supplies to power two cathodes. There are some publications from Bell Laboratories (Hollenberg [41]) and from the Radio Corporation of America (RCA) (i.e., Neergard [42]), where actual designs of two-beam devices are shown. But they also used relatively low voltages and two electron guns and, thus, it is easy to implement using two separate power supplies. Recent publications by Los Alamos National Laboratory [43], [44] describe how the two-stream instability using counterstreaming electron beams can be used for THz generation. Another recent work describes a two-electron-gun-powered TWT [45], but at relatively low voltages.

To our knowledge, the only work similar to ours was published in 1979, but the earlier work just describes a technique to decrease the current in an electron beam generated from a low impedance driver [46], [47]. The authors used two nested cathodes to generate two electron beams, but they intercepted the outer beam and used the lower current inner beam in their application. They calculate the difference in currents between the inner and outer beams, but do not consider the self-consistent energies in the two beams. Our work, on the other hand, self-consistently calculates the currents from, and energies of, two electron beams generated from two nested MICDs at a single cathode potential for a high power TWT that has not been published elsewhere. Although extensive research has been carried out on high power technologies [48–50], no single study exists that describes a multibeam TWT amplifier powered by two cathodes on a single cathode stalk at a single potential with

10–20% energy difference and comparable currents.

One of the greatest challenges in designing an HPM multi-stream TWT amplifier is how to generate two or more electron beams with different energies and with comparable currents from a single cathode at a single potential driven by a pulsed power generator. This study presents a novel idea that uses two nested coaxial magnetically insulated coaxial diodes (MICDs) using the University of New Mexico's (UNM's) SINUS-6 electron beam accelerator [51] to generate two electron beams with 10-20% energy difference from a single cathode stalk at a single potential with comparable currents. The details of the SINUS-6 are shown in [52–54] as well as briefly described in Section 1.2.

The aim of this study is to contribute to this area by exploring the theory, simulation, and experiments of generating two beams with 10%-20% energy difference and comparable currents for use in a multiple electron beam TWTA, and ultimately, validate all three methods. The purpose of this study is not to overwhelm readers by explaining things that are already explained in detail elsewhere. Rather, the author will touch on some background information, such as an overview of the particle-in-cell (PIC) code used in simulation or the SINUS-6 apparatus used in experiment, which will be briefly described in Chapters 4 and 5, respectively.

1.2 SINUS-6 background

The very first high current (30 kA) intense electron beam accelerator was introduced by Graybill in the late 1960's [55], [56]. After that, in different laboratories in the US, research on pulsed, high-current electron beam accelerators with electron beam parameters continually increasing expanded [57], [58]. Over 30,000 accelerators (in-

cluding conventional ones) are currently in use worldwide [59]. The majority of these devices are used in healthcare and in industrial applications. Pulsed power-driven electron beam accelerators, on the other hand, find their use primarily in areas like radiography [60] and HPM generation [61]. The NAGIRA radar was based on a SINUS-class pulsed power-driven backward wave oscillator (BWO) [62]. These high current accelerators are capable of operating at high repetition rates through the use of their Tesla transformer technology [63]. It was found that by using a Tesla transformer with a pulse forming line, it is possible to generate pulse-periodic nanosecond electron beam accelerators of 1-5000 J stored energy and electron energy of 0.2-2 MeV with 4-40 nanosecond pulse duration and an average beam power $>$ 100 kW [64].

In contrast with traditional electron beam accelerators available at the time, in the early 1970s, a number of accelerators were developed at the High-Current Electronics Institute (HCEI) of the Siberian Branch of the Soviet Academy of Sciences under the leadership of Academician G. A. Mesyats in 1977 and given the name SINUS [65], which is a Russian acronym for *high-current accelerator*. These SINUS series accelerators were developed by the HCEI to perform some practical applications, including HPM generation [66]. The SINUS-6 is a model of SINUS accelerators that was built for Prof. Schamiloglu at UNM in the early 1990s as a collaboration between researchers at the HCEI and UNM [67]. Each of these series of accelerators has different parameters for different applications. The basic design of all types of SINUS accelerators is the same. The SINUS-6 can produce 10-15 ns duration electron beams [68]. The common principle of the SINUS accelerators is quick release of streaming charged particles as a form of energy that propagates downstream in a drift tube [69].

The SINUS-6 electron beam accelerator with major components can be seen as labeled in Fig. 1.3. The main components are charging device (a.k.a as Tesla trans-

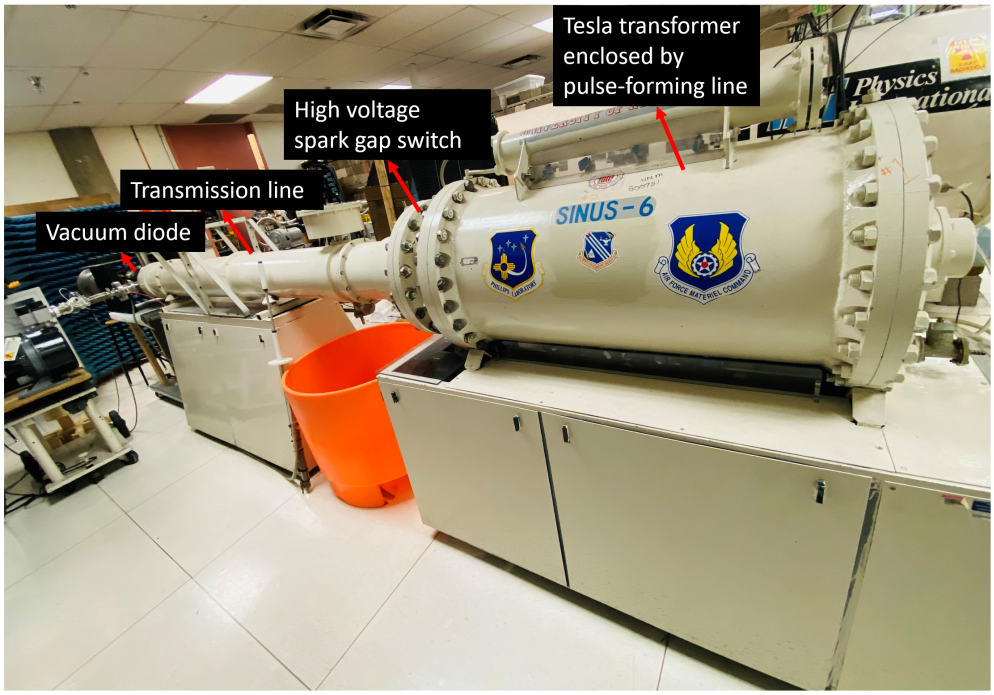

Figure 1.3: The SINUS-6 electron beam accelerator. (The photograph was taken in UNM's Pulsed Power, Beams, and Microwaves Laboratory, directed by Prof. Schamiloglu.)

former), energy storage capacitance which is basically a long oil filled coaxial line (a.k.a as pulse forming line), high voltage two or three electrodes spark gap switch, tapered transmission line (a.k.a wave transformer), and a vacuum diode. The vacuum diode is basically a cold explosive emission cathode or plasma cathode and it can be a planar, coaxial, or conical diode immersed in a strong magnetic field. Details of these cathodes are described in Chapter 5.

Among other types of cathodes [70], the cold emission cathode is found to be effective and most useful for high-current accelerators [71], [72]. Typically a coaxial diode is used in experiments for HPM generation [73]. The thickness of these cold, annular explosive cathodes is very thin. This thin emitting edge usually generates electron beams with sufficiently high electric field strength on the cathode's surface [74], about 10^7 V/cm, to cause explosive electron emission. Besides, different types of materials are used to generate high-current single pulsed electron beams [75], [76].

It is found that graphite explosive emission cathodes show the best performance in experiments [77], [78].

There are some disadvantages while conducting experiments using these type of accelerators. The whole process of beam formation, acceleration, and propagation is invisible from the outside. Most importantly, users cannot be close to the accelerators during operation because of x-ray hazard – they need to be inside the screen room. There are some complications in terms of taking measurements or related to diagnostics which are associated with these accelerators. The most challenging part, probably, is whether the beam is actually formed and aligned before taking any diagnostic measurements (a witness plate diagnostic is typically placed at the end of the uniform magnetic field region to view the imprint of the electron beam, verifying formation). In addition, it is challenging to directly measure the beam parameters. Another disadvantage of these accelerators is that they are large in terms of overall dimensions (*cf.* Fig. 1.3) and radiation shielding needs to be put in place where the electron beam dump is located since electrons, to conserve energy and momentum, cause the generation of Bremsstrahlung radiation there. Therefore, the diagnostics (i.e., beam formation, charged particle, beam position, beam current, cathode voltage, RF field, etc.) are very important, as they are termed the "eyes and ears" of the accelerators.

1.3 Magnetically insulated coaxial diodes (MICDs)

MICD is a terminology meaning magnetically insulated coaxial diode. It is a popular term dating back to the Soviet Union, and it describes a coaxial cathode immersed in an axial magnetic field along the tube. A simplified analytic model was developed by Fedosov *et al.* in 1977 [79] that describes the electron beam emitted from an

(a) **(b)**

Figure 1.4: Photographs of an (a) MICD immersed in a solenoidal magnetic field, and (b) MICD located inside of the vacuum tube.

MICD. This theory allows us to determine the current-voltage $(I-V)$ characteristics of an MICD by ignoring electron motion in the acceleration region. Friedman and Uri obtained the first experimental results related to an MICD in 1970 [80]. Fedosov derived the MICD theory for an infinite magnetic field. Later, Belomyttsev [81] extended the theory for a finite magnetic field. The main advantage of MICDs is they avoid the need for an anode foil in front of the cathode, which is extremely useful for applications where the beam can be extracted in a vacuum region. Therefore, the electron beam needs to be controlled and transported by an external applied magnetic field [82].

MICDs are the simplest configurations of several kA intense relativistic electron beam [83] sources. MICDs are commonly used in almost all relativistic O-type HPmmWVEDs driven by axially-propagating intense electron beams (e.g., BWOs [84–87], TWTs [88], [89], and multi-wave or overmoded Cherenkov generators [90]). MICDs of such HPmmWVEDs are usually tightly integrated with their electrodynamic systems, whose single specific purpose is transformation of relativistic electron

beam's kinetic energy into electromagnetic energy in the microwave and mm-wave regime with high power.

1.4 Overview of modeling of MICDs

The dissertation work is organized in three phases: analytic calculations, optimization simulations, and experiments (*cf.* in Fig. 1.5). Initial studies on generating two electron beams have been performed using a series of PIC simulations. To understand the underlying physics of the process of hollow electron beam generation, acceleration, and propagation in a uniform magnetic field from an MICD, first analytical calculations were performed, and PIC simulations were conducted for a single beam to validate the results with Fedosov's theory. Additionally, another benchmark simulation using ICEPIC [91] is performed to clarify the analytically derived Fedosov's solution with the results of actual experiments obtained from an MICD driven by the SINUS-6 accelerator. All computer simulations of an MICD are performed for a cylindrical cathode with an outer radius of 9 mm and 11 mm, and a grounded cylindrical smooth-walled waveguide with an inner radius 25 mm immersed in a strong axial magnetic field 3 T for input SINUS-6 voltages ranging from 100-600 kV. Results of both MAGIC and ICEPIC simulations and subsequent analyses of hollow electron beam parameters in an MICD show that both the analytically calculated "Fedosov" potential and "Fedosov" current almost perfectly correlate with results obtained in numerical simulations for maximum axial kinetic energy distribution of the beam electrons and transported electron beam current. Comparison of experimental measurements, PIC simulations, and analytical calculations shows very good agreement between all three [91], [92].

Agreement between simulation, analytical theory, and experiments for a single

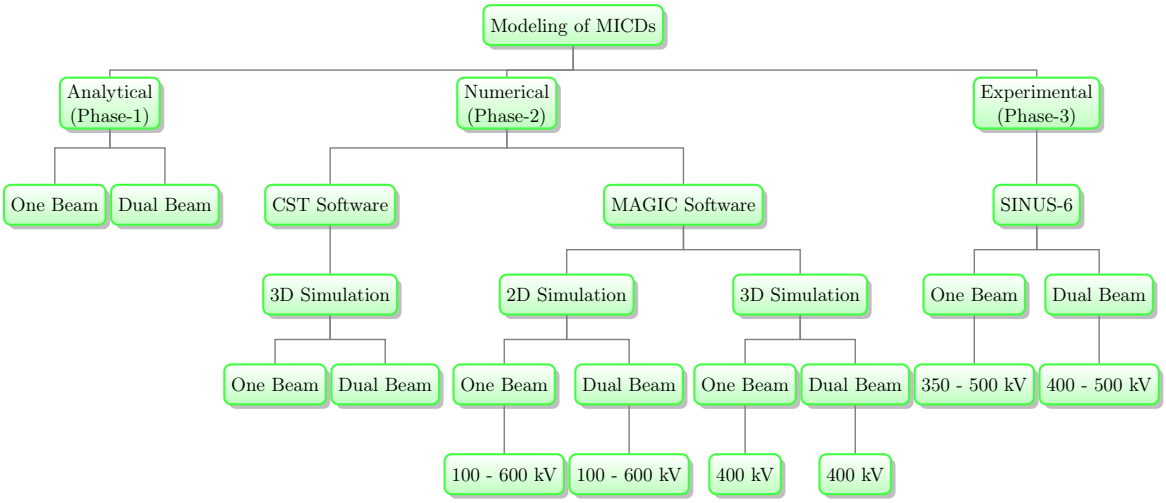

Figure 1.5: Overview of the modeling of nested MICDs.

beam helps to further study of understanding the process of nested MICDs, and electron beam generation, acceleration, and propagation in a drift tube. Two PIC codes are used in this research. Initially, the 3D simulation tool 'CST Particle Studio' PIC solver was used to simulate an annular explosive ring cathode in a straight pipe. Using CST was a viable alternative compared to other available PIC codes for a quick check, particularly on a small-scale-based geometry. The purpose of using the CST PIC solver was to design and investigate whether two electron beams can be produced from two explosive cathodes in a vacuum cylinder by applying a negative potential to the cathodes. Then the geometry was assessed numerically and we considered alternative geometries where two different energies can be achieved in this set-up. A number of CST simulations were performed based on different shapes of cathodes which are discussed in Appendix B in this study. No significant energy difference was found between the electron beams in these simulations. In addition, CST Particle Studio takes a very long time to run 3D simulations.

Afterwards, the MAGIC PIC code was used to further explore the geometry numerically. The initial MAGIC simulations were performed in 2D using two nonphysical power supplies to power the two cathodes. Another attempt was to use a foil

made of gold in front of the cathode to decrease one of the beams' energy to achieve an energy difference between the inner and outer electron beams. The results from these simulations point to the probability of a significant amount of energy spread due to the foil in addition to beam reflection from the foil. In addition, to further understand this problem, some simulations using the GamBet 2D Monte Carlo were performed by Dr. Portillo at UNM on different materials (i.e. C, Al, W). The Monte Carlo simulations revealed that both C and Al can reduce the energy of one of the beams going through the foil by 15%, but the energy spread due to the foil is large and the large beam emittance, as a result, could be a major concern. This finding led us to modify the model by eliminating the foil, and to design and evaluate a geometry to generate two beams from nested MICDs and compare the results with analytical calculations and experiment results.

1.5 Novel technique of nested MICDs at UNM

The purpose of this study is to specifically explore the relationship between the current-voltage and energy-voltage characteristics of intense multiple beam generation from nested MICDs, and their subsequent acceleration and transport in a smooth cylindrical vacuum channel. In order to gain greater understanding, this research follows a case study plan, with in-depth analyses of analytical theory and PIC simulations based on parameters relevant to experimental work. The analytical and simulation work presented here provide new insights into high power dual-beam technology.

In phase 1, the analytical derivation was performed by extending the conceptual framework proposed by Fedosov [79] for a single MICD to two MICDs. Fedosov's theory is a well-known theory that calculates the current and energy at the boundary

of an intense thin-walled electron beam immersed in an infinite magnetic field and transported in a vacuum channel. The theory was extended later by Belomytsev *et al.* [81] for the application of finite magnetic field and the estimation of external finite magnetic field also validates the approximation of an infinite magnetic field. As in the simulation model, the same geometry of two nested MICDs connected to a single cathode stalk at a single potential was used to perform the analytical derivation. The most remarkable finding was that the analytical theory and simulation results for multiple beam generation match each other extremely well. In both cases, there is about a 4-31% energy difference between the inner and outer electron beam for an applied voltage ranging from 100 - 600 kV and for different inner cathode radial positions.

In phase 2, a case study approach was followed to identify an optimal geometry from this nested MICD model. There are three main designs used to find the optimal geometry based on the axial and radial variations of the inner cathode position with respect to the outer cathode. The first case is where we fix the anode dimension and the radial and axial position (r, z) of the outer cathode based on the parameters used on the SINUS-6 electron beam accelerator. To begin with, the inner cathode radius is assumed to be halfway between the axis at $r = 0$ and the fixed outer cathode's radius. Initially PIC simulations are performed with the inner cathode's axial position identical to the outer cathode's axial position. Then the axial position of the inner cathode are scanned by increasing it a distance d beyond the axial position of the outer cathode. In the second case, a similar procedure is followed by sweeping the inner cathode's radius by $\frac{1}{4}$ and $\frac{3}{4}$ of the outer cathode's radius and scanning axially with respect to the outer cathode. Our goal was to assess the trends and to identify the optimal position from these cases where we can achieve comparable currents or minimum difference in current but maximum separation of energy with more than 10% energy difference between the two electron beams being the goal. The most

striking result from this series of simulations is that the two electron beam currents are comparable at a particular radial position of the inner cathode for fixed outer cathode position and the maximum energy difference of about 10% is achieved at that particular point as well. We will see that this radial position of the inner cathode is precisely what was found in the analytical theory as well.

An explanation for why two nested MICDs mounted on a single cathode stalk at a single potential generate two electron beams with different energies and comparable currents is that the electron beam space charge from the outer cathode screens the inner electron beam emitted from the inner cathode, thereby reducing the inner electron beam's energy. To verify this, the opposite configuration is tested where the inner cathode no longer extends beyond the axial position of the outer cathode. In this case, we observe that the current from the inner electron beam reduces to zero and the current from the outer electron beam increases to the Fedosov current for a single MICD.

In phase 3, given the constraints, it was not possible to complete the planned experiments. The completed part of the experiment - (i) all cathodes with different diameters were fabricated as mentioned in the analytic and simulation sections, (ii) maximum electron beam current extracted from a single beam was measured using a Rogowski coil placed at the input of beam source, (iii) emitted current is measured by a Faraday cup (FC) placed at a certain distance from MICDs to the output end of the vacuum tube, and (iv) two concentric beam rings were observed from the nested MICDs.

The total process of the generation of a high-current electron beam from MICDs in the drift space can be divided into three regions (*cf.* in Fig. 1.6). This dissertation work particularly focus on regions 2 and 3. Region 1 is explained briefly in Chapter 5, where the accelerating voltage is applied to the MICDs for electron beam generation

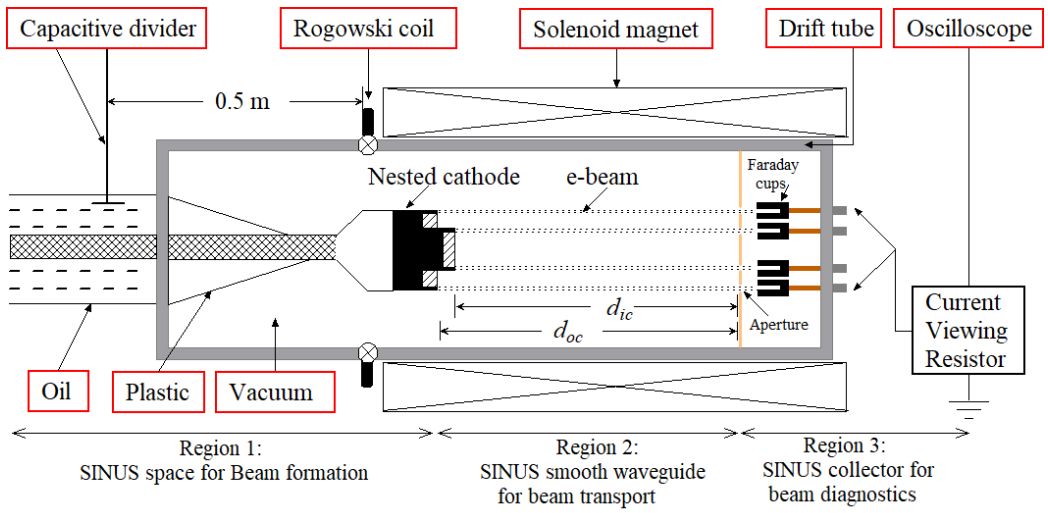

Figure 1.6: Schematic of the SINUS-6 electron beam accelerator showing 3 regions of beam formation, transport, and beam diagnostics.

and measured upstream in the oil-filled line using a capacitive voltage divider. In region 2, the beam is formed after it is emitted from the edge of the MICD and transported downstream in the smooth cylindrical waveguide immersed in a strong magnetic field. In region 3, a 'FC array (FCA)' is set-up at the end of the output window in such a way to obtain electron beam current from each beam separately. The goal here is to measure the maximum in pulsed electron beam current by dumping the electron beam into the FCA at some distance from the cathode. Once the current from each beam is known, a very small aperture 0.1 mm diameter will be placed in front of the FCA to measure the electron current density of each beam. The energy of the two beams can be estimated from the current densities measured by the FC. These experimental measurements will then be shared with our MURI collaborators at UC Irvine and will inform the beginning of a TWT design using the SINUS-6 electron beam accelerator.

1.6 Scope of dissertation

Our knowledge of two-beam high power amplifiers is primarily based on very limited publications on the subject. This study aims to broaden the present understanding of this field and develop a model of a device capable of generating two electron beams with 10-20% energy difference and comparable currents from a single high power cathode stalk at a single potential. The initial goal was to develop an analytic theory by reviewing the existing MICD theory for a single beam formulated by Fedosov that calculates the electron beam current and electron beam potential at the electron boundary of an MICD. Reviews of existing MICD theories can be found in Section 3.1.

This study focuses on the modeling and simulation of how to generate two electron beams with 10-20% energy difference and comparable currents from a single cathode stalk at a single potential. Generating multiple beams with different energies and comparable currents from a single power supply will be a breakthrough for the HPM community. The ultimate goal in this study is to enhance innovation in the electron beam accelerator community by designing a nested cathode with a given potential of up to 400-600 kV that can generate 10-20% energy difference and comparable currents of about 2-3 kA from a single cathode stalk at a single potential for application to a high power TWTA.

1.6.1 Chapter organization

The dissertation outlines in the following manner:

Chapter 1 - Introduction and Significance of Research: This chapter de-

scribes the significance of the research of multibeam generation for application in TWTs, a short review of applications of conventional TWTs, an overview of a dual-beam-driven TWT and why it is important to study this topic.

Chapter 2 - Literature Review: This chapter reviews the literature of conventional multi-beam TWTs and their applications.

Chapter 3 - Theoretical Considerations: This chapter illustrates the geometrical configuration of nested MICDs and presents a step-by-step mathematical derivation of the key results.

Chapter 4 - Particle-in-Cell Simulations: This chapter depicts the problem geometry of the simulation model in MAGIC, the 2D (2-dimensional) and 3D (3-dimensional) PIC code that is validated by analytical calculations.

Chapter 5 - Preliminary Experiments: This chapter presents a brief description of key components of the SINUS-6 electron beam accelerator, a detailed description of the hardware part, describes the diagnostic set-up at the output vacuum window, and reviews preliminary experimental results.

Chapter 6 - Analysis of Results: This chapter presents the results and analyzes the results from analytical theory, PIC simulations, and experiments.

Chapter 7 - Conclusion and Future Work: This chapter concludes the study by summarizing the results and suggesting future work.

Appendices - The appendices (Appendix A, Appendix B) contain detailed mathematical derivations and a set of data including diagrams, simulation results, and experimental results pertinent to the dissertation work, but are excluded from the document's main body to avoid clutter.

CHAPTER 2

LITERATURE REVIEW

To-date, there has been very little work done on dual-beam amplifiers. More importantly, related to the subject of multibeam generation, most of the research focuses on two cathodes powered by two different power sources. Hence, it is easy to implement two separate power supplies.

The very first two-stream amplifiers were proposed by Pierce and Haeff at about the same time, as can be seen in Figs. 2.1 and 2.2. In addition, a mathematical analysis of a two-stream growing wave tube amplifier was published by Neergard [42]. The Pierce design was a two-stream driven amplifier installed with two separated coaxial tubular cathodes connected to two separate power supplies. An input resonator R_1 with an input line L_1 is set-up at a certain distance in front of the cathodes and similarly an output resonator is installed at the end of the tube to collect the output power. The electron beams emitted from the cathodes with different velocities pass through the grids of the input resonator. Therefore, the space charge wave grows in the space between the input resonator and output resonator. The output power is collected by the output line L_2 as can be seen in the original structure (*cf.* in

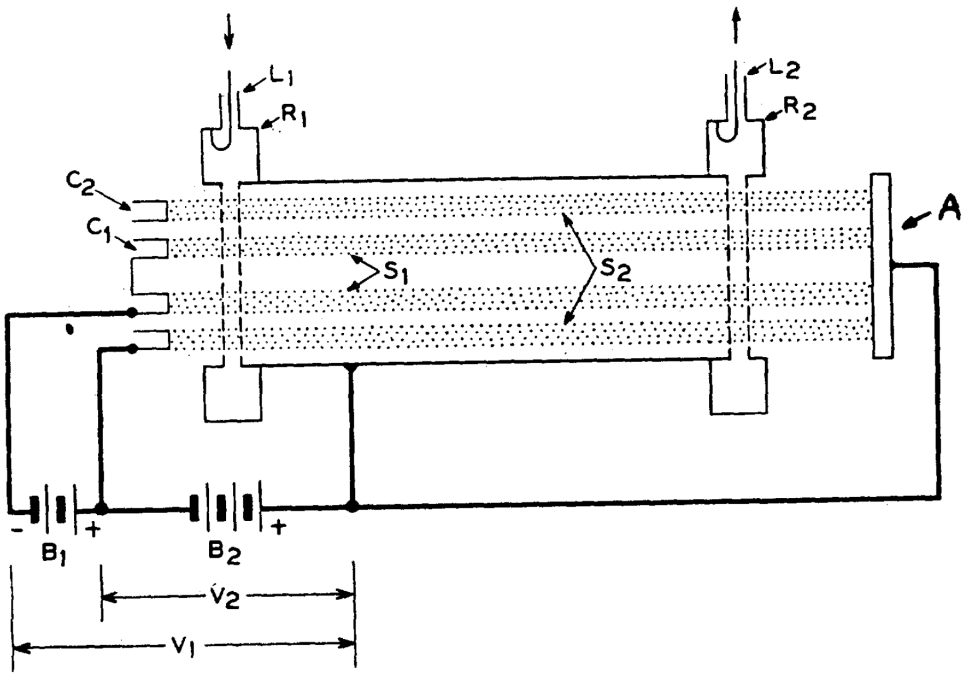

Figure 2.1: Two-stream amplifier designed by Pierce [38].

Fig. 2.1). The literature has highlighted brief theoretical calculations to compute the two-stream amplifier's gain by emphasizing the separation of the two-streams. However, the theoretical study shows this device is effective for low voltages of on the order of 1 kV connected with two separate power sources.

In contrast, Haeff's work shows a theoretical and an experimental study to generate high-frequency energy without using any resonant circuit or separate waveguide structure. Like Pierce, Haeff also used two separate cathodes in a long drift tube (hollow tube) to generate two beams with two different velocities by using two separate power supplies. The calculation of gain was obtained by adjusting the potential between the cathodes and the anode potential. The configuration can be seen in Fig. 2.2.

A design similar to ours with two annular cathodes to generate two electron beams by Hollenberg [41], but for low voltages and using two separate power supplies is shown

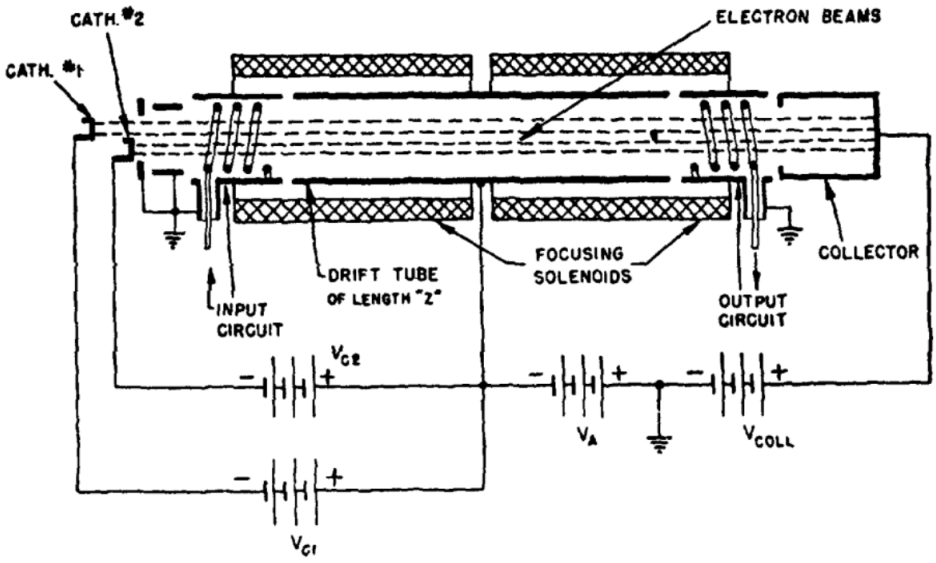

Figure 2.2: Two-stream amplifier designed by Haeff [39].

in Figs. 2.3 and 2.4. In this experimental study, two hollow tubular beams are used, and two streams interact with each other with different velocities. As can be seen in Fig. 2.4, the interaction happens at relatively low voltages (from 50 to 60 V) in the double-stream interaction region as labeled.

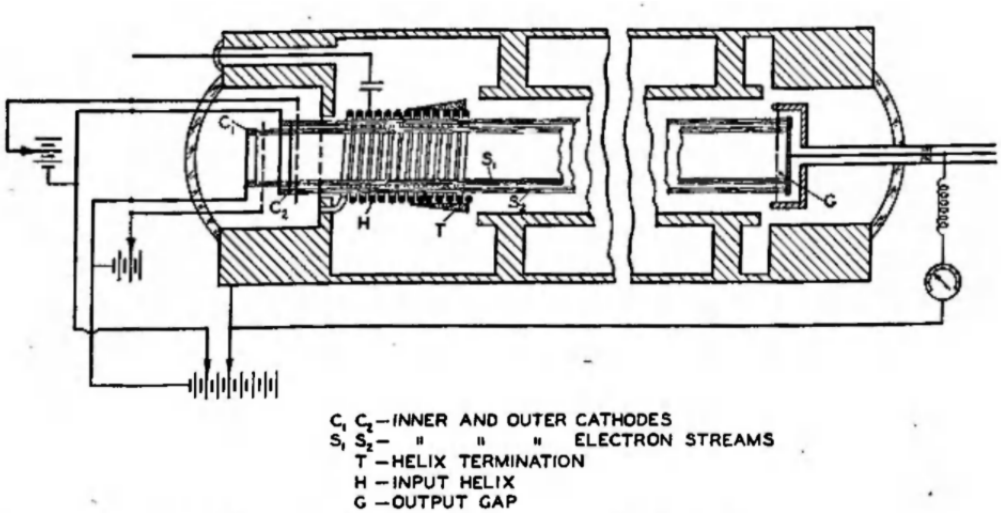

Figure 2.3: Two-stream traveling wave tube designed by Hollenberg [41].

In related work, a detailed theoretical study on the diocotron instability and its growth rate was developed by Chen and Palmadesso (*cf.* in Fig. 2.5). The config-

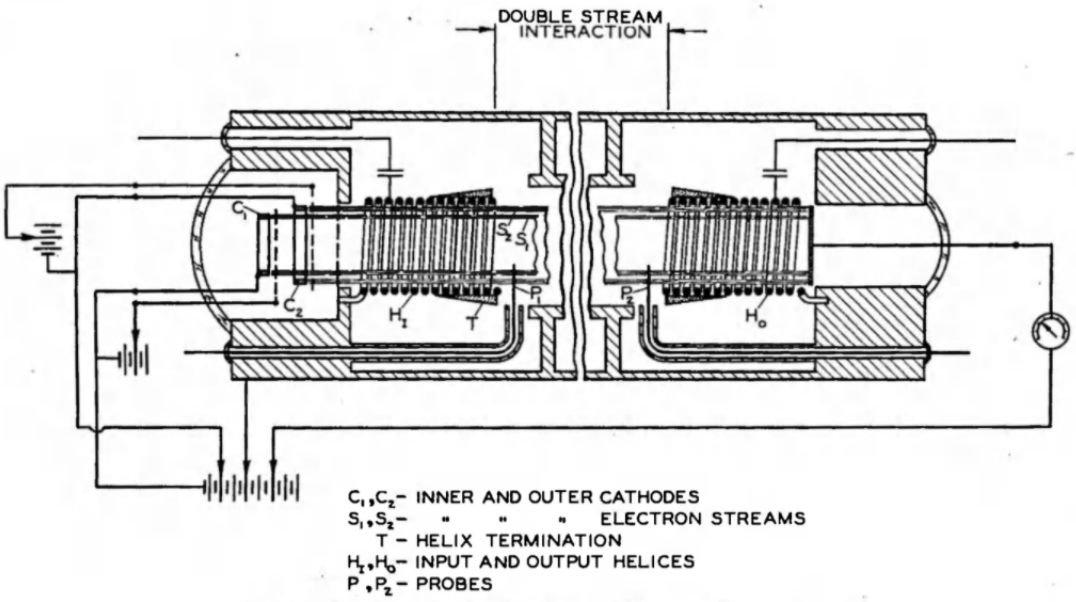

Figure 2.4: Two-stream helix traveling wave tube designed by Hollenberg [41].

uration is a simple geometry with two ring type beams inserted in a hollow tube in a strong uniform magnetic field. The article presents a detailed theoretical and numerical analysis of the two-ring based beam geometry.

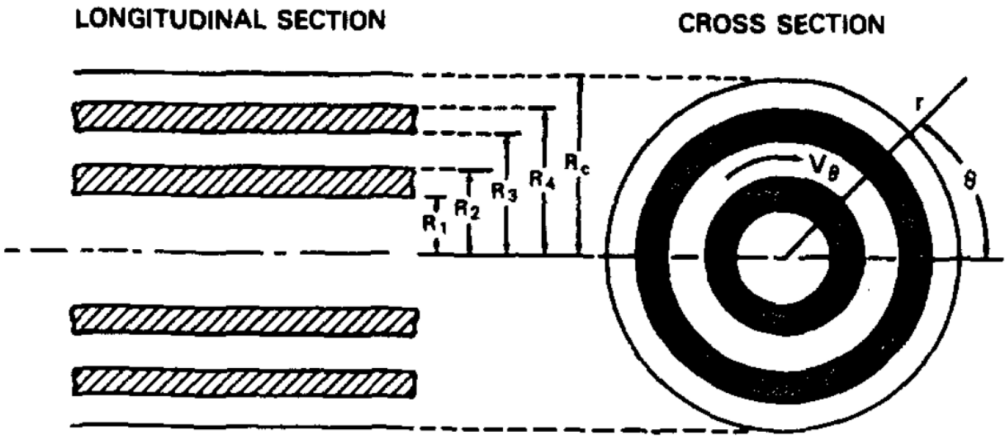

Figure 2.5: Two beam device designed by Chen and Palmadesso for studying the diocotron instability [93].

The approach that we are pursuing to generate two coaxial electron beams with 10-20% energy difference and comparable currents is based on two nested MICDs. Therefore, Fedosov's solution provides the theoretical foundation for its analytical

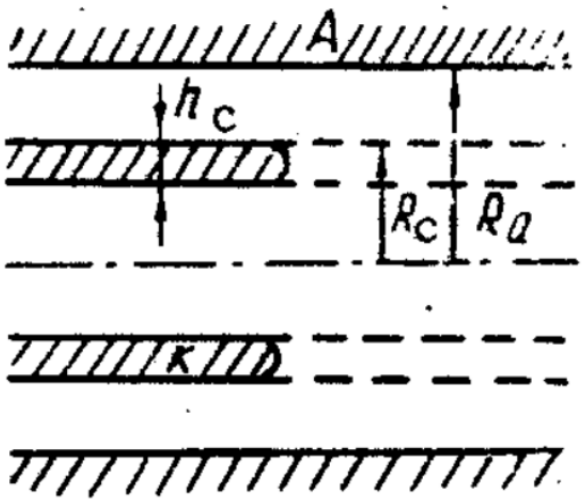

Figure 2.6: The original MICD geometry used by Fedosov in his calculation [79].

study. Fedosov's solution is based on a simple coaxial diode based geometry as can be seen in Fig. 2.6. A thin coaxial cathode (thickness $\sim h_c$) is inserted into a tube. The radius of the anode is R_a, the radius of the cathode is R_c, which includes the thickness of the beam, as shown in Fig. 2.6. There is no foil in this configuration and the entire system is immersed in a uniform external magnetic field. Fedosov developed a simplified analytic (magnetically insulated diode) MID theory that provides MID $I-V$ characteristics without consideration of electron motion in the acceleration region.

In Fedosov's calculation, the cathode is at ground potential and the anode is biased to a positive high voltage. Fedosov calculates the electron beam current and energy with a given potential in the system by taking into account the two boundary conditions at the anode and cathode: at the anode, $\gamma = \gamma_a =$ constant and at the cathode, $\gamma = 1$. By assuming a very thin beam, and self consistently solving Poisson's equations Fedosov's final solution gives the relativistic factor $\gamma_b = \sqrt{\frac{1}{4} + 2\gamma_a} - \frac{1}{2}$ at the external boundary of the beam in the tube. γ_b basically determines the current $I_b = I_0 \frac{(\gamma_a - \gamma_b)\sqrt{\gamma_b^2 - 1}}{2\gamma_b ln(\frac{r_a}{r_b})}$ and energy $E_k = \frac{c^2}{\eta}(\gamma_b - 1)$ of the electron beam emitted from

the MICD [26]. Therefore, Fedosov's calculation tells us what the beam current and energy generated from a coaxial cathode for both the relativistic and non-relativistic cases.

Recent work on a two-electron gun-powered TWT can be seen in Fig. 2.7 where two beams interact with each other for amplification and generation of microwaves radiations. According to the authors, two electron beams collide with one another with different velocities, and this leads to microwave generation and amplification in the longitudinal interaction region with internal feedback to the flow [45].

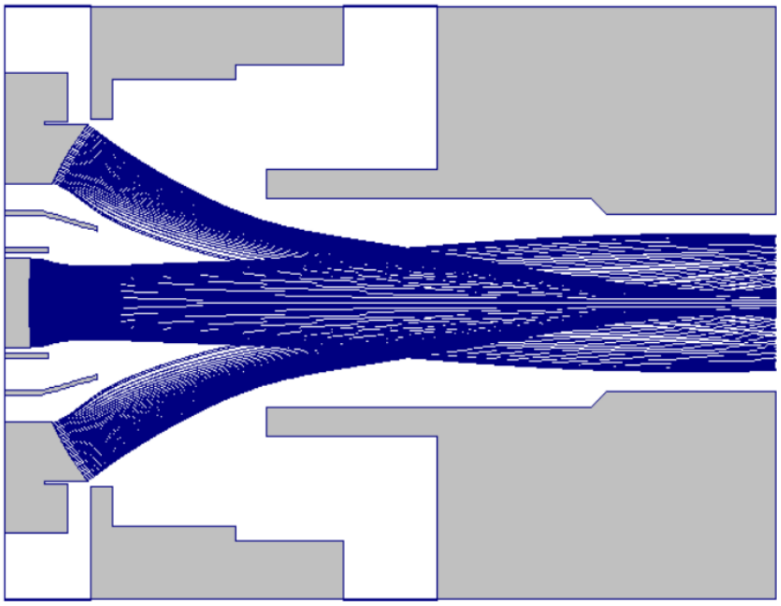

Figure 2.7: Two-stream TWT amplifier designed by Mozgovoi *et al.* [45] where two electron beams (middle blue is longitudinal beam and side blue beam is a passing beam) collide with each other with different velocities.

A publication by LANL [94] describes how the two-stream instability is used in a two-stream amplifier in the THz regime (*cf.* Fig. 2.8). This design is slightly different from other conventional two-stream designs. In this case, two separate electron guns with slightly different energies are injected into the device and amplification due to the two-stream instability occurs in the interaction region, as can be seen in Fig. 2.8.

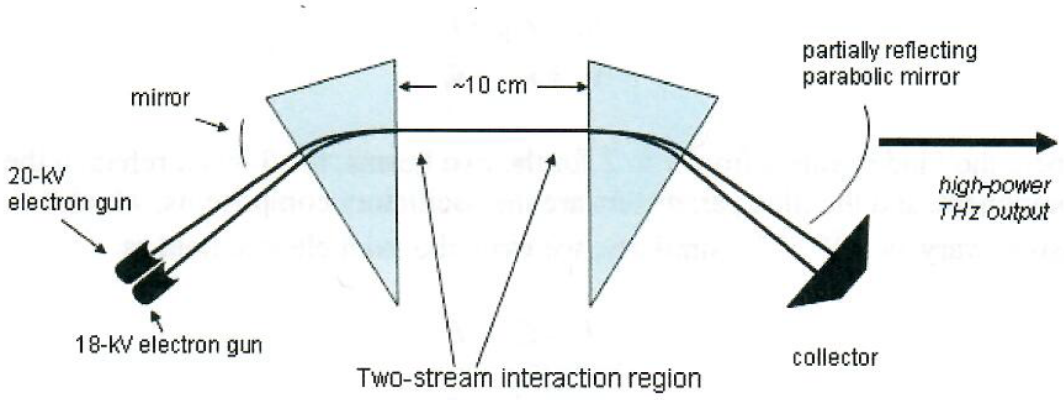

Figure 2.8: Two-stream amplifier designed by Carlsten *et al.* [94].

Again, this is also for low voltages and two separate power supplies are used to generate the two beams.

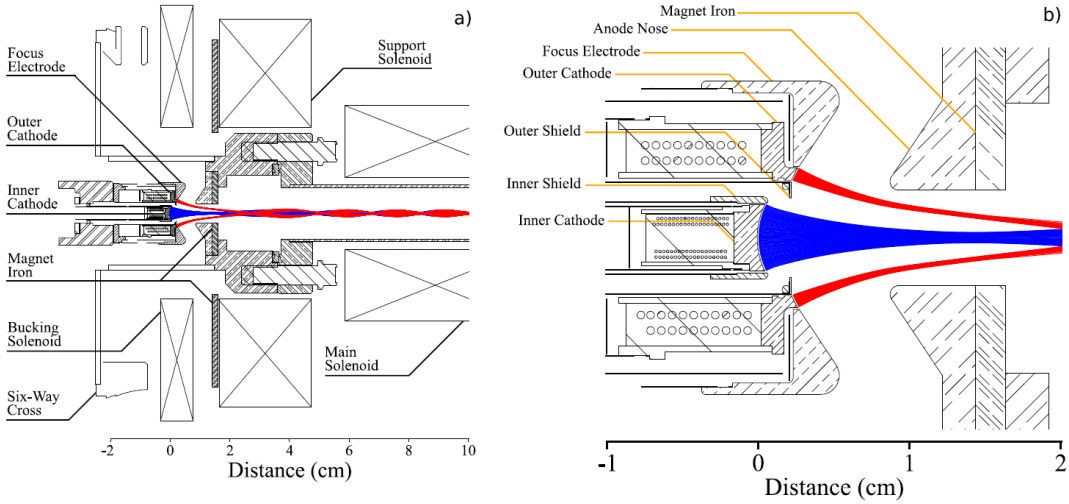

Figure 2.9: Two electron guns designed by Neben *et.al* where (a) two electron guns (middle blue is from inner cathode, red beam is from other cathode) with respect to the beam line and focusing solenoids, and (b) the cathode design, independently separated with inner (blue beam) and outer (red beam) shields in relation to the anode [44].

A very similar design of two coaxial beams nested in each other but independently separated with inner and outer shields is described by Neben *et al.* [44] (*cf.* in Fig. 2.9). This nested configuration is designed for broadband millimeter-wave RF applications utilizing the two-stream instability at low energies. The configuration seems to use confined flow focusing (magnetic flux threads through nested cathodes) rather than

Brillouin focusing, where magnetic fields are only introduced at the gun exit.

In the next chapter we delve into the analytical derivation for two nested MICDs.

CHAPTER 3

THEORETICAL CONSIDERATIONS

Intense electron beam formation in a vacuum drift tube is a complicated process [95] due to the strong space charge and self magnetic field of nanosecond pulsed duration electron beams, and intensive study on this field is still ongoing [96], [97]. In addition, space-charge-limited (SCL) current needs to taken into account. The SCL current is one of the most important phenomena in charged particle beams, especially in the relativistic case [98]. An analytic theory for the SCL current for a relativistic electron beam in a drift tube was developed in the 1970s [99]. A recent study on the partial SCL current for an edge-type MICD by Belomyttsev *et al.* [100] develops a mathematical basis that agrees with the previous theory and experimental results. The SCL current for a finite length drift tube has recently been studied by [101], [102]. In addition, a detailed analytic theory of the SCL current of a relativistic annular beam in a vacuum or smooth cylindrical waveguide (similar problem geometry illustrates in Fig. 3.1b) is briefly discussed in the books by Miller [57] and Tsimring [26].

A comprehensive study of the SCL current for the fully relativistic case is beyond the scope of this dissertation. This study, rather, focuses only on the possibility of the formation of two electron beams with different energies and comparable currents from a cathode at a single potential powered by a single power supply. Therefore, this section reviews the existing simplified analytic theory of an MICD by Fedosov *et al.* [79]. Simulation results from PIC codes and previous experimental results are also discussed following the MICD derivation. After reviewing the theory of an MICD for a single beam, the analytical derivation is extended for two nested MICDs. Results from PIC simulations and preliminary experimental results are also presented for validation.

3.1 Review of the theory for a single MICD

Fedosov basically modified and simplified the analytic theory of a magnetically insulated diode (MID). The theory allows us to obtain the $I-V$ relationship by neglecting electron motion in the acceleration region and he assumed the magnetic field to be infinite. The theory was later extended by Belomytsev *et al.* for the application of a finite magnetic field and the estimation of external finite magnetic field also validates the approximation of an infinite field [81].

The geometry of the MICD problem can be seen in Fig. 3.1. The author followed the notation for a cylindrical coordinate system (ρ, ϕ, z) (*cf.* in Fig. 3.1a) according to the ISO [103] standard. Figure 3.1b shows the axisymmetric cylindrical configuration for intense electron beam formation and propagation down the cylindrical tube with an external applied magnetic field parallel to the beam axis where cylindrical coordinates (ρ, ϕ, z) show that the $z-$axis is the symmetry of the geometry and Fig. 3.6 shows the schematic of MICD as labeled.

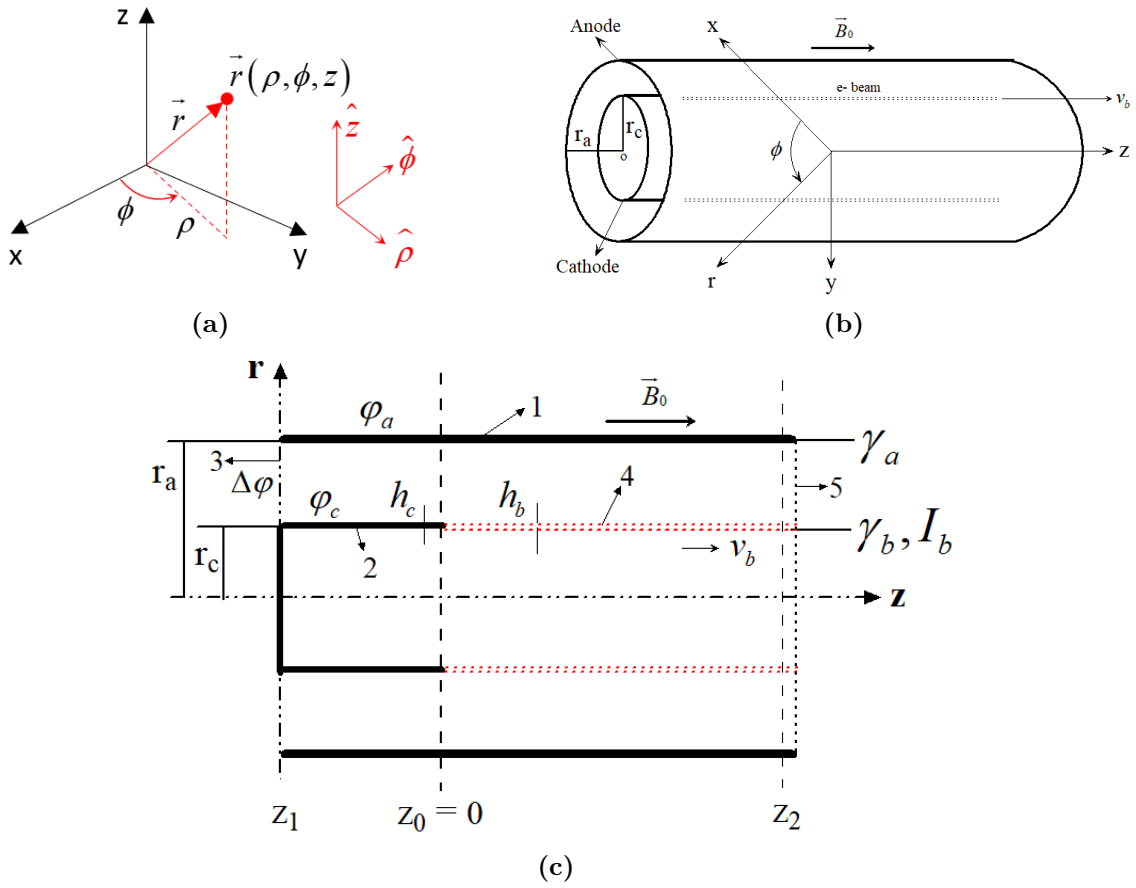

Figure 3.1: (a) Cylindrical coordinates followed for the geometry problem, (b) axisymmetric cylindrical configuration assuming intense electron beam propagation down the cylindrical tube with an external applied magnetic field strength parallel to the beam axis; cylindrical coordinates (ρ, ϕ, z) show that the $z-$axis is the symmetry of the geometry, and (c) MICD, cylindrical polar coordinates (r,θ) employ the $z-$axis coinciding with the symmetry axis. 1. Anode; 2. Annular Cathode; 3. Input Port; 4. Electron Beam; 5. Output Port.

Consider a very thin annular beam with radius r_b and a cylindrical anode (conductor) with radius r_a. The thickness of the beam must be much less than both the beam radius r_b and the gap r_g between r_a and r_c. Theoretically, in Fedosov's [79] calculation, the potential at the cathode's surface is taken as zero and the potential of the cylindrical surface as φ_a. Therefore, the potential difference between the anode's and cathode's surface will be $\Delta\varphi$, as shown in Fig. 3.1c. The electron beam propagates through the cylindrically symmetric drift tube with velocity v_{b_z} and non-zero $z-$components of electron space charge density $j_z = -\rho_z v_{b_z}$, where j_z is the constant

current density of the electron beam. An infinite uniform magnetic field is applied longitudinally to the beam axis. Since the motion of the electron in the acceleration region is not considered [79], [81], in this case the electron beam motion is 1-D (i.e, $v_\rho = v_\phi = 0$). We start with Poisson's equation [104] (from Maxwell's equation in free space and for the electric potential φ),

$$\nabla \cdot \mathbf{E} = \frac{\rho}{\epsilon_0}, \qquad \mathbf{E} = -\nabla\varphi \tag{3.1}$$

$$\nabla^2\varphi = -\frac{\rho}{\epsilon_0}. \tag{3.2}$$

Equation 3.1 can be expressed in a cylindrical coordinate system as

$$\frac{1}{r}\frac{\partial}{\partial r}\left(r\frac{\partial\varphi}{\partial r}\right) + \frac{1}{r^2}\frac{\partial^2\varphi}{\partial\theta^2} + \frac{\partial^2\varphi}{\partial z^2} = -\frac{1}{\epsilon_0}\rho(r,\theta,z). \tag{3.3}$$

In Eq. 3.3, all of the physical quantities are assumed to be time dependent, and therefore, the continuity equation tells us that the current density can be written in the form of electron velocity times electric potential as $j(z) = -e_0 n(z) v(z)$, which is a constant. Here, $j(z)$ is the current density in ampere per square meter (A/m^2), e_0 is the elementary electron charge in Coulombs (C), $n(z)$ is the electron density in per cubic meter (m^{-3}), and $v(z)$ is the the axial velocity in metres per second (m/s).

According to the conservation of energy, where the potential energy plus particle kinetic energy must be equal to the applied cathode/diode potential [57],

$$e_0\varphi(r) + (\gamma - 1)mc^2 = -e\varphi_c, \tag{3.4}$$

where $\gamma = \frac{m}{m_e}$ and φ_c are at a negative cathode potential. Rewriting the variables φ

and γ in terms of η, where $\eta = e_0/m_e$ and v respectively, we obtain

$$\varphi(r) = \frac{c^2}{\eta}(\gamma - 1). \tag{3.5}$$

The relativistic mass is given by

$$m = \frac{m_e}{\sqrt{1 - \frac{v^2}{c^2}}}. \tag{3.6}$$

Therefore,

$$\gamma = \frac{1}{\sqrt{1 - \frac{v^2}{c^2}}}, \qquad \text{where} \quad \frac{m}{m_e} = \gamma, \tag{3.7}$$

or

$$v = c\sqrt{1 - \frac{1}{\gamma^2}}. \tag{3.8}$$

We will also need the relativistic momentum equation, given by

$$p = m\gamma v \tag{3.9}$$

or

$$p = mc\sqrt{\gamma^2 - 1}. \tag{3.10}$$

The beam equations and the boundary conditions for the geometry of the problem are given by

$$(\nabla \times \mathbf{E})_\theta = 0 \tag{3.11}$$

$$\frac{\partial \mathbf{E}_r}{\partial z} - \frac{\partial \mathbf{E}_z}{\partial r} = 0 \tag{3.12}$$

$$\frac{dp}{dt} = -e_0 E_z \tag{3.13}$$

$$j = -\rho v \tag{3.14}$$

$$(E_z)_{r=r_c,z<0} = 0 \tag{3.15}$$

$$(p)_{r=r_c,z=0} = 0 \tag{3.16}$$

$$(\varphi)_{r=r_c,z<0} = \varphi_c = 0 \tag{3.17}$$

$$(\varphi)_{r=r_a} = \varphi_a. \tag{3.18}$$

To obtain the electric field in the axial and radial direction, we can relate Maxwell's equation 3.1 with the momentum equation 3.13. The resultant equation is

$$-e_0 E_z(\nabla \cdot E) = \frac{\rho}{\epsilon_0}\frac{dp}{dt}. \tag{3.19}$$

Assuming a steady-state solution when the electron beam velocity does not vary with time, $v = \frac{dz}{dt}$, and substituting Eq. 3.14 into 3.19 results in

$$E_z(\nabla \cdot E) = -\frac{-j/v}{e_0\epsilon_0}\frac{dp}{dz}\cdot\frac{dz}{dt} = \frac{j}{e_0\epsilon_0}\frac{dp}{dz}. \tag{3.20}$$

Using the identity

$$f\nabla\cdot\vec{A} = \nabla\cdot(f\vec{A}) - \vec{A}\cdot\nabla f, \tag{3.21}$$

the left hand side of Eq. 3.20 can be rewritten as

$$E_z(\nabla \cdot E) = \nabla\cdot(E_z\vec{E}) - \vec{E}\cdot\nabla E_z. \tag{3.22}$$

For a cylindrical polar coordinate system (r,θ,z)

$$\nabla\cdot\vec{A} = \frac{1}{r}\frac{\partial}{\partial r}(rA_r) + \frac{1}{r}\frac{\partial A_\theta}{\partial\theta} + \frac{\partial A_z}{\partial z} \tag{3.23}$$

$$\nabla f = \frac{\partial f}{\partial r}\hat{r} + \frac{1}{r}\frac{\partial f}{\partial\theta}\hat{\theta} + \frac{\partial f}{\partial z}\hat{z} \tag{3.24}$$

so that the right hand side of Eq. 3.22 can be rewritten using Eqs. 3.23 and 3.24 as

$$E_z(\nabla \cdot E) = \frac{1}{r}\frac{\partial}{\partial r}(rE_zE_r) + \frac{1}{r}\frac{\partial}{\partial \theta}(E_zE_\theta) + \frac{\partial}{\partial z}(E_zE_z) - (E_r\hat{r} + E_\theta\hat{\theta} + E_z\hat{z})\cdot \left[\frac{\partial E_z}{\partial r}\hat{r} + \frac{1}{r}\frac{\partial E_z}{\partial \theta}\hat{\theta} + \frac{\partial E_z}{\partial z}\hat{z}\right]. \quad (3.25)$$

Assuming azimuthal symmetry, Eq. 3.25 reduces to

$$E_z(\nabla \cdot \vec{E}) = \frac{1}{r}\frac{\partial}{\partial r}(rE_zE_r) + \frac{\partial}{\partial z}(E_zE_z) - (E_r\hat{r} + E_z\hat{z}) \cdot \left[\frac{\partial E_z}{\partial r}\hat{r} + \frac{\partial E_z}{\partial z}\hat{z}\right] \quad (3.26)$$

and

$$E_z(\nabla \cdot \vec{E}) = \frac{1}{r}\frac{\partial}{\partial r}(rE_zE_r) + \frac{\partial}{\partial z}E_z^2 - E_r\frac{\partial E_z}{\partial r} - E_z\frac{\partial E_z}{\partial z}. \quad (3.27)$$

Since $(\nabla \times \vec{E})_\theta = \frac{\partial E_r}{\partial z} - \frac{\partial E_z}{\partial r} = 0$, we replace $\frac{\partial E_z}{\partial r}$ with $\frac{\partial E_r}{\partial z}$ and Eq. 3.27 becomes

$$E_z(\nabla \cdot \vec{E}) = \frac{1}{r}\frac{\partial}{\partial r}(rE_zE_r) + \frac{\partial}{\partial z}\left(\frac{E_z^2 - E_r^2}{2}\right). \quad (3.28)$$

Using

$$\nabla \cdot \vec{A} = \frac{1}{r}\frac{\partial}{\partial r}(rA_r) + \frac{\partial A_z}{\partial z}, \quad (3.29)$$

where

$$A_r = E_zE_r \quad (3.30)$$

$$A_z = \left(\frac{E_z^2 - E_r^2}{2}\right) \quad (3.31)$$

and substituting Eq. 3.29 into Eq. 3.20 results in

$$\nabla \cdot \vec{A} = \frac{j}{e_0\epsilon_0}\frac{dp}{dz}. \quad (3.32)$$

To integrate Eq. 3.32, let us assume we are going to perform a surface integration over the volume of the vacuum space between radii r_c and r_a and cross section z_1 and

z_2, including the beam (*cf.* in Fig. 3.1c). By using Gauss's theorem

$$\iiint_V (\nabla \cdot \mathbf{A})\,\mathrm{d}V = \oiint_{S(V)} \mathbf{A} \cdot \hat{\mathbf{n}}\,\mathrm{d}S \tag{3.33}$$

$$\iiint_V \frac{j}{e_0\epsilon_0}\frac{dp}{dz}\,\mathrm{d}V = \oiint_{S(V)} \mathbf{A} \cdot \hat{\mathbf{n}}\,\mathrm{d}S \tag{3.34}$$

$$\frac{1}{e_0\epsilon_0}\iiint_V j\frac{dp}{dz}\,\mathrm{d}V = \oiint_{S(V)} \mathbf{A} \cdot \hat{\mathbf{n}}\,\mathrm{d}S \tag{3.35}$$

and assuming azimuthal symmetry, Eq. 3.35 reduces to

$$\frac{1}{e_0\epsilon_0}\oiint_{S(V)} j\frac{dp}{dz}\cdot\mathrm{d}S = \oint_P (\mathbf{A}\cdot n)\,\mathrm{d}P = \oint_P A_n\,\mathrm{d}P, \tag{3.36}$$

where P is the perimeter of the problem, $\hat{\mathbf{n}}$ is a vector normal to the perimeter boundary, A_n is the component of vector A normal to the perimeter boundary, and the integral in the right hand side of Eq. 3.36, which is the integral around the perimeter of the problem, may be represented as the sum of five line integrals taken counter-clockwise around the perimeter of the problem, starting from the point ($z = z_1, r = r_a$),

$$\oint_P A_n\,\mathrm{d}P = -\int_{r_a}^{r_c} A_{z=z_1}\,\mathrm{d}r + \int_{z_1}^{z_0} A_{r=r_c}\,\mathrm{d}z + \int_{z_0}^{z_2} A_{r=r_b}\,\mathrm{d}z + \int_{r_c}^{r_a} A_{z=z_2}\,\mathrm{d}r - \int_{z_2}^{z_1} A_{r=r_a}\,\mathrm{d}z, \tag{3.37}$$

where r_b is the beam radius, which is equal to the cathode radius r_c in the strong magnetic field approximation. Considering that $E_z = 0$ over the cathode and anode surfaces, which results in $A_r = 0$ in Eq. 3.30, nullifying the second and fifth integrals

in Eq. 3.37, which results in

$$\oint_P A_n \, \mathrm{d}P = -\int_{r_a}^{r_c} A_{z=z_1} \, \mathrm{d}r + \int_{z_0}^{z_2} A_{r=r_b} \, \mathrm{d}z + \int_{r_c}^{r_a} A_{z=z_2} \, \mathrm{d}r. \tag{3.38}$$

Substituting Eqs. 3.31 and 3.30 into Eq. 3.38 results in

$$\oint_P A_n \, \mathrm{d}P = -\int_{r_a}^{r_c} \left(\frac{E_z^2 - E_r^2}{2}\right)_{z=z_1} \mathrm{d}r + \int_{z_0}^{z_2} (E_z E_r)_{r=r_b} \, \mathrm{d}z + \int_{r_c}^{r_a} \left(\frac{E_z^2 - E_r^2}{2}\right)_{z=z_2} \mathrm{d}r. \tag{3.39}$$

Assuming that $E_z = 0$ for $z = z_1$ and $z = z_2$ if z_1 and z_2 are sufficiently far from the plane $z_0 = 0$, Eq. 3.39 reduces to

$$\oint_P A_n \, \mathrm{d}P = -\int_{r_a}^{r_c} \left(\frac{E_r^2}{2}\right)_{z=z_1} \mathrm{d}r + \int_{z_0}^{z_2} (E_z E_r)_{r=r_b} \, \mathrm{d}z - \int_{r_c}^{r_a} \left(\frac{E_r^2}{2}\right)_{z=z_2} \mathrm{d}r. \tag{3.40}$$

The second integral on the right hand side of Eq. 3.40 is small for thin beams $h_c \approx h_b << r_c, r_a, r_a - r_c$. The volume integral of the right hand side of Eq. 3.32 is

$$\frac{1}{e_0 \epsilon_0} \int_V j \frac{dp}{dz} \, \mathrm{d}\tau = \frac{1}{e_0 \epsilon_0} \left[\int_0^{z_2} \frac{dp}{dz} \, \mathrm{d}z \int_S j \, \mathrm{d}\sigma\right] = \frac{I p_b}{e_0 \epsilon_0}. \tag{3.41}$$

Boundary conditions: Assume that the initial momentum $p(0) = (p)_{z=0} = 0$ and $p_b = p(z_2) = p_2$ is the electron momentum far from the MICD $z_2 >> r_c, r_a$. Neglecting the final integral in Eq. 3.40, we obtain

$$\int_{r_c}^{r_a} E_{r1}^2 r \, \mathrm{d}r - \int_{r_c}^{r_a} E_{r2}^2 r \, \mathrm{d}r = \frac{I_b p_b}{e_0 \epsilon_0} \tag{3.42}$$

since the cross-section $z = z_1$ and $z = z_2$ geometrically is similar to a uniform coaxial

line. The electric field at the plane $z = z_1$ is

$$E_{r1} = \frac{\varphi_a}{r \ln\left(\frac{r_a}{r_c}\right)} \tag{3.43}$$

and the electric field in the plane $z = z_2$ is

$$E_{r2} = -\frac{I_b}{2\pi r v_b \epsilon_0}. \tag{3.44}$$

To find I_b, we need to find the potential difference across the beam-tube gap

$$\varphi_a - \varphi_b = -\int_{r_b}^{r_a} E_{r2}\, \mathrm{d}r = \frac{I_b}{2\pi r \epsilon_0 v_b} \ln\left(\frac{r_a}{r_b}\right), \tag{3.45}$$

where the beam radius is equal to the cathode radius, $r_b = r_c$. Thus, the beam current is given by

$$I_b = \frac{(\varphi_a - \varphi_b) 2\pi\epsilon_0 v_b}{\ln\left(\frac{r_a}{r_b}\right)}. \tag{3.46}$$

Notice that Eq. 3.46 depends on the beam potential. Therefore, from Eq. 3.5,

$$I_b = \frac{2\pi\epsilon_0 v_b c^2 (\gamma_a - 1)(\gamma_b - 1)}{\eta \ln\left(\frac{r_a}{r_b}\right)}. \tag{3.47}$$

Using $v_b = \frac{c}{\gamma_b}\sqrt{\gamma_b^2 - 1}$,

$$\boxed{I_b = I_F = 4\pi\epsilon_0 \frac{c^3}{\eta} \frac{(\gamma_a - \gamma_b)\sqrt{\gamma_b^2 - 1}}{2\gamma_b \ln\left(\frac{r_a}{r_b}\right)} = I_{\text{Alfven}} \frac{(\gamma_a - \gamma_b)\sqrt{\gamma_b^2 - 1}}{2\gamma_b \ln\left(\frac{r_a}{r_b}\right)}}. \tag{3.48}$$

Equation 3.48 is the beam current (a.k.a Fedosov current), which is the ideal current $I_{\text{Alfven}} = 4\pi\epsilon_0 \frac{c^3}{\eta}$, $\gamma_a = 1 + \frac{e_0 \varphi_a}{m_e c^2}$ for a given potential φ_a, which depends on γ_b and

γ_a. Replacing E_{r1}, E_{r2}, I_b in Eq. 3.42 we find the relativistic factor γ_b at the external boundary of the beam, given by

$$\int_{r_b}^{r_a}\left[\frac{\varphi_a}{r\ln\left(\frac{r_a}{r_c}\right)}\right]r\,\mathrm{d}r-\int_{r_b}^{r_a}\left[-\frac{I_b}{2\pi r v_b\epsilon_0}\right]r\,\mathrm{d}r=\frac{4\pi\epsilon_0c^3}{\eta}\frac{(\gamma_a-\gamma_b)\sqrt{\gamma_b^2-1}}{2\gamma_b\ln\left(\frac{r_a}{r_b}\right)}\frac{p_b}{\pi e_0\epsilon_0} \tag{3.49}$$

$$(\gamma_a-1)^2-(\gamma_a-\gamma_b)^2=\frac{2(\gamma_a-\gamma_b)(\gamma_b^2-1)}{\gamma_b} \tag{3.50}$$

$$\gamma_b^2+\gamma_b-2\gamma_a=0 \tag{3.51}$$

and, finally

$$\boxed{\gamma_b=\sqrt{\left(\frac{1}{4}+2\gamma_a\right)}-\frac{1}{2}}. \tag{3.52}$$

This expression for γ_b [79] gives us the ultimate solution of what is the beam current (in Fig. 3.1c) and energy of a thin electron beam propagating in a smooth cylindrical long drift tube.

Equation 3.48 is our desired electron beam current (a.k.a Fedosov [79] current). Once we know the electron beam current I_b, we can find the electron beam energy (a.k.a Fedosov potential) from Eq. 3.46 or from the well known equation $E_k=\varphi_b=(\gamma_b-1)m_ec^2$.

3.1.1 Space-charge-limited current

As mentioned earlier, space charge effects on intense relativistic electron beams are complicated processes and this chapter will be limited to studying a beam generated from an MICD. Space charge is limited by the electrostatic potential depression associated with the unneutralized beam space charge [57], as can be seen in Fig. 3.2.

In the case of an MICD, the generated electron beam is very thin and propagates in a long smooth cylindrical waveguide with radius r_a and the thickness of the beam must be less than both the beam radius and anode radius. Thus, the electrostatic potential will be constant across the thin beam and Eq. 3.3 reduces to a homogeneous solution [99].

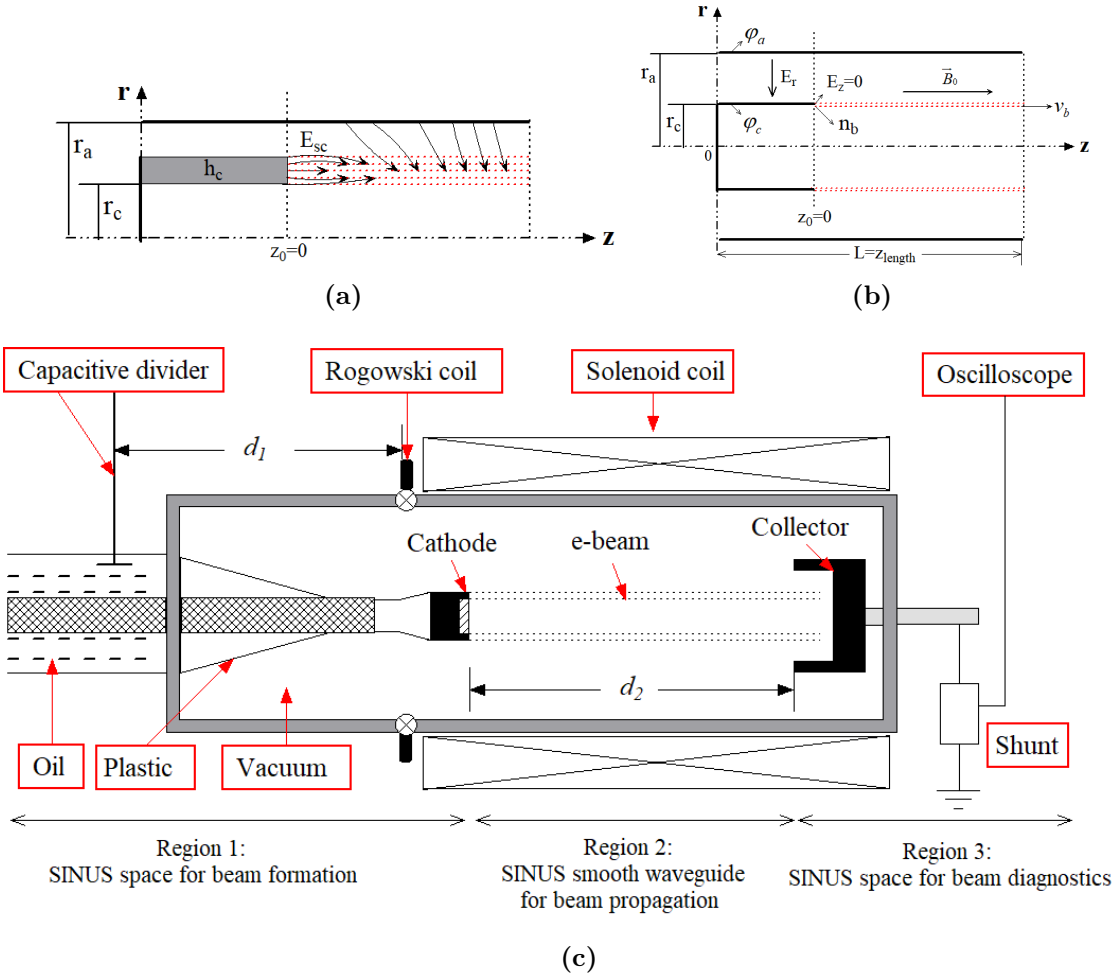

Figure 3.2: (a) Beam space formulation in a typical MICD [26]. (b) The electric field points from anode down to the cathode. (c) Schematic of the current set-up of the electron beam accelerator at UNM showing three regions of the electron beam to be thoroughly studied.

The mathematical derivation of the SCL current in the case of an MICD follows from the previous section's analysis from Poisson's equation, the conservation of energy, the continuity equation, and the boundary conditions that require the net

electric field at the cathode to be zero. Poisson's equation reduces to 1D as

$$\frac{d^2\varphi(z)}{dz^2} = \frac{e_0 n(z)}{\epsilon_0}, \tag{3.53}$$

where $\varphi(z)$ is the potential in volts, e is the elementary charge, $n(z)$ is the electron density in cm^{-3}, and ϵ_0 is the permittivity of the free space. According to the conservation of energy,

$$e_0\varphi(z) = \frac{1}{2}m_e[v(z)]^2, \tag{3.54}$$

where m_e is the electron mass and $v(z)$ is the electron velocity in m/s. According to the continuity equation, the current density j is constant and independent of z. Thus, j at a point z can be be written in terms of the space charge density $n(z)$, electron charge e_0, and the velocity v(z), as

$$j = -e_0 n(z)v(z). \tag{3.55}$$

Taking the second derivative of the potential $\varphi(z)$ in Eq. 3.55 with respect to z yields

$$\frac{d^2\varphi(z)}{dz^2} = -\frac{j}{\epsilon_0}\left(\frac{m_e}{2e_0}\right)^{1/2}\varphi(z)^{-1/2}. \tag{3.56}$$

Equation 3.56 needs to be integrated twice to obtain the current density j which was first calculated by Child as [105]

$$j(z) = 2.33 \times 10^{-6}\varphi(z)^{3/2}z^{-2}. \tag{3.57}$$

Child's equation 3.57 was later independently derived and applied to electron beams in high vacuum by Langmuir [106]. Multiplying both sides of Eq. 3.57 by the area of the cathode gives the electron current across a finite planar diode. Use of this Child-Langmuir relationship to find the total SCL current density applies if the cathode

radius is much bigger than the anode-cathode gap. This requirement is necessary to reduce edge effects. However, in many cases, assumptions which allow this derivation are physically unrealistic. To understand fully, each assumption needs to be carefully considered. The SCL current derivation was extended for the relativistic case for an infinite planar diode in [107], [108]. In addition, Poisson's equation for relativistic velocities in terms of elliptic integrals was derived by [109]

$$\frac{1}{r}\frac{\partial}{\partial r}(r\frac{\partial \varphi}{\partial r}) = 0. \tag{3.58}$$

Details of the derivation of Eq. 3.58 can be found in [99].

To calculate the SCL current for this specific MICD geometry (*cf.* Fig. 3.2a), taking the derivative of Eq. 3.48 with respect to γ_b yields

$$\frac{\partial I_F}{\partial \gamma_b} = \frac{2\pi\epsilon_0 c^3}{\eta \ln\left(\frac{r_a}{r_b}\right)}\left[\frac{(\gamma_a - \gamma_b)}{\sqrt{\gamma_b^2 - 1}} - \frac{\gamma_a\sqrt{\gamma_b^2 - 1}}{\gamma_b^2}\right]. \tag{3.59}$$

Letting $\frac{\partial I_F}{\partial \gamma_b} = 0$ to obtain maximum current I_F,

$$\frac{2\pi\epsilon_0 c^3}{\eta \ln\left(\frac{r_a}{r_b}\right)}\left[\frac{(\gamma_a - \gamma_b)}{\sqrt{\gamma_b^2 - 1}} - \frac{\gamma_a\sqrt{\gamma_b^2 - 1}}{\gamma_b^2}\right] = 0 \tag{3.60}$$

$$\frac{(\gamma_a - \gamma_b)}{\sqrt{\gamma_b^2 - 1}} = \frac{\gamma_a\sqrt{\gamma_b^2 - 1}}{\gamma_b^2} \tag{3.61}$$

$$\boxed{\gamma_a = \gamma_b^3} \quad \text{or} \quad \boxed{\gamma_b = \gamma_a^{\frac{1}{3}}.} \tag{3.62}$$

In Eq. 3.48, the current is zero when either $\gamma_b = 1$ (full potential depression) or $\gamma_b = \gamma_a$ (zero potential depression). Therefore, the maximum current occurs when $\gamma_b = (\gamma_a)^{\frac{1}{3}}$ (*cf.* in Eq. 3.62). Replacing the condition $\gamma_b = \gamma_a^{\frac{1}{3}}$ in Eq. 3.48 gives the

maximum or SCL current,

$$I_{max} = I_{scl} = \frac{2\pi\epsilon_0 c^3}{\eta \ln\left(\frac{r_a}{r_b}\right)}(\gamma_a^{2/3} - 1)^{3/2}. \tag{3.63}$$

The theoretically calculated electron beam energy (a.k.a Fedosov potential), electron beam current (a.k.a Fedosov current), and SCL current as a function of applied voltage are shown in Fig. 3.3.

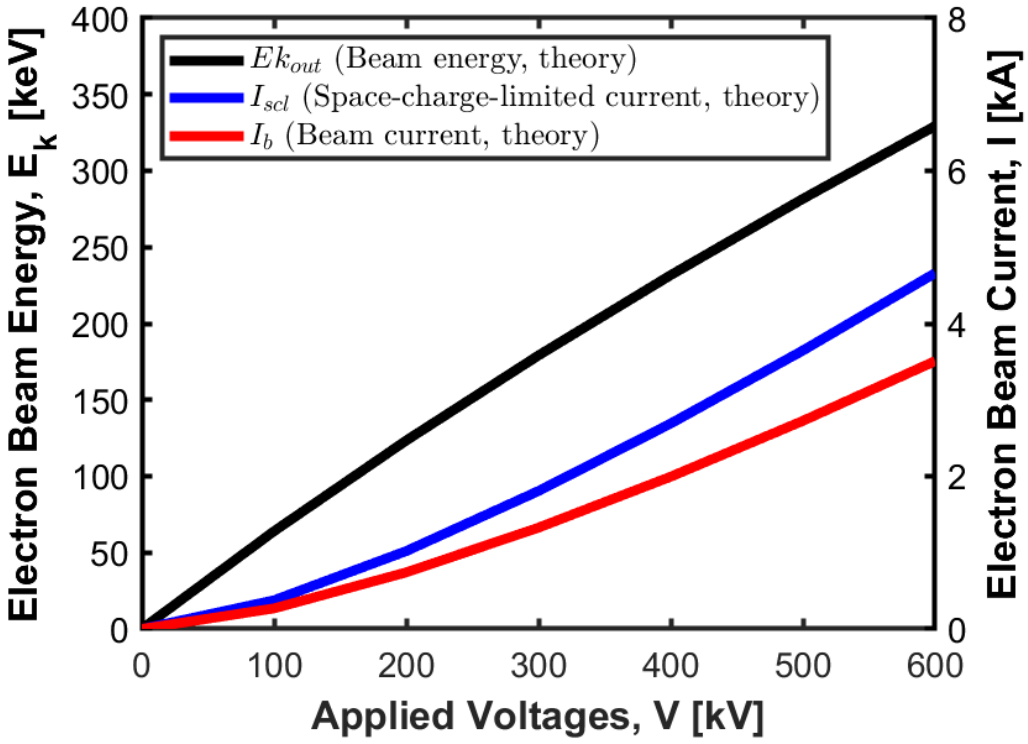

Figure 3.3: Analytically calculated Fedosov current and energy for an MICD. The black, red, and blue lines show the calculated electron beam energy, beam current (I_b), and SCL current (I_{scl}), respectively, for applied voltages ranging from 0 - 600 kV. Here, $I_{scl} > I_b$.

A comparison of the analytic and simulation results are shown in Figs. 3.4 and 3.5.

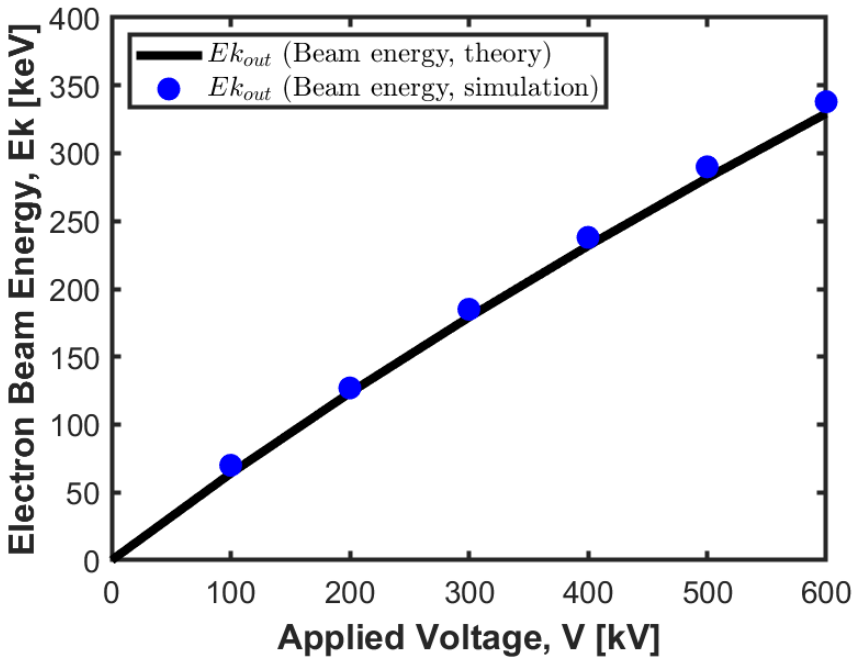

Figure 3.4: Analytically calculated electron beam energy (black) and simulated energy from MAGIC simulations (blue filled circle) for applied voltages ranging from 0 - 600 kV.

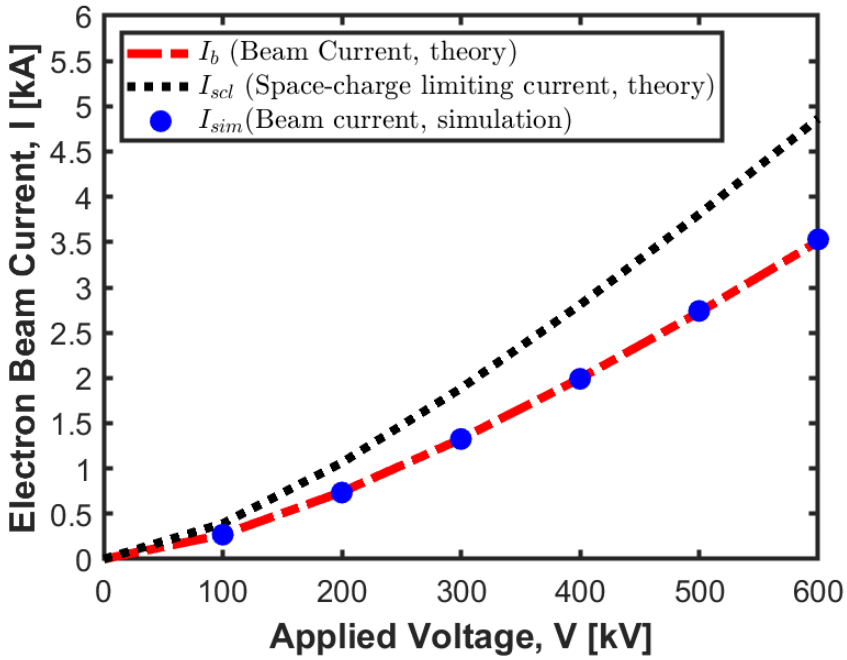

Figure 3.5: Analytically calculated electron beam current (red dash), SCL current (black dot), and simulation current (blue circle) for applied voltages ranging from 0 - 600 kV.

3.2 Extension of Fedosov's calculation to two nested MICDs

This section presents the extension of Fedosov's [79] analytic MICD theory to two nested MICDs. Our goal is to find a simplified analytical solution for two nested MICDs that will validate simulation results and ultimately both theory and simulation will be validated by experiments. Comparison of the results of theory and simulations of nested MICDs are also presented at the end of this section. Chapter 4 will present details of the PIC simulations.

Figure 3.6a shows the geometry set-up in the $r-z$ plane for two nested MICDs as labeled. The design parameters of the MICDs are listed in Table 3.1. We follow a similar approach to what was used in Fedosov's [79] calculation for the mathematical derivation for two nested MICDs. Consider two very thin annular beams with radius $r_{ib}(\textit{'inner'})$, $r_{ob}(\textit{'outer'})$ and a cylindrical anode (conductor) with radius r_a that are immersed in an infinite magnetic field. The thickness of the beams $h_{ib} = h_{ob} = h_b$ must be much less than both the beam radius r_{ob} and the gap between r_a and r_{oc}. Theoretically, the potential at the cathode's surface is taken as zero and the potential of the cylindrical surface as φ_a. Therefore, the potential difference between the anode's and cathode's surface will be $\Delta\varphi$, as shown in Fig. 3.6a. Both electron beams are injected with the same potential and propagate through the cylindrically symmetric drift tube. Assume that an electron leaves the outer emitter with initial velocity $v_{z_{ob}}$, mass m_e, and charge density $j_{z_{ob}} = -e_0 n_{e_{ob}} v_{z_{ob}}$. Similarly, an electron leaves the inner cathode with initial velocity $v_{z_{ib}}$, mass m_e, and charge density $j_{z_{ib}} = -e_0 n_{e_{ib}} v_{z_{ib}}$, where $j_{z_{ob}}$ and $j_{z_{ib}}$ are the constant current densities of the outer and inner beams, respectively. Our assumption for the two nested MICDs is that the

Table 3.1: Design parameters of two nested MICDs in a vacuum tube.

Inputs				Outputs	
Design Parameters	Symbols	Values	Units	Parameters	Units
Anode potential	φ_a	100-500	kV	I_{ib} [a]	A
Cathode potential	φ_c	0	kV	I_{ob} [b]	A
Anode radius	r_a	2.5	cm	γ_{ib} [c]	unitless
Anode length	z_1 to z_3	16.5	cm	γ_{ob} [d]	unitless
Outer cathode radius	r_{oc}	0.9	cm	Ek_{ib} [e]	keV
Outer cathode length	z_1 to z_0	4.9	cm	Ek_{ob} [f]	keV
Cathode thickness	h_c	0.02	cm		
Inner cathode radius	r_{ic}	$r_{ic} < r_{oc}$	cm		
Inner cathode length	z_1 to z_2	$l_{ic} < l_{oc}$	cm		

[a]Inner electron beam current, [b]Outer electron beam current, [c]Relativistic factor at the external boundary of the inner electron beam, [d]Relativistic factor at the external boundary of the outer electron beam, [e]Inner electron beam energy at the output end, [f]Outer electron beam energy at the output end.

inner emitter's axial position extends beyond that of the outer emitter's by a distance d. (It should be noted that in experiments the anode is grounded and the cathode is at negative high voltage. Our decision to have the anode be at a large positive potential with respect to the cathode is to be consistent with the original Fedosov [79] derivation.)

As can be seen in Fig. 3.6, the inner emitter is extended beyond the outer emitter, so the boundary conditions are not the same for both emitters along z. Thus, another boundary condition is applied in the plane z_2 at the end of the inner emitter. The axial axis of the tube from z_1 to z_3 divides into three cross-sections z_1, z_2, and z_3, which are geometrically similar to a uniform coaxial line, as can be seen in Fig. 3.7. Assume a homogeneous region between $z = z_0$ to $z = z_2$, right above the inner cathode where we can find the relativistic factor γ_h (dimensionless) for the outer beam at the boundary z_2 (*cf.* Fig. 3.6). Also, we assume that the potential of the outer electron

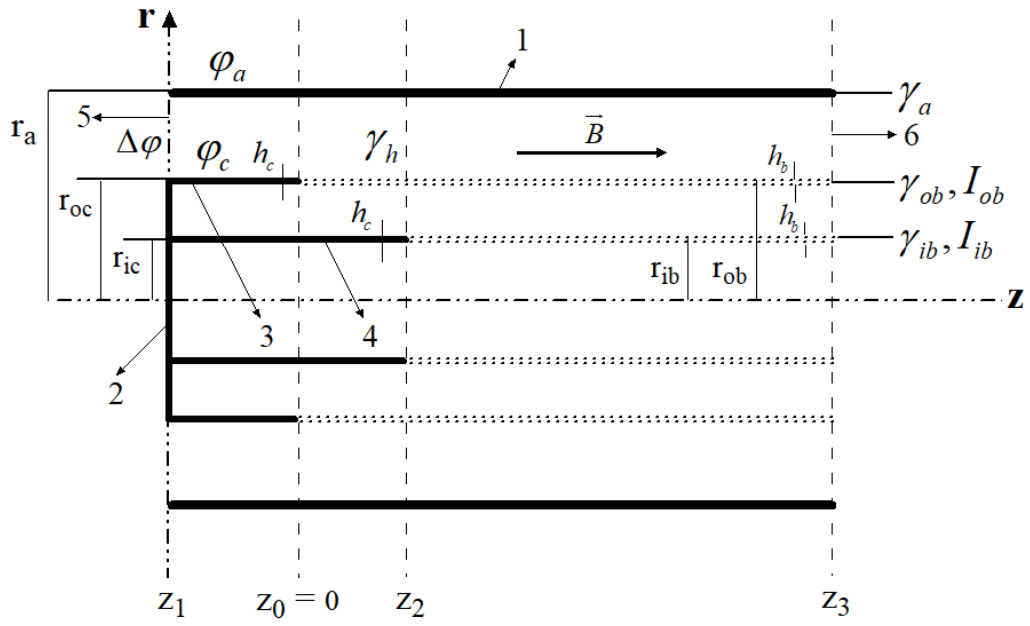

(a) MICDs schematic

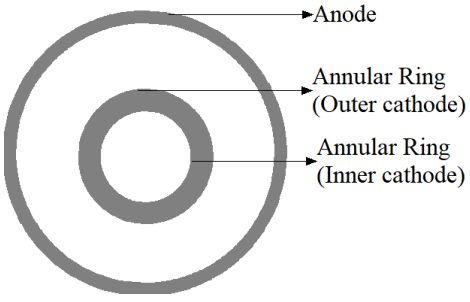

(b) Frontview of MICDs

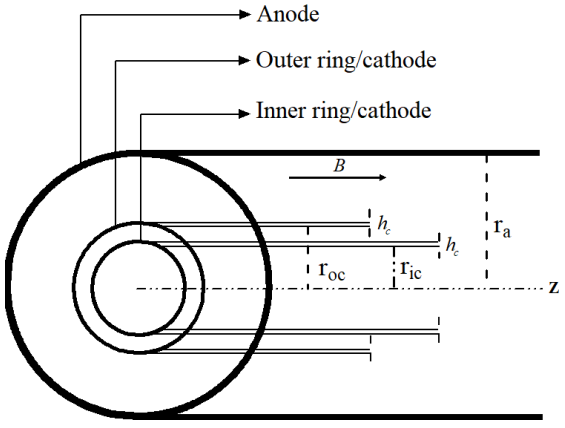

(c) Endview of MICDs

Figure 3.6: Top - Schematic of two nested MICDs in a vacuum tube. 1. Anode; 2. a single cathode stalk; 3. outer emitter/cathode; 4. inner emitter/cathode; 5. Input Port; 6. Output Port. Left - Front view of the drift tube. Right - End view of the drift tube.

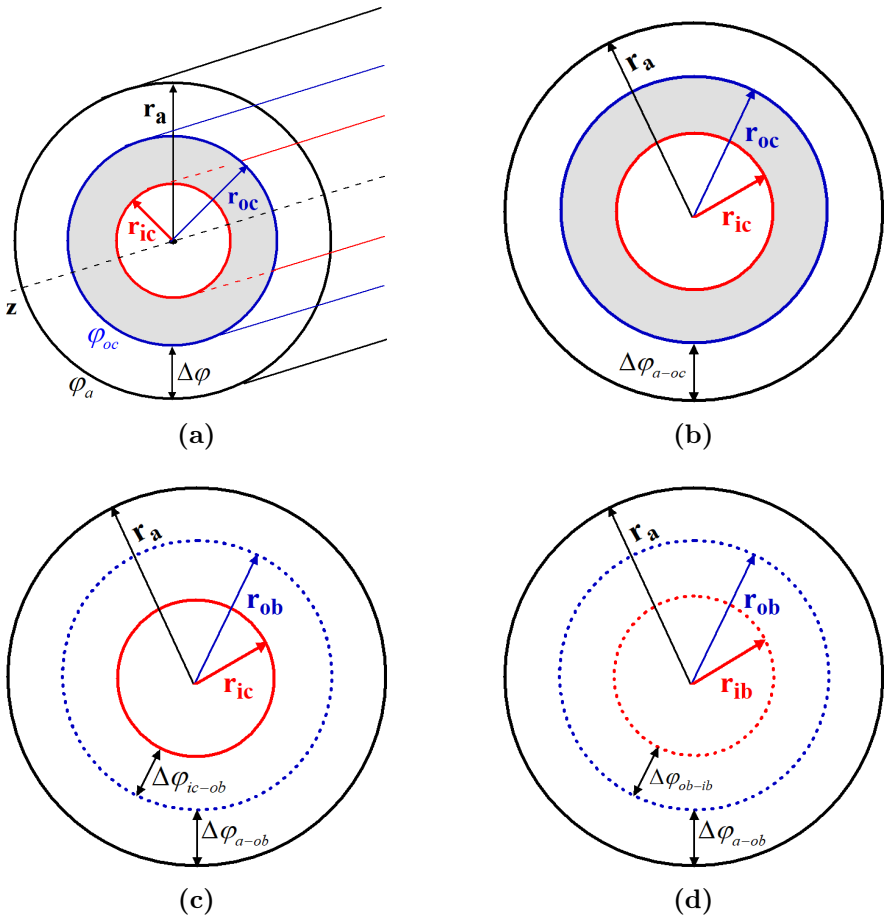

Figure 3.7: Cross-section views of the two nested MICDs in a vacuum tube at various planes referenced in Fig. 3.6a. (a) 3D view of the two nested MICDs. (b) Front view of the z_1 plane where solid circumferences represent inner and outer cathodes. (c) View of the z_2 plane, which is at the tip of the inner emitter where solid red and dashed blue circumferences present 'inner cathode' and 'outer electron beam', respectively. (d) View of the z_3 plane at the 'output' end where there are only two nested electron beams (dashed red and dashed blue), but no cathodes.

beam in the plane z_2 is φ_h.

We will take into account these three cross-sections (z_1, z_2, z_3) in the derivation with the aim of obtaining solutions for the relativistic factors γ_{ob} and γ_{ib} for the outer and inner beams, respectively. Starting with the beam equations and boundary conditions. According to conservation of energy,

$$m_e c^2 - e_0 \varphi_a = m_e c^2 + e_0 \varphi_c. \tag{3.64}$$

The equation of motion in the z direction is given by

$$\frac{dp}{dt} = -e_0 E_z \tag{3.65}$$

and the current density is

$$j = -\rho v. \tag{3.66}$$

The boundary conditions for the outer cathode are

$$(E_z)_{r=r_{oc}} = 0, \tag{3.67}$$

$$(p_{ob})_{r=r_{oc},z_0=0} = 0, \tag{3.68}$$

$$(\varphi)_{r=r_a} = \varphi_a, \quad \text{and} \tag{3.69}$$

$$(\varphi_c)_{r=r_{oc},z_0<0} = 0. \tag{3.70}$$

The boundary conditions for the inner cathode are

$$(E_z)_{r=r_{ic}} = 0, \tag{3.71}$$

$$(p_{ib})_{r=r_{ic},z_2=0} = 0, \text{ and} \tag{3.72}$$

$$(\varphi_c)_{r=r_{ic},z_2<0} = 0. \tag{3.73}$$

The divergence of the electric field is $\nabla \cdot \mathbf{E} = \frac{\rho}{\epsilon_0}$, where ϵ_0 is the vacuum permittivity [in unit F/m] and ρ is the volume charge density [in C/m^3]. In cylindrical coordinates, we have $(\nabla \times \mathbf{E})_\varphi = \frac{\partial \mathbf{E}_r}{\partial z} - \frac{\partial \mathbf{E}_z}{\partial r} = 0$. We now apply Gauss' law to find the electric field in the plane delineated by z_1

$$E_{r1} = \frac{\varphi_a}{r \ln(\frac{r_a}{r_{oc}})}. \tag{3.74}$$

The initial momentum of the inner beam is $(p_{ib})_{r=r_{ic},z_2=0} = 0$ in the plane $z = z_2$. However, in the plane $z = z_2$, the outer electron beam is already established and the momentum of the outer beam in the plane $z = z_2$ is $(p_{ob})_{r=r_{ob},z=z_2} \neq 0$; thus, the jump in the electric field from the outer beam to the inner beam in the plane $z = z_2$ is

$$E_{r2_{(h+)}} = -\frac{I_{h+}}{2\pi r v_h \epsilon_0}. \tag{3.75}$$

Here, q_h is the outer electron beam charge per unit length and v_h is the velocity of the outer electron beam. The jump in the electric field from the outer beam to the inner beam in the plane $z = z_2$ is given by

$$E_{r2_{(h-)}} = -\frac{I_{h-}}{2\pi r v_h \epsilon_0}. \tag{3.76}$$

To obtain the equation for the outer electron beam current in the plane $z = z_2$, we find the potential difference of the outer beam – anode gap and the outer beam – inner cathode gap in the plane $z = z_2$. We assume $r_h = r_{ob}$, where ob =outer beam. Therefore, the potential difference across the outer beam – anode gap in the plane $z = z_2$ is given by

$$\varphi_a - \varphi_h = -\int_{r_h}^{r_a} E_{r2_{(h+)}} dr = \frac{I_{h+}}{2\pi\epsilon_0\ v_h} \ln\left(\frac{r_a}{r_h}\right) = \frac{I_{h+}}{2\pi\epsilon_0 v_h} \ln\left(\frac{r_a}{r_{ob}}\right). \tag{3.77}$$

The potential difference across the outer beam – inner cathode gap in the plane $z = z_2$ is given by

$$\varphi_c - \varphi_h = -\int_{r_h}^{r_{ic}} E_{r2_{(h-)}} dr = \frac{I_{h-}}{2\pi\epsilon_0 v_h} \ln\left(\frac{r_{ic}}{r_{ob}}\right). \tag{3.78}$$

Hence, from Eq. (3.77),

$$\frac{I_{h+}}{2\pi\epsilon_0 v_h}\ln\left(\frac{r_a}{r_{ob}}\right)=\frac{c^2}{\eta}(\gamma_a-1)-\frac{c^2}{\eta}(\gamma_h-1)$$

and

$$I_{h+}=\frac{2\pi\epsilon_0 c^3}{\eta}\frac{(\gamma_a-\gamma_h)(\sqrt{\gamma_h^2-1})}{\gamma_h\ln\left(\frac{r_a}{r_{ob}}\right)}\,. \tag{3.79}$$

Equation (3.79) is similar to Fedosov's [79] beam current equation for a single MICD [26]. Similarly, from Eq. (3.78) where we assume the potential of the inner cathode $\varphi_c=0$, we obtain

$$I_{h-}=\frac{2\pi\epsilon_0 c^3}{\eta}\frac{(\gamma_h-1)(\sqrt{\gamma_h^2-1})}{\gamma_h\ \ln\left(\frac{r_{ob}}{r_{ib}}\right)}\,.$$

We now can calculate the total current $I_h=I_{h+}-I_{h-}$ in the plane $z=z_2$, which is given as

$$\Rightarrow I_h=\frac{2\pi\epsilon_0 c^3(\sqrt{\gamma_h^2-1})}{\eta\gamma_h}\left[\frac{(\gamma_a-\gamma_h)}{\ln\left(\frac{r_a}{r_{ob}}\right)}-\frac{(\gamma_h-1)}{\ln\left(\frac{r_{ob}}{r_{ib}}\right)}\right]. \tag{3.80}$$

We will now find the equation for γ_h in the plane $z=z_2$. Integrating over the volume between radii r_{ic} and r_a and cross-sections z_1 and z_2 and apply conservation of momentum in the z direction for the system [2] in Fig. 3.6 to obtain

$$\int_{r_{ic}}^{r_a}E_{r1}^2 r dr-\int_{r_{ic}}^{r_a}E_{r2}^2 r dr=\frac{I_h p_h}{\pi e_0\epsilon_0}. \tag{3.81}$$

We solve Eq. 3.81 to obtain a solution for γ_h as

$$(\gamma_a-1)^2-(\gamma_a-\gamma_h)^2-(\gamma_h-1)^2\frac{1-g}{g}=\frac{2(\gamma_h^2-1)}{\gamma_h}\left[\frac{\gamma_a-\gamma_h}{1-g}-\frac{\gamma_h-1}{g}\right](1-g), \tag{3.82}$$

which yields the solution for γ_h (where $\gamma_h > 1$)

$$\gamma_h = \frac{\sqrt{(8\gamma_a - 8)g + 9} - 1}{2}, \tag{3.83}$$

where the geometrical factor $g = \frac{\ln(\frac{r_{ob}}{r_{ib}})}{\ln(\frac{r_a}{r_{ib}})}$ and $r_{ib} < r_{ob} < r_a$. Similarly, the total current I_{ob} is obtained in plane z_3,

$$I_{ob} = \frac{2\pi\epsilon_0 c^3(\sqrt{\gamma_{ob}^2 - 1})}{\eta\gamma_{ob}} \left[\frac{(\gamma_a - \gamma_{ob})}{\ln\left(\frac{r_a}{r_{ob}}\right)} - \frac{(\gamma_{ob} - \gamma_{ib})}{\ln\left(\frac{r_{ob}}{r_{ib}}\right)} \right]. \tag{3.84}$$

Expressing Eq. 3.84 in terms of $\ln(r_a/r_{ib})$,

$$I_{ob} = \frac{2\pi\epsilon_0 c^3}{\eta \ \ln\left(\frac{r_a}{r_{ib}}\right)} \frac{\sqrt{\gamma_{ob}^2 - 1}}{\gamma_{ob}} \left[\frac{\gamma_a - \gamma_{ob}}{1 - g} - \frac{\gamma_{ob} - \gamma_{ib}}{g} \right]. \tag{3.85}$$

In a manner similar to finding the outer electron beam current solution, we will now find the solution for the inner electron beam current I_{ib} in the same plane $z = z_3$. The electric field and beam current in the plane $z = z_3$ for the inner beam are given by

$$E_{r3_{(ib)}} = \frac{q_{ib}}{2\pi r\epsilon_0} = -\frac{I_{ib}}{2\pi r v_{ib}\epsilon_0} \quad \text{and} \tag{3.86}$$

$$I_{ib} = \frac{2\pi\epsilon_0 c^3}{\eta \ln(\frac{r_{ob}}{r_{ib}})} \frac{(\gamma_{ob} - \gamma_{ib})\sqrt{\gamma_{ib}^2 - 1}}{\gamma_{ib}} \ . \tag{3.87}$$

Expressing Eq. 3.87 in terms of $\ln(r_a/r_{ib})$,

$$I_{ib} = \frac{2\pi\epsilon_0 c^3}{\eta \ \ln(r_a/r_{ib})} \frac{\sqrt{\gamma_{ib}^2 - 1}}{\gamma_{ib}} \frac{(\gamma_{ob} - \gamma_{ib})}{g}. \tag{3.88}$$

Eq. 3.87 (for inner electron beam current I_{ib}) is our desired solution for the inner electron beam current in the system at $z = z_3$. We have two unknowns (γ_{ob} and γ_{ib}) in

the equations for I_{ob} and I_{ib}. Therefore, we should now focus on finding the relativistic factor at the external boundaries for both the inner and outer electron beams in the drift tube. We integrate over the volume between radii r_{ic} and r_a and cross-sections $z = z_1$ and $z = z_3$ and apply conservation of momentum in the z direction for the system [79], [2] shown in Fig. 3.6 to obtain

$$\int_{r_{ic}}^{r_a} E_{r1}^2 r dr - \int_{r_{ib}}^{r_a} E_{r3}^2 r dr = \frac{p_{ob} I_{ob} + p_{ib} I_{ib}}{\pi e_0 \epsilon_0} \tag{3.89}$$

$$\Rightarrow (\gamma_a - 1)^2 - (\gamma_a - \gamma_{ob})^2 - (\gamma_{ob} - \gamma_{ib})^2 \frac{1-g}{g} - 2\left[\frac{(\gamma_{ob}^2 - 1)}{\gamma_{ob}} \left(\frac{\gamma_a - \gamma_{ob}}{1-g} - \frac{\gamma_{ob} - \gamma_{ib}}{g}\right) + \frac{(\gamma_{ib}^2 - 1)}{\gamma_{ib}} \frac{(\gamma_{ob} - \gamma_{ib})}{g}\right](1-g) = 0\,. \tag{3.90}$$

The final expression from the derivation of Eq. (3.89) is Eq. (3.90), where the geometrical factor $g = \frac{\ln(\frac{r_{ob}}{r_{ib}})}{\ln(\frac{r_a}{r_{ib}})}$ for $r_{ib} < r_{ob} < r_a$. We know that the current remains same in the system for a given value of γ and a narrow beam [98], [99]. Thus, the equation for the current I_h of the outer electron beam in the plane $z = z_2$ and the equation of the current I_{ob} for the outer electron beam in the plane $z = z_3$ are equal. Therefore, by equating $I_h = I_{ob}$ (Eqs. (3.80 and 3.84)), we obtain

$$\frac{2\pi\epsilon_0 c^3 \left(\sqrt{\gamma_h^2 - 1}\right)}{\eta \ln\left(\frac{r_a}{r_{ib}}\right) \gamma_h} \left[\frac{\gamma_a - \gamma_h}{1-g} - \frac{\gamma_h - 1}{g}\right] = \frac{2\pi\epsilon_0 c^3}{\eta \ln\left(\frac{r_a}{r_{ib}}\right)} \frac{\sqrt{\gamma_{ob}^2 - 1}}{\gamma_{ob}} \left[\frac{\gamma_a - \gamma_{ob}}{1-g} - \frac{\gamma_{ob} - \gamma_{ib}}{g}\right]. \tag{3.91}$$

Removing the constants from both sides of Eq. (3.91) and substituting the solution for γ_h from Eq. (3.83) into Eq. (3.91) yields

$$\sqrt{(\gamma_{ob}^2 - 1)}\,((\gamma_{ib} - \gamma_a)g + (\gamma_{ob} - \gamma_{ib})) - \gamma_{ob} C = 0, \tag{3.92}$$

where C is the constant in Eq. (3.93). For a given anode potential, $\gamma_a = 1 + \frac{\eta \varphi_a}{c^2}$, g

is the geometrical factor given earlier, and C is given by

$$C = \frac{\left(\sqrt{(8\gamma_a - 8)g + 9} + (2 - 2\gamma_a)g - 3\right)\sqrt{-2\sqrt{(8\gamma_a - 8)g + 9} + (8\gamma_a - 8)g + 6}}{2(\sqrt{(8\gamma_a - 8)g + 9} - 1)}. \tag{3.93}$$

The solution of Eqs. (3.90 and 3.92) yields γ_{ob} and γ_{ib} that ultimately determine the electron beam current and energy for the electron beams in the system.

3.3 Calculation of the SCL current for MICDs

The outer electron beam current is given by

$$I_{ob} = \frac{2\pi\epsilon_0 c^3}{\eta\ \ln\left(\frac{r_a}{r_{ib}}\right)} \frac{\sqrt{\gamma_{ob}^2 - 1}}{\gamma_{ob}} \left[\frac{\gamma_a - \gamma_{ob}}{1 - g} - \frac{\gamma_{ob} - \gamma_{ib}}{g}\right]. \tag{3.94}$$

In Eq. 3.94, the outer current will be zero for two cases, when $\gamma_{ob} = 1$ (full potential depression) and $\gamma_{ob} = \gamma_a = \gamma_{ib}$ (zero potential depression). Taking the derivative of Eq. 3.94 with respect to γ_{ob}, the current I_{ob} will be maximum for the condition $\frac{\partial I_{ob}}{\partial \gamma_{ob}} = 0$. The solution of γ_{ib} from Eq. 3.92 is,

$$\gamma_{ib} = \frac{\sqrt{\gamma_{ob}^2 - 1}\,(g\gamma_a - \gamma_{ob}) + C\gamma_{ob}}{(g - 1)\sqrt{\gamma_{ob}^2 - 1}}. \tag{3.95}$$

Using this solution for γ_{ib} in Eq. 3.94 yields

$$I_{ob_{max}} = I_{ob_{SCL}} = \frac{2\pi\epsilon_0 c^3}{\eta\ \ln\left(\frac{r_a}{r_{ib}}\right)} \frac{C}{g(g - 1)} = \frac{2\pi\epsilon_0 c^3}{\eta\ \ln\left(\frac{r_{ob}}{r_{ib}}\right)} \frac{C}{(g - 1)}. \tag{3.96}$$

Equation 3.96 does not have any dependence on the relativistic factors γ_{ob} or γ_{ib}. It only depends on the geometrical factor and γ_a. The maximum current can be obtained from Eq. 3.96 where C is given by Eq. 3.93.

Similarly, in Eq. 3.88, the inner electron beam current will be zero for two cases: $\gamma_{ib} = 1$ (full potential depression) and $\gamma_{ib} = \gamma_{ob}$ (zero potential depression). Taking the derivative of Eq. 3.88 with respect to γ_{ib}, the current I_{ib} will be maximum for the condition $\frac{\partial I_{ib}}{\partial \gamma_{ib}} = 0$ that corresponds to the point at $\gamma_{ib}^3 = \gamma_{ob}$. Thus,

$$I_{ib_{max}} = I_{ib_{SCL}} = \frac{2\pi\epsilon_0 c^3}{\eta \ \ln(r_a/r_{ib})} \frac{(\gamma_{ib}^2 - 1)^{\frac{3}{2}}}{g} = \frac{2\pi\epsilon_0 c^3}{\eta \ \ln(r_a/r_{ib})} \frac{(\gamma_{ob}^{\frac{2}{3}} - 1)^{\frac{3}{2}}}{g}. \tag{3.97}$$

3.4 Theoretical results with SINUS-6 parameters

In order to obtain the calculated data in Matlab, we will now look at three cases for which parameters are listed in Table 3.1:

a Case 1, $r_{ic} = \frac{1}{2} r_{oc}$

b Case 2, $r_{ic} = \frac{1}{4} r_{oc}$

c Case 3, $r_{ic} = \frac{3}{4} r_{oc}$.

The analytic results for the Case 1, $r_{ic} = \frac{1}{2} r_{oc}$ are shown in Fig. 3.8, and calculated data presented in Table 3.2. All data are collected when the inner cathode is halfway between the axis and the inner radius of the outer cathode. As can be seen from Fig. 3.8, at lower applied voltages <100 kV, the difference between the outer electron beam current or energy and the inner one is small. But at higher voltages >100 kV, the difference increases for both current and energy. The formula used to obtain the percentage difference between inner and outer electron beam energy is

$$\text{Energy difference } \% = \left| \frac{\text{Difference of } E_{k_{ob}} \& E_{k_{ib}}}{\text{Average of } E_{k_{ib}} \& E_{k_{ob}}} \right| \times 100\%. \tag{3.98}$$

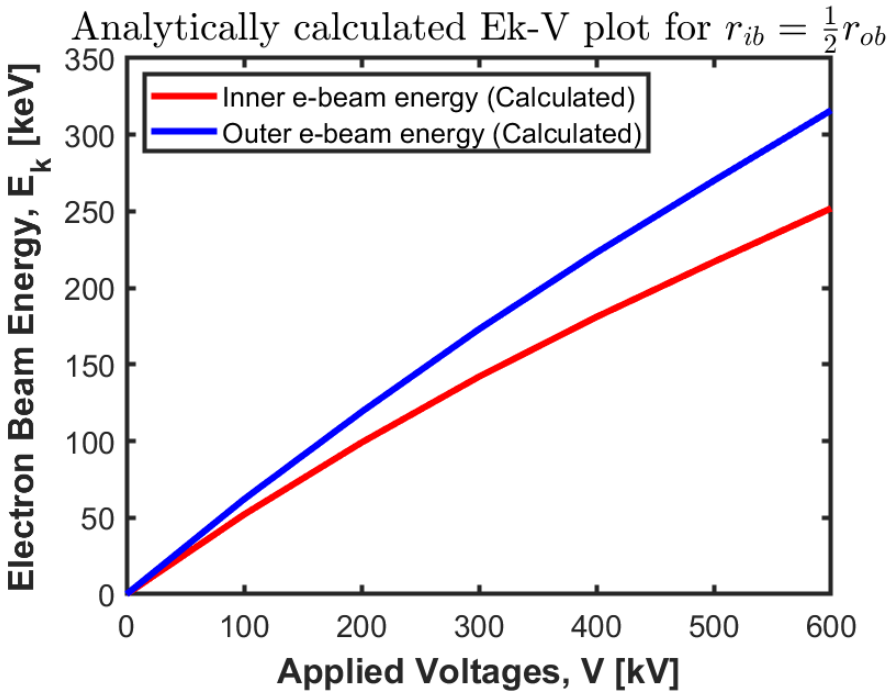

(a) Ek vs. V

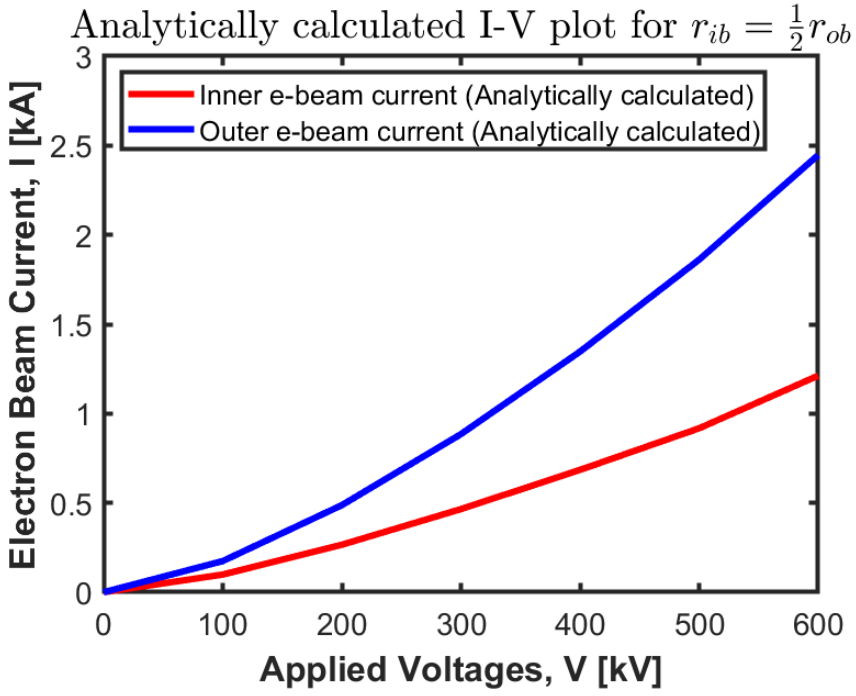

(b) I vs. V

Figure 3.8: Plot shows theoretical results of (a) electron beam energy and (b) electron beam current from inner (red) and outer (blue) emitters for applied voltages ranging from 100 - 600 kV using actual experimental SINUS-6 parameters for $r_{ic} = \frac{1}{2} r_{oc}$.

Table 3.2: Calculated data of electron beam current and beam energy from each cathode for applied voltages ranging from 100 - 600 kV using SINUS-6 [51] parameters for $r_{ic} = \frac{1}{2}r_{oc}$.

Voltage	r_a	r_{oc}	r_{ic}	h_c	$I_{ib.cal}$	$I_{ob.cal}$	$E_{k_{ib.cal}}$	$E_{k_{ob.cal}}$	Energy Diff.
[kV]	[cm]	[cm]	[cm]	[cm]	[kA]	[kA]	[keV]	[keV]	%
100	2.5	0.9	0.45	0.02	0.0990	0.1744	52	62	17.0
200	2.5	0.9	0.45	0.02	0.2658	0.4873	99	119	18.0
300	2.5	0.9	0.45	0.02	0.4652	0.8847	142	173	19.6
400	2.5	0.9	0.45	0.02	0.6847	1.3465	181	223	21.0
500	2.5	0.9	0.45	0.02	0.9175	1.8612	217	270	22.0
600	2.5	0.9	0.45	0.02	1.2120	2.4469	252	316	23.0

*r_a = Radius of the anode. r_{oc} = radius of the outer cathode. r_{ic} = radius of the inner cathode. $h_{oc} = h_{ic} = h_c$ = thickness of the both cathodes. $I_{ib.cal}$ = calculated inner beam current. $I_{ob.cal}$ = calculated outer beam current. $E_{k_{ib.cal}}$ = calculate inner beam energy. $E_{k_{ob.cal}}$ = calculate outer beam energy.

Analytic results for Case 2, $r_{ic} = \frac{1}{4}r_{oc}$ are shown in Fig. 3.9, and calculated data presented in Table 3.3. As can be seen from Fig. 3.9, at lower applied voltages $<$ 100 kV, the difference between outer electron beam current or energy is small. But at higher voltages $>$ 100 kV, the difference gets higher. Unlike Fig. 3.8, the calculated outer electron beam current is much higher than the calculated inner electron beam current.

Analytic results for Case 3, $r_{ic} = \frac{3}{4}r_{oc}$ are shown in Fig. 3.10, and calculated data presented in Table 3.4. Unlike Figs. 3.8 and 3.9, both outer and inner electron beam show comparable currents but with some energy differences. Table 3.4 shows the energy difference in this case from 9.5-13% for the applied voltages ranging from 100 - 600 kV.

A more detailed comparison between the electron beam currents and kinetic en-

Table 3.3: Calculated data of electron beam current and beam energy from each cathode for applied voltages ranging from 100 - 600 kV using SINUS-6 [51] parameters for $r_{ic} = \frac{1}{4}r_{oc}$.

Voltage	r_a	r_{oc}	r_{ic}	h_c	$I_{ib.cal}$	$I_{ob.cal}$	$E_{k_{ib.cal}}$	$E_{k_{ob.cal}}$	Energy Diff.
[kV]	[cm]	[cm]	[cm]	[cm]	[kA]	[kA]	[keV]	[keV]	%
100	2.5	0.9	0.24	0.02	0.0661	0.2071	49	62	24
200	2.5	0.9	0.24	0.02	0.1762	0.5757	92	120	26
300	2.5	0.9	0.24	0.02	0.3067	1.0406	131	173	27
400	2.5	0.9	0.24	0.02	0.4492	1.5775	167	224	29
500	2.5	0.9	0.24	0.02	0.5994	2.1724	200	272	30
600	2.5	0.9	0.24	0.02	0.7927	2.8568	232	317	31

*r_a = Radius of the anode. r_{oc} = radius of the outer cathode. r_{ic} = radius of the inner cathode. $h_{oc} = h_{ic} = h_c$ = thickness of the both cathodes. $I_{ib.cal}$ = calculated inner beam current. $I_{ob.cal}$ = calculated outer beam current. $E_{k_{ib.cal}}$ = calculate inner beam energy. $E_{k_{ob.cal}}$ = calculate outer beam energy.

Table 3.4: Calculated data of electron beam current and beam energy from each cathode for applied voltages ranging from 100 - 600 kV using SINUS-6 [51] parameters for $r_{ic} = \frac{3}{4}r_{oc}$.

Voltage	r_a	r_{oc}	r_{ic}	h_c	$I_{ib.cal}$	$I_{ob.cal}$	$E_{k_{ib.cal}}$	$E_{k_{ob.cal}}$	Energy Diff.
[kV]	[cm]	[cm]	[cm]	[cm]	[kA]	[kA]	[keV]	[keV]	%
100	2.5	0.9	0.675	0.02	0.1435	0.1294	57	62	9.5
200	2.5	0.9	0.675	0.02	0.3880	0.3633	108	120	10
300	2.5	0.9	0.675	0.02	0.684	0.670	156	174	11
400	2.5	0.9	0.675	0.02	1.014	1.013	200	224	11.8
500	2.5	0.9	0.675	0.02	1.4	1.4	240	272	12.5
600	2.5	0.9	0.675	0.02	1.8265	1.8237	281	318	13

*r_a = Radius of the anode. r_{oc} = radius of the outer cathode. r_{ic} = radius of the inner cathode. $h_{oc} = h_{ic} = h_c$ = thickness of the both cathodes. $I_{ib.cal}$ = calculated inner beam current. $I_{ob.cal}$ = calculated outer beam current. $E_{k_{ib.cal}}$ = calculate inner beam energy. $E_{k_{ob.cal}}$ = calculate outer beam energy.

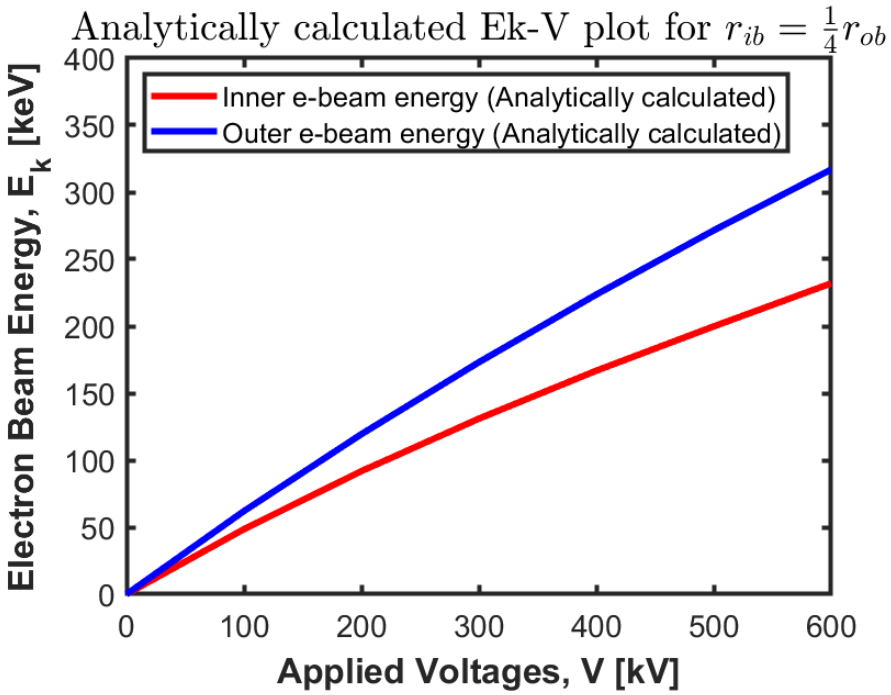

(a) Ek vs. V

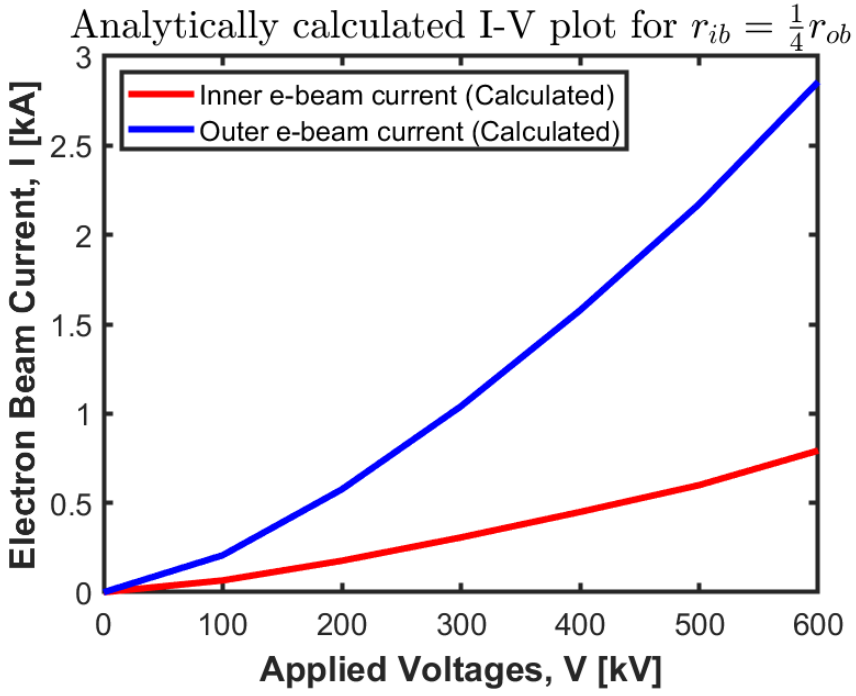

(b) I vs. V

Figure 3.9: Plot shows theoretical results of (a) electron beam energy and (b) electron beam current from inner (red) and outer (blue) emitters for applied voltages ranging from 100 - 600 kV using SINUS-6 experimental [51] parameters for $r_{ic} = \frac{1}{4} r_{oc}$.

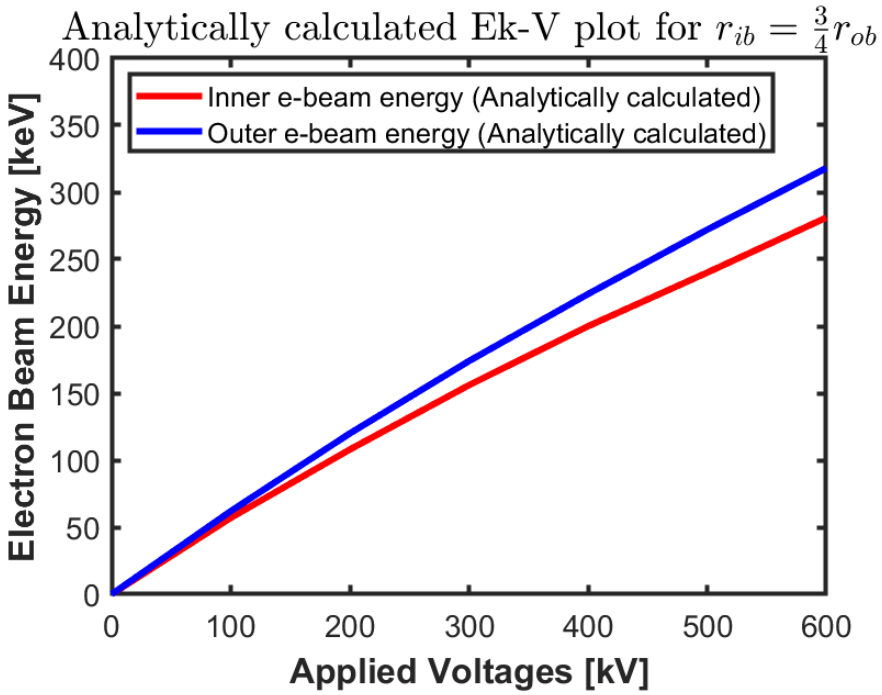

(a) Ek vs. V

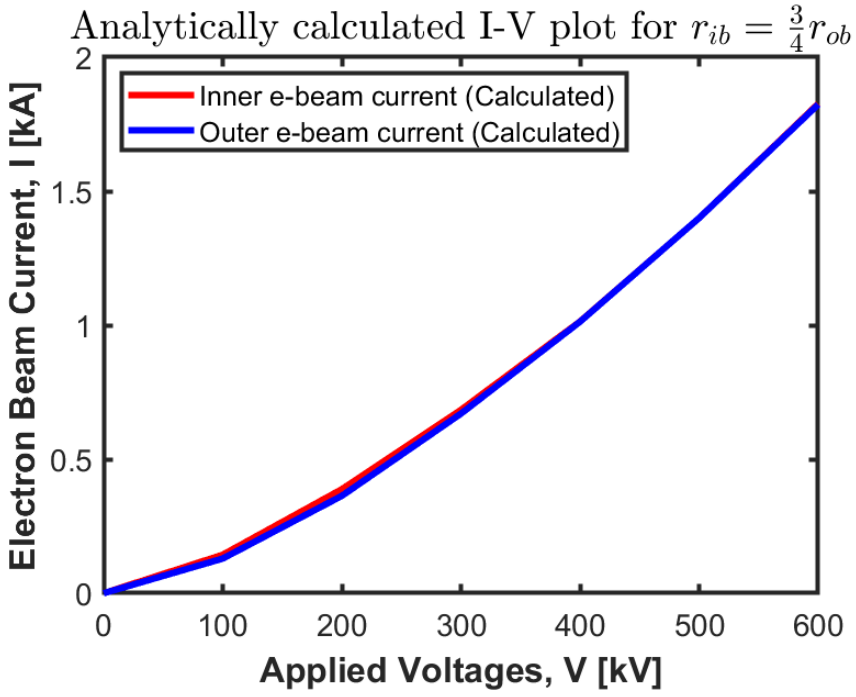

(b) I vs. V

Figure 3.10: Plot shows theoretical results of (a) electron beam current and (b) electron beam energy from inner (red) and outer (blue) emitters for applied voltages ranging from 100 - 600 kV actual experimental SINUS-6 parameters for $r_{ic} = \frac{3}{4} r_{oc}$.

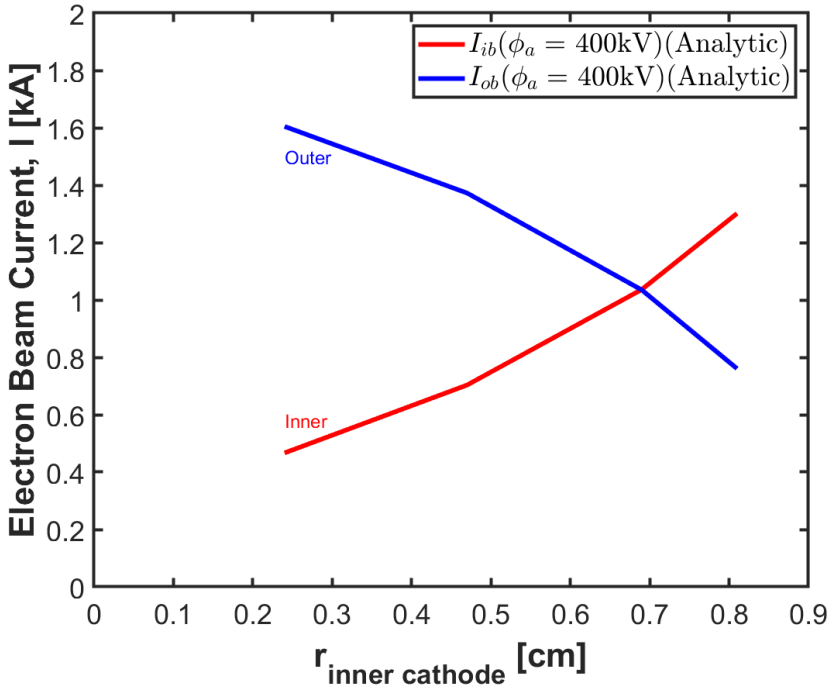

Figure 3.11: Plot illustrates the calculated electron beam current from the inner (red) and outer (blue) beam as a function of the radius of the inner cathode r_{ic}.

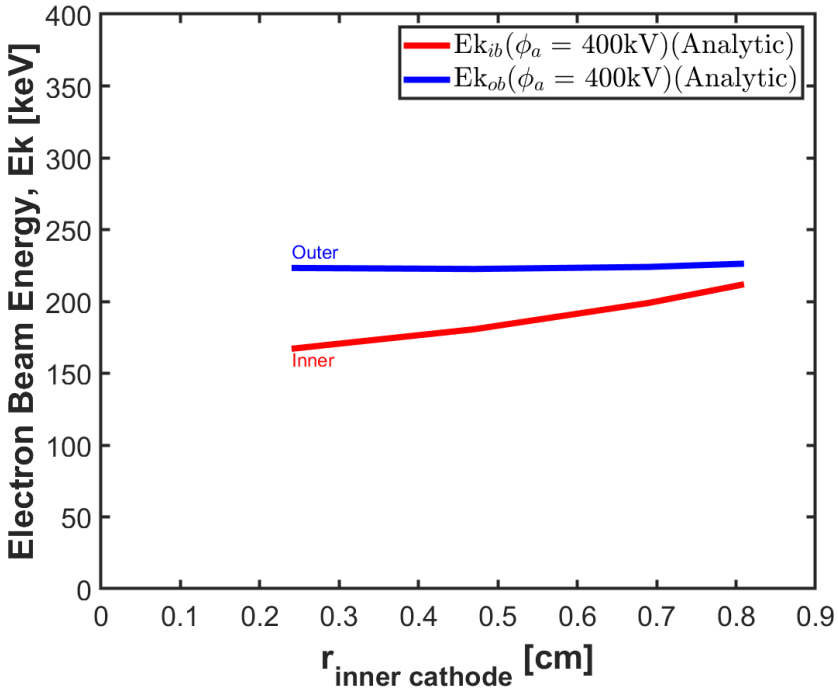

Figure 3.12: Plot illustrates the calculated electron beam energy from the inner (red) and outer (blue) beam as a function of the radius of the inner cathode r_{ic}.

ergies on the same plot as a function of the *'inner'* cathode's radius can be seen in Fig. 3.11 and Fig. 3.12. In both figures, the x-axis represents the radial position of the inner cathode from $r_{ic} = 0$ to r_{ic} =0.81 cm and the y-axis represents the electron beam current in [kA] (in Fig. 3.11) and energy in [keV] (in Fig. 3.12). The most striking result can be seen in this case, the two electron beam currents meet at the same point of 0.69 cm (viz., radial position of inner cathode) and a greater than 10% energy difference is achieved between the two beams (*cf.* in Figs. 3.11 and 3.12).

3.5 Derivation when both cathodes have the same length

[nb: When there is no axial difference between the cathodes - meaning the axial positions of both cathodes are the same.]

Figure 3.13 shows a 2D symmetric schematic in the $r-z$ plan of two nested MICD of identical length, parameters are listed in the Table 3.5.

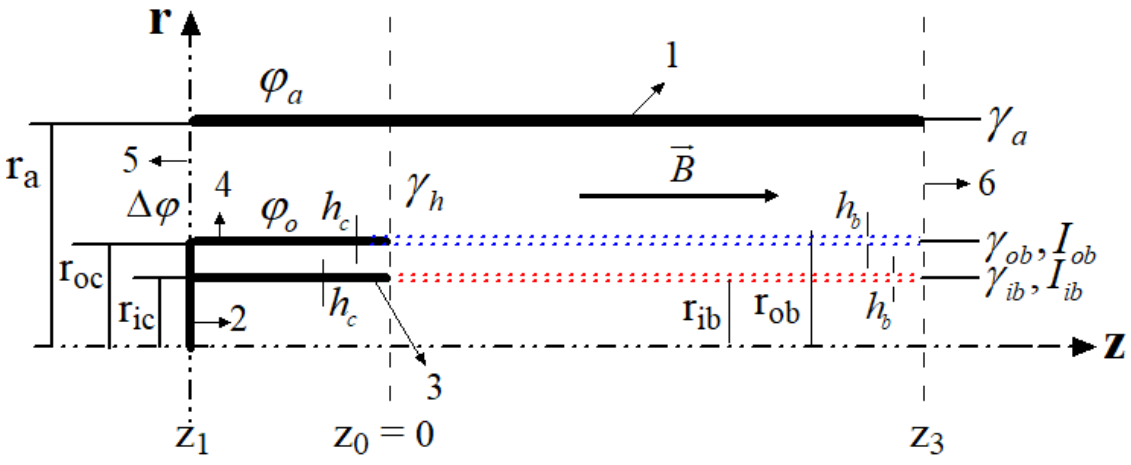

Figure 3.13: Schematic of two nested MICDs in a vacuum tube. 1. anode; 2. cathode stalk; 3. inner cathode; 4. outer cathode; 5. input Port; 6. output port.

Table 3.5: Design parameters of two nested MICDs in a vacuum tube when both cathodes have the same length.

Inputs				Outputs	
Design Parameters	Symbols	Values	Units	Parameters	Units
Anode potential	φ_a	+	kV	I_{ib} [a]	A
Cathode potential	φ_c	0	kV	I_{ob} [b]	A
Anode radius	r_a	2.5	cm	γ_{ib} [c]	unitless
Anode length	z_1 to z_3	16.5	cm	γ_{ob} [d]	unitless
Outer cathode radius	r_{oc}	0.9	cm	Ek_{ib} [e]	keV
Outer cathode length	z_1 to z_0	4.9	cm	Ek_{ob} [f]	keV
Inner cathode radius	r_{ic}	$r_{ic} < r_{oc}$	cm		
Inner cathode length	z_1 to z_2	4.9	cm		
Both Cathode thickness	h_c	0.02	cm		

[a]Inner electron beam current, [b]Outer electron beam current, [c]Relativistic factor at the external boundary of the inner electron beam, [d]Relativistic factor at the external boundary of the outer electron beam, [e]Inner electron beam energy at the output end, [f]Outer electron beam energy at the output end.

The solutions for this geometry are

$$I_{ob} = \frac{2\pi\epsilon_0 c^3}{\eta\ \ln\left(r_a/r_{ib}\right)} \frac{\sqrt{\gamma_{ob}^2 - 1}}{\gamma_{ob}} \left[\frac{\gamma_a - \gamma_{ob}}{1-g} - \frac{\gamma_{ob} - \gamma_{ib}}{g}\right] \tag{3.99}$$

and

$$I_{ib} = \frac{2\pi\epsilon_0 c^3}{\eta\ \ln(r_a/r_{ib})} \frac{\sqrt{\gamma_{ib}^2 - 1}}{\gamma_{ib}} \frac{(\gamma_{ob} - \gamma_{ib})}{g} \tag{3.100}$$

$$\Rightarrow (\gamma_a - 1)^2 - (\gamma_a - \gamma_{ob})^2 - (\gamma_{ob} - \gamma_{ib})^2 \frac{1-g}{g} = 2\left[\frac{(\gamma_{ob}^2 - 1)}{\gamma_{ob}} \left(\frac{\gamma_a - \gamma_{ob}}{1-g} - \frac{\gamma_{ob} - \gamma_{ib}}{g}\right) + \frac{(\gamma_{ib}^2 - 1)}{\gamma_{ib}} \frac{(\gamma_{ob} - \gamma_{ib})}{g}\right](1-g). \tag{3.101}$$

It should be noted here that we only have solutions at the 'Output Port' (in the plane z_2). We do not have any additional boundary here and, therefore, no other equation of current as we obtained in the previous section (for example, Eq. 3.80). Now, the question is how do we solve Eqs. 3.99, 3.100 and 3.101 numerically? If we can somehow solve Eq. 3.101 and obtain the solutions for γ_{ob} and γ_{ib}, we can determine the current and energy.

To obtain expressible analytic solution from this symbolic algebraic Eq. 3.101 is too difficult or it may not be possible to compute or derive analytically. In this case, an empirical strategy or numerical approach is necessary. It also requires computer simulation. We know for any applied potential $\gamma_a = 1 + \frac{\eta\varphi_a}{c^2}$. Here γ_a is known. We also know $\gamma_a > \gamma_{ob} > \gamma_{ib}$. This means that γ_{ob}, γ_{ib} must lie between 1 and γ_a. If we select values between 1 and γ_a, and insert them in Eqs. (3.99, 3.100, and 3.101), we are able to find a solution.

Let us perform one simulation using MAGIC 2D where the radius of the inner cathode $= \frac{3}{4}$ of the outer radius. The applied voltage is 400 kV and the magnetic field is 3 T. The thickness of each cathode is 0.02 cm. Simulation results are shown in Figs. 3.14 and 3.15.

Let us check the analytical results using Eqs. 3.99 and 3.100 for applied voltage 400 kV, radius of the anode $r_a = 2.5$ cm, outer cathode radius $r_{oc} = 0.9$ cm, inner cathode radius $r_{ic} = \frac{3}{4}r_{oc}$, geometrical factor $g = \frac{\ln(\frac{r_{oc}}{r_{ic}})}{\ln(\frac{r_a}{r_{ic}})}$, and assume $\gamma_{ob} = 1.4890, \gamma_{ib} = 1.4688$. We obtain

$$I_{ob} = I_o = \frac{2\pi\epsilon_0 c^3}{\eta\ \ln\left(r_a/r_{ib}\right)} \frac{\sqrt{\gamma_{ob}^2 - 1}}{\gamma_{ob}} \left[\frac{\gamma_a - \gamma_{ob}}{1-g} - \frac{\gamma_{ob} - \gamma_{ib}}{g}\right] = 1.396 \text{ kA}$$

and

$$I_{ib} = I_i = \frac{2\pi\epsilon_0 c^3}{\eta\ \ln(r_a/r_{ib})} \frac{\sqrt{\gamma_{ib}^2 - 1}}{\gamma_{ib}} \frac{(\gamma_{ob} - \gamma_{ib})}{g} = 450.677 \text{ kA}.$$

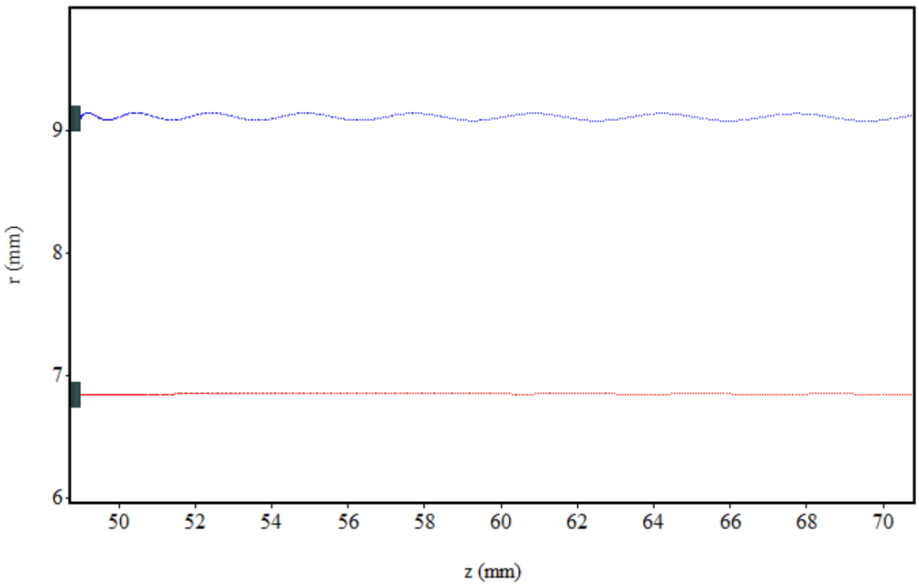

(a) Electron beams show macroparticle

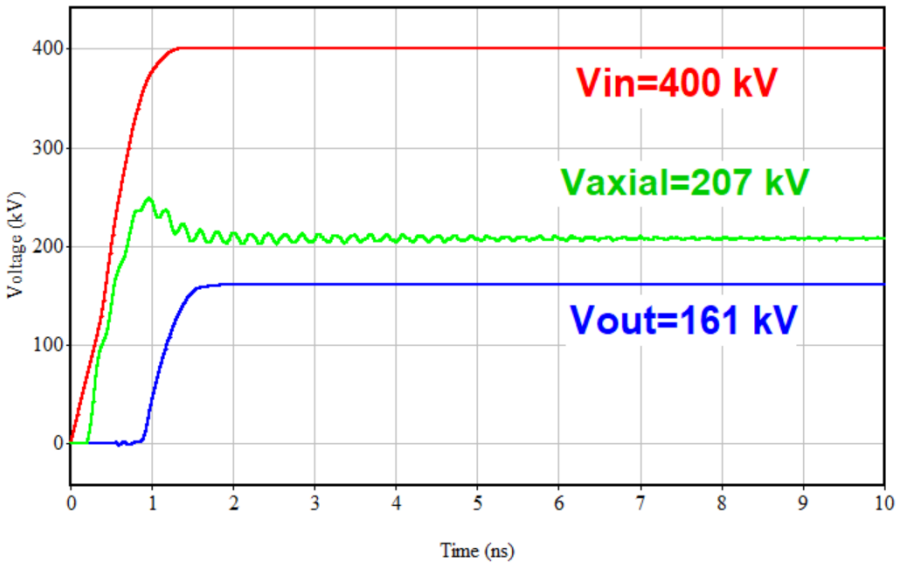

(b) Voltage profile

Figure 3.14: Results obtained from MAGIC simulations show: (a) macroparticles of inner (red) and outer (blue) emitters, and (b) applied voltage(red) at the 'Input Port', axial potential(green) from the 'Input Port' to the 'Output Port', and output potential(blue) at the 'Output Port'.

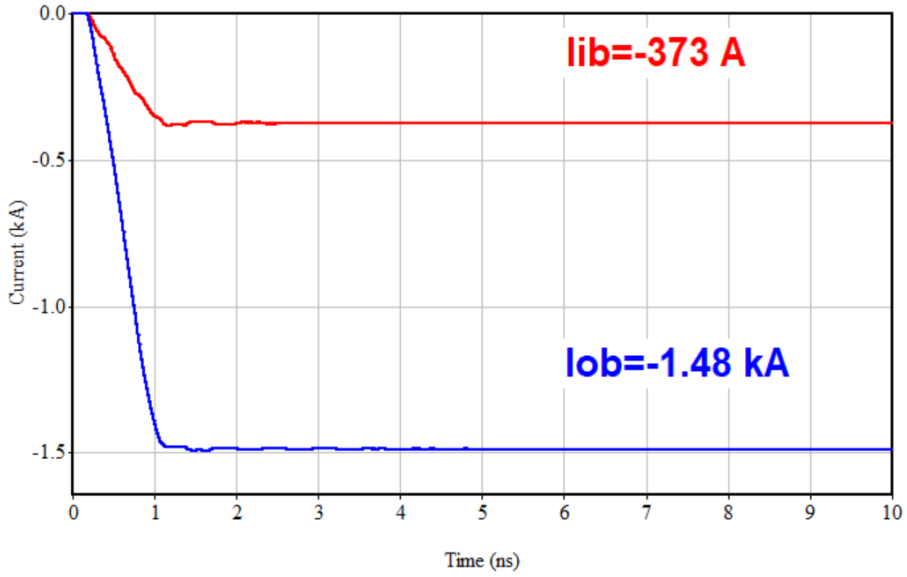

(a) Beam current profile

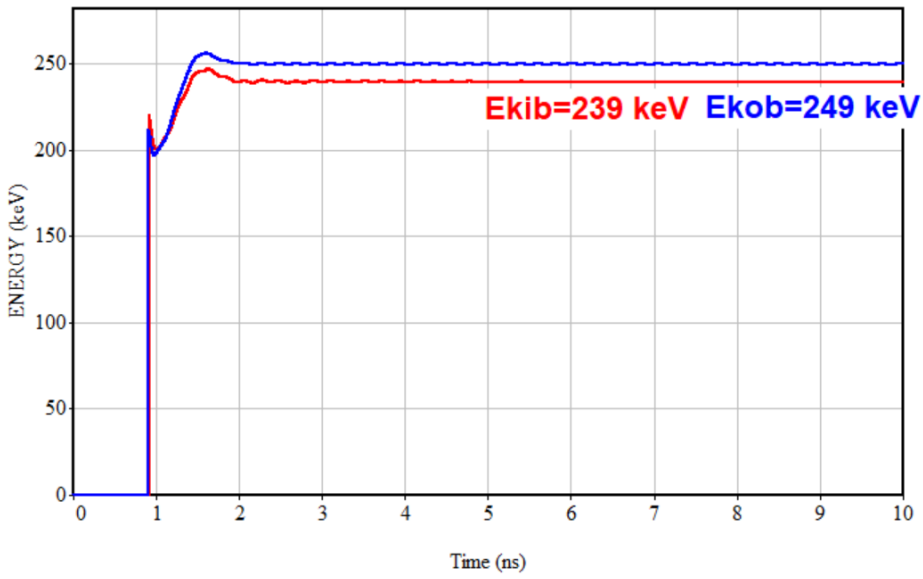

(b) Beam energy profile

Figure 3.15: Results obtained from MAGIC simulations show: (a) emitted electron beam current from the inner (red) and outer (blue) emitters, and (b) average energy generated from the inner (red) and outer (blue) beams.

For the electron beam potentials at the 'Output Port', we have $\varphi_{ib} = 240$ kV and $\varphi_{ob} = 250$ kV, which is in excellent agreement with simulations, as shown in Fig. 3.15b. The energy difference in this case, $\Delta E_k = 4\%$.

CHAPTER 4

PARTICLE-IN-CELL SIMULATIONS

4.1 Overview of particle-in-cell (PIC) code - MAGIC

The PIC simulations are conducted in two phases - 2D axisymmetric MAGIC simulations for rapid scoping and more comprehensive 3D MAGIC simulations. Actual experimental parameters from the SINUS-6 electron beam accelerator at UNM are used in both the 2D and 3D PIC simulations to study the electron beam transport through the vacuum channel and the final beam energies and currents.

The MAGIC PIC code uses the FDTD (finite-difference-time-domain) method to solve Maxwell's equations to obtain the electromagnetic fields (for example, in a cylindrical coordinate system $E_r, E_\varphi, E_z, B_r, B_\varphi, B_z$) that are defined at discrete locations in space and time. By defining some initial known parameters of the electron beam, the MAGIC PIC code computes the interactions or relations between electrons and electromagnetic fields in space and time. At the same time the code uses a short

time step (δt) to advance these electromagnetic fields in time. In a similar manner, with each new time increment added to δt, Maxwell's equations are solved throughout the simulation space and in time. The Lorentz force equation is solved to advance particle (electrons in this case) positions and momenta in time. The charge-density and current density of the simulated electron beams are calculated self-consistently using the continuity algorithm [110]. The MAGIC PIC code follows the Courant stability criterion for each time step

$$\chi < \left[\frac{2-3\gamma^2+2\gamma^3}{2(1-3\gamma^2+2\gamma^3)}\right]^{1/2}, \quad 0 \leq \gamma \leq \frac{1}{2},$$
$$\chi < (3\gamma)^{1/2}, \quad \frac{1}{2} \leq \gamma \leq 1, \tag{4.1}$$

where $\chi^2 = c^2\delta t^2 \sum_{i=1,N} \frac{1}{(\delta x_i)}^2$ is the Courant ratio squared, δx_i is the cell size in meters, and N is the number of dimensions (2 or 3).

Before studying multiple electron beam generation, a series of PIC simulations for a single MICD is performed. It is found that results are consistent between Fedosov's theory and the numerical simulations. Details of the simulation model set-up, and results are discussed below for a single and two nested MICDs.

4.2 Numerical modeling of a single MICD

The simple geometry in MAGIC is shown in Fig. 4.1, where an annular, thin-walled explosive emission cathode is inserted in a drift tube. Parameters are listed in Table 4.1. Since the cathode is very thin, we assume the thickness in the simulation to be one cell size, h_c=0.02 cm. A conductor is connected from $r = 0$ to the inner radius of the cathode with $dz = 0.5$ cm. The 'Input Port' for applying the potential is connected between the outer radius of the cathode to the inner radius of the anode.

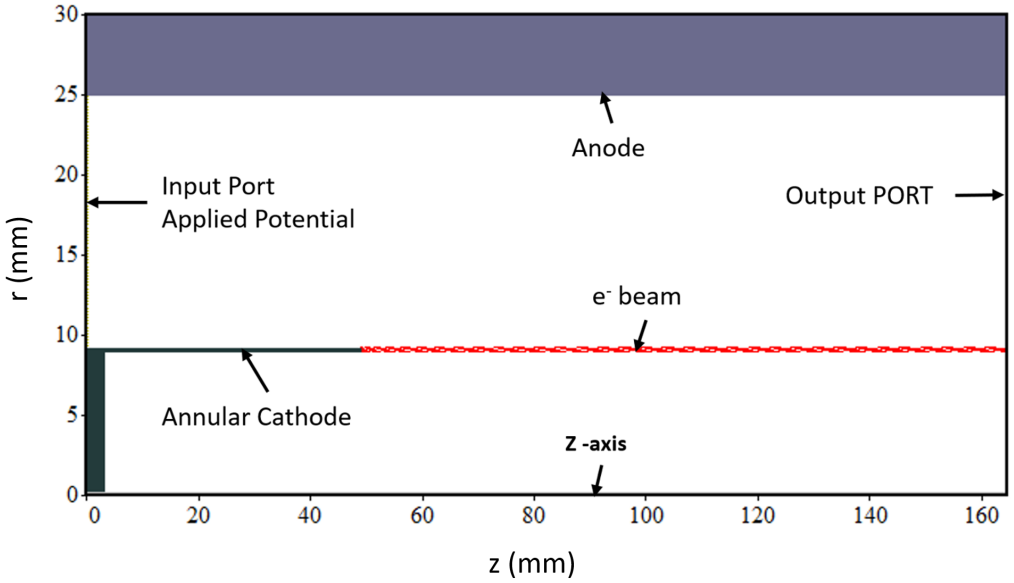

Figure 4.1: MAGIC model of a single MICD.

The 'Output Port' is set-up at the end of the drift tube from z_{end}=16.45 cm to inner radius of the anode, r_{anode} = 2.5 cm. The anode and cathode parameters are based on the SINUS-6 electron beam accelerator in UNM's Pulsed Power, Beams, and Microwaves Laboratory (*cf.* Fig. 1.3).

The MAGIC simulation model set-up and results obtained with (i) an axially symmetric hollow waveguide with inner radius 2.5 cm and total length 40 cm; (ii) an explosive emission annular cathode (*cf.* Fig. 4.2) with axial length 49 mm, outer

Table 4.1: Design parameters of a MICD based on SINUS-6 parameters.

Design Parameters	Values
Applied potential	400 kV
Anode length	16.45 cm
Anode radius	2.5 cm
Cathode radius	0.9 cm
Cathode length	4.9 cm
Cathode thickness	0.02 cm
Magnetic field	2 T, 3 T
Simulation cell size	0.02 cm

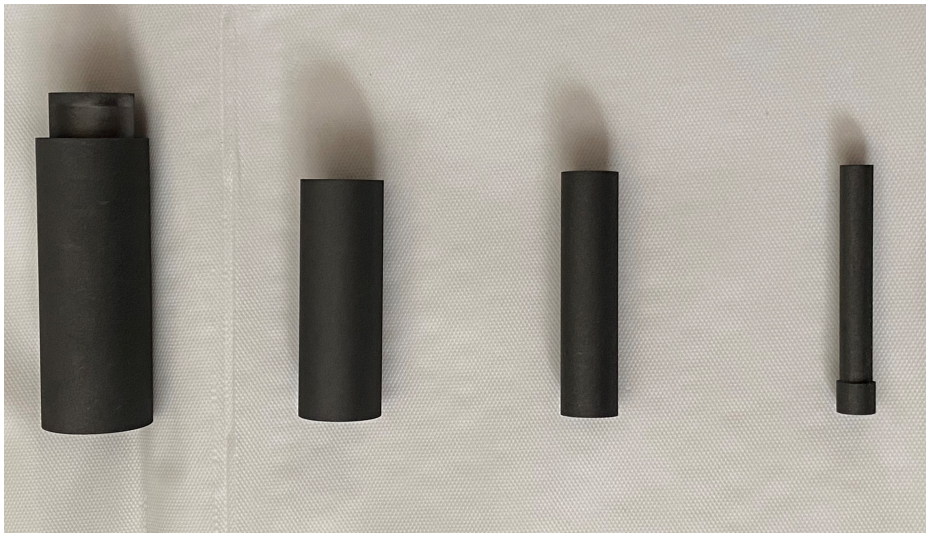

(a) Cathodes with different diameters

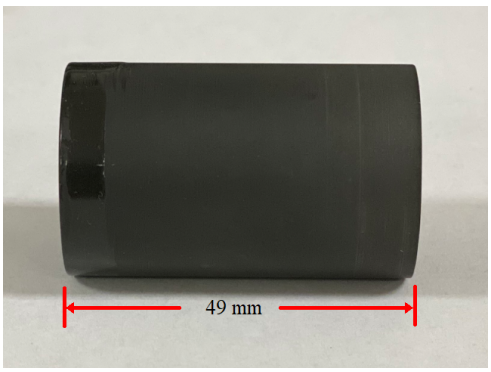

(b) Side view

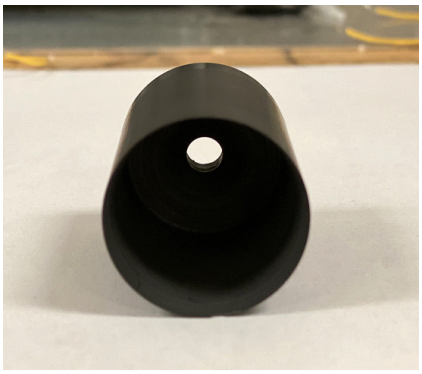

(c) Front view

Figure 4.2: (a) Photograph of cylindrical cathodes with different diameters, nested MICDs, 18 mm, 13.5 mm, 9 mm, 4.5 mm; (b) side view of axial length 4.9 cm; (c) front view of the thin, annular explosive emission cathode used on analytic, simulation and SINUS-6 electron beam accelerator.

radius 9 mm, and radial thickness 0.2 mm; (iii) applied voltages ranging 100 kV - 600 kV; (iv) the uniform axial magnetic field strength is 0.5, 1, 2.0 and 3 T; (v) three different radius based cylindrical cathodes (i.e., r_c=9 mm, 11.15 mm, 15.3 mm) (*cf.* Fig. 4.2a) are used. Axially uniform magnetic fields of $B_{0.5} = 0.5$ T, $B_1 = 1$ T, $B_2 = 2$ T, and $B_3 = 3$ T were set-up sequentially during the simulations.

4.2.1 Simulation results for a single MICD

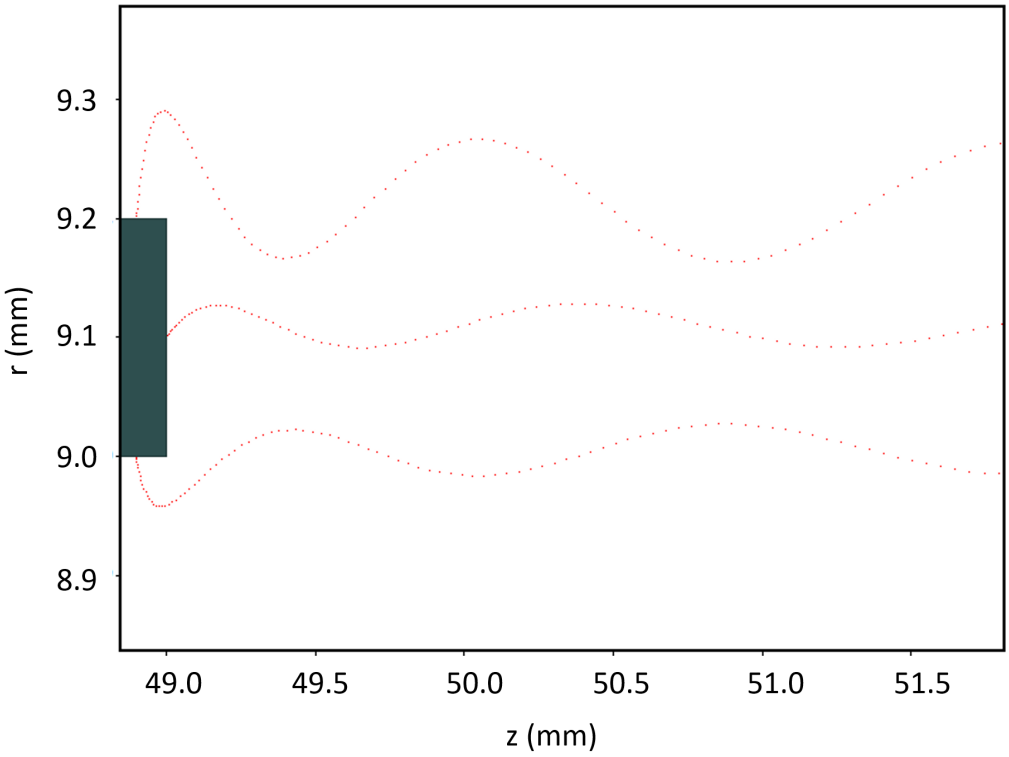

Figure 4.3: Macroparticles emitted from the cathode.

Figure 4.3 shows the macroparticles emitted from the cathode. Figure 4.4 shows static electric field contour plot that illustrates the accelerating field. Simulation results obtained from MAGIC 2D are shown in Figs. 4.5 and 4.6. Figure 4.5 illustrates applied voltage (red) on the cathode and electron beam current (blue) emitted from the cathode for an applied voltage of 400 kV as function of time for a 3 T magnetic field. Figure 4.6 shows applied voltage (red) on the cathode and electron beam energy (blue) emitted from the cathode for an applied voltage of 400 kV as function of time for a 3 T magnetic field. In both cases, the simulation results are performed with a 18 mm diameter cathode and for a simulation time of 10 ns.

Comparison of the results obtained from MAGIC as well as analytically calculated Fedosov current and energy are presented in Fig. 4.7. These simulations are

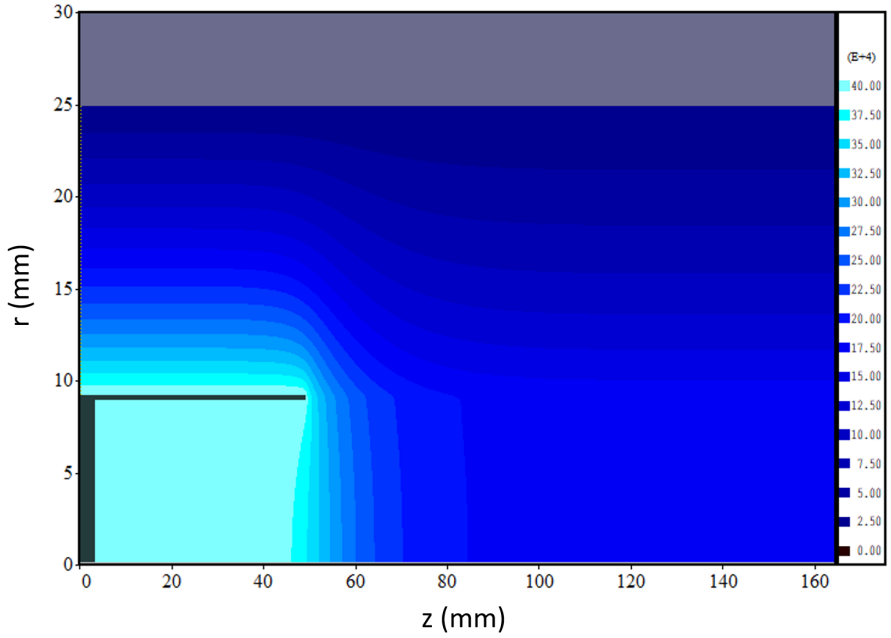

Figure 4.4: Static electric field contour plot illustrates the accelerating field.

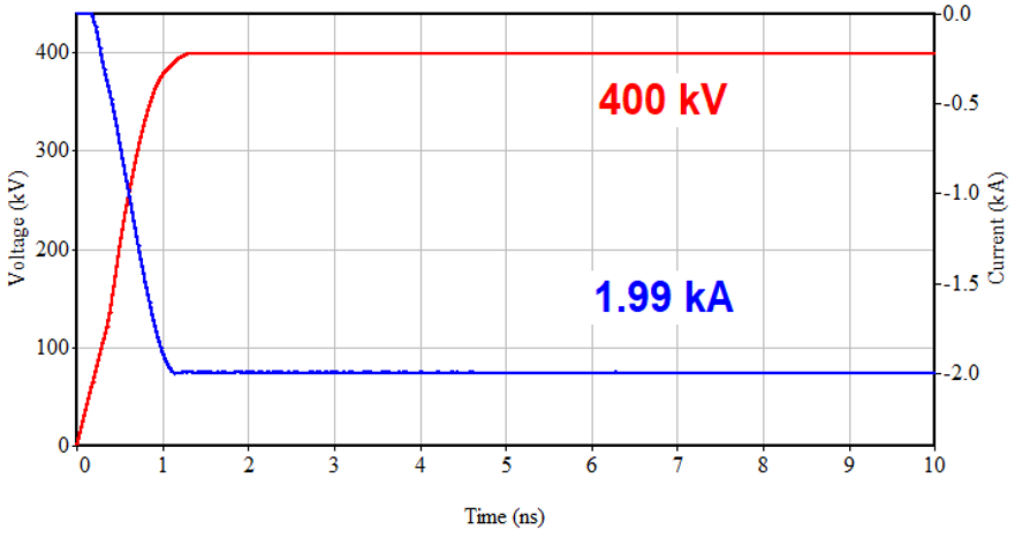

Figure 4.5: MAGIC 2D simulation showing applied voltage (red) on the cathode and electron beam current (blue) emitted from the cathode for an applied voltage of 400 kV as function of time for a 3 T magnetic field.

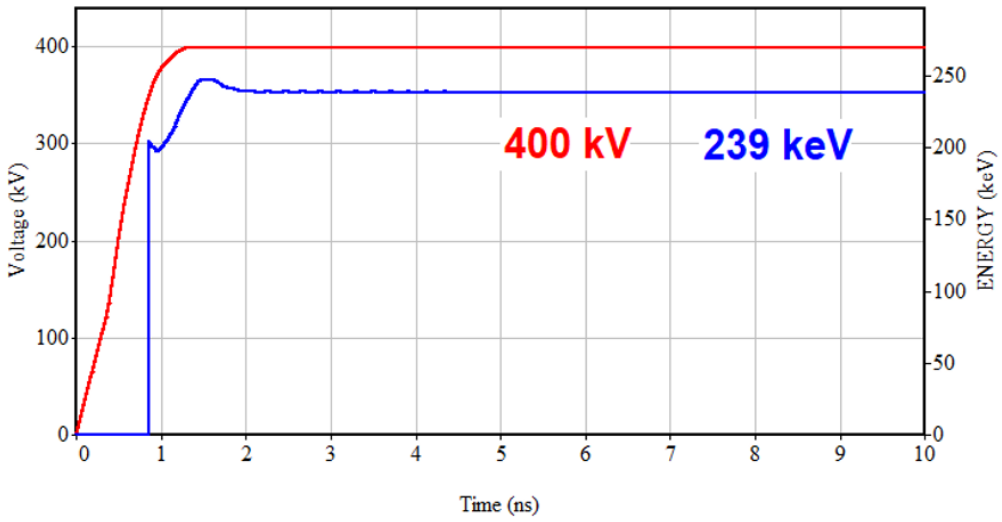

Figure 4.6: MAGIC 2D simulation shows applied voltage (red) on the cathode and electron beam energy (blue) emitted from the cathode for an applied voltage of 400 kV as function of time for a 3 T magnetic field.

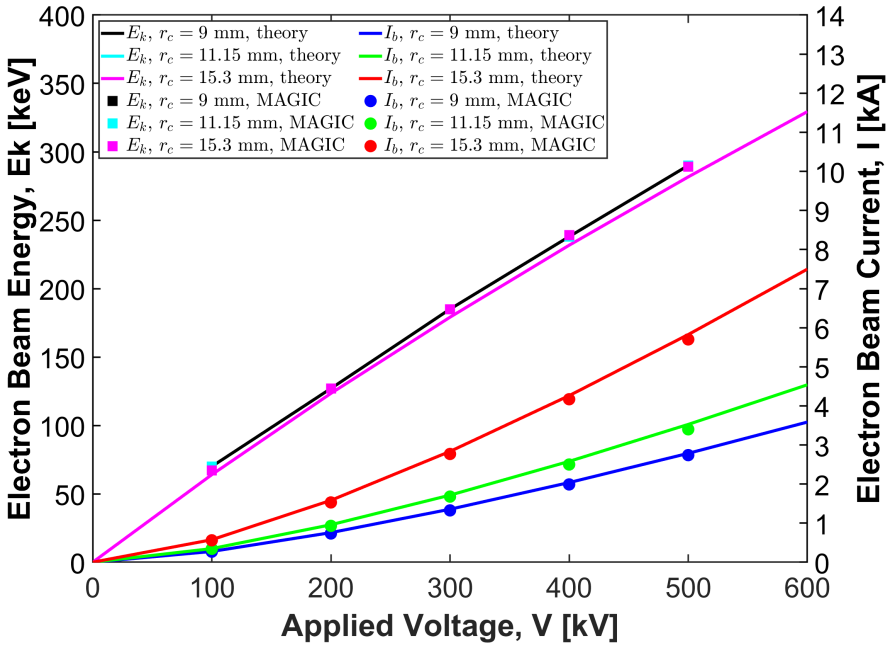

Figure 4.7: Analytical "Fedosov" current obtained in MAGIC simulations shows electron beam energy and currents as a function of applied voltages.

performed with three different cathode diameters as shown in Fig. 4.2a. As can be seen both MAGIC and Fedosov's theory agree well with each other.

4.3 Numerical modeling of two nested MICDs

The simulation model set-up is similar to what was described in Section 4.2 with the addition of another cathode as shown is in Fig. 4.8. The simulation parameters are listed in Table 4.2. Cathodes with different diameters are used as MICDs, shown in Fig. 4.2a. A general schematic of MICDs can be seen in Fig. 4.9.

As mentioned in Section 1.5, a case study approach was followed to identify an optimal geometry from this nested MICD model as follows:

1. the same negative potential applied to the outer and inner cathodes within a range of -100 to -500 kV
2. the radius of the anode $= r_a = 2.5$ cm
3. the radius of the outer cathode $r_{oc} = 0.9$ cm [oc=outer cathode]
4. the radius of the inner cathode $= r_{ic} = r_{var} * r_{oc}$, [ic=inner cathode]
5. the length of the outer cathode $z_{oc} = 4.9$ cm
6. the length of the inner cathode $z_{ic} = (4.9 + d)$ cm
7. the length of the anode $z_{oc} + 11.55$ cm $= (4.9 + 11.55)$ cm
8. the thickness of the both outer and inner cathodes, $= h_{ic} = h_{oc} = h_c = 0.02$ cm (one simulation cell size).

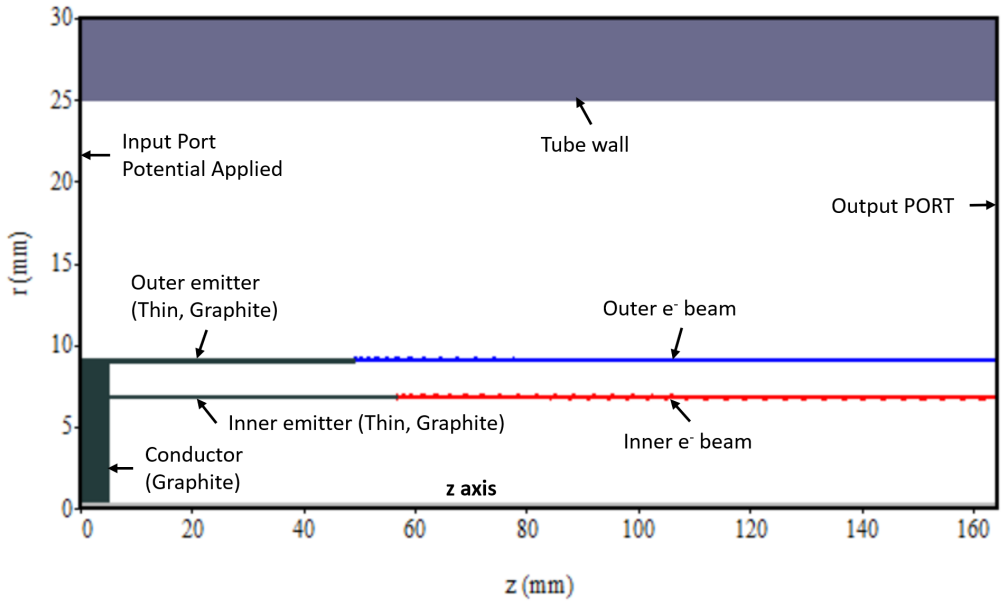

Figure 4.8: MAGIC model set-up with two nested MICDs in a hollow tube showing the emitted inner electron beam (red) and the outer electron beam (blue).

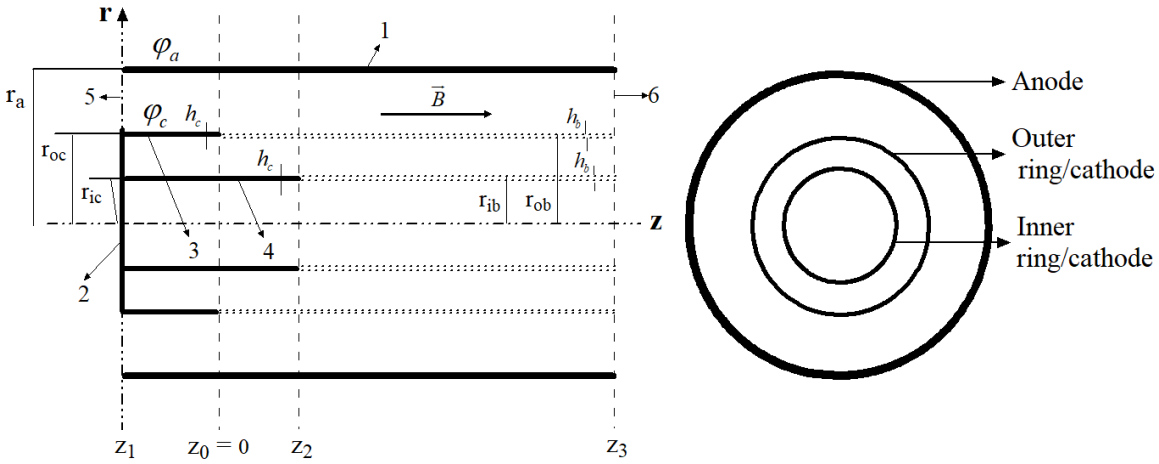

Figure 4.9: Left - Schematic of two nested MICDs in a vacuum tube. 1. Anode; 2. a single cathode stalk; 3. outer emitter/cathode; 4. inner emitter/cathode; 5. 'Input Port'; 6. 'Output Port'. Right - End view of the drift tube including MICDs.

Table 4.2: Parameters of two nested MICDs for simulation model.

Design Parameters	Symbols	Value	Unit
Anode potential	φ_a	0	kV
Cathode potential	φ_c	100 - 600	kV
Anode radius	r_a	2.5	cm
Anode length	z_1 to z_3	16.4	cm
Outer cathode radius	r_{oc}	0.9	cm
Outer cathode length	z_1 to z_0	4.9	cm
Cathode thickness	h_c	0.02	cm
Inner cathode radius	$r_{ic} < r_{oc}$	0.22 - 0.78	cm
Inner cathode length	z_1 to z_2	0 - 7.9	cm
Distance, d	z_0 to z_2	0 - 3.0	cm

4.3.1 Simulation results for two nested MICDs

The PIC simulations are conducted in two phases - 2D axisymmetric MAGIC simulations [110] for rapid scoping and more comprehensive 3D MAGIC simulations. Actual experimental parameters from the SINUS-6 electron beam accelerator at UNM are used in both 2D and 3D PIC simulations to study electron beam transport (*cf.* in Fig. 4.10, shows macroparticle) through the vacuum channel and the final beam energies and currents. Figures 4.11a to Fig. 4.11f show obtained simulated phase space plot of axial momentum of the inner electron beam (red) and outer electron beam (blue) for applied voltages ranging from 100 kV to 600 kV and a magnetic field of 1 T as a function of time. Static electric field contour plots illustrates the accelerating field can be seen in Fig. 4.12.

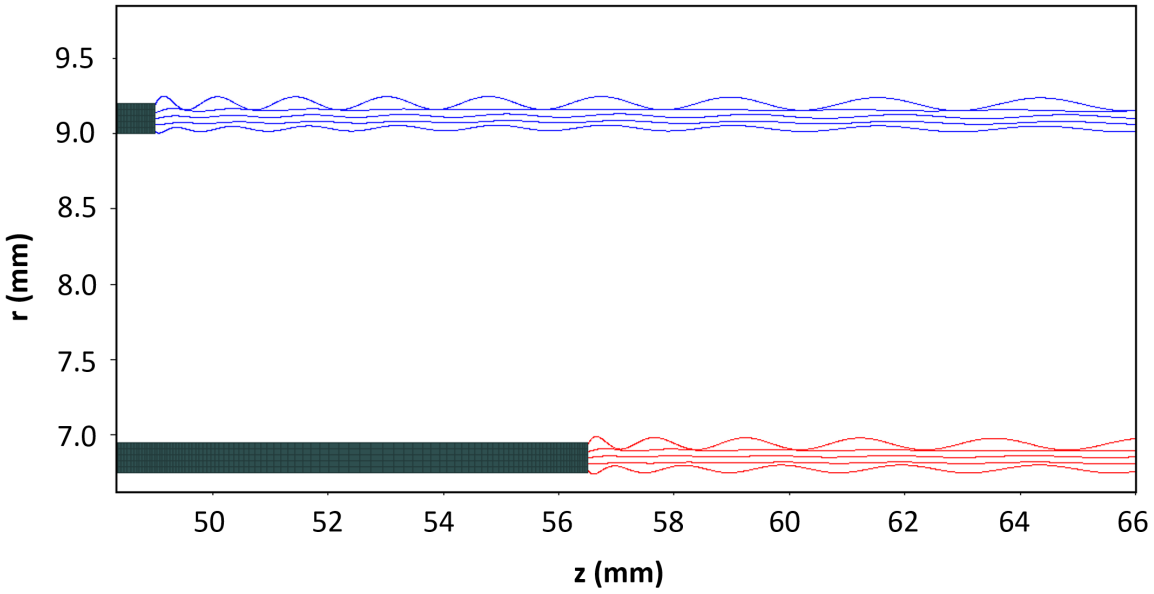

Figure 4.10: MAGIC model shows macro particles emitted from the inner (red) and the outer electron beam (blue).

Fig. 4.13a to Fig. 4.13d show obtained simulated phase space plot of energy of the inner electron beam (red) and outer electron beam (blue) for applied voltages ranging from 100 kV to 400 kV and a magnetic field of 3 T as a function of time.

4.3.2 Empirical strategy to find axial distance

As can be seen in Section 4.3, the two variables r_{var} (in the radial direction) and d (in the axial direction) are the main key factors for the numerical model in MAGIC (*cf.* in Fig. 4.14 and Fig. 4.15).

Figure 4.14 shows an empirical strategy to find both the radial and axial gap between the inner and outer cathode. Thus, for the algorithms/steps in MAGIC simulation, initially we:

1. fix the outer cathode radius and axial position (r, z) to match the SINUS-6 parameters;

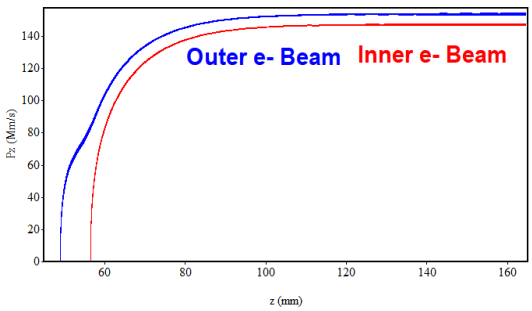

(a) Axial momentum (p_z), 100 kV

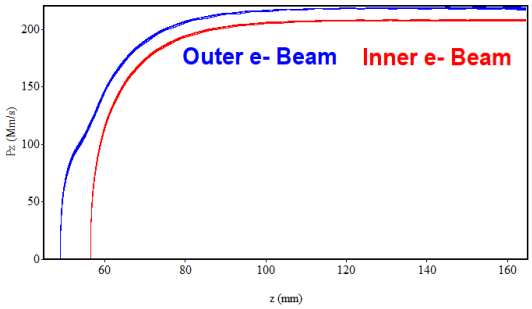

(b) Axial momentum (p_z), 200 kV

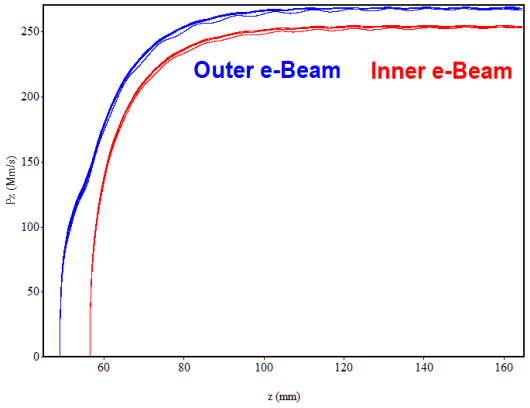

(c) Axial momentum (p_z), 300 kV

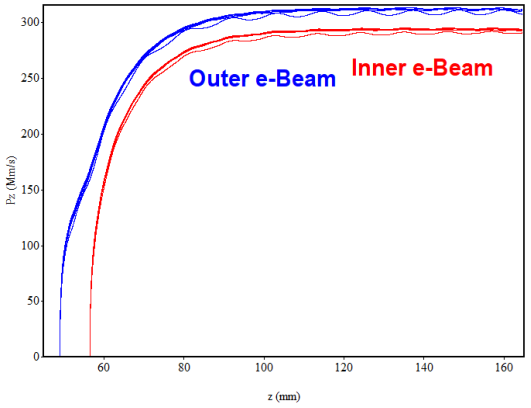

(d) Axial momentum (p_z), 400 kV

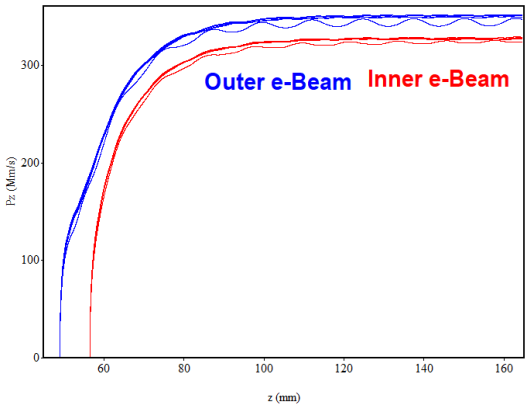

(e) Axial momentum (p_z), 500 kV

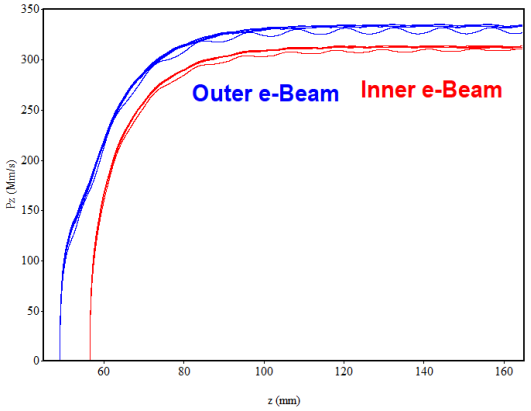

(f) Axial momentum (p_z), 600 kV

Figure 4.11: The momentum of the inner beam's electrons (red) and the outer beam's electrons (blue) are shown for cathode voltages of (a) 100 kV, (b) 200 kV, (c) 300 kV, (d) 400 kV, (e) 500 kV, and (f) 600 kV.

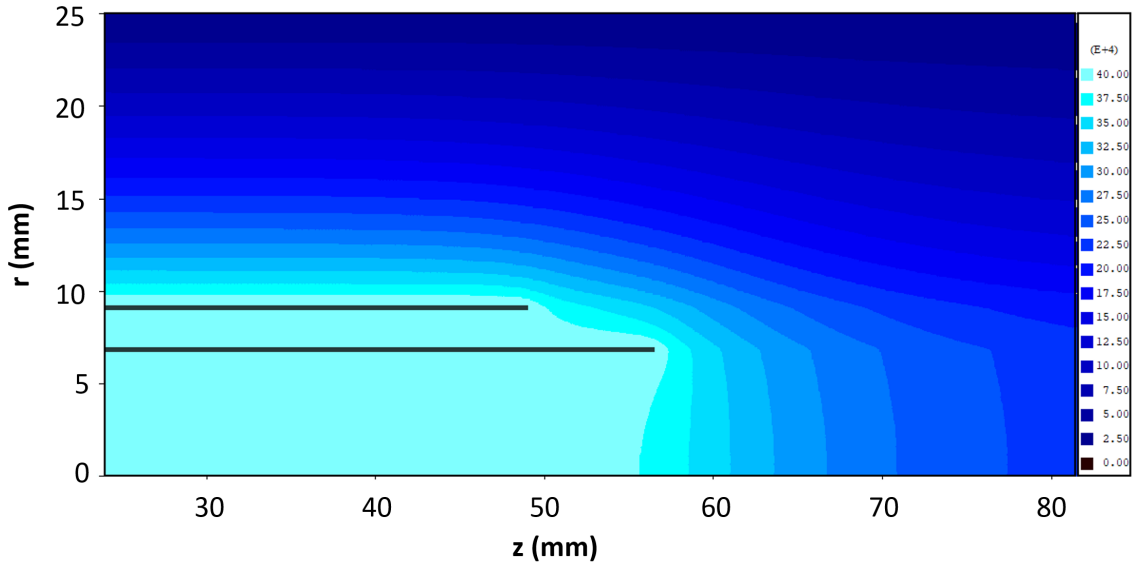

Figure 4.12: Static electric field contour plot illustrates the accelerating field.

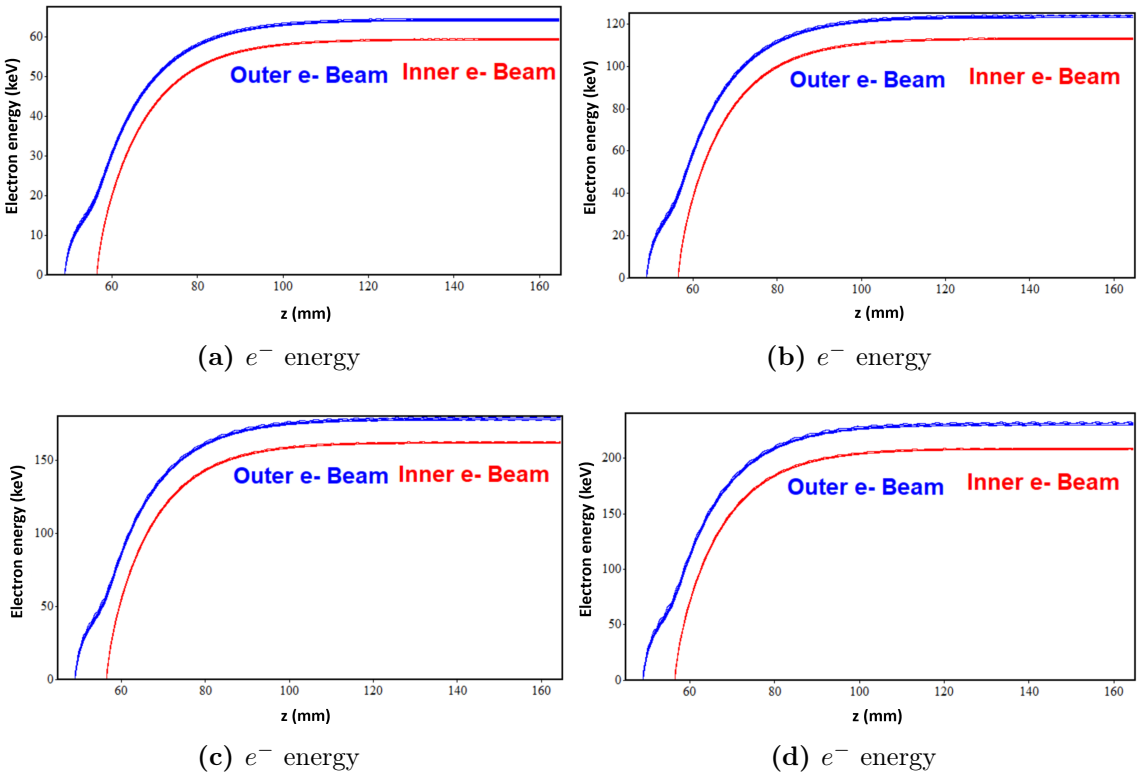

(a) e^- energy

(b) e^- energy

(c) e^- energy

(d) e^- energy

Figure 4.13: The energy of the inner beam's electrons (red) and the outer beam's electrons (blue) are shown for cathode voltages of (a) 100 kV, (b) 200 kV, (c) 300 kV, and (d) 400 kV.

2. fix the inner cathode radius halfway between $r = 0$ and the outer cathode radius, $r_{ic} = \frac{1}{2}\ r_{oc}$ (let us assume this is 'CASE 1' with $r_{var1} = \frac{1}{2}$);

3. fix both outer and inner cathode lengths, whereas $z_{ic} = z_{oc}$;

4. perform simulations by increasing axial extent of the inner cathode by -

   (a) $d_1 = 2.5$ mm

   (b) $d_2 = 5.0$ mm

   (c) $d_3 = 7.5$ mm

   (d) $d_4 = 10.0$ mm

   (e) $d_5 = 15.0$ mm

   (f) $d_6 = 20.0$ mm

   (g) $d_6 = 30.0$ mm;

5. repeat 1, 3-4 with $r_{ic} = \frac{1}{4}\ r_{oc}$ (let us assume this is 'CASE 2' with $r_{var2} = \frac{1}{4}$);

6. repeat 1, 3-4 with $r_{ic} = \frac{3}{4}\ r_{oc}$ (let us assume this is 'CASE 3' with $r_{var3} = \frac{3}{4}$);

7. repeat 1-6 for the applied voltages ranging from 100 kV to 600 kV in 100 kV increments.

Each r_{var} corresponds to six variations of axial positions of d of the inner cathode. Therefore, we have the following function for the radial position of the inner cathode

$$f(r_{ic}) = \begin{cases} r_{var1} r_{oc}, & r_{var1} = \frac{1}{4}, \quad 0 < r_{ic} < \frac{1}{2} r_{oc} \\ r_{var2} r_{oc}, & r_{var2} = \frac{1}{2}, \quad \frac{1}{2} r_{oc} \leq r_{ic} < \frac{3}{4} r_{oc} \\ r_{var3} r_{oc}, & r_{var3} = \frac{3}{4}, \quad \frac{3}{4} r_{oc} \leq r_{ic} < r_{oc}. \end{cases}$$

Similarly, for the axial position of the inner cathode we have

$$f(z_{ic}) = \begin{cases} z_{oc} + d_1, & d_1 = 2.5 \text{ mm} \\ z_{oc} + d_2, & d_2 = 5.0 \text{ mm} \\ z_{oc} + d_3, & d_3 = 7.5 \text{ mm} \\ z_{oc} + d_4, & d_4 = 10.0 \text{ mm} \\ z_{oc} + d_5, & d_5 = 12.5 \text{ mm} \\ z_{oc} + d_6, & d_6 = 15.0 \text{ mm}. \end{cases}$$

The function for both the radial and axial positions of the inner cathode emitter can be seen as written as

$$f(r_{ic}, z_{ic}) = \begin{cases} r_{var} r_{oc} & \frac{1}{4} \leq r_{var} \leq \frac{3}{4} \\ z_{oc} + d & 2.5 \text{ mm} \leq d \leq z_{end}, \end{cases}$$

where z_{end} is the anode length.

MAGIC simulations are optimized by following different scaling geometries shown in Fig. 4.14a, Fig. 4.14b, and Fig. 4.14c. The variations (increasing of d by 2.5 mm) of the inner cathode's length can also be seen in Fig. 4.15. The results obtained from MAGIC simulations based on scaling of different geometries described in Fig. 4.14a and Fig. 4.15 can be seen in Fig. 4.16 and Fig. 4.17. Figure 4.16 shows six plots with the same voltage applied to MICDs and output beam voltage for different lengths of inner cathode with extension d and with inner cathode $r_{ic} = \frac{1}{4} r_{oc}$. Figure 4.17 shows six plots with the same voltage applied to MICDs and extracted output electron beam current for different lengths of inner cathode with extension d and with inner cathode

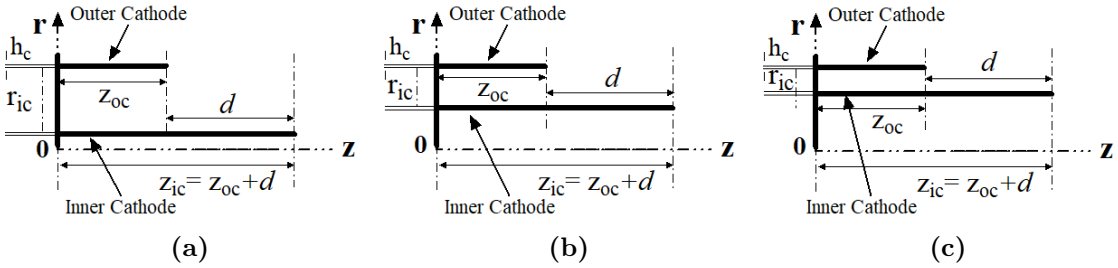

Figure 4.14: Schematic showing the radial position of the inner cathode's radius is at (a) $\frac{1}{4}$, (b) $\frac{1}{2}$, and (c) $\frac{3}{4}$ of the outer cathode's radius, respectively, where z_{oc} =outer cathode's length, z_{ic} =inner cathode's length, d =difference between the length of the inner and outer cathodes.

radius $r_{ic} = \frac{1}{4}r_{oc}$.

Similarly, Fig. 4.18 and Fig. 4.19 shows the $I - V$ characteristics for both beams for five axial lengths of the inner cathode with extension d and with inner cathode radius $r_{ic} = \frac{1}{2}r_{oc}$.

Figure 4.20, Fig. 4.21, and Fig. 4.22 show the $I - V$ and $E_k - V$ characteristics for both beams for 8 axial lengths of the inner cathode with extension d and with inner cathode radius $r_{ic} = \frac{3}{4}r_{oc}$.

The electron beam energy measured at the output end of the drift tube of each beam can be seen in Fig. 4.23a. Figure 4.23a represents both electron beam energy and current as a function of the inner cathode's length for applied voltage 400 kV and a magnetic field of 2 T. As can be seen, when both cathodes have the same length, meaning when both beams start propagating from the tip of the cathodes at the same axial position at 4.9 cm, we do not see any space charge screening effect near the surface of both cathodes at $z = 4.9$ cm (*cf.* in Fig. 4.23a). Therefore, a minimal energy difference but a maximum difference in currents can be seen between both beams.

It can be concluded that, as we extend the length of the inner cathode beyond

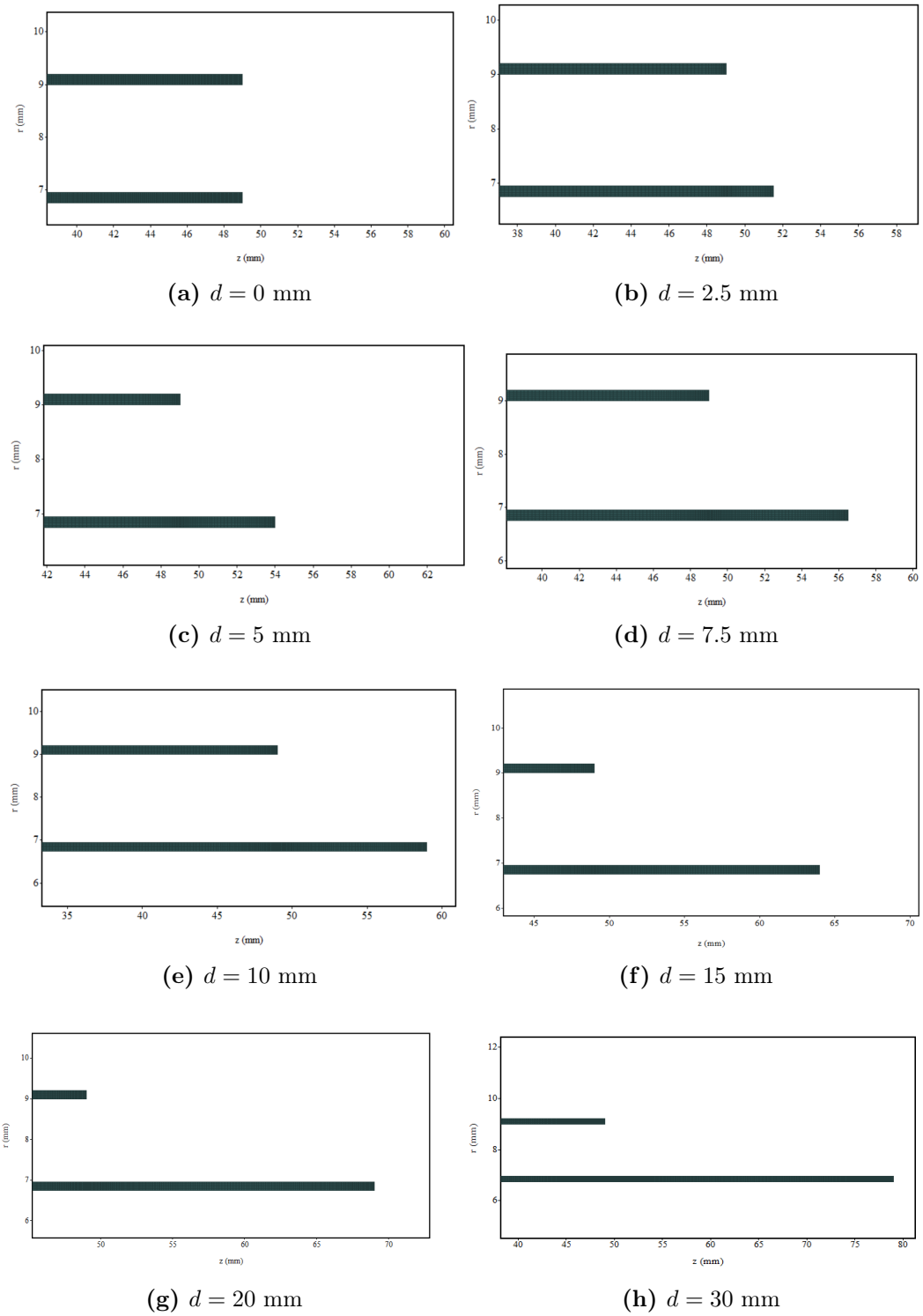

(a) $d = 0$ mm **(b)** $d = 2.5$ mm

(c) $d = 5$ mm **(d)** $d = 7.5$ mm

(e) $d = 10$ mm **(f)** $d = 15$ mm

(g) $d = 20$ mm **(h)** $d = 30$ mm

Figure 4.15: Schematic shows of the variations of the inner cathode's length by 2.5 mm. Geometry of the problem is for the case $r_{ic} = \frac{3}{4} r_{oc}$.

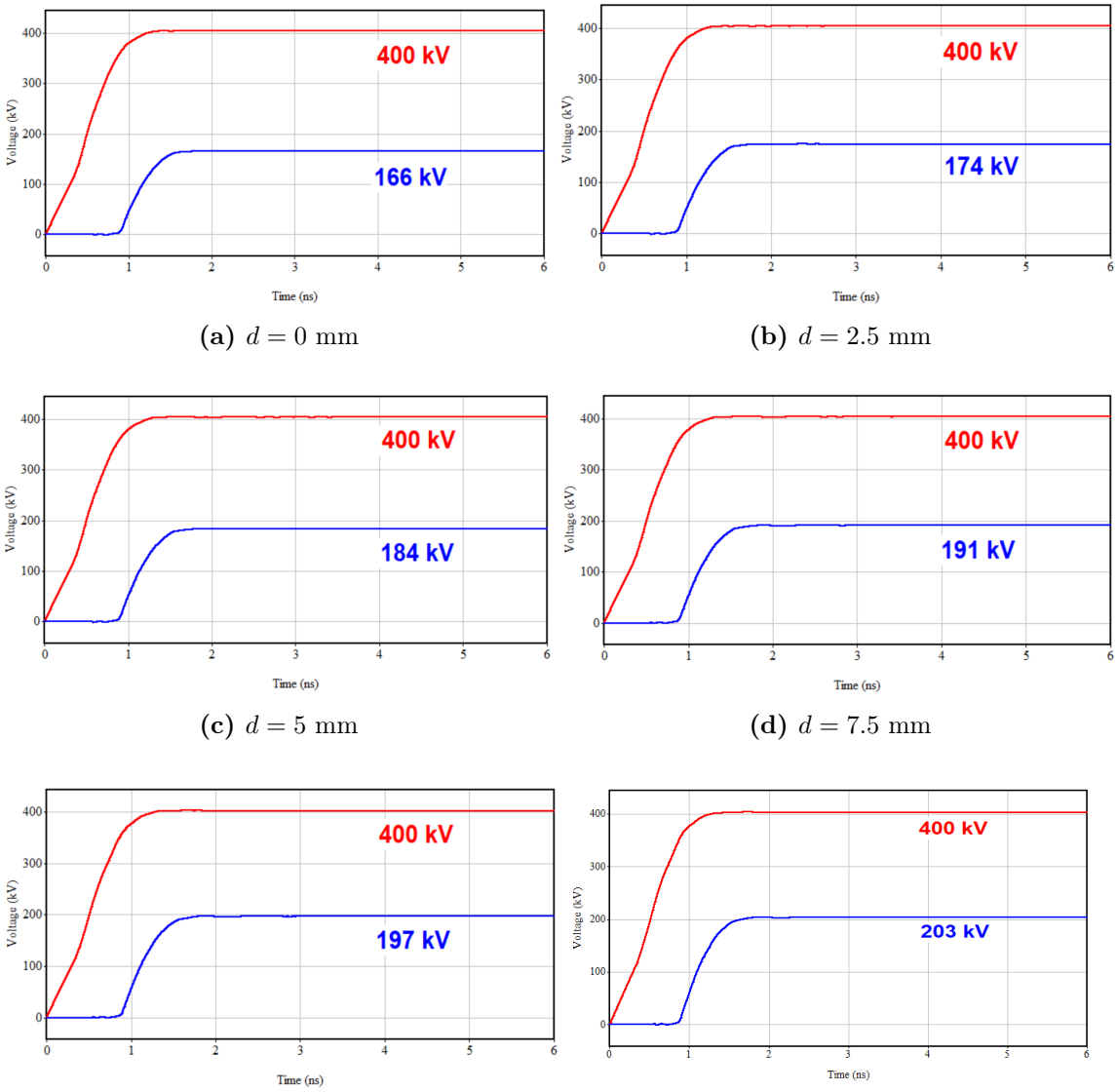

(a) $d = 0$ mm **(b)** $d = 2.5$ mm

(c) $d = 5$ mm **(d)** $d = 7.5$ mm

(e) $d = 10$ mm **(f)** $d = 15$ mm

Figure 4.16: MAGIC 2D simulations show the same voltage applied (red, V_{in}) to the two nested MICDs and output beam voltage (blue, V_{out}) for (a) d =0 mm, (b) $d = 2.5$ mm, (c) $d = 5$ mm, (d) $d = 7.5$ mm, (e) $d = 10$ mm, and (f) $d = 15$ mm. In this case, the position of the inner cathode is $r_{ic} = \frac{1}{4} r_{oc}$, input voltage V_{in}=-400 kV, and magnetic field=2 T.

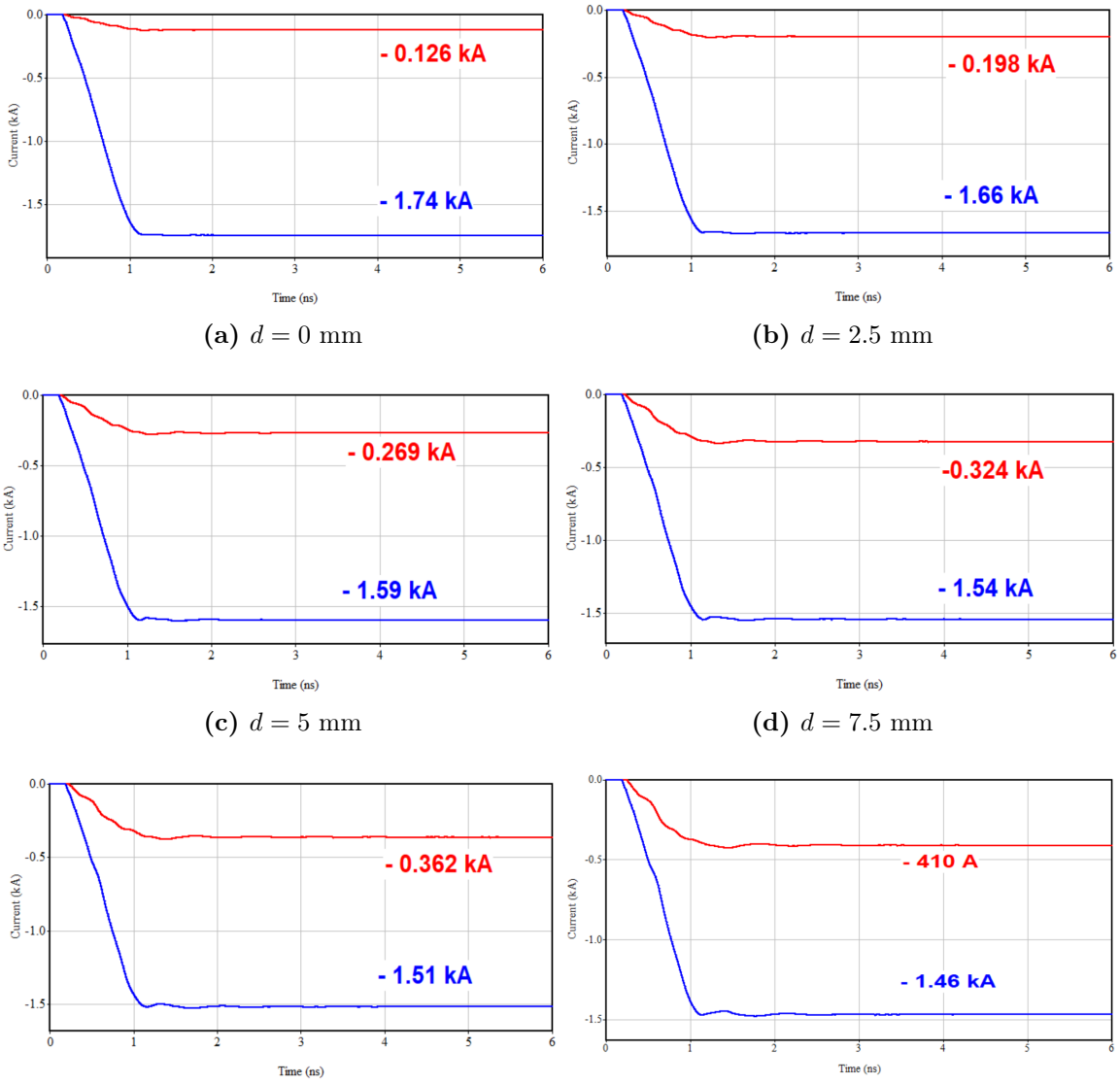

(a) $d = 0$ mm **(b)** $d = 2.5$ mm

(c) $d = 5$ mm **(d)** $d = 7.5$ mm

(e) $d = 10$ mm **(f)** $d = 15$ mm

Figure 4.17: MAGIC 2D simulations show the electron beam currents emitted from the inner(red) and outer(blue) cathodes for different lengths of inner cathode for (a) d =0 mm, (b) $d = 2.5$ mm, (c) $d = 5$ mm, (d) $d = 7.5$, (e) $d = 10$ mm, and (f) $d = 15$ mm. In this case, the position of the inner cathode is $r_{ic} = \frac{1}{4} r_{oc}$, input voltage V_{in}=-400 kV, and magnetic field=2 T.

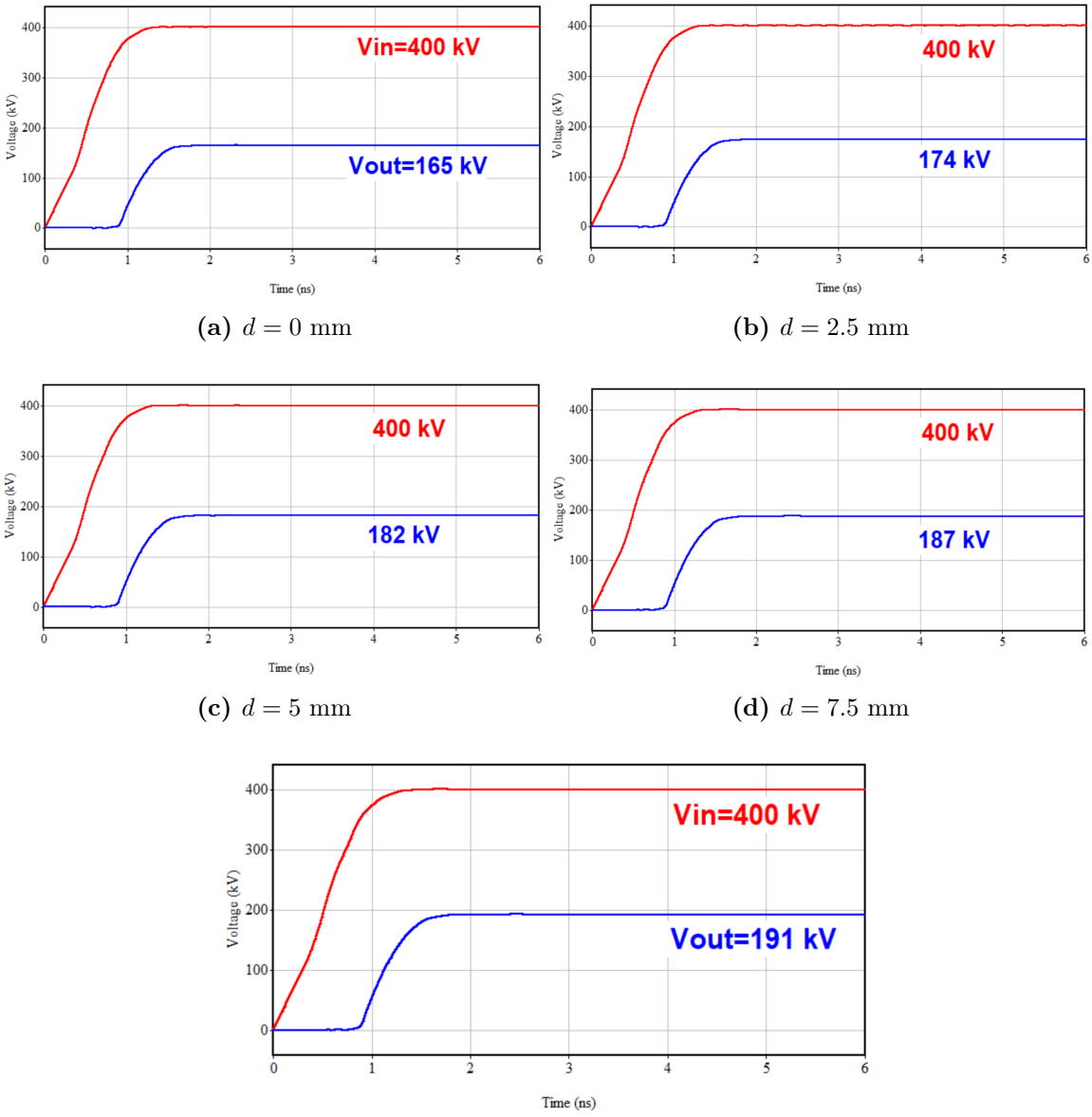

(a) $d = 0$ mm **(b)** $d = 2.5$ mm

(c) $d = 5$ mm **(d)** $d = 7.5$ mm

(e) $d = 10$ mm

Figure 4.18: MAGIC 2D simulations show the same voltage applied (red, V_{in}) to the two nested MICDs and output beam voltage (blue, V_{out}) for (a) d =0 mm, (b) $d = 2.5$ mm, (c) $d = 5$ mm, (d) $d = 7.5$, and (e) $d = 10$ mm. In this case, the position of the inner cathode is $r_{ic} = \frac{1}{2} r_{oc}$, input voltage V_{in}=-400 kV, and magnetic field=2 T.

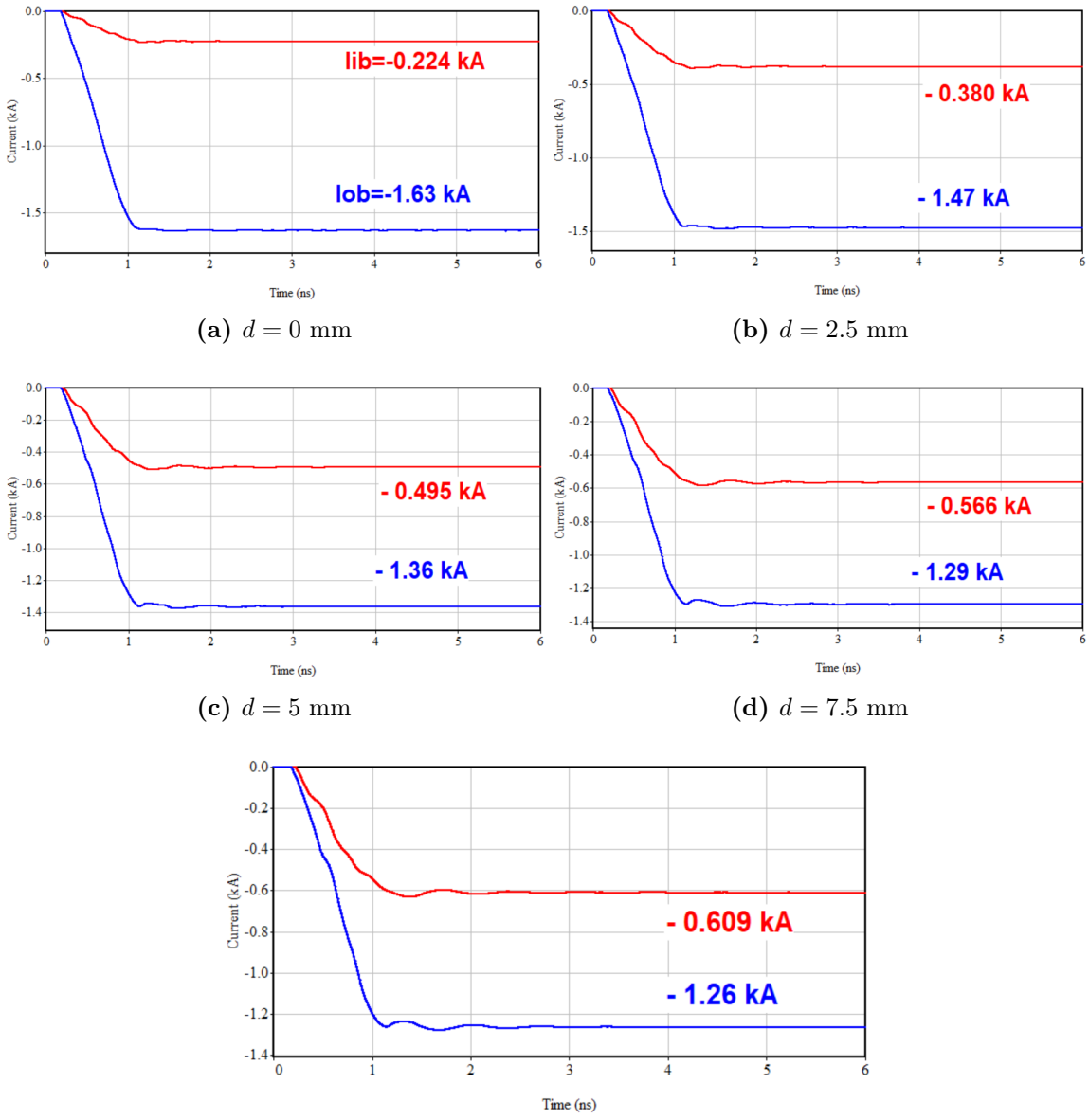

(a) $d = 0$ mm **(b)** $d = 2.5$ mm

(c) $d = 5$ mm **(d)** $d = 7.5$ mm

(e) $d = 10$ mm

Figure 4.19: MAGIC 2D simulations show the electron beam currents emitted from the inner(red) and outer(blue) cathodes for different lengths of inner cathode for (a) d =0 mm, (b) $d = 2.5$ mm, (c) $d = 5$ mm, (d) $d = 7.5$, and (e) $d = 10$ mm. In this case, the position of the inner cathode is $r_{ic} = \frac{1}{2} r_{oc}$, input voltage V_{in}=-400 kV, and magnetic field=2 T.

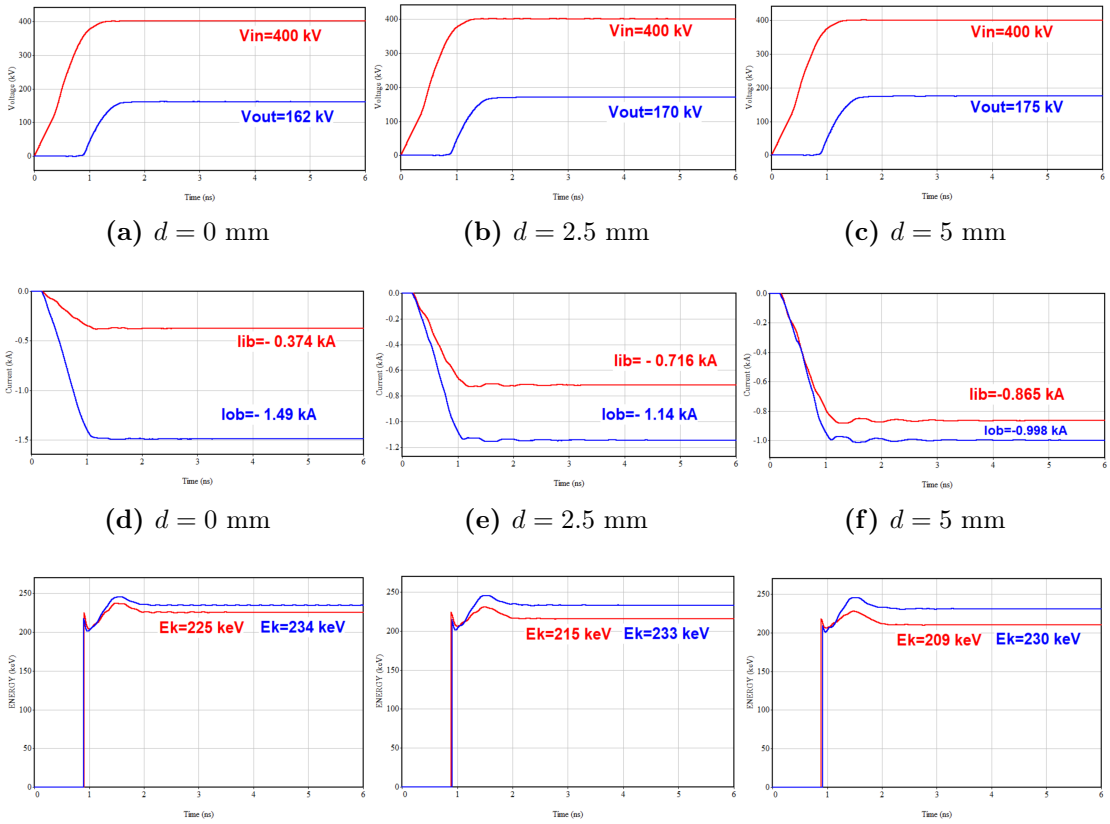

(a) $d = 0$ mm **(b)** $d = 2.5$ mm **(c)** $d = 5$ mm

(d) $d = 0$ mm **(e)** $d = 2.5$ mm **(f)** $d = 5$ mm

(g) $d = 0$ mm **(h)** $d = 2.5$ mm **(i)** $d = 5$ mm

Figure 4.20: MAGIC 2D simulations show the same voltage applied (red, V_{in}) to the two nested MICDs and output beam voltage (blue, V_{out}) for (a) d =0 mm, (b) $d = 2.5$ mm, and (c) $d = 5$ mm. The electron beam currents and energies emitted from the inner (red) and outer (blue) cathodes for different lengths of inner cathode for (d) d =0 mm, (e) $d = 2.5$ mm, (f) $d = 5$ mm, and (g) d =0 mm, (h) $d = 2.5$ mm, (i) $d = 5$ mm, respectively. In this case, the position of the inner cathode is $r_{ic} = \frac{3}{4} r_{oc}$, input voltage V_{in}=-400 kV, and magnetic field=2 T.

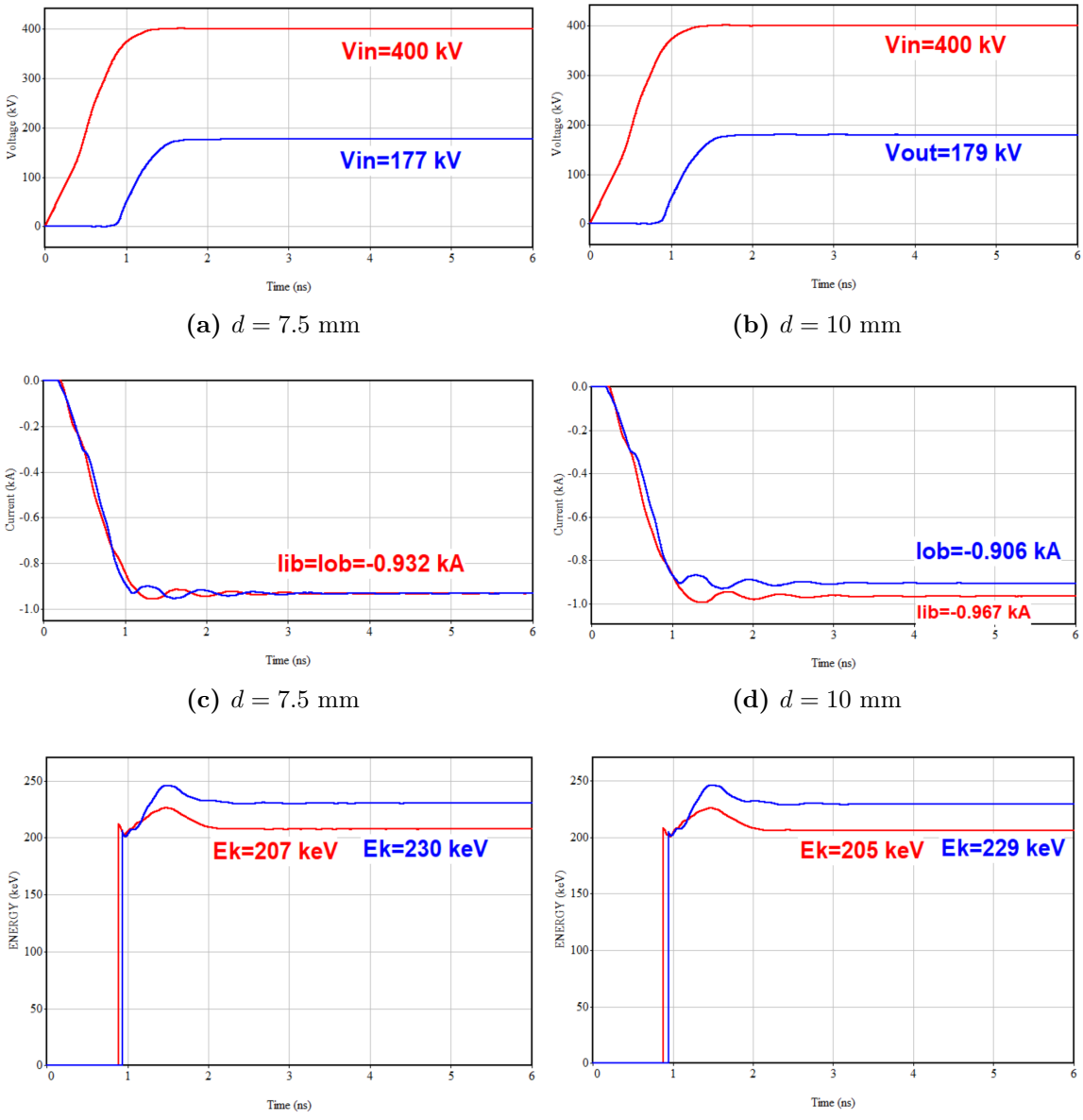

(a) $d = 7.5$ mm **(b)** $d = 10$ mm

(c) $d = 7.5$ mm **(d)** $d = 10$ mm

(e) $d = 7.5$ mm **(f)** $d = 10$ mm

Figure 4.21: MAGIC 2D simulations show the same voltage applied (red, V_{in}) to the two nested MICDs and output beam voltage (blue, V_{out}) for (a) $d = 7.5$ mm and (b) $d = 10$ mm. The electron beam currents and energies emitted from the inner (red) and outer (blue) cathodes for different lengths of inner cathode for (c) $d = 7.5$ mm, (d) $d = 10$ mm, and (e) $d = 7.5$ mm, (f) $d = 10$ mm, respectively. In this case, the position of the inner cathode is $r_{ic} = \frac{3}{4} r_{oc}$, input voltage V_{in}=-400 kV, and magnetic field=2 T.

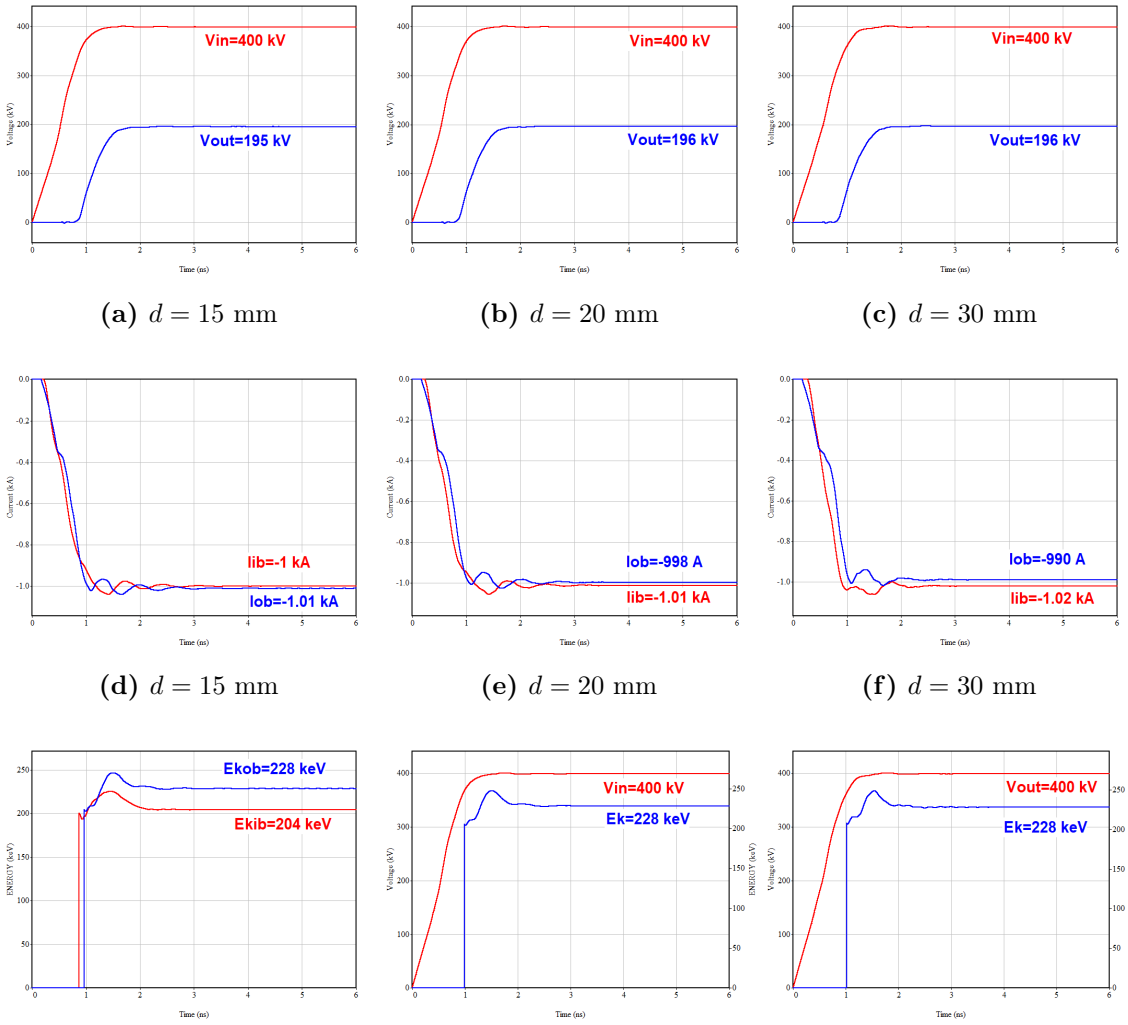

(a) $d = 15$ mm **(b)** $d = 20$ mm **(c)** $d = 30$ mm

(d) $d = 15$ mm **(e)** $d = 20$ mm **(f)** $d = 30$ mm

(g) $d = 15$ mm **(h)** $d = 20$ mm **(i)** $d = 30$ mm

Figure 4.22: MAGIC 2D simulations show the same voltage applied (red, V_{in}) to the two nested MICDs and output beam voltage (blue, V_{out}) for (a) $d = 15$ mm, (b) $d = 20$ mm, and (c) $d = 30$ mm. The electron beam currents and energies emitted from the inner (red) and outer (blue) cathodes for different lengths of inner cathode for (d) $d = 15$ mm, (e) $d = 20$ mm, (f) $d = 30$ mm and (g) $d = 15$ mm, (h) $d = 20$ mm, (i) $d = 30$ mm, respectively. In this case, the position of the inner cathode is $r_{ic} = \frac{3}{4} r_{oc}$, input voltage V_{in}=-400 kV, and magnetic field=2 T.

Table 4.3: Simulated data of electron beam current and electron beam energy from each cathode obtained from MAGIC simulations with uniform resolution (1,1) for applied voltages 100 - 500 kV and magnetic field 1 T for the case $r_{ic} = \frac{3}{4} r_{oc}$.

φ_a [a]	r_a [b]	r_{oc} [c]	r_{ic} [d]	h_c [e]	I_{ib} [f]	I_{ob} [g]	Ek_{ib} [h]	Ek_{ob} [i]	Ek Diff.[j]
[kV]	[cm]	[cm]	[cm]	[cm]	[kA]	[kA]	[keV]	[keV]	%
100	2.5	0.9	0.675	0.02	0.129	0.115	63	68	7.6
200	2.5	0.9	0.675	0.02	0.354	0.327	121	131	8
300	2.5	0.9	0.675	0.02	0.626	0.602	174	190	8.7
400	2.5	0.9	0.675	0.02	0.931	0.931	224	247	9.7
500	2.5	0.9	0.675	0.02	1.26	1.29	271	300	10
600	2.5	0.9	0.675	0.02	1.6	1.7	315	351	10.8

[a]Applied potential; [b]radius of the anode; [c]radius of the outer cathode; [d]radius of the inner cathode; [e]thickness of the beam; [f]inner e-beam current; [g]outer e-beam current; [h]inner e-beam energy; [i]outer e-beam energy; [j]% energy difference of inner and outer e-beam.

the outer cathode, then the space charge of the outer beam starts screening the inner beam and apparently both electron beams meet at some point with some energy difference (*cf.* in Fig. 4.23a) or show equilibrium currents at (0.675 cm, 5.65 cm) in Fig. 4.21c that we are interested in. Figure 4.21d shows interesting results where we observe for the first time $I_{ob} < I_{ib}$ for $d = 10$ mm. This result led us to better understand how the energy difference and current difference depend on the increased length of the inner cathode.

Table 4.3 shows simulated data of electron beam current and electron beam energy from each cathode obtained from MAGIC simulations with uniform simulation space resolution (1,1) for applied voltages 100 - 600 kV and magnetic field 1 T for the case $r_{ic} = \frac{3}{4} r_{oc}$. I_{ib} and I_{ob} in row #6 show comparable currents for each beam for an applied voltage of 400 kV with a 9.7% energy difference.

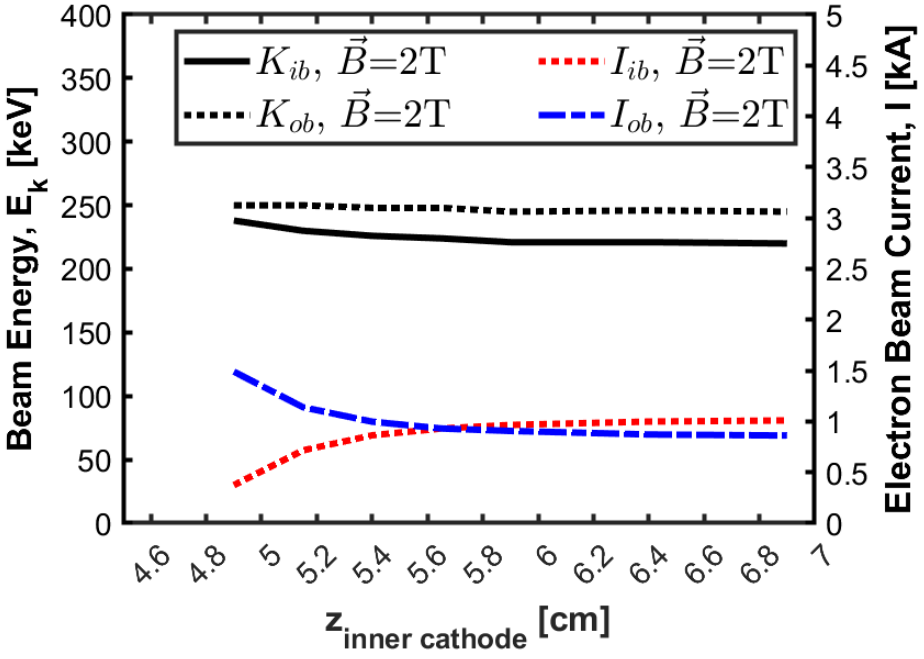

(a)

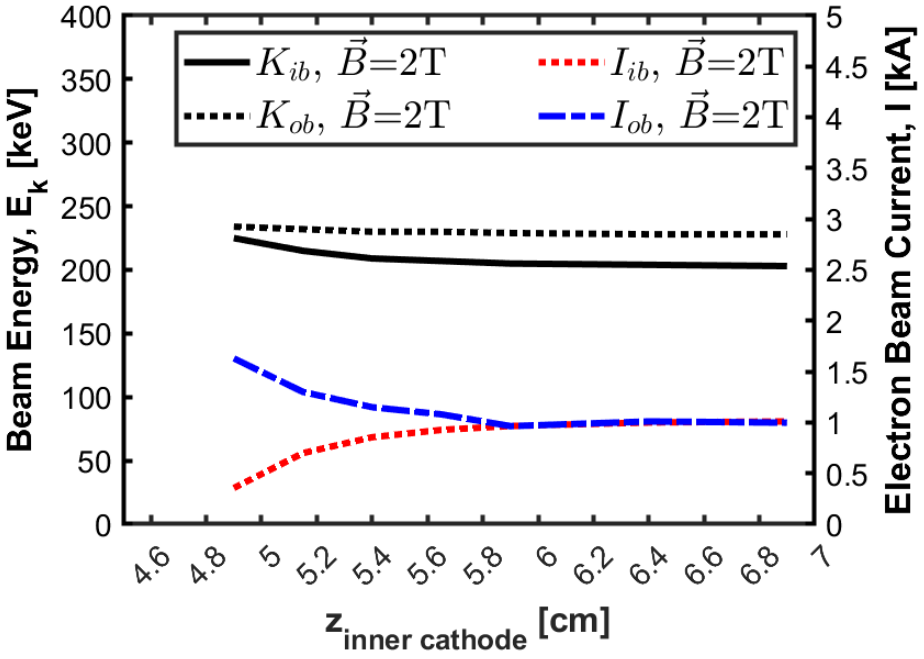

(b)

Figure 4.23: Plot shows results obtained from MAGIC PIC code for applied voltage of 400 kV and a magnetic field of 2 T as function of the z_{ic} (a) with uniform lower resolution, (b) with higher resolution.

Table 4.4: Simulated data of electron beam current and electron beam energy from each cathode obtained from MAGIC simulations with *higher* resolution (5,5) for applied voltages 100 - 500 kV and magnetic field 1 T for the case $r_{ic} = \frac{3}{4} r_{oc}$.

φ_a [a]	r_a [b]	r_{oc} [c]	r_{ic} [d]	I_{ib} [e]	I_{ob} [f]	Ek_{ib} [g]	Ek_{ob} [h]	Ek Diff.[i]
[kV]	[cm]	[cm]	[cm]	[kA]	[kA]	[keV]	[keV]	%
100	2.5	0.9	0.67	0.13	0.14	58	63	8
200	2.5	0.9	0.67	0.35	0.39	110	121	9.5
300	2.5	0.9	0.67	0.62	0.72	156	172	9.7
400	2.5	0.9	0.67	0.93	1.1	203	223	9
500	2.5	0.9	0.67	1.2	1.5	237	263	10
600	2.5	0.9	0.67	1.09	1.3	228	252	10

[a]Applied potential; [b]radius of the anode; [c]radius of the outer cathode; [d]radius of the inner cathode; [e]inner e-beam current; [f]outer e-beam current; [g]inner e-beam energy; [h]outer e-beam energy; [i]% energy difference of inner and outer e-beam.

Thus, we increased the mesh resolutions of the simulation model and ran a series of simulations in a similar manner. The MAGIC simulation results obtained with higher resolution can be seen in Fig. 4.23b which we find very interesting. Figure 4.23b also shows electron beam energy and current as function of z_{ic} for applied voltage 400 kV and magnetic field 2 T. As in Fig. 4.23a, we observe a similar trend that, at a particular length, both currents are comparable with about 10% energy difference between both beams. But in this case, we do not observe $I_{ob} < I_{ib}$; rather, we observe comparable currents as both beams travel down the drift tube.

Table 4.4 shows simulated data of electron beam current and electron beam energy from each cathode obtained from MAGIC simulations with a higher resolution (5,5) for applied voltages 100 - 600 kV and magnetic field 1 T for the case $r_{ic} = \frac{3}{4} r_{oc}$. Unlike in Table 4.3, I_{ib} and I_{ob} in row #6 show a slightly higher value for the outer electron

Table 4.5: Simulated data of electron beam current and electron beam energy from each cathode obtained from MAGIC simulations with higher resolution (5,5) for applied voltages 100 - 500 kV and magnetic field 2 T for the case $r_{ic} = \frac{1}{2} r_{oc}$.

φ_a [a]	r_a [b]	r_{oc} [c]	r_{ic} [d]	I_{ib} [e]	I_{ob} [f]	Ek_{ib} [g]	Ek_{ob} [h]	Ek Diff.[i]
[kV]	[cm]	[cm]	[cm]	[kA]	[kA]	[keV]	[keV]	%
200	2.5	0.9	0.45	0.216	0.464	116	132	13
300	2.5	0.9	0.45	0.380	0.846	167	191	13
400	2.5	0.9	0.45	0.563	1.3	214	247	14
500	2.5	0.9	0.45	0.760	1.79	258	301	15

[a]Applied potential; [b]radius of the anode; [c]radius of the outer cathode; [d]radius of the inner cathode; [e]inner e-beam current; [f]outer e-beam current; [g]inner e-beam energy; [h]outer e-beam energy; [i]% energy difference of inner and outer e-beam.

beam current than the inner electron beam current value an applied voltage of 400 kV with a 9% energy difference. As can be seen, I_{ib} and I_{ob} in row #4 tend to show comparable currents for an applied voltage of 200 kV with a 9.5% energy difference.

Table 4.5 shows simulated data of electron beam current and electron beam energy from each cathode obtained from MAGIC simulations with a higher resolution (5,5) for applied voltages 200 - 500 kV and magnetic field 1 T for the case $r_{ic} = \frac{1}{2} r_{oc}$. Unlike in Tables 4.3 and 4.4, I_{ib} and I_{ob} in row #5 do not show comparable currents for an applied voltage of 400 kV but shows higher value of 14% energy difference.

Table 4.6 shows simulated data of electron beam current and electron beam energy from each cathode obtained from MAGIC simulations with a higher resolution (5,5) for applied voltages 200 - 500 kV and magnetic field 1 T for the case $r_{ic} = \frac{1}{4} r_{oc}$. Unlike in Tables 4.3 and 4.4, I_{ib} and I_{ob} in row #5 do not show comparable currents for an applied voltage of 400 kV but shows higher value of 16% energy difference.

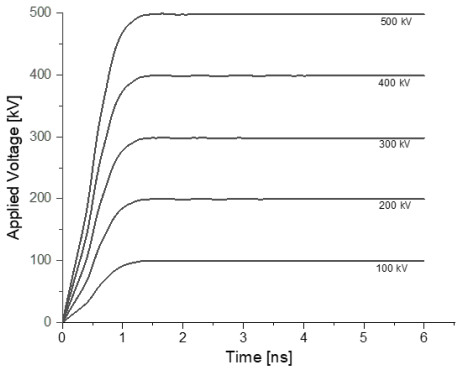

(a)

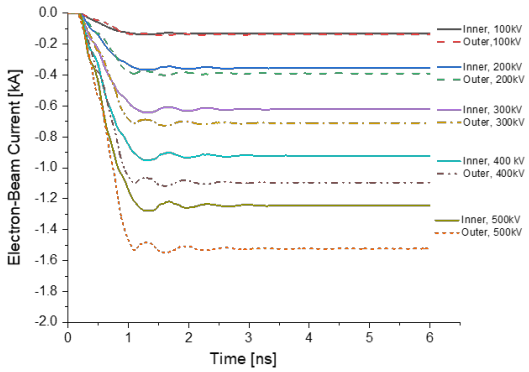

(b)

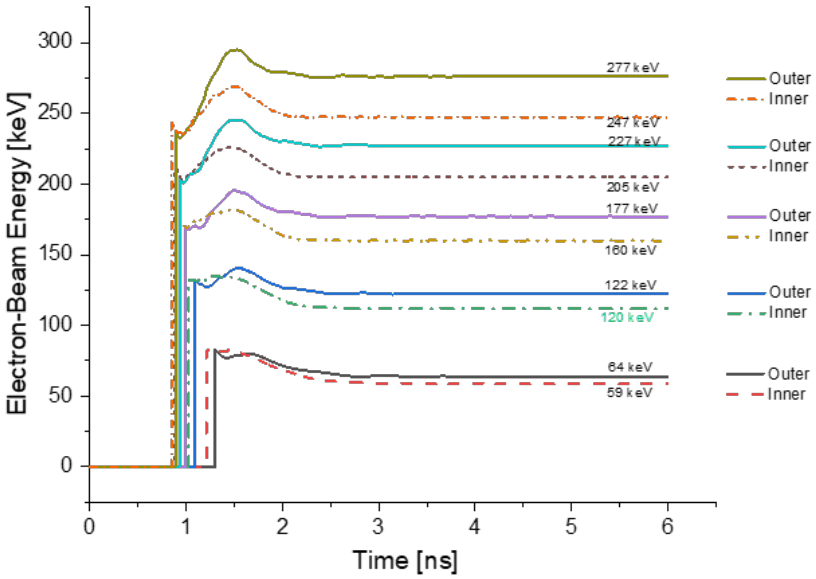

(c)

Figure 4.24: Plot shows data from MAGIC PIC simulations of two nested MICDs as a function time, (a) applied voltages applied to the MICDs, (b) Electron beam currents obtained from MAGIC PIC simulation, (c) Electron beam energy obtained from MAGIC PIC simulation for different applied voltages ranging from 100 - 500 kV for a magnetic field of 3 T. The total simulation time was 10 ns.

Table 4.6: Simulated data of electron beam current and electron beam energy from each cathode obtained from MAGIC simulations with higher resolution (5,5) for applied voltages 100 - 500 kV and magnetic field 2 T for the case $r_{ic} = \frac{1}{4} r_{oc}$.

φ_a [a]	r_a [b]	r_{oc} [c]	r_{ic} [d]	I_{ib} [e]	I_{ob} [f]	Ek_{ib} [g]	Ek_{ob} [h]	Ek Diff.[i]
[kV]	[cm]	[cm]	[cm]	[kA]	[kA]	[keV]	[keV]	%
200	2.5	0.9	0.225	0.123	0.558	116	131	12
300	2.5	0.9	0.225	0.216	1.04	165	191	14
400	2.5	0.9	0.225	0.318	1.5	212	249	16
500	2.5	0.9	0.225	0.430	2	257	304	16.7

[a]Applied potential; [b]radius of the anode; [c]radius of the outer cathode; [d]radius of the inner cathode; [e]inner e-beam current; [f]outer e-beam current; [g]inner e-beam energy; [h]outer e-beam energy; [i]% energy difference of inner and outer e-beam.

We are primarily interested in studying the $I - V$ characteristics and current density distribution near the peak of the MICDs so that we can calculate the energy of each beam. To understand this, a detailed simulation result for different cases is shown in Fig. 4.24. Figure 4.24a represents the same voltages ranging from 100 kV to 500 kV applied to MICDs for a magnetic field of 2 T as a function of time. Figure 4.24b shows the electron beam currents emitted from both outer and inner cathodes against each applied voltages that presented in Fig. 4.24a. As can be seen in each applied voltage, the outer electron beam's current is always more significant than the inner electron beam's current indicates that the current density of the inner beam is higher than the current density of the outer beam. At lower applied voltage ranging from 100 -200 kV there is not much current difference can be seen in this case. Similarly, Fig. 4.24c shows electron beam energy against each applied voltage as a function of time for magnetic field 2 T. As in Fig. 4.24b, there is also not any energy difference at lower applied voltages.

A more clear view of current density at the diode's surfaces for each applied voltage

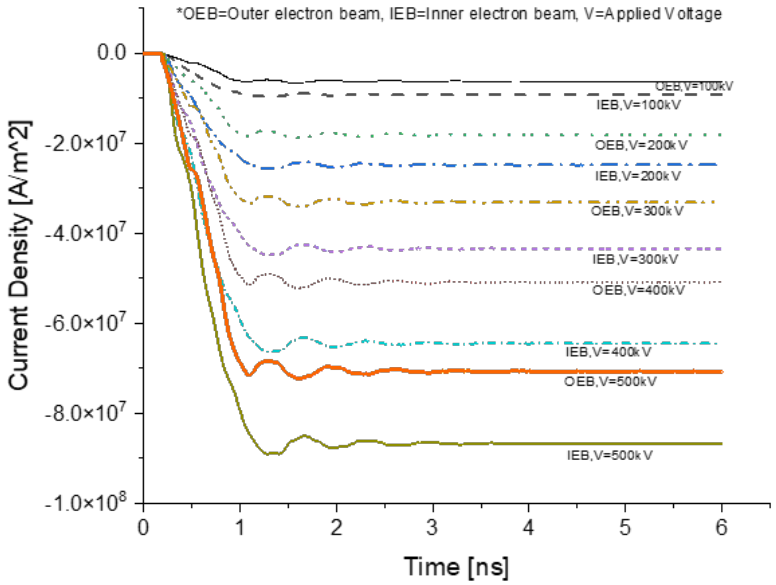

Figure 4.25: Plot shows simulated current density for MICDs in different solid and dashed colored lines for different applied voltages ranging from 100 - 500 kV for a magnetic field of 3 T as a function of time.

ranging from 100 - 500 kV for magnetic field 2 T as a function of time can be seen in Fig. 4.25. Different solid and dashed lines show the electron current densities at the peak of each cathode's surface. A closer view reveals that the current density of the inner electron beam is always greater than the current density of the outer electron beam as the emission area of the inner cathode is smaller than the emission area of the outer cathode. This led us to determine the electron density for each beam by applying the usual formula as we already know the electron velocity/momentum and electron beam current emitted from a known emission area.

Another simulation of axial electric field as a function of time for different applied voltages ranging from 100 kV to 500 kV and with magnetic field 2 T can be seen in Fig. 4.26.

Figure 4.27a and Fig. 4.27b illustrate emitted outer and inner electron beam cur-

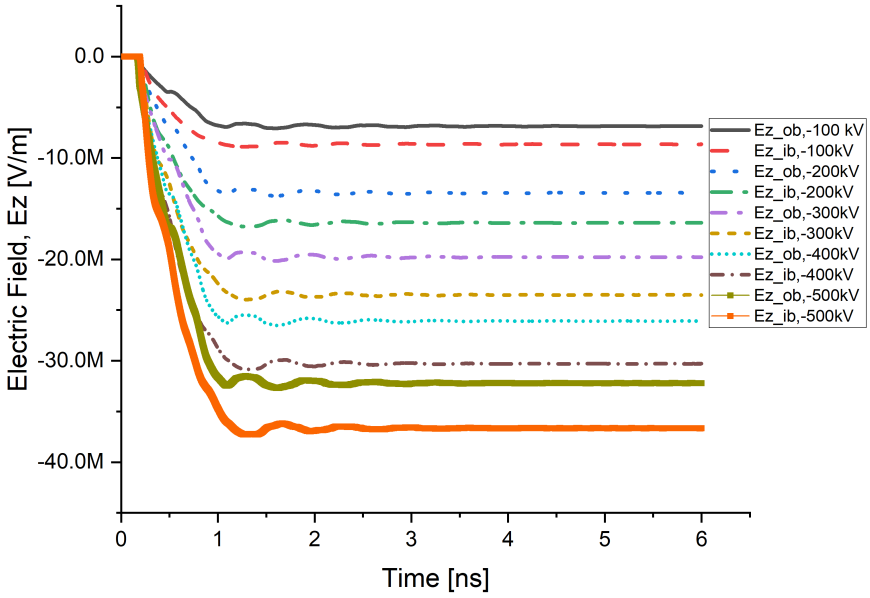

Figure 4.26: Plot shows simulated axial electric field as a function of time. Applied voltage is 100 to 500 kV, magnetic field 2 T.

rents for applied voltages ranging from 100 kV to 500 kV as a function of the radius of the inner cathode. Both plots show a similar trend of beam current dependency on the variations of the inner cathode's radius. Figure 4.27 explains that comparable currents for two beams powered by a single cathode at a single potential is possible when the inner cathode is close to the outer cathode. As the inner cathode is positioned radially further away from the outer cathode, the difference between currents increases.

4.3.3 Magnetic field effect

We also investigated the effect of the magnetic field on multiple electron beam generation by running a series of simulations. PIC simulations with different applied magnetic fields show that there is not any significant difference in the obtained re-

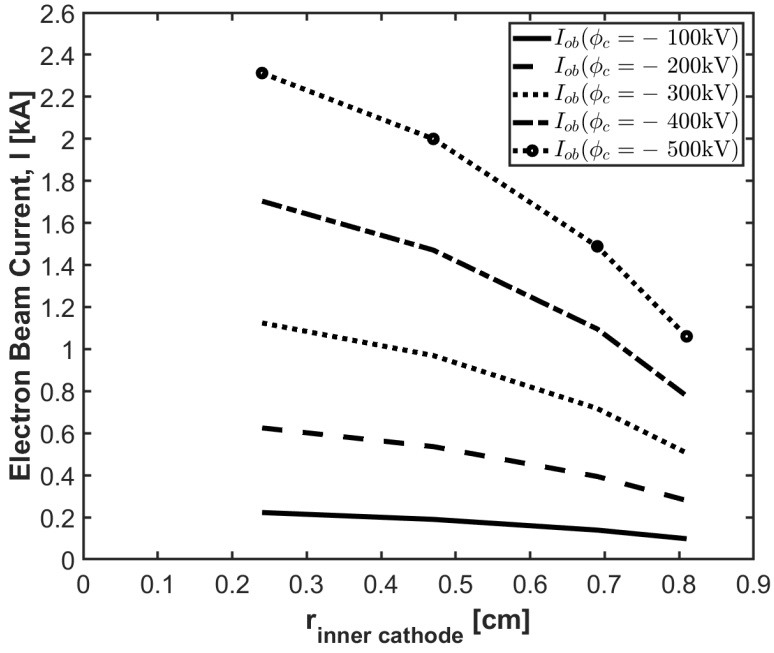

(a)

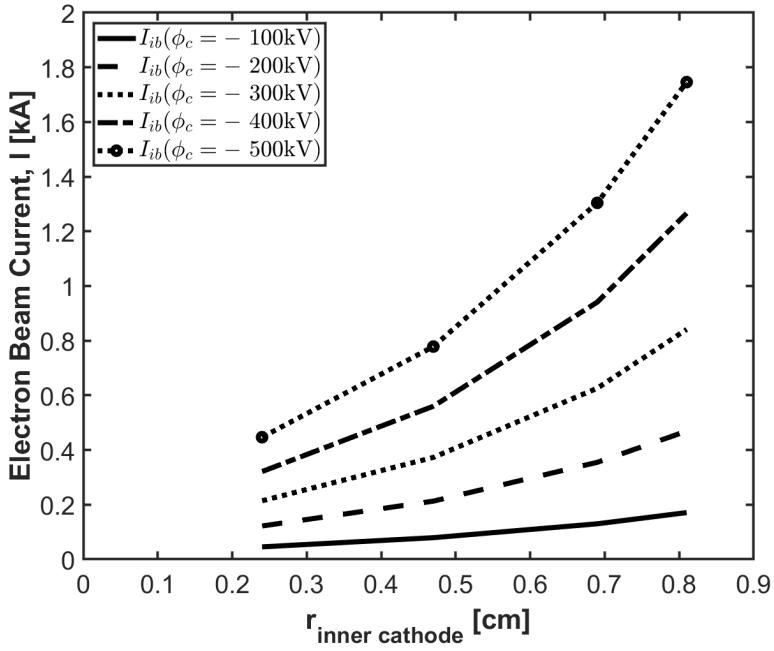

(b)

Figure 4.27: Plot shows data from MAGIC PIC simulations of two nested MICDs - (a) MAGIC PIC simulated outer electron beam current (c) MAGIC PIC simulated inner electron beam current for different applied voltages ranging from 100 - 500 kV for a magnetic field of 3 T as a function time and the radius of the inner cathode r_{ic}.

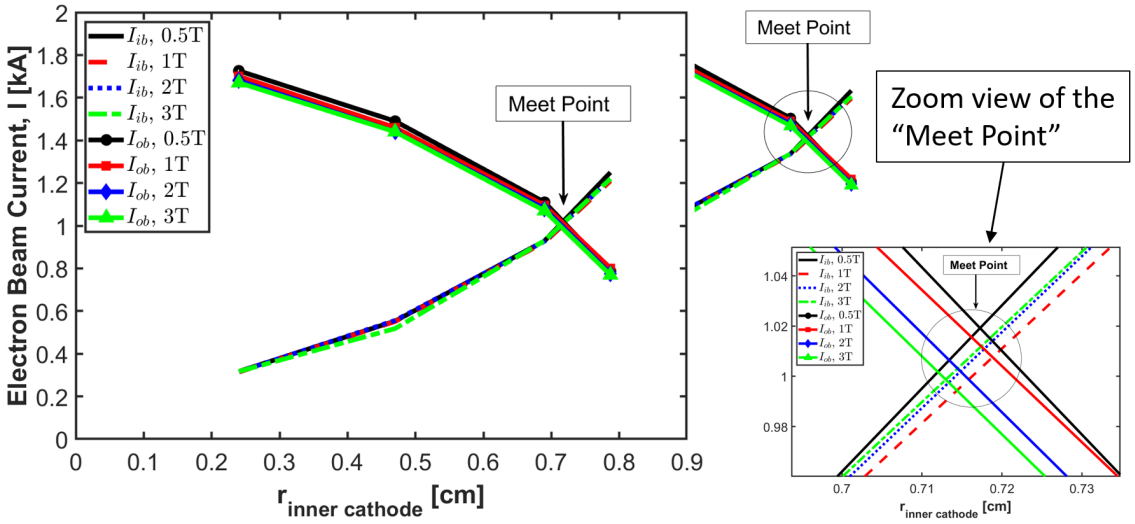

Figure 4.28: Plot shows results obtained from the MAGIC PIC code for different magnetic field values (0.5 T, 1 T, 2 T, 3 T) where both electron beam currents meet at a particular point. The plot on the right shows a zoomed view of the intersection point.

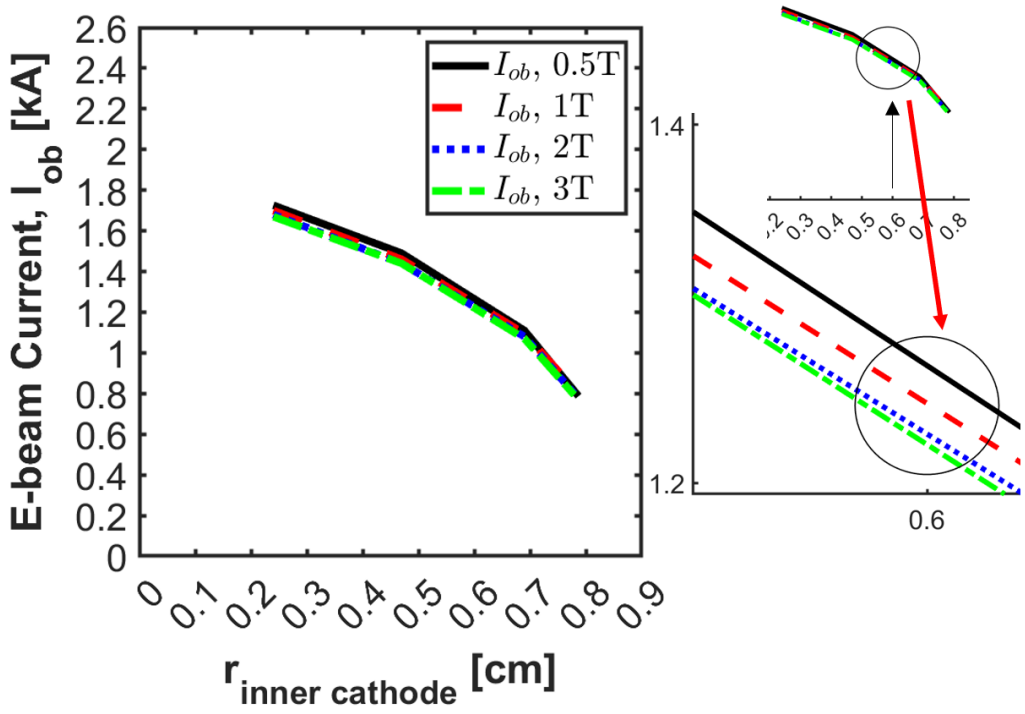

Figure 4.29: Plot shows a zoomed view of the emitted electron beam current from the outer electron beam measured at the end of the drift tube for different values of the applied magnetic field.

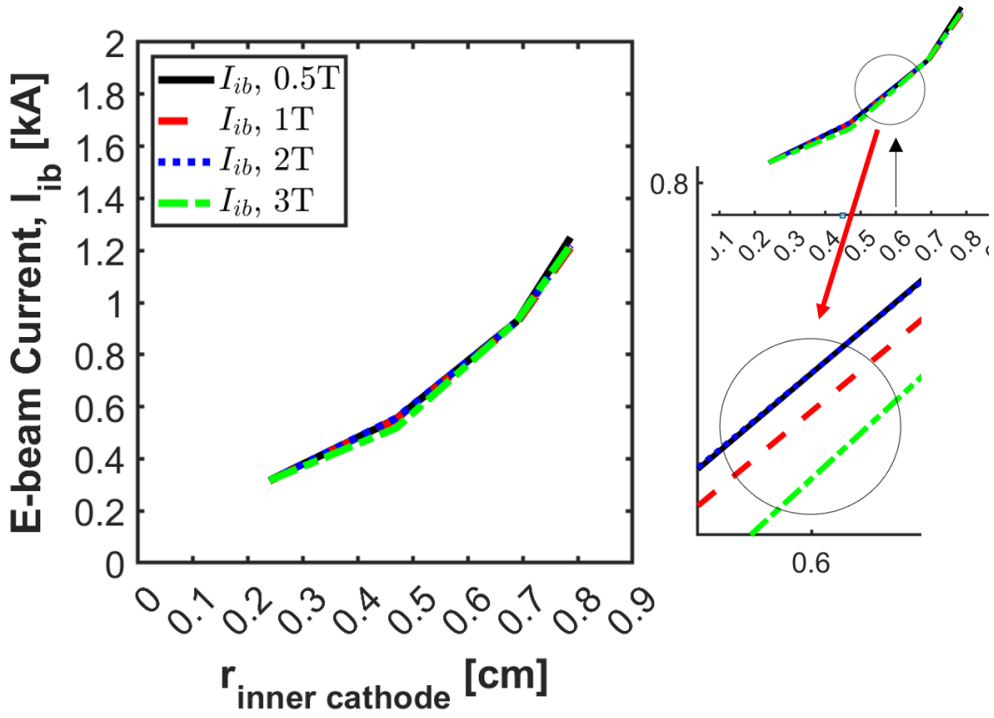

Figure 4.30: Plot shows emitted electron beam current from inner electron beam measured at the end of the drift tube for different values of the applied magnetic field.

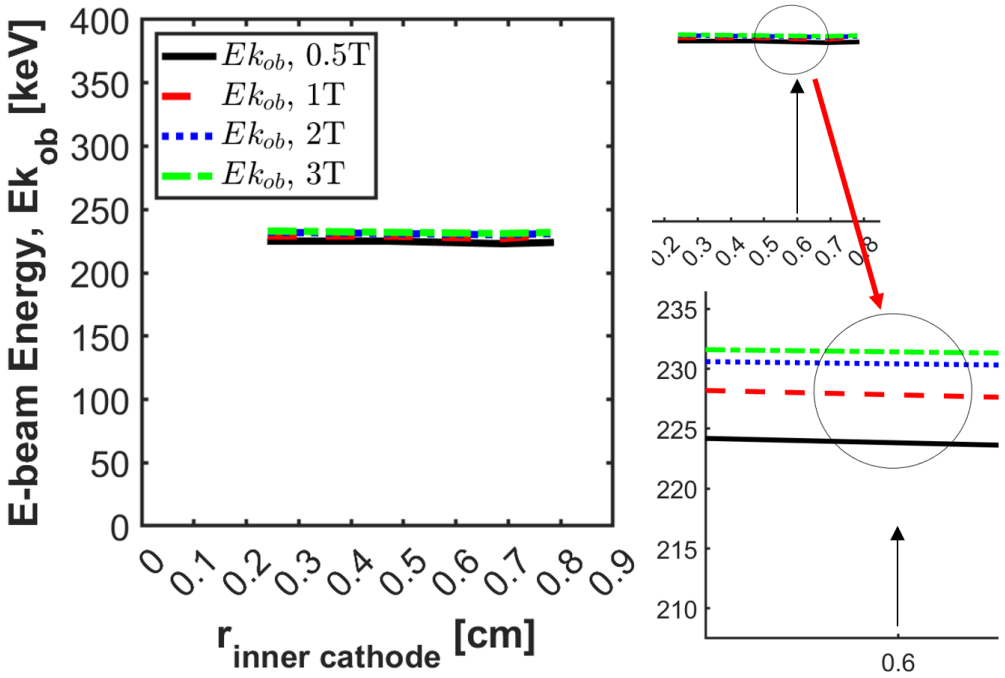

Figure 4.31: Plot shows extracted beam energy for outer electron beam at the end of the drift tube for different values of the applied magnetic field.

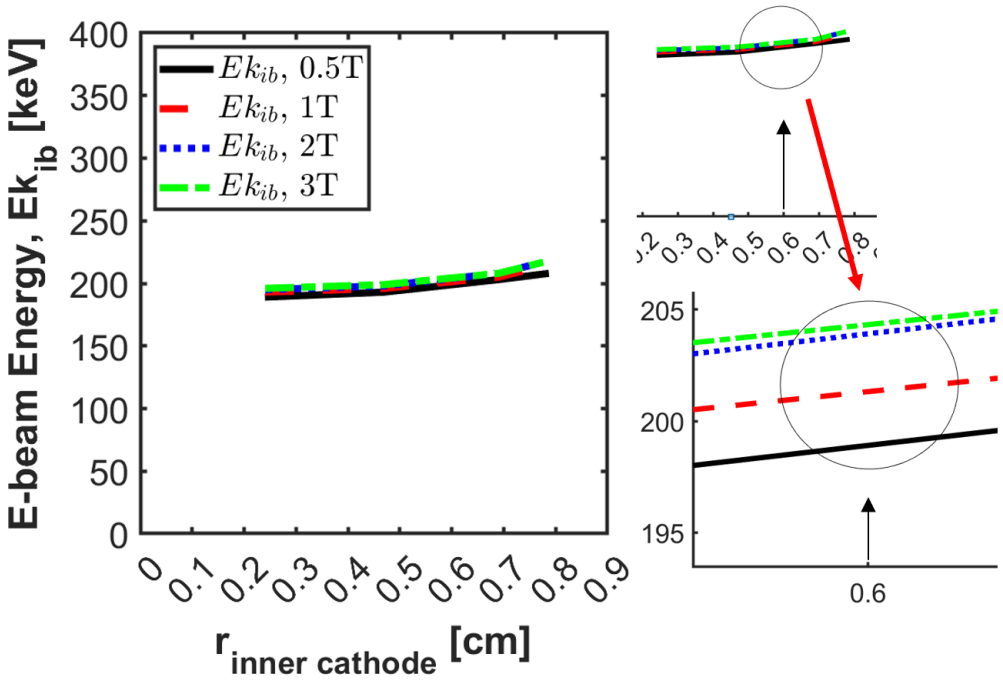

Figure 4.32: Plot shows extracted beam energy for inner electron beam at the end of the drift tube for different values of the applied magnetic field.

sults, as can be seen in Fig. 4.28. In this case, both currents meet at a particular point in Fig. 4.28 where different values of magnetic field (i.e. 0.5 T, 1 T, 2 T, 3 T) are applied. After a brief analysis, it can be concluded that, at some point, even applying higher or an infinite magnetic field, the results do not change significantly after 3 T, as can be seen in Figs. 4.29 and 4.30. Similarly, in the case of extracted output beam voltage or beam energy in Fig. 4.31 and Fig. 4.32, beam voltage actually does not vary much for different applied magnetic fields. In both cases, side zoom views can tell the difference is only a few keV after applying different values of magnetic field.

CHAPTER 5

PRELIMINARY EXPERIMENTS

5.1 SINUS-6 electron beam accelerator

The SINUS-6 is a high current, 10 - 15 ns short pulse electron beam accelerator. The main components of SINUS-6 are a Tesla transformer, a pulse-forming line, a high voltage spark gap switch, a transmission line, and a cold-cathode vacuum diode represented as a block diagram in Fig. 5.1.

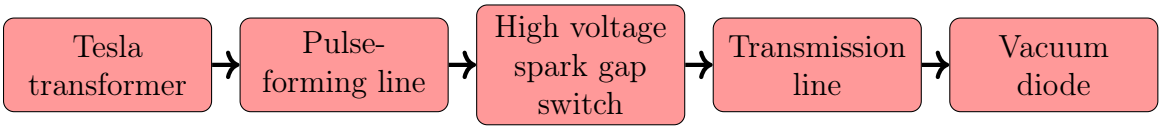

Figure 5.1: Block diagram of the SINUS-6 electron beam accelerator.

The SINUS-6 accelerator can be operated in a single shot regime with applied voltages up to 700 kV and current 6 kA for a pulse duration of about 12 ns. As can be seen in the block diagram, a 'Tesla transformer' basically comprises two inductively coupled circuits that convert a constant charge voltage to a high-voltage pulsed voltage. The primary winding of the Tesla transformer is single turn, while the secondary winding has 3,500 turns and the entire system is enclosed by a 'pulse

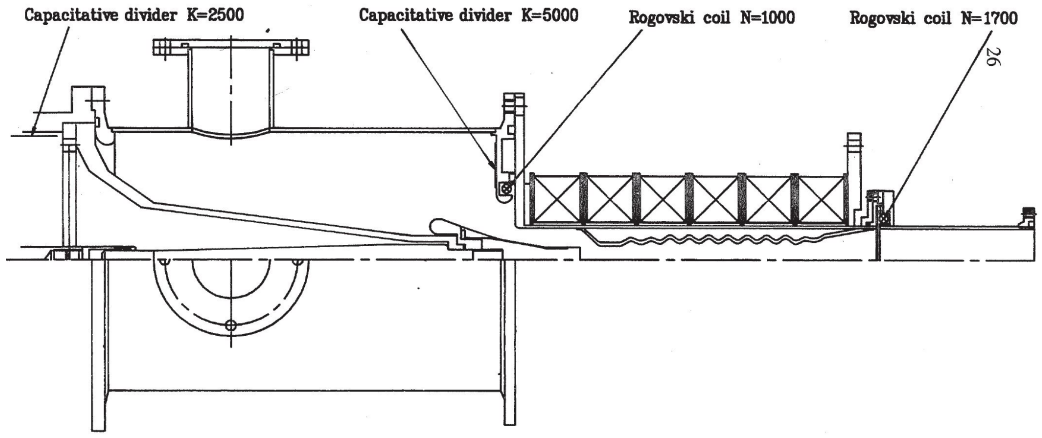

Figure 5.2: Vacuum diode region in SINUS-6 electron beam accelerator.

forming line'. A pulse forming line is an oil-filled coaxial line with impedance of about 22 Ω and electric field stress of about 180 kV/cm. The transit period for the pulse forming line is 12 ns. Transformer oil is used for insulation of the high voltage of the pulse forming line.

The SINUS-6 accelerator uses [51] a high-pressure nitrogen-filled spark gap switch as the high-voltage switch where the maximum gauge pressure is about 22 atmospheres. The transmission line is a long, nonuniform adiabatic tapered wave line and needs to match the 'pulse forming line' with the vacuum diode's impedance. Like the pulse forming line, the input impedance of the transmission line is about 22 Ω, and the output impedance is about 130 Ω, and transmission oil is used for high voltage insulation. The vacuum diode region is shown in Fig. 5.2 is where a cold, thin-walled, explosive emission cathode is immersed in a magnetic field.

5.2 Experimental set-up

In high-current electron beam accelerators, typically a coaxial cold explosive (preferably graphite depending on nature of experiment) emission cathode is used (*cf.* in

Fig. 5.3). Figure 5.3 shows all the cathodes with different diameters that are used in experiments (note that these identical cathodes are also used as the basis for the analytical calculations as well as the PIC simulations).

The annular cathode needs to be very thin with a sharp emitting edge to form electron beams. Explosive emission cathodes are very thin to make sure that the electric field strength on the cathode's surface is about 10^7 V/cm [64]. This cold explosive cathode needs to be immersed in a uniform magnetic field and the magnetic field strength has a great influence on the electron beam formation inside the waveguide (*cf.* in Fig. 5.4).

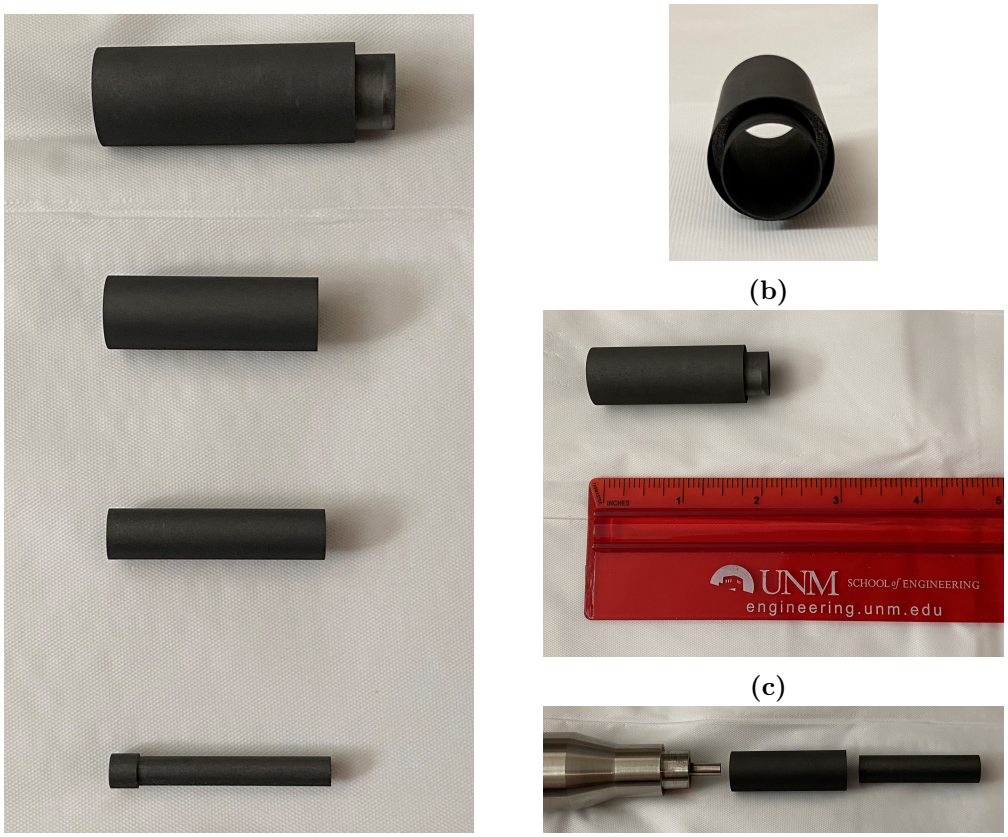

Figure 5.3: (a) Thin annular graphite cathodes with different diameters. (b) Front view of the MICDs. (c) Side view of the MICDs. (d) MICDs with cathode shank holder.

Figure 5.5 shows the beam dump or electron collector made of graphite material

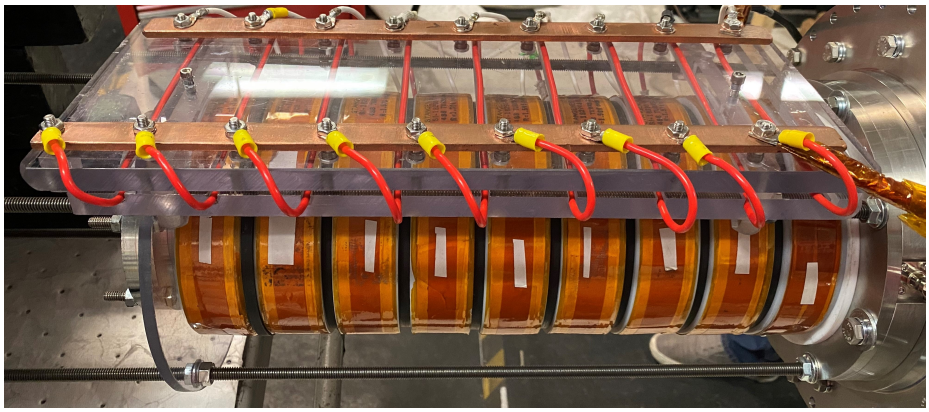

(a)

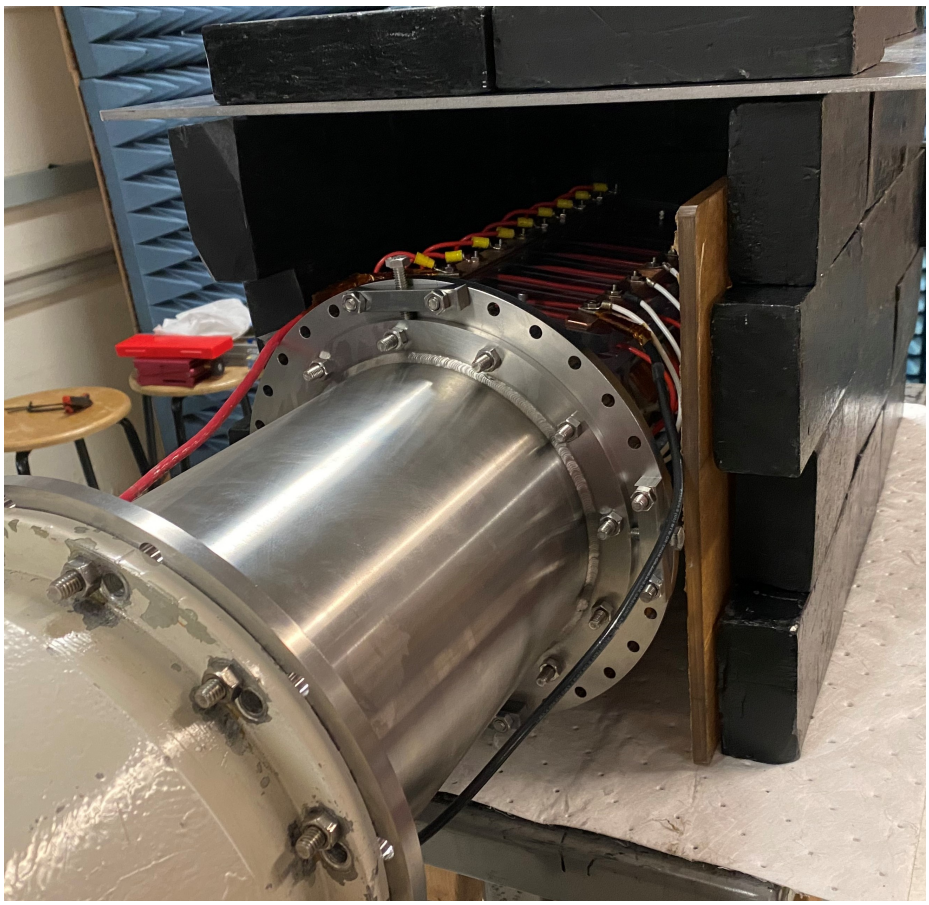

(b)

Figure 5.4: (a) Vacuum MICD immersed in a magnetic field. (b) Side view of the vacuum chamber immersed in a magnetic field, and surrounded by radiation shielding of black brick walls and absorbing foam; the MICD is inside the vacuum chamber.

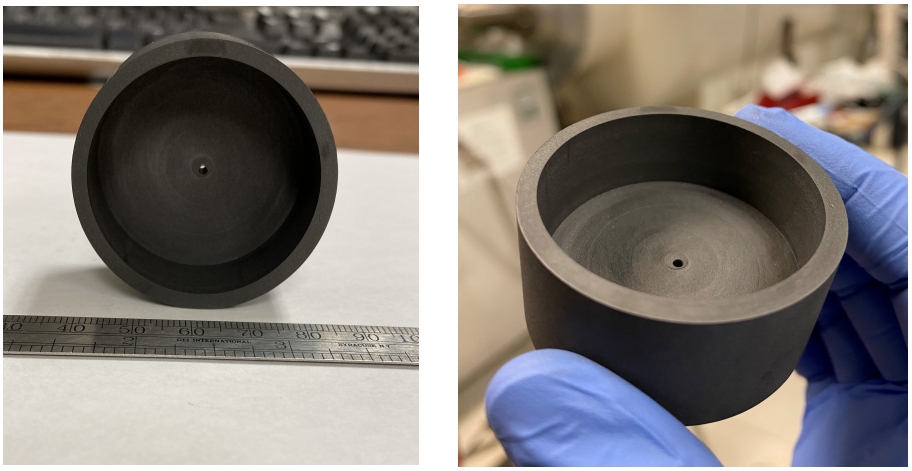

(a) (b)

Figure 5.5: (a) Front view, (b) side view of the collector cup made of graphite material with 44.45 mm diameter to capture the electron beam.

with 44.45 mm diameter to capture the spent electron beam. The FC diagnostic with this graphite collector is set up at the end of the drift tube output window where the FC probe comprises a semi-rigid coaxial cable with a center conductor connected to a graphite collector (cup), as shown in Fig. 5.6. The charge captured by the FC is measured across a shunt or current-viewing-resistor (CVR) and the signal is then registered by an oscilloscope.

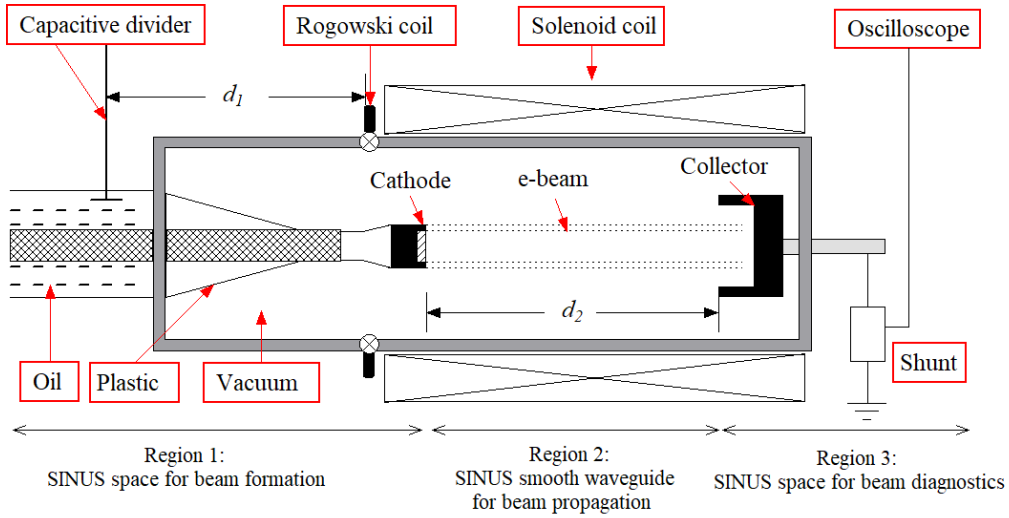

Figure 5.6: The schematic shows the demo set-up of the electron beam current measurements of the vacuum and air-side in the accelerator.

In a similar manner, to capture the electron beams emitted from nested cathodes or MICDs, a Faraday cup array (FCA) is set up at the end of the drift tube output window. The FCA probes comprise four semi-rigid coaxial cables with each of their center conductors connected to four graphite collector (four cups), as shown in Fig. 5.7. Four cups can be placed in order to measure the current density of the inner and outer electron beams with different aperture sizes (as labeled in Fig. 5.7). In this case, four signal responses passing via four apertures can be registered by the oscilloscope simultaneously if there are channels available. Otherwise, four signals can be recorded individually by an oscilloscope without breaking vacuum and opening up the system following each shot.

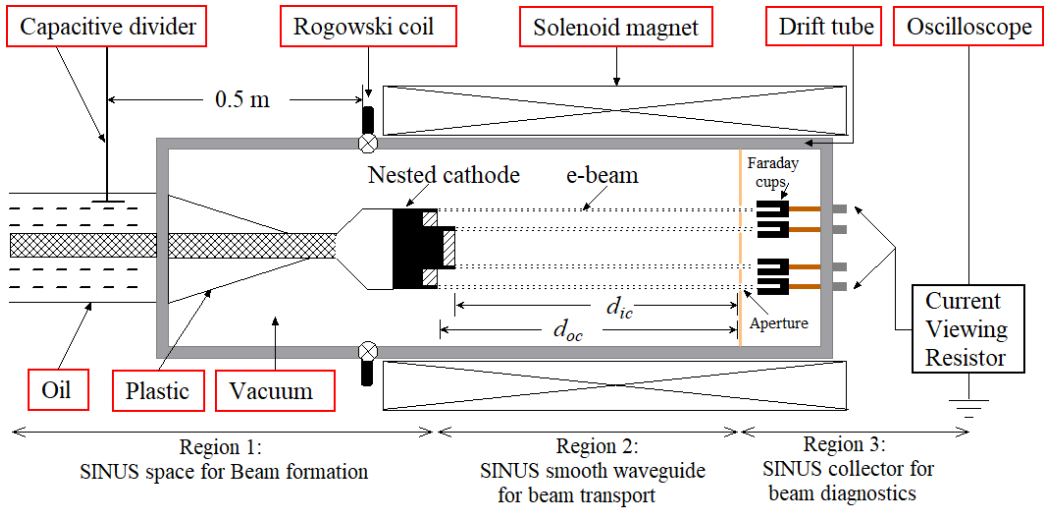

Figure 5.7: Schematic of the current set-up of the electron beam accelerator at UNM shows three regions of the electron beam to be thoroughly studied and the demo set-up of the electron beam current measurements from MICDs by Farday cup array.

5.3 Diagnostics procedure of pulsed electron beam

As mentioned earlier, the goal of the experiment is to validate the experimentally measured parameters of two thin annular electron beams produced from two nested MICDs on the SINUS-6 by using analytical calculations and PIC simulations. The

experimental measurements of the electron beam parameters are performed by direct monitoring of

i. pulsed accelerating voltage applied to the nested MICDs. Pulsed accelerating voltage is measured via a capacitive voltage divider mounted at the end of the transmission line upstream from the cathode's edge (capacitive divider K=2500 in Fig. 5.2).

ii. the total or maximum pulsed electron beam current that is generated from the tip of nested MICDs and measured with a Rogowski coil before propagating downstream in a smooth-walled cylindrical waveguide immersed in a strong magnetic field (Rogowski coil N=1000 in Fig. 5.2).

iii. the pulsed electron beam current emitted from the MICD (for a single beam case) that is dumped into a FC (*cf.* in Fig. 5.5) and is measured via a CVR (*cf.* shunt labeled in Fig. 5.6).

iv. the pulsed electron beam current generated from MICDs is measured via CVR separately dumping the beams into the FCA (*cf.* FCs labeled in Fig. 5.7) -

   (a) block the inner beam first, measure the outer beam current via CVR by dumping the electron beam into the FCA.

   (b) block the outer beam, and measure the inner beam current via CVR by dumping the beam into FCA.

v. once the electron beam currents from the inner and outer cathodes are known, in a similar manner, the electron beam current density is measured separately by passing the beam through a very small aperture $\leq$0.1 mm by the following methods

(a) block the inner beam first, and calculate current density by passing the outer beam current via 0.1 mm aperture.

(b) block the outer beam, and calculate current density by passing the inner beam current via 0.1 mm aperture.

vi. once the electron beam current and current density calculated via. FC array from the inner and outer electron beam are known, electron beam energy can be calculated by the following method -

(a) integrate the inner and outer electron beam current to obtain the electron charge for each case.

(b) obtain the charge density (C/m^{-3}) from calculated charge for each beam.

(c) from known charge, charge density, and current density, it is possible to estimate electron velocity.

(d) from the electron velocity it is possible to know the electron beam energy.

5.4 Preliminary experimental results

5.4.1 Beam current diagnostics via the FC

The FC is one of the most simplest methods to measure electron or ion beam current density [111]– [112]. The basic principle of the FC (typical design looks like a cup) is that electrons are absorbed by a block of conductive material (e.g., graphite, brass, Copper, Al, etc.) in the form of a cup, and the resulting current from the FC can be measured across a shunt resistor or CVR. This measurement ultimately results in the electron beam current by applying Ohm's law if a shunt resistor or CVR is used. There are some limitations of FC uses for application to high-energy electron/ion

beams. In the case of high current/energy measurements, the absorbing material needs to be thicker than the stopping power depth for the charged particle to avoid complicating factors, such as backscattering/secondary particles. Graphite material is widely used to reduce the backscattered electrons [113].

In this dissertation work, a number of FC set-up were attempted to obtain the electron beam current via a CVR. RG-58 coaxial cable is connected from the output port of the CVR to the oscilloscope (Tektronix DPO 71254C) located in the screen room. A basic schematic design with FC set-up of the electron beam measurements is shown in Fig. 5.6. The actual hardware parts, diagnostics set-up, and preliminary experimental results of measuring electron beam formation are shown in Fig. 5.8.

Figure 5.9 shows signal responses from the capacitive voltage divider probe (yellow), Rogowski coil (blue), and FC (pink) as recorded by the oscilloscope (Tektronix DPO 71254C). In this case, a single cathode with 18 mm diameter and 49 mm long used placed for $I-V$ measurements. The gas pressure in the gas switch is set to about 106 psi to obtain an accelerating voltage of 400 kV. The pulsed accelerating voltage is measured via a capacitive voltage divider mounted near the end of the transmission line. The total electron beam current is obtained from the Rogowski coil placed near the cathode source (MICD). These signals are registered by the oscilloscope via long coaxial cables inside the screen room (Faraday cage). The electron beam currents emitted from the edge of the MICDs are measured by a FC. The FC is fed by a semi-rigid coaxial feed-through with a center conductor and placed in the vacuum side at the end of the pipe window port. The distance between beam emitting surface to FC is about 8.9 cm. The output end of the center conductor of the semi-rigid coaxial cable is connected to a a CVR where the output BNC port of the CVR is connected to the oscilloscope. The voltage drop signal across the CVR is monitored by the oscilloscope, which ultimately gives us the FC measurements, as can be seen

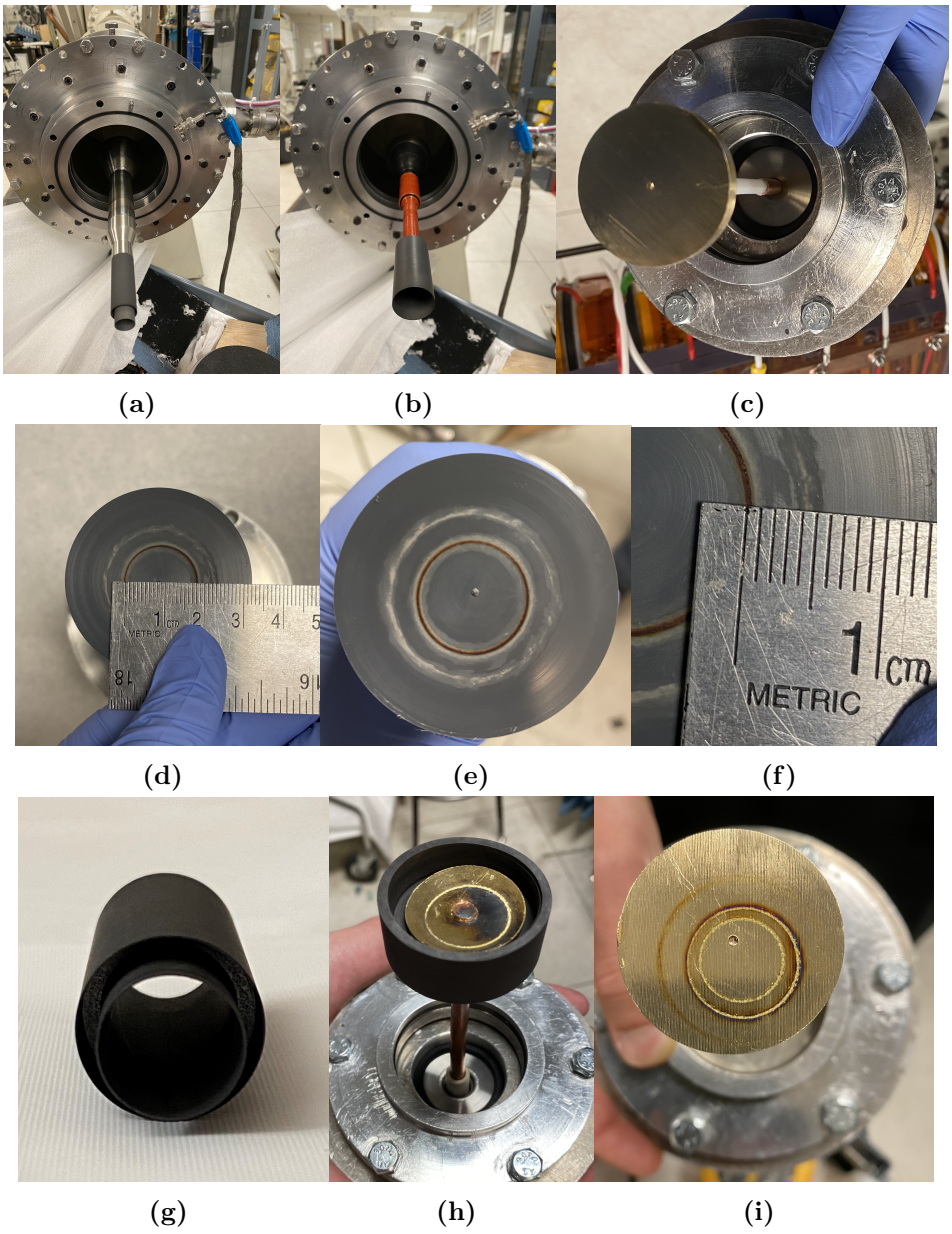

Figure 5.8: (a) MICDs connected to cathode shank with cathode holder, (b) MICD connected to to a polished shank with cathode holder, (d) scale shows beam diameter ≈18 mm, (e) annular electron beam ring on the plastic witness plate, (f) scale shows beam thickness ≈0.2 mm, (g) front view of nested MICDs, (h) beam dumped into FC with brass plate to observe beam diameter to place a aperture plate to measure current density, (i) two beam rings on brass plate, [note* -not aligned]. In this case, accelerating voltage is about 400 kV, magnetic field strength is 2 T.

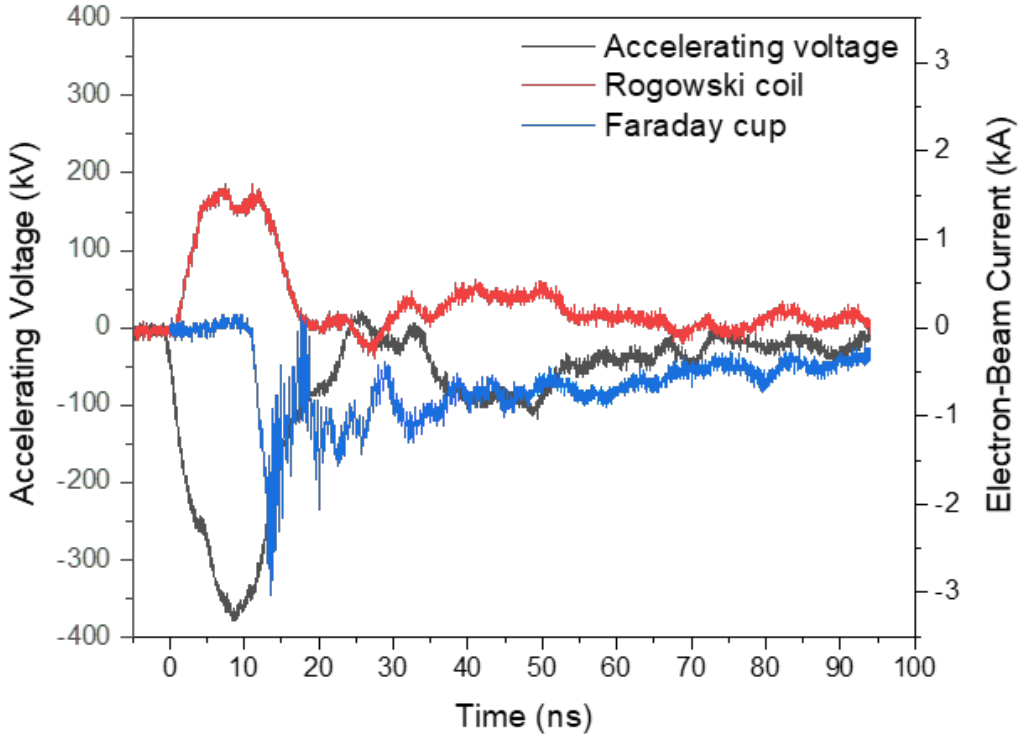

Figure 5.9: Responses from the capacitive voltage divider probe (black), Rogowski coil (red), and FC (blue).

by the blue signal in Fig. 5.9.

Theoretically, the FC signal should be similar to the signal of the total electron beam current signal (i.e., Rogowski coil signal, red color), as can be seen in Fig. 5.9. The peak amplitude of the FC signal seems slightly higher than the peak value of the signal response from the Rogowski coil. In addition, the FC signal shows some oscillations and negative DC-offset values after 10 ns. If we line up the two signals to compare their pulse shape without considering the cable lengths (due to unavailability of the cable time delay calibration measurements data), we can see that both signals (Rogowski coil, FC) seem to have the same pulsewidth (*cf.* in Fig. 5.10). Figure 5.10 shows a clear view of how two signals are lined up. The bottom plot shows the horizontal axis is time shifted backward to align the FC with the Rogowski coil. The

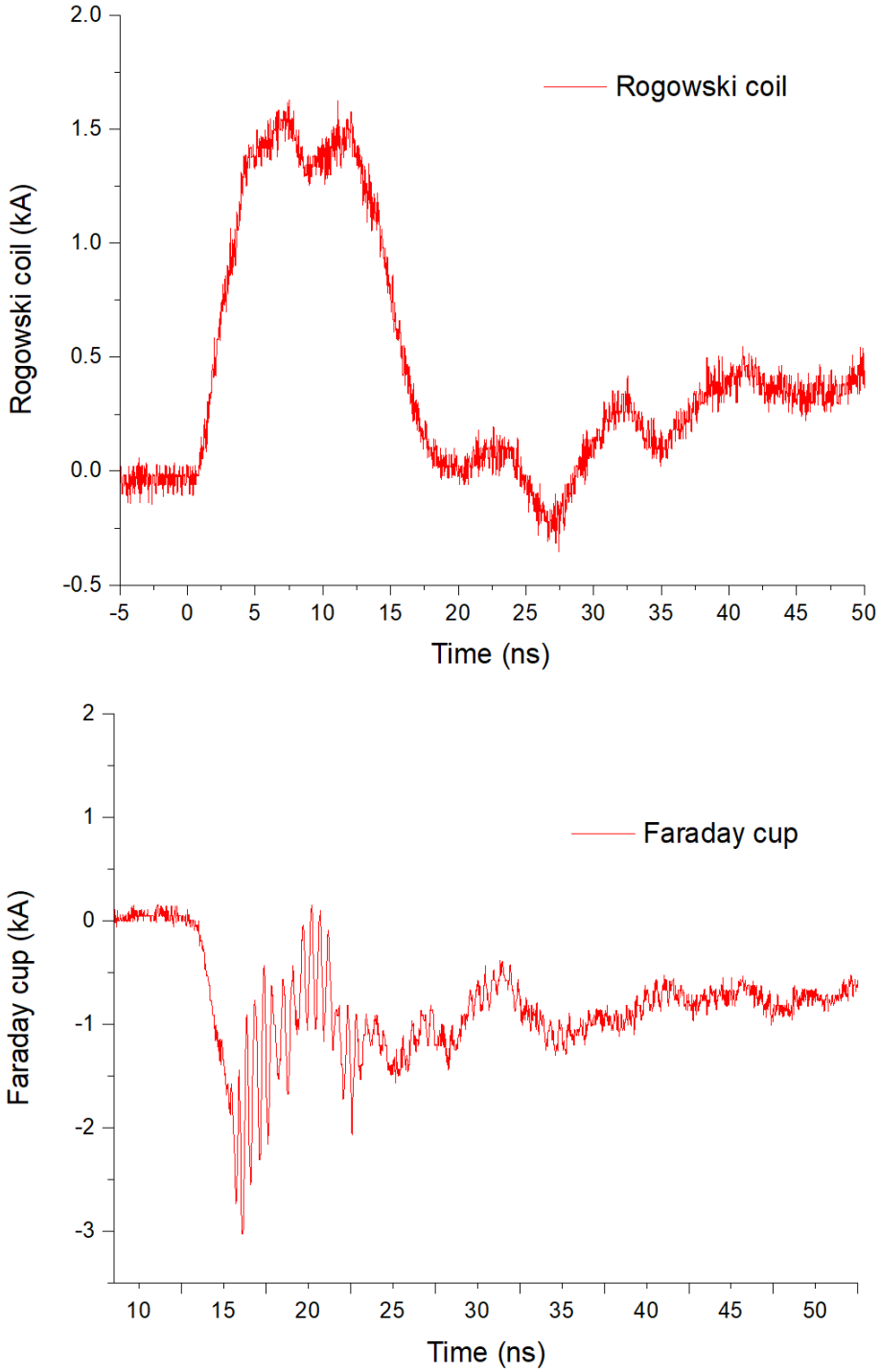

Figure 5.10: Top - experimental oscillogram from Rogowski coil. Bottom - the horizontal axis (time) of the FC signal is shifted backward to line up with Rogowski coil's signal. The curves were lined up to ease comparison and cable lengths were not accounted for.

time shift of the FC signal (>10 ns) is intended to align and compare the pulsewidth of the two signals, but requires knowledge of cable lengths to calculate delay time correctly. However, this may also give us a sense of the time-of-flight of the beam electrons through a known drift tube length, which may also help us to check the calculated electron beam energies.

CHAPTER 6

ANALYSIS OF RESULTS

6.1 Analysis of analytic, simulation, and experimental results

In this section we analyze the data obtained from analytic (in Section 3.4), simulation (in Section 4.3) and preliminary results from experiments (in Section 5.4).

In order to achieve two electron beams with comparable currents and maximum energy difference, we find that the best position for the inner cathode's radius is $\frac{3}{4}$ of the outer cathode's radius. In this case, we achieve similar currents, $I_{ib} \approx I_{ob}$ ($I_{ib} = 1036.5$ A and $I_{ob} = 1035$ A) but more than 10% energy difference from both electron beams, while the inner beam's radius is 0.69 cm and outer beam's radius is 0.92 cm (*cf.* Table 6.1). It is also important to note that we have performed a series of MAGIC PIC simulations and the results are consistent between analytic predictions and the numerical simulation. (It should be pointed out that here we are considering two nested MICDs, but that this derivation can be extended to three or more nested

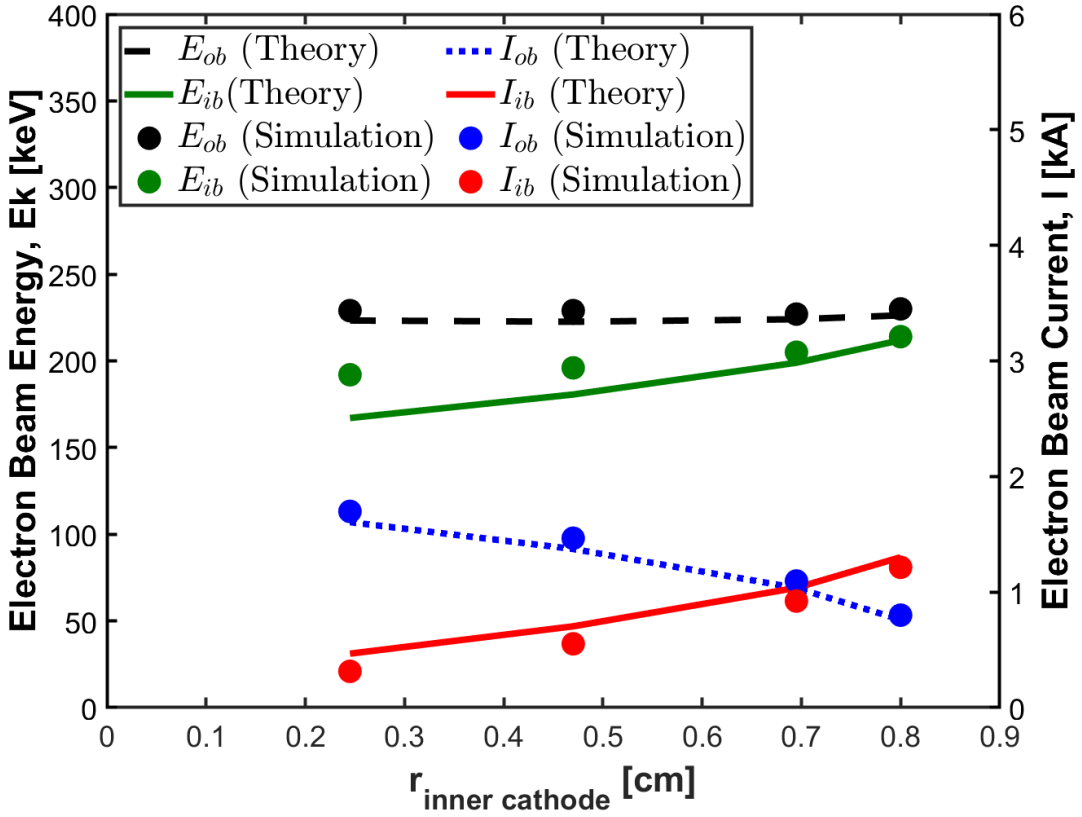

Figure 6.1: Analytical and simulation results of outer and inner electron beam currents and analytical and simulation results of outer (black) and inner electron beam energies as a function of the radius of the inner cathode r_{ic}.

MICDs.)

The electron beam currents and kinetic energies on the same plot as a function of the inner cathode's radius is shown in Fig. 6.1, where the inner cathode varies from 0.225 cm to 0.8 cm for an applied voltage of 400 kV. The most striking result is that the two electron beam currents meet at the same point at 0.69 cm (viz., radial position of inner cathode) and a greater than 10% energy difference between two beams is achieved exactly at that point (*cf.* in Fig. 6.1). The data are presented in Table 6.1. For an applied voltage of 400 kV, r_{ic} = 0.69 cm, and r_{oc} = 0.92 cm, the energy difference is about 11.8% (in theory) and about 9% (in simulations), but both electron beam currents are comparable ($I_{ib.cal}$ = 1036 A, $I_{ob.cal}$ = 1034

A, $I_{ib.sim}$ = 941 A, $I_{ob.sim}$ = 1095 A) from both theory and simulations. In this case (while, $r_{ic} = \frac{3}{4}r_{oc} = 0.69$ cm) we achieve more than 10% energy difference and comparable currents that we are seeking. Remarkably, simulations also give us similar results as theory where about a 9% energy difference and about the same electron beam currents ($I_{ib.sim} = 941$ A, $I_{ob.sim} = 1095$ A) are obtained. In addition, for other cases (while the inner cathode's radii are $r_{ic} = \frac{1}{4}r_{oc} = 0.24$ cm and $r_{ic} = \frac{1}{2}r_{oc} = 0.47$ cm), more than 10% energy difference can be achieved in both theory and simulations.

A comparison of theory and simulation results for outer electron beam currents from two nested MICDs is shown in Fig. 6.2. There are five different colors representing five different applied voltages ranging from 100 - 500 kV and the solid lines with different colors show the calculated data and different markers with associated solid lines show simulated data obtained using the MAGIC PIC code in both Figs. 6.2a and 6.2b. The x-axis shows the inner cathode's radial position from $r_{ic} = 0.24$ cm to $r_{ic} = 0.81$ cm (where, $r_{ic} < r_{oc} = 0.92$ cm), and the y-axis represents the beam current [kA]. As can be seen, the calculated and simulated outer electron beam currents show excellent agreement for applied voltages ranging from 100 - 300 kV. Good agreement can be seen for applied voltages ranging from 400 - 500 kV as well. Similarly, in Fig. 6.2b the calculated and simulated inner electron beam currents show fairly good agreement for applied voltages of 100 - 200 kV. Good agreement can be seen for 300 - 500 kV as well. Both figures illustrate that, when the inner cathode is radially farther away from the outer cathode (i.e., at r_{ic} =0.225 cm), we observe that the outer electron beam current is greater than the inner electron beam current. As both electron beams get closer, the outer electron beam's space charge starts screening the inner electron beam. If both electron beams are very close to each other (i.e., r_{ic} =0.8 cm), we observe that the inner electron beam current is greater than the outer electron beam current.

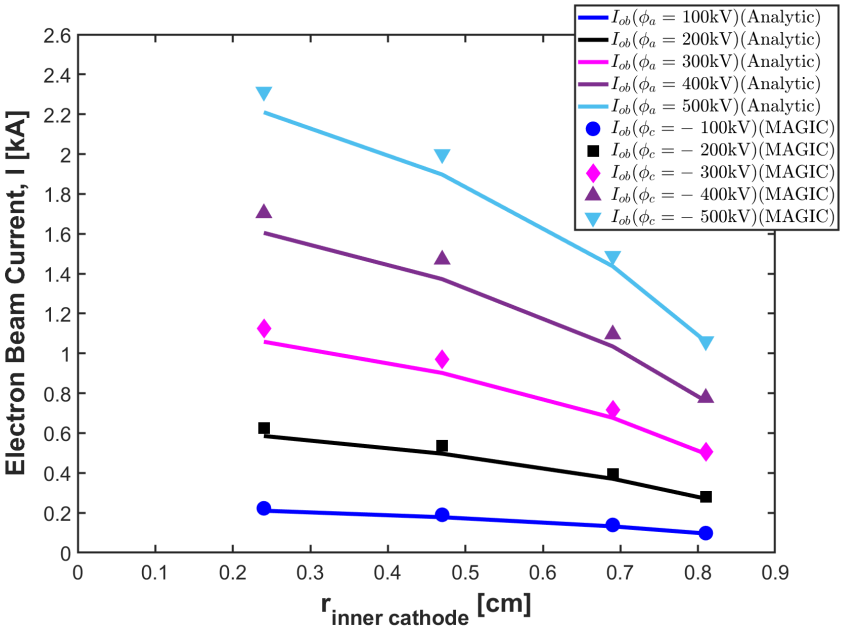

(a) Analytics and simulations of I_{ob} as a $f(r_{ic})$

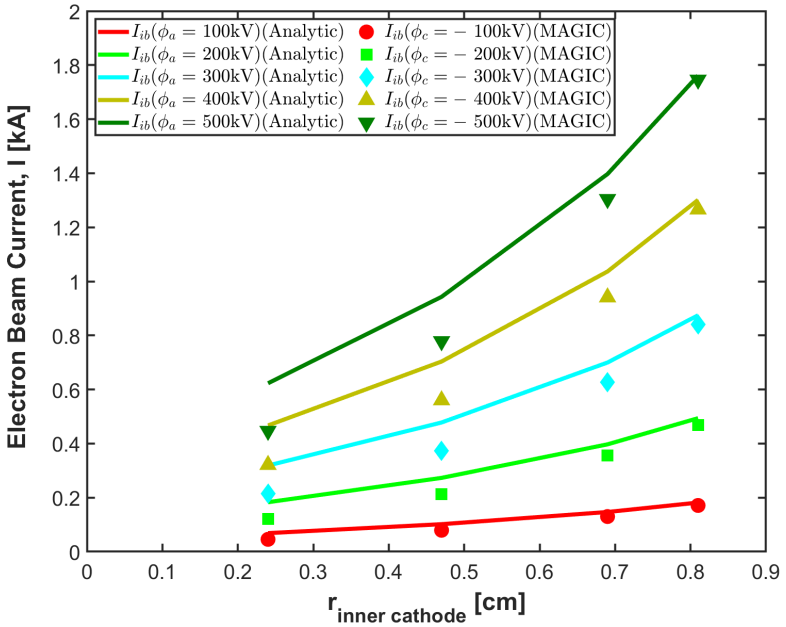

(b) Analytics and simulations of I_{ib} as a $f(r_{ic})$

Figure 6.2: Plot shows data from analytically calculated and MAGIC PIC simulations of two nested MICDs as a function of the radius of the inner cathode r_{ic}. (a) The solid lines with different colors show the calculated outer electron beam current and different markers associated with each solid line corresponds to MAGIC PIC simulated outer electron beam current, and (b) the solid lines with different colors show the calculated inner electron beam current and different markers associated with each solid line corresponds to MAGIC PIC simulated inner electron beam current for different applied voltages ranging from 100 - 500 kV for a magnetic field of 3 T. The total simulation time was 10 ns.

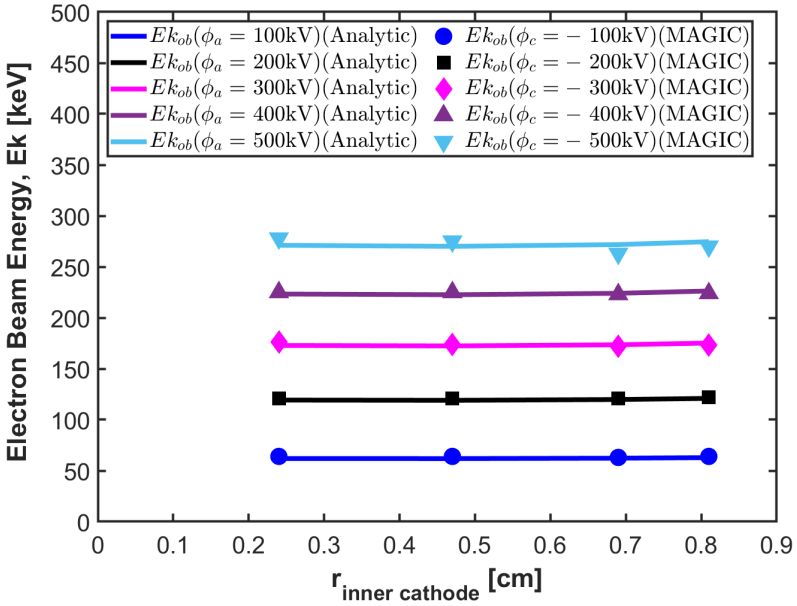

(a) Analytical calculations and simulations of Ek_{ob} as a function of r_{ic}

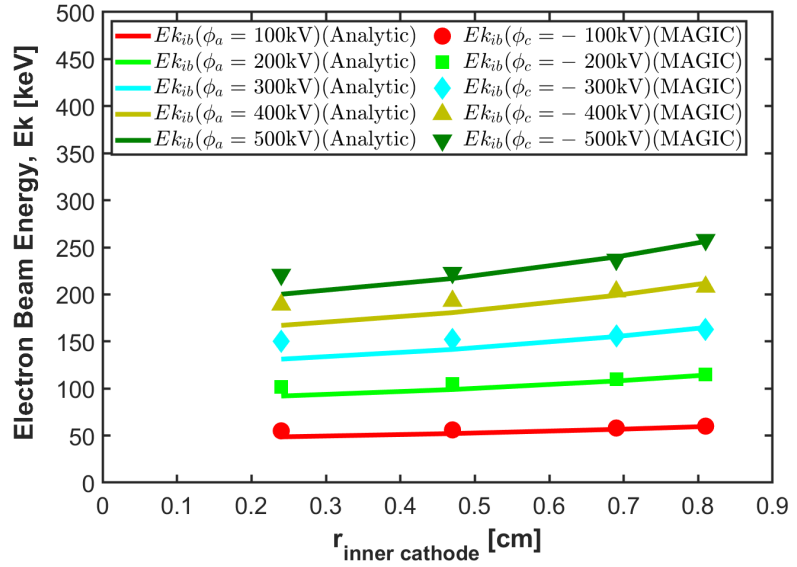

(b) Analytical calculations and simulations of Ek_{ib} as a function of r_{ic}

Figure 6.3: Plot shows data from analytically calculated and MAGIC PIC simulation of two nested MICDs as a function of the radius of the inner cathode r_{ic}. (a) The solid lines with different colors show the calculated outer electron beam energy and the filled circles associated with each solid line corresponds to MAGIC PIC simulated outer electron beam energy, and (b) the solid lines with different colors show the calculated inner electron beam energy and the filled circles associated with each solid line corresponds to MAGIC PIC simulated inner electron beam energy for different applied voltages ranging from 100 - 500 kV for a magnetic field of 3 T. The total simulation time was 10 ns.

If we now focus on the electron beam energy plots (*cf.* in Fig. 6.3), we observe both theory and simulations for the case of the outer electron beam energy show excellent agreement for applied voltages ranging from 100 – 500 kV (*cf.* in Fig. 6.3a). Good agreement is observed for the inner electron beam at comparatively lower voltages (i.e., 100 kV and 200 kV) (*cf.* in Fig. 6.3b), but at higher applied voltages >200 kV, a slight difference between the analytical and simulation results can be seen, as is shown in Fig. 6.3b). As in Fig. 6.2, a linear relationship between the beam energies and radial gap of the two beams is observed. The energy difference is greater than 15% for both theory and simulations when the radial gap between the two electron beams is larger. We achieve a decent energy difference of 9-11% at r_{ic}=0.69 cm with comparable currents as we discussed earlier.

We were interested in the dependence of the electron beam parameters for different values of applied magnetic field ($\vec{B}$ = 0.5 T, $\vec{B}$ = 1 T, $\vec{B}$ = 2 T, $\vec{B}$ = 3 T) and the results are consistent between analytical predictions and PIC simulations, as shown in Fig. 6.4. Both Fig. 6.4a and Fig. 6.4b show excellent agreement between analytical calculations and simulations for different magnetic fields. At lower applied voltages (i.e., at 100 kV) both curves overlap, meaning we do not see any energy difference; but at higher applied voltages >100 kV, both beams start apart from each other and we observe a greater energy difference. Similar trends can be seen in Fig. 6.4b where both electron beams appear to be same value at 100 kV and 400 kV, but as we increase voltage, the outer electron beam current tends to be higher than the inner beam's current. Both plots illustrate that analytical and simulation results do not show significant difference (only a few kev or a few Amps difference) for different magnetic fields. Our interest is in the geometry where $r_{ib} = \frac{3}{4} r_{ob}$ and at 400 kV we see consistent results for different magnetic fields where we achieve more than 10% energy difference with comparable currents.

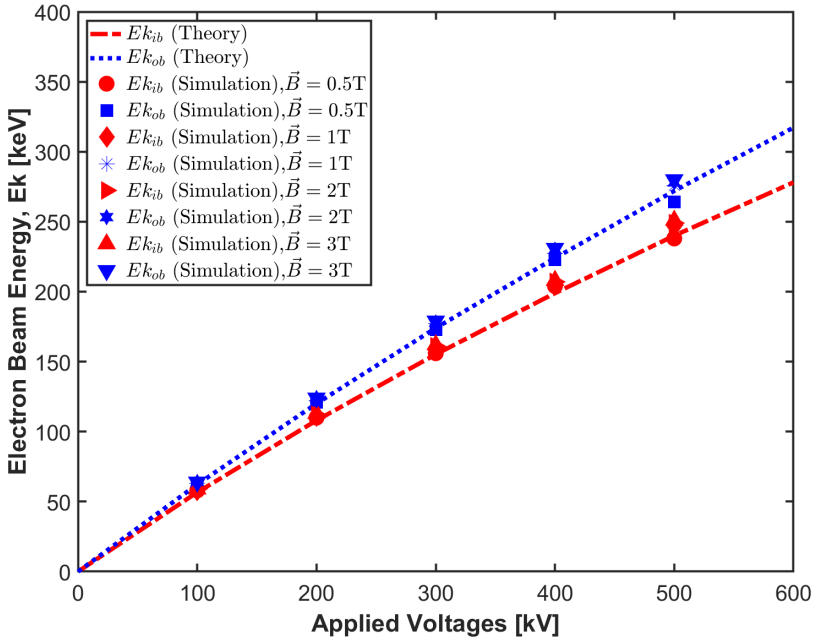

(a) Ek_{ob} and Ek_{ib} with different magnetic fields

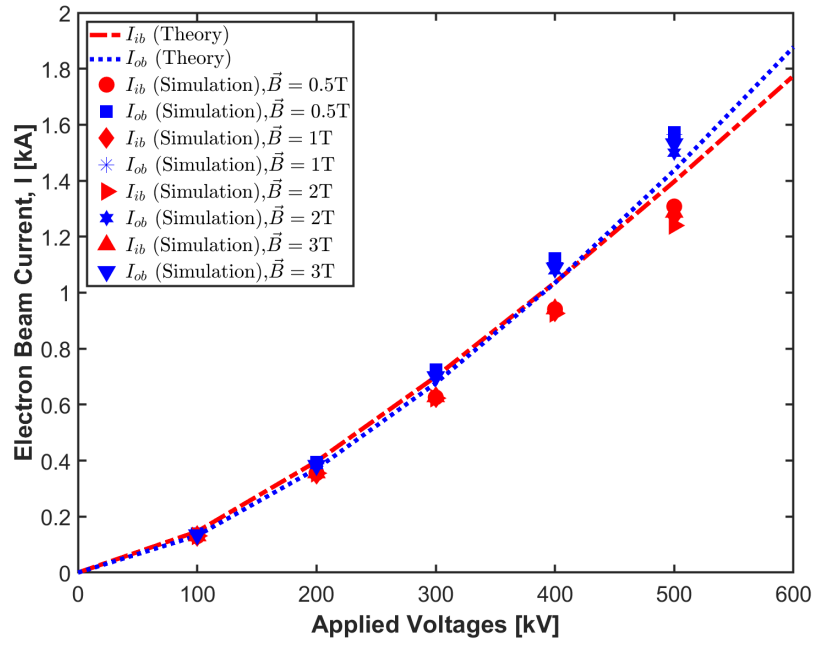

(b) I_{ob} and I_{ib} with different magnetic fields

Figure 6.4: Plot shows the analytically calculated (red dash dot, blue dotted lines) and MAGIC PIC simulated (with different markers) inner and 'outer' electron beam (a) energies, and (b) currents for different applied voltages ranging from 0 - 600 kV and magnetic fields of $\vec{B} = 0.5, 1, 2, 3$ T, for a total simulation time of 10 ns. For both plots, the inner beam's radius is $r_{ib} = \frac{3}{4} r_{ob}$.

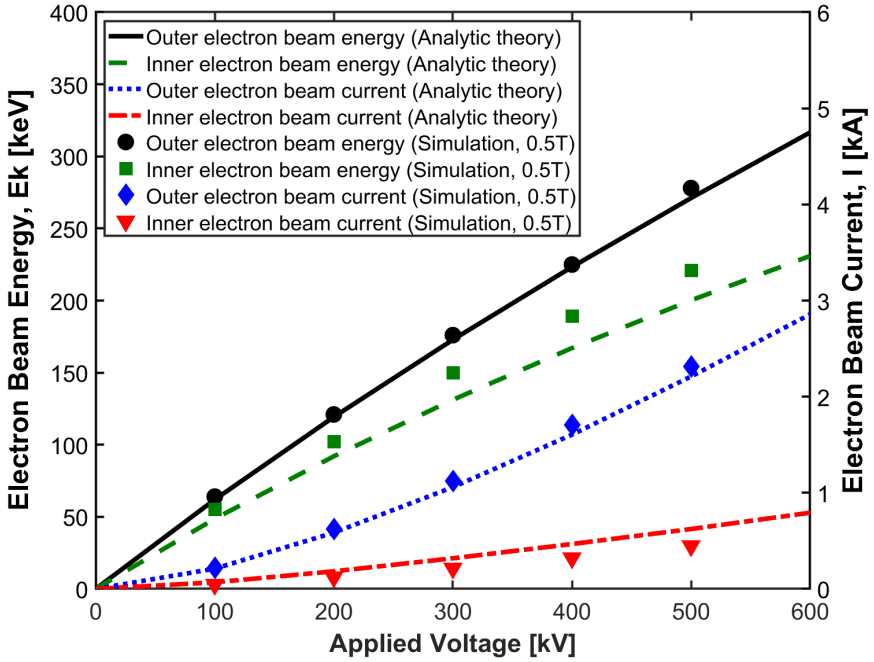

(a) Ek and current I as a function of applied voltages for $\vec{B} = 0.5\text{T}$ and $r_{ib} = \frac{1}{4} r_{ob}$

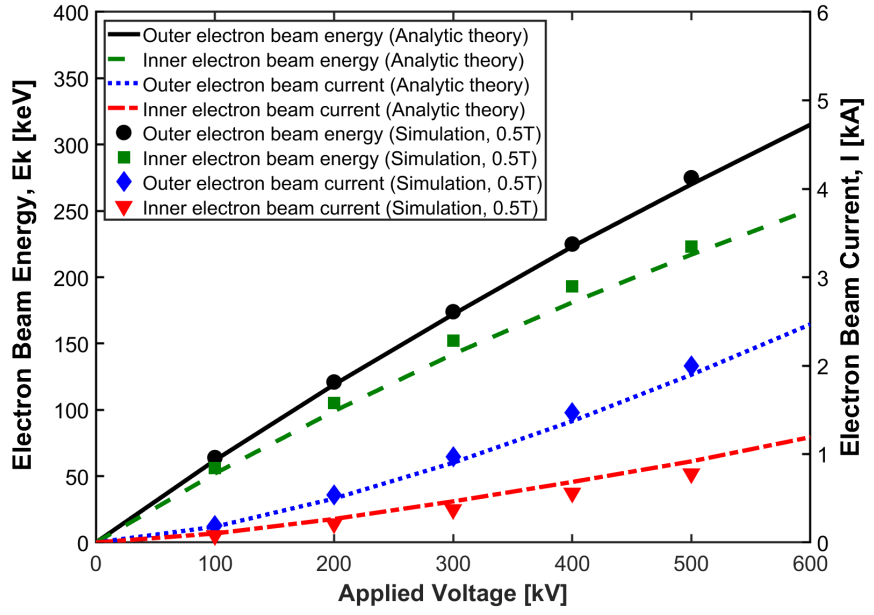

(b) Ek and current I as a function of applied voltages for $\vec{B} = 0.5\text{T}$ and $r_{ib} = \frac{1}{2} r_{ob}$

Figure 6.5: Plot shows the analytically calculated (solid black, green dash, dotted blue, and red dash dot lines) and MAGIC PIC simulated (filled markers with different colors) inner and outer electron beam current and energy as a function of applied voltages for (a) $\vec{B} = 0.5$ T and $r_{ib} = \frac{1}{4} r_{ob}$, and (b) $\vec{B} = 0.5$ T and $r_{ib} = \frac{1}{2} r_{ob}$.

Table 6.1: Calculated and simulated data of electron beam current and electron beam energy from each cathode for different cases for an applied voltage of 400 kV and magnetic field of 3 T (in simulations).

[a]ϕ_a	[b]r_a	[c]r_{oc}	[d]r_{ic}	[e]h_c	[f]$I_{ib.cal}$	[g]$I_{ob.cal}$	[h]$I_{ib.sim}$	[i]$I_{ob.sim}$	[j]$E_{ib.cal}$	[k]$E_{ob.cal}$	[l]ΔE	[m]$E_{ib.sim}$	[n]$E_{ob.sim}$	[o]ΔE
[kV]	[cm]	[cm]	[cm]	[cm]	[kA]	[kA]	[kA]	[kA]	[keV]	[keV]	%	[keV]	[keV]	%
400	2.5	0.92	0.24	0.02	0.46	1.6	0.32	1.7	167	223	28	189	225	17
400	2.5	0.92	0.47	0.02	0.70	1.37	0.56	1.47	181	223	20	193	225	15
400	2.5	0.92	0.69	0.02	1.03	1.03	0.94	1.09	199	224	11	203	223	9
400	2.5	0.92	0.81	0.02	1.3	0.76	1.26	0.77	212	226	6	208	224	7

[a] Applied voltage.
[b] Anode radius.
[c] Outer cathode's radius.
[d] Inner cathode's radius.
[e] Thickness of the cathode.
[f] Inner electron beam current (theory).
[g] Outer electron beam current (theory).
[h] Inner electron beam current (simulation).
[i] Outer electron beam current (simulation).
[j] Inner electron beam energy (theory).
[k] Outer electron beam energy (theory).
[l] Energy difference between inner ($E_{ib.cal}$) and outer. ($E_{ob.cal}$) electron beam energy (theory).
[m] Inner electron beam energy (simulation).
[n] Outer electron beam energy (simulation).
[o] Energy difference between inner ($E_{ib.sim}$) and outer ($E_{ob.sim}$) electron beam energy (simulation).

We also investigated other radial positions (i.e., $r_{ib} = \frac{1}{4}r_{ob}$ and $r_{ib} = \frac{1}{2}r_{ob}$) of the inner beam with respect to the outer beam, as shown in Fig. 6.5. Both analytically calculated and simulation currents agree fairly well; the outer electron beam energy shows excellent agreement for both cases, the inner (green) electron beam energy simulation curves show a little difference from the analytical calculations. In this case, it is important to point out that, at higher applied voltages, the gap between the two electron beam currents increases as the difference between energies increases. The trend for the difference between *inner* and *outer* electron beam currents and energies indicates that the radial difference between the two cathodes and their relative axial separation are key factors in determining what can lead to two electron beams with

comparable currents and maximum energy difference.

We focus next on the electron beam density and plasma frequency as a function of the inner cathode's radius for an applied voltage of 400 kV since these are critical parameters in designing a multi-stream TWT [4]. We calculate electron density for the inner and outer electron beams from the relationships between charge density, current density, and electron velocity, given by,

$$n_{e_{ib}} = \frac{I_{ib}\gamma_{ib}}{e_0 A_{ib} c\sqrt{\gamma_{ib}^2-1}}, \quad \text{and} \tag{6.1}$$

$$n_{e_{ob}} = \frac{I_{ob}\gamma_{ob}}{e_0 A_{ob} c\sqrt{\gamma_{ob}^2-1}}. \tag{6.2}$$

We find the electron plasma frequency corresponding to the inner and outer electron beams using the relation between electron density and electron plasma frequency that is given by [26]

$$\omega_{p_{ib}} = \sqrt{\frac{n_{e_{ib}} e_0^2}{m_0 \epsilon_0}}, \tag{6.3}$$

$$\omega_{p_{ob}} = \sqrt{\frac{n_{e_{ob}} e_0^2}{m_0 \epsilon_0}}, \tag{6.4}$$

where the plasma frequency can also be calculated by [114] $\frac{w_p}{2\pi} = f_p \approx 9\sqrt{n_e}$ (n_e in m^{-3}).

Figure 6.6 shows the electron density and electron plasma frequency as a function of the inner beam's radius where inner and outer denote electron beam density as a function of the inner beam's radius for an applied voltage of 400 kV. Fig. 6.6a shows the inner and outer electron beam density for an applied voltage of 400 kV as a function of the inner beam radius r_{ib} and Fig. 6.6b shows the corresponding plot

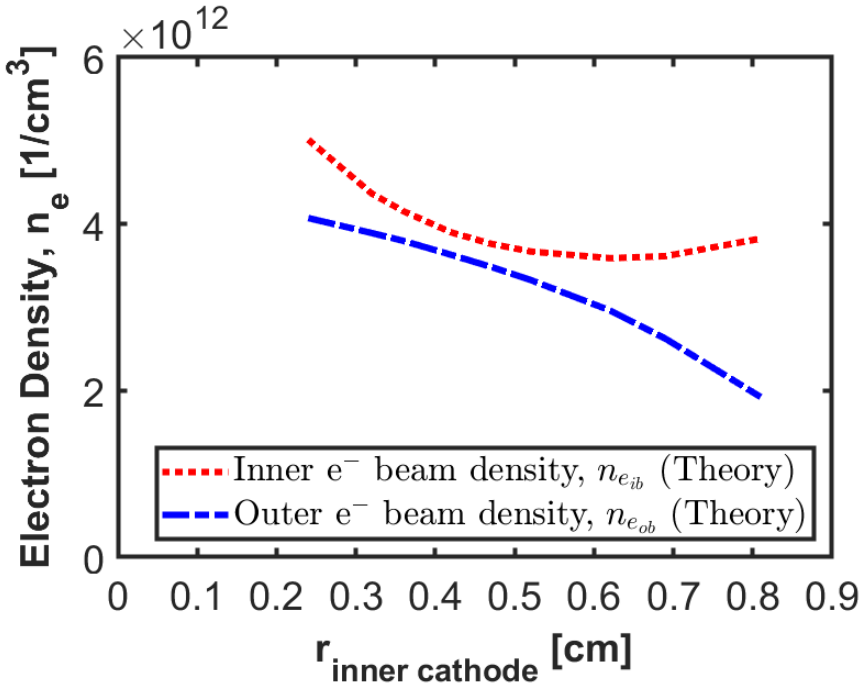

(a) Electron density as a function of r_{ib}

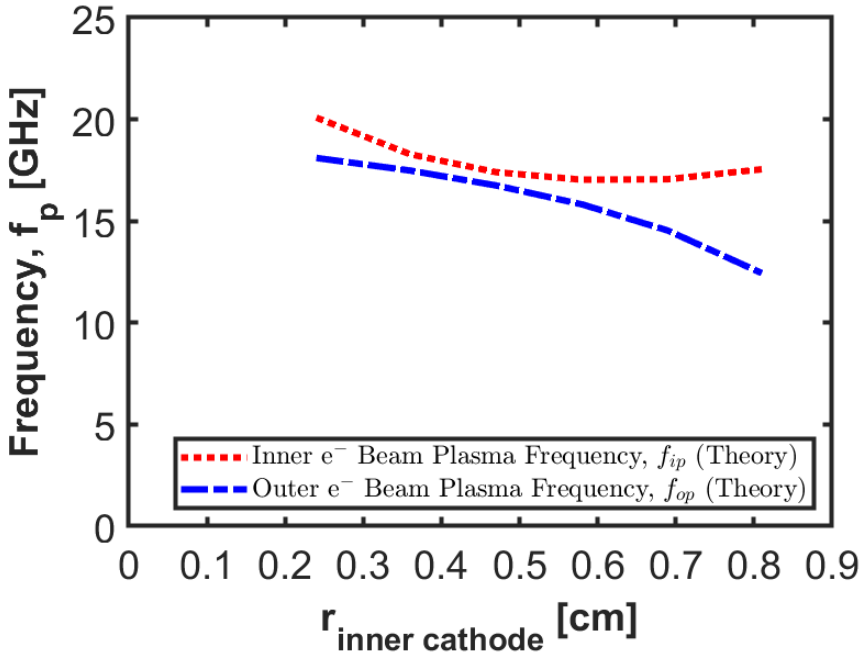

(b) Electron plasma frequency as a function of r_{ib}

Figure 6.6: Plot shows the calculated (a) inner dotted red and outer blue dash electron beam density, and (b) inner dotted red and outer blue dash electron beam plasma frequency for the applied potential of 400 kV as a function of the radius of the inner beam r_{ib}.

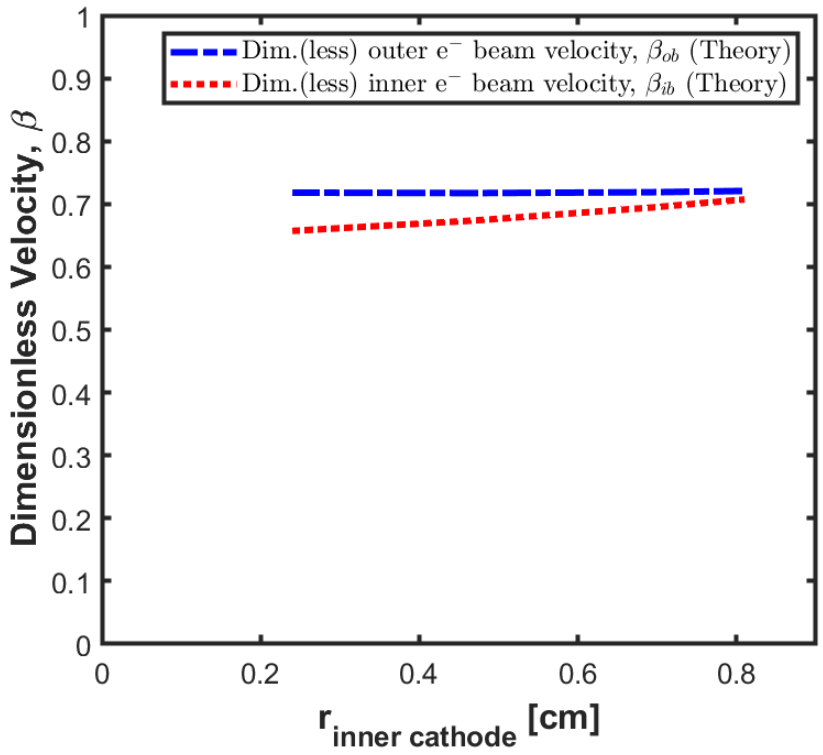

Figure 6.7: The dotted red and the blue dash dot lines show the calculated dimensionless velocity β for the inner and outer electron beams as a function of r_{ic} for an applied potential 400 kV.

for plasma frequency. In this case, the outer electron beam plasma frequency is lower than the inner electron beam plasma frequency. An explanation for this is that, since the radius of the inner electron beam is less than the outer electron beam's radius, its current density is greater, resulting in a higher plasma frequency.

The dimensionless inner and outer electron beam velocities as a function of r_{ib} can be seen in Fig. 6.7, where $\beta_{ib} = \frac{1}{\gamma_{ib}}\sqrt{\gamma_{ib}^2 - 1}$ and $\beta_{ob} = \frac{1}{\gamma_{ob}}\sqrt{\gamma_{ob}^2 - 1}$ correspond to the inner and outer electron beam dimensionless velocities, respectively. In Fig. 6.7, the x-axis represents the inner cathode's radial position from 0.24 cm to 0.81 cm and the y-axis represents the β value from 0 to 1. The blue dash dot and the dotted red lines show the analytically calculated dimensionless velocities β_{ob} for the outer and β_{ib} inner electron beams, respectively, as a function of r_{ib} for an applied voltage of 400 kV. At

the inner cathode's radius $r_{ic} = 0.69$ cm, the β value for the outer electron beam is β_{ob} =0.7187 and the β value for the inner electron beam is β_{ib} =0.6941. The velocity for the two beams are in this case $v_{ob} = 2.16 \times 10^8$ m/s (outer) and $v_{ib} = 2.08 \times 10^8$ m/s (inner), respectively.

Preliminary experimental results show that it is possible to obtain the electron beam current separately using the FC diagnostic. Figure 5.9 shows experimental measurements from SINUS-6 of oscillograms of accelerating voltage (negative polarity, black signal) and maximum electron beam current (positive polarity, red signal) from the Rogowski coil, and electron beam current from the FC (negative polarity, pink signal). The voltage waveform from the capacitive voltage divider registered on the oscilloscope is calculated by Eq. 6.5. The coaxial cable to measure accelerating voltage is connected to a 40 dB attenuator before the oscilloscope. The calibration factor (CF) for the capacitive voltage divider is 2450 [115], [116]

$$V_{accl.}\ \text{kV} = \frac{V_{scope}\ (\text{V}) \times 100\ (40\text{dB})}{1000} \times 2450\ (\text{CF}). \tag{6.5}$$

Similarly, the total current obtained from the Rogowski coil by using Eq. 6.6. The CF for the Rogowski coil is measured to be 24.97 A/V,

$$I_{tot.}\ \text{in A} = \frac{V_{scope}\ (\text{mV}) \times 100\ (40\text{dB})}{1000}(\text{V}) \times 24.97\ \left(\frac{\text{A}}{\text{V}}\right). \tag{6.6}$$

The electron beam current collected at the graphite collector is calculated using Eq. 6.7. One end of the coaxial cable connected to the output end of the BNC port of the CVR and the other end of the coaxial cable is connected to the oscilloscope with 20 dB attenuator. The CVR model is W-2-0025-4FC with 2 ns rise-time purchased

from T&M Research Products, Inc. Albuquerque, NM [117].

$$I_{out.} \text{ in A} = \frac{V_{scope} \text{ (mV)} \times 10 \text{ (20dB)}}{1000}\text{(V)} \times \frac{1}{R_{shunt}}. \tag{6.7}$$

CHAPTER 7

CONCLUSION AND FUTURE WORK

7.1 Conclusion

The research presented in this dissertation is the first study of multi-electron beam generation with different energies from a single cathode at a single potential with application to a multi-stream TWT. We demonstrated the generation of two beams with comparable currents and with an energy difference of about 4%–31% for applied voltages ranging from 100 - 600 kV and depending on the radial position of the inner cathode with respect to the outer cathode and the relative axial extension of the inner cathode with respect to the outer cathode using both analytical theory and PIC simulations. One of the significant findings to emerge from both analytical theory and PIC simulations is that, at a certain value of inner cathode radius and a certain axial extent of the inner cathode compared to the outer cathode, the beam currents for both inner and outer electron beam are comparable and that greater

than 10% energy difference can be achieved. This is highly important for the multi-stream TWT amplifier concept [4]. Experiments are still ongoing in the *Pulsed Power, Beams, and Microwaves Laboratory* at UNM to validate these findings. It should be noted that this technique for generating two electron beams with approximately 10% difference in energies and comparable currents from two MICDs on a cathode stalk at a single potential is most effective when the beams have a significant space charge. This restricts the parameter range of feasibility to, roughly, voltages >100 kV and currents >1 kA.

The methods and results of this study are summarized below:

1. Both quantitative and qualitative techniques have been approached for all three analytic, simulation and experiment methods.

2. A simplified analytic mathematical derivation for multiple beams has been achieved by following Fedosov's theory for a single MICD and extending it to two nested MICDs.

3. A benchmarked PIC (MAGIC) simulation is optimized to study multiple electron beam generation from MICDs powered by a single cathode at a single potential.

4. A case study approach is followed to identify an optimal geometry from this nested cathode model by -

   (a) considering the actual parameters used in the SINUS-6 electron beam accelerator

   (b) taking into account the present experimental set-up at the *Pulsed Power, Beams, and Microwaves Laboratory* at UNM where -

i. voltage is measured by using a capacitive voltage divider mounted upstream in the oil section from the edge of the cathode.

ii. the cathode shank is connected to the cathode stalk/holder in the diode region and an explosive annular graphite cathode in connected to the cathode shank.

iii. a Rogowski coil is placed in the middle of the cathode shank holder and the explosive cathode.

iv. the 40 cm-length vacuum tube is surrounded by 9 solenoid coils to provide a uniform magnetic field.

v. the graphite cathode is immersed inside the vacuum.

(c) fixing the position (r, z) of the outer cathode with actual parameters used in experiments on Sthe INUS-6 electron beam accelerator.

(d) applying voltage ranging from 100 kV - 600 kV.

(e) applying uniform magnetic field ranging from 0.5 T, 1 T, 2 T, 3 T in analytical, simulation, and experimental work.

(f) applying an infinite magnetic field in simulation in order to align with theoretical hypothesis.

(g) varying inner cathode's radius radially with respect to the outer cathode's radius.

(h) varying inner cathode's length axially with respect to the outer cathode's length.

(i) an empirical strategy is followed in this case to find out the exact length.

5. An optimal geometry to obtain energy difference can be identified for -

(a) a fixed radius of the outer cathode.

(b) the position of the radius of the inner cathode is less than the radius of the outer cathode.

(c) the axial length of the inner cathode must be greater than the axial length of the outer cathode to achieve a minimum % of energy difference.

(d) the axial length of the inner cathode needs to be at least 15% increased from the fixed axial length of the outer cathode.

6. PIC simulation results show that the outer beam space charge screens the space charge of the inner beam, and in that case, a comparable current with 10% energy difference can be achieved when two beams are radially close to each other and axially inner beam is longer than the outer beam. A detailed result can be seen in Table 4.3 and 4.4 for the case of $r_{ic} = \frac{3}{4} r_{oc}$.

7. Analytical and simulation results agree well with one another *cf.* in Table 6.1.

7.2 Future work

The methodology presented here can be extended to generate three or more nested beams from a single cathode stalk at a single potential. The analytical derivation needs to be expanded for the possibility of more than two beams to be used. In addition, finding an analytical theory of axial length dependency of the geometry of the problem needs to be studied.

Because of the limited time, it was not feasible to complete the experimental work. The experimental steps described in Section 5.3 should be performed or repeated thoroughly in order to measure the electron beam current, current density, and energy from each beam separately in experiment. In this case, a qualitative and quantitative approach will be used to validate the analytical and simulation results.

Most HPM devices use annular explosive emission cathodes or tubular electron beams [118] in experiments. We attempted to perform simulations with different shapes of cathodes in the CST PIC solver. The goal was to check if these cathodes can potentially produce two beams, as can be seen in Table B.1 in appendix B. These simulations were performed using a 3D explosive emission model environment by applying a negative cathode potential immersed in an axially uniform magnetic field of about 1 T. No significant energy difference was found in the electron beams in these simulations. In addition, CST Particle Studio takes a very long time to perform the 3D simulations. To further understand the problem, we moved to the MAGIC PIC code to study the two-beam-producing cathode geometries and the characteristics of the resultant beams in a drift tube. In the end, we selected the two annular emitters (second entry in the Table B.1) as two nested MICDs to pursue in analytical calculations, PIC simulations, and experiments. Revisiting these different cathodes in CST or performing simulations in another benchmark software would be worthwhile in the future.

In addition to using these several shaped cathodes, most HPM devices also use cylindrical or toroidal drift spaces in experiments [119]. Thus, the need for developing analytics corresponding to more than one dimension may be necessary. The mathematical derivation or analysis for the MICDs for momentum distribution $p_\theta \neq 0$ is very difficult to analyze. The author had attempted to see if there is any significant contribution of the momentum or energy in the ρ and θ direction (*cf.* in Fig. B.1). Considering 3D in the analytical derivation exceeds the scope of this dissertation. However, the MAGIC 3D PIC simulation results are consistent with MAGIC 2D and the analytical results. Self-consistently solving Poisson's equation for in 3D is a complicated process and requires a numerical approach or computer simulations [120].

Considering a very thin annular beam is one of the essential assumptions for the

geometry of the problem. The thickness of the beam must be much less than both the beam radius and the gap between the outer radius of the cathode and the inner radius of the anode. Both analytical and simulation results suggest that there might be a rational relation between the radius of the MICDs, the axial length of the MICDs (including both cathodes), and the gap between the outer radius of MICDs to the inner radius of the anode/drift tube. Finding this relationship in terms of using two or multiple beams in HPM devices could be a great invention.

In experiments using the SINUS-6 electron beam accelerator, a high magnetic field strength of 2-3 T is typically used, so self-magnetic field can be considered as negligible. The strong magnetic field regarding MICDs and the electrons emitted from graphite cathode (i.e., poco) allow 1D electron flows in the drift tube. Previous experimental results from Andreev [116] show significant contribution by the SCL current and this rise of limiting current could be a concern. It is now known since over a almost a century that there is a maximum current that can pass through a vacuum pipe in either the relativistic or nonrelativistic regime [105], [106]. This limiting current is known as the SCL current. If the beam current is less than the SCL current, the beam becomes laminar and then there are two possible solutions corresponding to high velocity and low density [121]. For the case when the beam current is greater than the SCL current, there is no solution found yet [57]. It has been shown that the existence of the steady state flow of current exceeding the SCL limited current (I_{SCL}) is not possible [99]. In the case of electron beam current greater than SCL current, a virtual cathode would form in front of the source cathode [122]. This virtual cathode leads to reduced emitted current from the cathode while injected current increases [123]. The virtual cathode is a point where a fraction of the beam comes to rest and introduces instability in the beam [124]. Knowledge of the SCL current is required to measure accurately in many high frequency electron beam devices or any vacuum electron devices (VEDs), plasma produced devices, and HPM

devices [125]. To generate HPM, the community uses electron beams with high voltage and high current. Therefore, relativistic effects must be considered in terms of the SCL current.

Appendix A

To obtain the equation for the outer electron beam current in the plane $z = z_2$, we find the potential difference of the outer beam - anode gap and the outer beam - inner cathode gap in the plane $z = z_2$. We assume $r_h = r_{ob} = r_o$, where ob =outer beam. Therefore, the potential difference across the outer beam - anode gap in the plane $z = z_2$ is given by

$$\phi_a - \phi_h = -\int_{r_h}^{r_a} E_{r2_{(h+)}} dr = \frac{I_{h+}}{2\pi\epsilon_0\ v_h} \ln\left({}^{r_a}/_{r_h}\right) = \frac{I_{h+}}{2\pi\epsilon_0 v_h} \ln\left({}^{r_a}/_{r_o}\right). \tag{A.1}$$

The potential difference across the outer beam - inner cathode gap in the plane $z = z_2$ is given by

$$\phi_i - \phi_h = -\int_{r_h}^{r_i} E_{r2_{(h-)}} dr = \frac{I_{h-}}{2\pi\epsilon_0 v_h} \ln\left({}^{r_i}/_{r_h}\right) = \frac{I_{h-}}{2\pi\epsilon_0 v_h} \ln\left({}^{r_i}/_{r_o}\right). \tag{A.2}$$

We have

$$\phi_a = \frac{c^2}{\eta}(\gamma_a - 1) \tag{A.3}$$

and

$$\phi_h = \frac{c^2}{\eta}(\gamma_h - 1). \tag{A.4}$$

The relativistic mass is given by

$$m = \frac{m_e}{\sqrt{1 - \frac{v^2}{c^2}}}. \tag{A.5}$$

Here $\gamma = \frac{m}{m_e}$ and

$$v = \frac{c}{\gamma}\sqrt{\gamma^2 - 1}. \tag{A.6}$$

We will also need the relativistic momentum equation

$$p = mc\sqrt{\gamma^2 - 1}. \tag{A.7}$$

From Eq. A.6, we have the outer beam velocity in the γ_h region as

$$v_h = \frac{c}{\gamma_h}\sqrt{\gamma_h^2 - 1}. \tag{A.8}$$

We now utilize Eqs. A.3, A.4, A.8 in Eqs. A.1 and A.2 and our goal is find the total current I_h for the outer electron beam in the plane $z = z_2$.

Hence, from Eq. (A.1),

$$I_{h+} = \frac{2\pi\epsilon_0\ c^3}{\eta}\frac{(\gamma_a - \gamma_h)(\sqrt{\gamma_h^2 - 1})}{\gamma_h\ \ln\left(r_a/r_o\right)}. \tag{A.9}$$

Equation A.9 is similar to Fedosov's beam current equation for a single MICD [26].

Similarly, from Eq. A.2, where we assume the potential of the inner cathode $\phi_i = 0$, we obtain

$$I_{h-} = \frac{2\pi\epsilon_0\ c^3}{\eta}\frac{(\gamma_h - 1)(\sqrt{\gamma_h^2 - 1})}{\gamma_h\ \ln\left(r_o/r_i\right)}. \tag{A.10}$$

We now can calculate the total current $I_h = I_{h+} - I_{h-}$ in the plane $z = z_2$, which is

given as

$$I_h = I_{h+} - I_{h-} \tag{A.11}$$

$$\Rightarrow I_h = \frac{2\pi\epsilon_0\ c^3(\sqrt{\gamma_h^2 - 1})}{\eta\gamma_h}\left[\frac{(\gamma_a - \gamma_h)}{\ln\left({}^{r_a}/_{r_o}\right)} - \frac{(\gamma_h - 1)}{\ln\left({}^{r_o}/_{r_i}\right)}\right]. \tag{A.12}$$

Multiplying both sides of Eq. A.12 by $\ln\left({}^{r_a}/_{r_i}\right)$ we obtain

$$\Rightarrow I_h \ln\left({}^{r_a}/_{r_i}\right) = \frac{2\pi\epsilon_0\ c^3(\sqrt{\gamma_h^2 - 1})}{\eta\gamma_h}\left[\frac{(\gamma_a - \gamma_h)}{\ln\left({}^{r_a}/_{r_o}\right)} - \frac{(\gamma_h - 1)}{\ln\left({}^{r_o}/_{r_i}\right)}\right]\ln\left({}^{r_a}/_{r_i}\right). \tag{A.13}$$

For simplicity, assume that the geometrical factor g is given by

$$g = \frac{\ln\left({}^{r_o}/_{r_i}\right)}{\ln\left({}^{r_a}/_{r_i}\right)} \tag{A.14}$$

and

$$\frac{1}{g} = \frac{\ln\left({}^{r_a}/_{r_i}\right)}{\ln\left({}^{r_o}/_{r_i}\right)}. \tag{A.15}$$

Therefore,

$$1 - g = 1 - \frac{\ln\left({}^{r_o}/_{r_i}\right)}{\ln\left({}^{r_a}/_{r_i}\right)} = \frac{\ln\left({}^{r_a}/_{r_i}\right) - \ln\left({}^{r_o}/_{r_i}\right)}{\ln\left({}^{r_a}/_{r_i}\right)} = \frac{\ln\left({}^{r_a}/_{r_o}\right)}{\ln\left({}^{r_a}/_{r_i}\right)} \tag{A.16}$$

and

$$\frac{1 - g}{g} = \frac{\frac{\ln({}^{r_a}/_{r_o})}{\ln({}^{r_a}/_{r_i})}}{\frac{\ln({}^{r_o}/_{r_i})}{\ln({}^{r_a}/_{r_i})}} = \frac{\ln\left({}^{r_a}/_{r_o}\right)}{\ln\left({}^{r_o}/_{r_i}\right)}. \tag{A.17}$$

Hence, from Eq. A.13,

$$\Rightarrow I_h \ln\left({}^{r_a}/_{r_i}\right) = \frac{2\pi\epsilon_0\ c^3(\sqrt{\gamma_h^2 - 1})}{\eta\gamma_h}\left[\frac{(\gamma_a - \gamma_h)}{\frac{\ln({}^{r_a}/_{r_o})}{\ln({}^{r_a}/_{r_i})}} - \frac{(\gamma_h - 1)}{\frac{\ln({}^{r_o}/_{r_i})}{\ln({}^{r_a}/_{r_i})}}\right]$$

$$\Rightarrow I_h = \frac{2\pi\epsilon_0 c^3 \left(\sqrt{\gamma_h^2 - 1}\right)}{\eta\gamma_h \ln\left(r_a/r_i\right)} \left[\frac{\gamma_a - \gamma_h}{1-g} - \frac{\gamma_h - 1}{g}\right]. \tag{A.18}$$

γ_h is the unknown in Eq. A.18.

We will now find the equation for γ_h in the plane $z = z_2$. We integrate over the volume between radii r_i and r_a and cross-sections z_1 and z_2 and apply conservation of momentum in the z direction for the system [2] in Fig. 3.6 to obtain

$$\int_{r_i}^{r_a} E_{r1}^2 r dr - \int_{r_i}^{r_a} E_{r2}^2 r dr = \frac{I_h p_h}{\pi e_0 \epsilon_0} \tag{A.19}$$

$$\Rightarrow \int_{r_o}^{r_a} E_{r1}^2 r dr - \int_{r_o}^{r_a} E_{r2}^2 r dr - \int_{r_i}^{r_o} E_{r2}^2 r dr = \frac{I_h p_h}{\pi e_0 \epsilon_0} \tag{A.20}$$

$$\Rightarrow \frac{\phi_a^2}{ln\left(r_a/r_o\right)} - \left(\frac{I_{h+}}{2\pi\epsilon_0 v_h}\right)^2 ln\left(r_a/r_o\right) - \left(\frac{I_{h-}}{2\pi\epsilon_0 v_h}\right)^2 ln\left(r_o/r_i\right) = \frac{I_h p_h}{\pi e_0 \epsilon_0}. \tag{A.21}$$

Replacing ϕ_a from Eq. A.3, v_h from Eq. A.8, I_{h+} from Eq. A.9, and I_{h-} from Eq. A.10 inserting into the LHS of Eq. A.21 yields

$$\text{LHS} = \frac{c^4(\gamma_a - 1)^2}{\eta^2 \ln\left(r_a/r_o\right)} - \frac{c^4(\gamma_a - \gamma_h)^2}{\eta^2 \ln\left(r_a/r_o\right)} - \frac{c^4 (\gamma_h - 1)^2}{\eta^2 \ln\left(r_o/r_i\right)}. \tag{A.22}$$

We will now work on the RHS by replacing I_h from Eq. A.18 and p_h from Eq. A.7 to obtain

$$\text{RHS} = \frac{2c^4(\gamma_h^2 - 1)}{\eta^2\gamma_h \ln(r_a/r_i)} \left[\frac{\gamma_a - \gamma_h}{1-g} - \frac{\gamma_h - 1}{g}\right]. \tag{A.23}$$

Finally, we equate LHS = RHS and multiply both sides of Eqs. A.22 and A.23 by $\frac{\eta^2}{c^4}$

and $\ln(r_a/r_o)$ to obtain

$$(\gamma_a-1)^2-(\gamma_a-\gamma_h)^2-(\gamma_h-1)^2\frac{1-g}{g}=\frac{2(\gamma_h^2-1)}{\gamma_h}\left[\frac{\gamma_a-\gamma_h}{1-g}-\frac{\gamma_h-1}{g}\right](1-g). \quad \text{(A.24)}$$

The solution of the quadratic (Equation A.24) is obtained by using the software PTC Mathcad Prime 6.0.0.0:

$$\gamma_h=\begin{bmatrix} 1 \\ \frac{\sqrt{(8\gamma_a-8)g+9}-1}{2} \\ -\frac{\sqrt{(8\gamma_a-8)g+9}-1}{2} \end{bmatrix} \quad \text{(A.25)}$$

which yields the solution for γ_h (where $\gamma_h > 1$)

$$\gamma_h=\frac{\sqrt{(8\gamma_a-8)g+9}-1}{2}. \quad \text{(A.26)}$$

If we use γ_h in Eq. A.18, we obtain the equation for the outer electron beam current with all variables known. We know the current remains the same in the system and, therefore, we will use this known current equation to solve the equations far away from the cathode in the plane $z = z_3$.

The jump in the electric field from the inner beam to the outer beam in the plane $z = z_3$ is given by

$$E_{r3_{(ob+)}}=\frac{q_{ob+}}{2\pi r\epsilon_0}=-\frac{I_{ob+}}{2\pi r v_o\epsilon_0}. \quad \text{(A.27)}$$

The jump in the electric field from the outer beam to the inner beam in the plane $z = z_3$ is given by

$$E_{r3_{(ob-)}}=\frac{q_{ob-}}{2\pi r\epsilon_0}=-\frac{I_{ob-}}{2\pi r v_o\epsilon_0}. \quad \text{(A.28)}$$

The potential difference across the outer beam - anode gap is given by

$$\phi_a - \phi_{ob} = -\int_{r_{ob}}^{r_a} E_{r3_{(ob+)}} dr = \frac{I_{ob+}}{2\pi\epsilon_0 v_o} \ln\left({}^{r_a}/_{r_{ob}}\right). \tag{A.29}$$

The potential difference across the outer beam - inner beam gap is given by

$$\phi_{ob} - \phi_{ib} = -\int_{r_{ib}}^{r_{ob}} E_{r3_{(ob-)}} dr = \frac{I_{ob-}}{2\pi\epsilon_0 v_o} \ln\left({}^{r_{ob}}/_{r_{ib}}\right). \tag{A.30}$$

To simplify the notation we assume $\phi_{ob} = \phi_o$, $\phi_{ib} = \phi_i$, $I_{ob} = I_o$, $r_{ob} = r_o$, and $r_{ib} = r_i$.

We now replace ϕ_a and ϕ_o from Eq. A.3 and v_o from Eq. A.6 and we use them in Eq. A.29 to obtain the equation for current $I_{(o+)} = I_{ob}$ from the outer electron beam far away from the outer cathode in the plane $z = z_3$

$$I_{o+} = \frac{2\pi\epsilon_0 c^3}{\eta} \frac{\sqrt{\gamma_o^2 - 1}(\gamma_a - \gamma_o)}{\gamma_o \ \ln\left({}^{r_a}/_{r_o}\right)}. \tag{A.31}$$

Similarly, Eq. A.30 gives us

$$I_{o-} = \frac{2\pi\epsilon_0 c^3}{\eta} \frac{\sqrt{\gamma_o^2 - 1}(\gamma_o - \gamma_i)}{\gamma_o \ \ln\left({}^{r_o}/_{r_i}\right)}. \tag{A.32}$$

Now, the total current $I_o = I_{o+} - I_{o-}$ is given by

$$I_o = \frac{2\pi\epsilon_0 c^3(\sqrt{\gamma_o^2 - 1})}{\eta\gamma_o} \left[\frac{(\gamma_a - \gamma_o)}{\ln\left({}^{r_a}/_{r_o}\right)} - \frac{(\gamma_o - \gamma_i)}{\ln\left({}^{r_o}/_{r_i}\right)}\right]. \tag{A.33}$$

Multiply both sides of Eq. A.33 by $\ln\left({}^{r_a}/_{r_i}\right)$ to obtain

$$\Rightarrow I_o \ \ln\left({}^{r_a}/_{r_i}\right) = \frac{2\pi\epsilon_0 c^3(\sqrt{\gamma_o^2 - 1})}{\eta\gamma_o} \left[\frac{(\gamma_a - \gamma_o)}{\ln\left({}^{r_a}/_{r_o}\right)} - \frac{(\gamma_o - \gamma_i)}{\ln\left({}^{r_o}/_{r_i}\right)}\right] \ln\left({}^{r_a}/_{r_i}\right). \tag{A.34}$$

Using Eqs. A.14 and A.16 in Eq. A.34 yields

$$I_o = \frac{2\pi\epsilon_0 c^3}{\eta\ \ln\left(r_a/r_i\right)} \frac{\sqrt{\gamma_o^2 - 1}}{\gamma_o} \left[\frac{\gamma_a - \gamma_o}{1-g} - \frac{\gamma_o - \gamma_i}{g}\right]. \tag{A.35}$$

This equation for current I_o is our desired solution for the outer electron beam current in the system at $z = z_3$.

In a manner similar to finding the outer electron beam current solution, we will now find the solution for the inner electron beam current $I_{ib} = I_i$ in the same plane $z = z_3$. The electric field in the plane $z = z_3$ for the inner beam is given by

$$E_{r3_{(ib)}} = \frac{q_{ib}}{2\pi r\epsilon_0} = -\frac{I_{ib}}{2\pi r v_{ib}\epsilon_0} = -\frac{I_i}{2\pi r v_i \epsilon_0}. \tag{A.36}$$

The potential difference across the outer beam - inner beam gap is given by

$$\phi_o - \phi_i = -\int_{r_i}^{r_o} E_{r3} dr = \frac{I_i}{2\pi\epsilon_0 v_i} \ln\left(r_o/r_i\right) \tag{A.37}$$

$$I_i = \frac{2\pi\epsilon_0 c^3}{\eta\ \ln(r_o/r_i)} \frac{\left(\sqrt{\gamma_i^2 - 1}\right)(\gamma_o - \gamma_i)}{\gamma_i}. \tag{A.38}$$

Multiplying Eq. A.38 by both sides by $\ln(r_a/r_i)$ yields

$$I_i\ \ln(r_a/r_i) = \frac{2\pi\epsilon_0 c^3}{\eta\ \ln(r_o/r_i)} \frac{\sqrt{\gamma_i^2 - 1}}{\gamma_i} (\gamma_o - \gamma_i) \ln(r_a/r_i). \tag{A.39}$$

Using $g = \frac{\ln(r_o/r_i)}{\ln(r_a/r_i)}$ Eq. A.39 becomes

$$I_i = \frac{2\pi\epsilon_0 c^3}{\eta\ \ln(r_a/r_i)} \frac{\sqrt{\gamma_i^2 - 1}}{\gamma_i} \frac{(\gamma_o - \gamma_i)}{g}. \tag{A.40}$$

This equation for current I_i is our desired solution for the inner electron beam current

in the system at $z = z_3$.

We have two unknowns (γ_o and γ_i) in the equations for I_o and I_i. Therefore, we should now focus on finding the relativistic factor at the external boundaries for both the inner and outer electron beams in the drift tube. We integrate over the volume between radii r_i and r_a and cross-sections $z = z_1$ and $z = z_3$ and apply conservation of momentum in the z direction for the system [2] shown in Fig. 3.6 to obtain

$$\int_{r_i}^{r_a} E_{r1}^2 r dr - \int_{r_i}^{r_a} E_{r3}^2 r dr = \frac{p_o I_o + p_i I_i}{\pi e_0 \epsilon_0}. \tag{A.41}$$

In order to solve Eq. A.41, let us solve the LHS first by replacing E_{r1} and E_{r3} using Eqs. 3.74, A.27, A.28 to obtain

$$\text{LHS} = \int_{r_o}^{r_a} E_{r1}^2 r dr - \int_{r_o}^{r_a} E_{r3}^2 r dr - \int_{r_i}^{r_o} E_{r3}^2 r dr \tag{A.42}$$

$$\text{LHS} = \left(\frac{\phi_a}{\ln(r_a/r_o)}\right)^2 \ln(r_a/r_o) - \left(\frac{I_{o+}}{2\pi\epsilon_0 v_o}\right)^2 \ln(r_a/r_o) - \left(\frac{I_i}{2\pi\epsilon_0 v_i}\right)^2 \ln(r_o/r_i). \tag{A.43}$$

Using $\phi_a = \frac{c^2}{\eta}(\gamma_a - 1)$ from Eq. A.3, $v = \frac{c}{\gamma}\sqrt{\gamma^2 - 1}$ from Eq. A.6, I_{o+} from Eq. A.31, and I_i from Eq. A.40 in Eq. A.43, we obtain

$$\Rightarrow \text{LHS} = \frac{c^4}{\eta^2}\frac{(\gamma_a - 1)^2}{\ln(r_a/r_o)} - \left[\frac{2\pi\epsilon_0 c^3}{\eta\ 2\pi\epsilon_0\ \frac{c}{\gamma_o}\sqrt{\gamma_o^2 - 1}}\frac{\sqrt{\gamma_o^2 - 1}(\gamma_a - \gamma_o)}{\gamma_o\ \ln(r_a/r_o)}\right]^2 \ln(r_a/r_o) - \left[\frac{2\pi\epsilon_0 c^3}{\eta\ 2\pi\epsilon_0\ \frac{c}{\gamma_i}\sqrt{\gamma_i^2 - 1}}\frac{\sqrt{\gamma_i^2 - 1}(\gamma_o - \gamma_i)}{\gamma_i\ \ln(r_o/r_i)}\right]^2 \ln(r_o/r_i) \tag{A.44}$$

$$\Rightarrow \text{LHS} = \frac{c^4}{\eta^2}\frac{(\gamma_a - 1)^2}{\ln(r_a/r_o)} - \frac{c^4}{\eta^2}\frac{(\gamma_a - \gamma_o)^2}{\ln(r_a/r_o)} - \frac{c^4}{\eta^2}\frac{(\gamma_o - \gamma_i)^2}{\ln(r_o/r_i)}. \tag{A.45}$$

Next we will solve the RHS of Eq. A.41 by replacing $p_o = m_o\gamma_o v_o = m_e c\sqrt{\gamma_o^2 - 1}$ and $p_i = m_o\gamma_i v_i = m_e c\sqrt{\gamma_i^2 - 1}$ from Eq. A.7, and I_o, I_i from Eqs. A.35 and A.40, respectively, to obtain

$$\text{RHS} = \frac{2\pi m_e \epsilon_0 c^4}{\eta\pi e_0\epsilon_0 \ \ln(r_a/r_i)}\left[\frac{(\gamma_o^2-1)}{\gamma_o}\left(\frac{\gamma_a-\gamma_o}{1-g} - \frac{\gamma_o-\gamma_i}{g}\right) + \frac{(\gamma_i^2-1)}{\gamma_i}\frac{(\gamma_o-\gamma_i)}{g}\right]. \tag{A.46}$$

Equating Eqs. A.45 and A.46 we obtain

$$\Rightarrow \frac{c^4}{\eta^2}\frac{(\gamma_a-1)^2}{\ln(r_a/r_o)} - \frac{c^4}{\eta^2}\frac{(\gamma_a-\gamma_o)^2}{\ln(r_a/r_o)} - \frac{c^4}{\eta^2}\frac{(\gamma_o-\gamma_i)^2}{\ln(r_o/r_i)} = \frac{2c^4}{\eta^2 \ \ln(r_a/r_i)}\left[\frac{(\gamma_o^2-1)}{\gamma_o}\left(\frac{\gamma_a-\gamma_o}{1-g} - \frac{\gamma_o-\gamma_i}{g}\right) + \frac{(\gamma_i^2-1)}{\gamma_i}\frac{(\gamma_o-\gamma_i)}{g}\right]. \tag{A.47}$$

Multiply both sides of Eq. A.47 by $\frac{\eta^2}{c^4}$ and $\ln(r_a/r_o)$, replace $\frac{1-g}{g} = \frac{\ln(r_a/r_o)}{ln(r_o/r_i)}$ using Eq. A.17, and using $1-g = \frac{\ln(r_a/r_o)}{\ln(r_a/r_i)}$ yields

$$\Rightarrow (\gamma_a-1)^2 - (\gamma_a-\gamma_o)^2 - (\gamma_o-\gamma_i)^2\frac{1-g}{g} = 2\left[\frac{(\gamma_o^2-1)}{\gamma_o}\left(\frac{\gamma_a-\gamma_o}{1-g} - \frac{\gamma_o-\gamma_i}{g}\right) + \frac{(\gamma_i^2-1)}{\gamma_i}\frac{(\gamma_o-\gamma_i)}{g}\right](1-g). \tag{A.48}$$

In summary, we have the following system of equations in Eqs. (A.49, A.50, A.51, A.52, and A.54) to be solved:

$$I_h = \frac{2\pi\epsilon_0 c^3\left(\sqrt{\gamma_h^2-1}\right)}{\eta\gamma_h \ln(r_a/r_i)}\left[\frac{\gamma_a-\gamma_h}{1-g} - \frac{\gamma_h-1}{g}\right], \tag{A.49}$$

$$I_o = \frac{2\pi\epsilon_0 c^3}{\eta\ \ln\left({}^{r_a}/_{r_i}\right)} \frac{\sqrt{\gamma_o^2 - 1}}{\gamma_o} \left[\frac{\gamma_a - \gamma_o}{1-g} - \frac{\gamma_o - \gamma_i}{g}\right], \tag{A.50}$$

$$I_i = \frac{2\pi\epsilon_0 c^3}{\eta\ \ln({}^{r_a}/_{r_i})} \frac{\sqrt{\gamma_i^2 - 1}}{\gamma_i} \frac{(\gamma_o - \gamma_i)}{g}, \tag{A.51}$$

$$(\gamma_a - 1)^2 - (\gamma_a - \gamma_h)^2 - (\gamma_h - 1)^2 \frac{1-g}{g} = \frac{2(\gamma_h^2 - 1)}{\gamma_h} \left[\frac{\gamma_a - \gamma_h}{1-g} - \frac{\gamma_h - 1}{g}\right](1-g), \tag{A.52}$$

$$\gamma_h = \frac{\sqrt{(8\gamma_a - 8)g + 9} - 1}{2}, \tag{A.53}$$

$$\Rightarrow (\gamma_a - 1)^2 - (\gamma_a - \gamma_o)^2 - (\gamma_o - \gamma_i)^2 \frac{1-g}{g} = 2\left[\frac{(\gamma_o^2 - 1)}{\gamma_o}\left(\frac{\gamma_a - \gamma_o}{1-g} - \frac{\gamma_o - \gamma_i}{g}\right) + \frac{(\gamma_i^2 - 1)}{\gamma_i}\frac{(\gamma_o - \gamma_i)}{g}\right](1-g). \tag{A.54}$$

We know that the current remains same in the system. Thus, the equation of the current I_h for the outer electron beam in the plane $z = z_2$ and the equation of the current I_o for the outer electron beam in the plane $z = z_3$ are equal. Therefore, by equating $I_h = I_o$, we obtain

$$\frac{2\pi\epsilon_0 c^3 \left(\sqrt{\gamma_h^2 - 1}\right)}{\eta \ln\left({}^{r_a}/_{r_i}\right)\gamma_h} \left[\frac{\gamma_a - \gamma_h}{1-g} - \frac{\gamma_h - 1}{g}\right] = \frac{2\pi\epsilon_0 c^3}{\eta\ \ln\left({}^{r_a}/_{r_i}\right)} \frac{\sqrt{\gamma_o^2 - 1}}{\gamma_o} \left[\frac{\gamma_a - \gamma_o}{1-g} - \frac{\gamma_o - \gamma_i}{g}\right]. \tag{A.55}$$

By removing the constant term from both sides of Eq. A.55, we have

$$\frac{\sqrt{\gamma_h^2-1}}{\gamma_h}\left[\frac{\gamma_a-\gamma_h}{1-g}-\frac{\gamma_h-1}{g}\right]=\frac{\sqrt{\gamma_o^2-1}}{\gamma_o}\left[\frac{\gamma_a-\gamma_o}{1-g}-\frac{\gamma_o-\gamma_i}{g}\right]. \tag{A.56}$$

Now substituting the solution of γ_h from Eq. A.53 in Eq. A.56 yields

$$\frac{\sqrt{(8\gamma_a-8)g+9}+((2-2\gamma_a)g-3)\sqrt{-(2\sqrt{(8\gamma_a-8)g+9}+(8\gamma_a-8)g+6)}}{2(\sqrt{(8\gamma_a-8)g+9}-1)} = \frac{((\gamma_i-\gamma_a)g+(\gamma_o-\gamma_i))\sqrt{(\gamma_o-1)(\gamma_o+1)}}{\gamma_o}. \tag{A.57}$$

Let us assume that the LHS of Eq. A.57 is a constant as all variables are known here. Thus assume,

$$\frac{\left(\sqrt{(8\gamma_a-8)g+9}+(2-2\gamma_a)g-3\right)\sqrt{-2\sqrt{(8\gamma_a-8)g+9}+(8\gamma_a-8)g+6}}{2\left(\sqrt{(8\gamma_a-8)g+9}-1\right)}=C \tag{A.58}$$

where $\gamma_a = 1+\frac{\eta\phi_a}{c^2}$ and $g=\frac{\ln(r_o/r_i)}{\ln(r_a/r_i)}$.

Therefore, Eq. A.57 becomes

$$((\gamma_i-\gamma_a)g+(\gamma_o-\gamma_i))\sqrt{(\gamma_o-1)(\gamma_o+1)}-\gamma_o C=0. \tag{A.59}$$

We now have a system of nonlinear equation with two equations (Eqs. A.54 and A.59) in two unknown variables. One equation is linear and one is nonlinear. We solve the system of nonlinear equation using a Matlab solver and obtain the values for γ_o and γ_i, which ultimately determine the current and the energy of the outer and

inner electron beams in the drift tube.

Summary of the steps:

1. Apply boundary $z = z_2$ at the end of the inner cathode.
2. Solve the equation for current of the outer electron beam in the plane $z = z_2$.
3. The outer electron beam current equation has γ_h. To obtain the solution for γ_h, we integrate over the volume between radii r_o and r_a, and the cross-sections z_1 and z_2. Apply conservation of momentum in the z direction for the system.
4. After integration and some math, we obtain the solution for γ_h.
5. We use this γ_h in the expression for the outer electron beam current I_h in the z_2 plane and, thus, the current expression now has all known variables.
6. We follow similar steps to find the outer electron beam current I_{ob} and the inner electron beam current I_{ib} far away from the cathode in the plane $z = z_3$.
7. Both current equations in the plane z_3 have two unknowns γ_o, γ_i. Therefore, to get the solutions for γ_o, γ_i, we integrate over the volume between radii r_o and r_a, and cross-sections z_1 and z_3. Apply the conservation of momentum in the z direction for the system.
8. We now have a total of three equations to solve in the plane $z = z_3$.
9. Each of three equations has at least two unknown variables. So how do we solve these?
10. We know that the current remains the same in the system.
11. Thus, we equate both electron beam currents $I_h = I_o$ in the planes $z = z_2$ and $z = z_3$.

12. We now have a system of equations with two equations in two unknown variables. One equation is linear and one is nonlinear.

13. But this nonlinear system of equations is not possible to solve by using any traditional method. Therefore, we use the Matlab solver to solve the nonlinear system of equations to obtain the solutions for the two unknown variables γ_o and γ_i which ultimately determine the electron beam currents and energies for both beams.

Appendix B

Table B.1: CST modeling of designing two-cathode based model to generate two electron beams with different beam energies.

Proposed dual beam emitters in CST	CST schematic
Solid beam is in the middle and the outside is annular beam	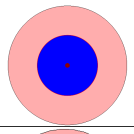
Two annular emitters	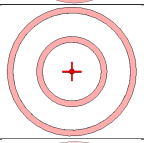
Two solid emitters	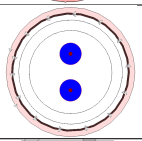
One solid cathode in the middle and another slightly tilted annular beam outside of solid cathode	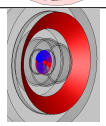
Tuning fork-based with two-emitters	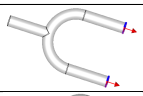
Tuning fork-based with three-emitters	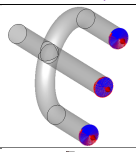
Cathode with half-half diameter (one is slightly smaller than other one)	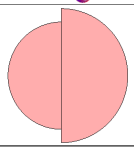

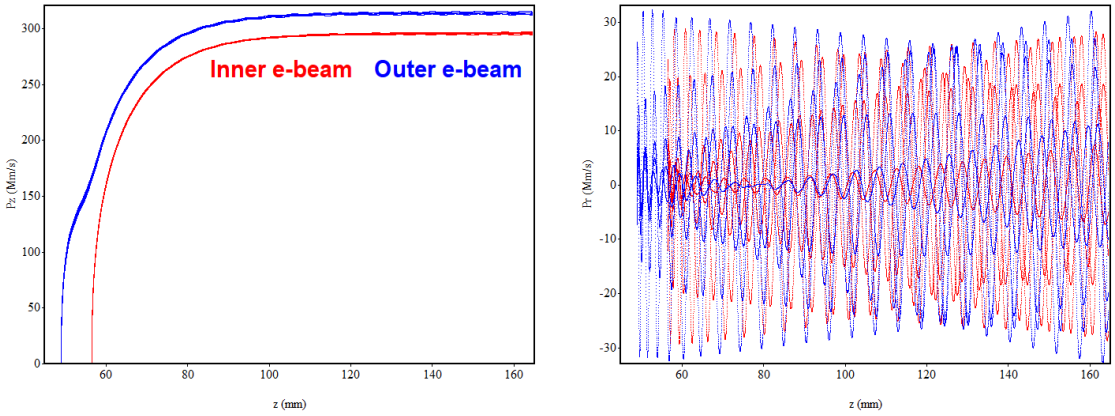

(a) All Particles(z,P_z)

(b) All Particles(z,P_r)

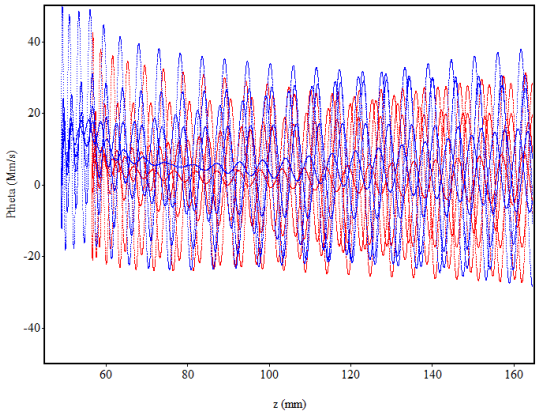

(c) All Particles(z,P_θ)

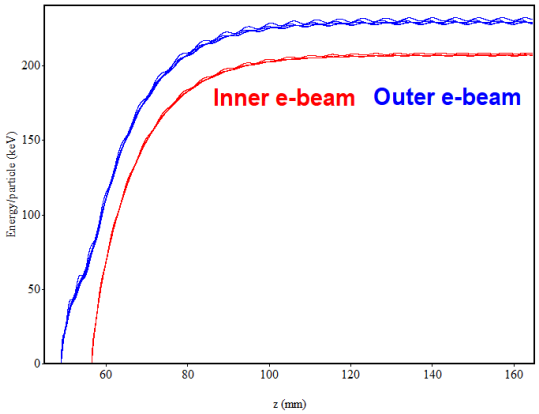

(d) All Particles(z,$E_k(z)$)

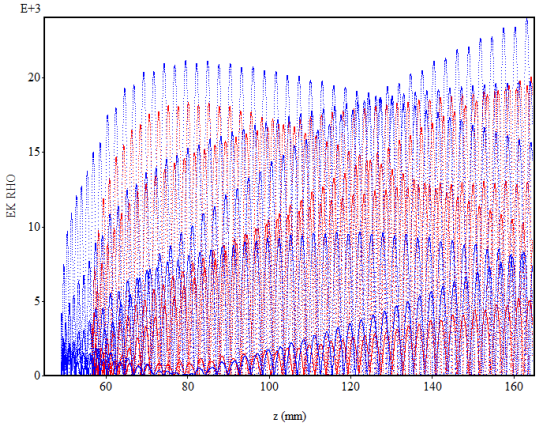

(e) All Particles(z,$E_k(\rho)$)

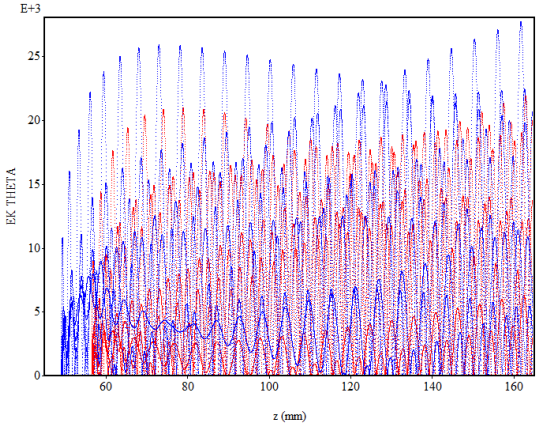

(f) All Particles(z,$E_k(\theta)$)

Figure B.1: MAGIC simulations show (a) momentum of particles in z, (b) momentum of particles in ρ, (c) momentum of particles in θ, (d) energy of particles in z, (b) energy of particles in ρ, and (c) energy of particles in θ.

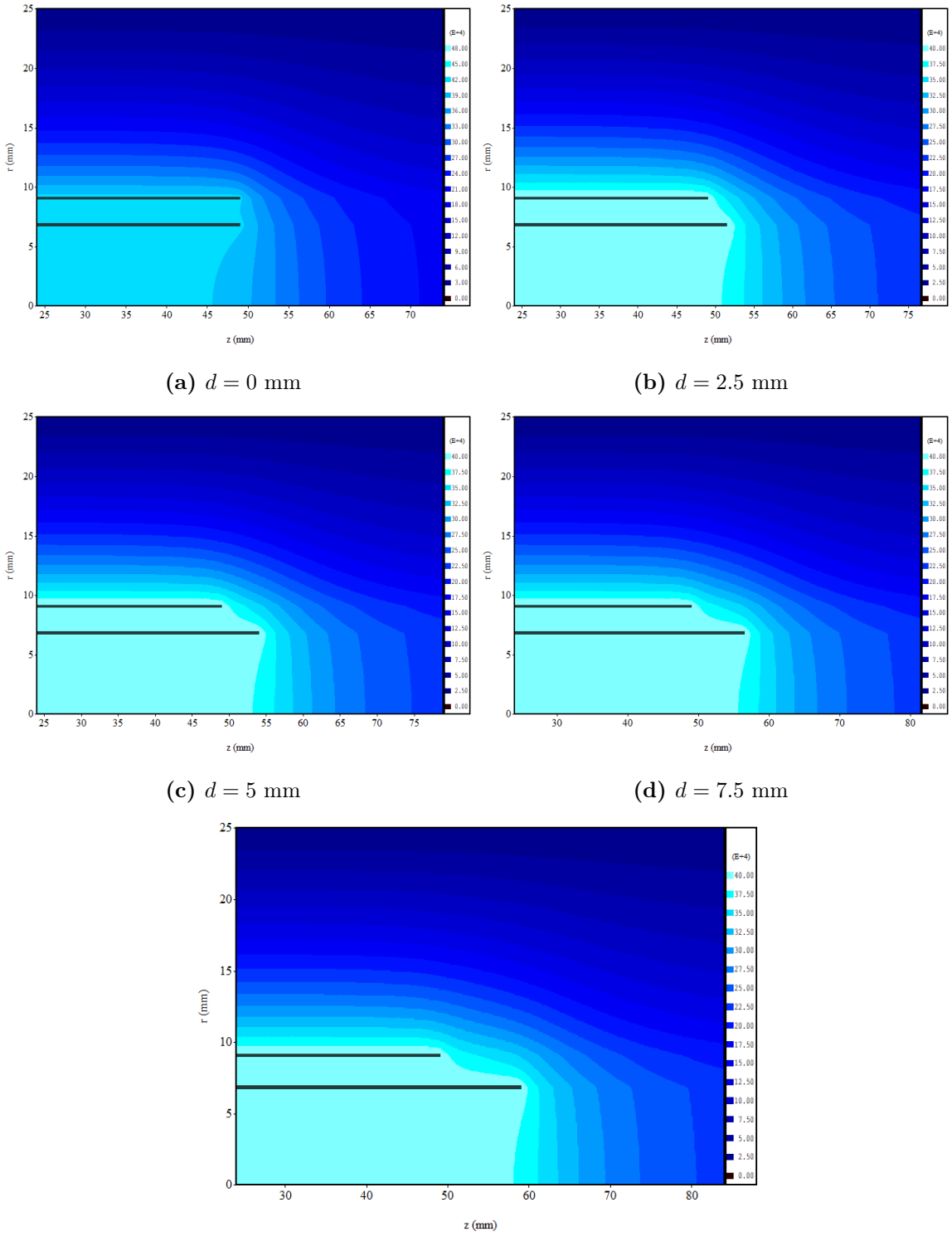

(a) $d = 0$ mm

(b) $d = 2.5$ mm

(c) $d = 5$ mm

(d) $d = 7.5$ mm

(e) $d = 10$ mm

Figure B.2: MAGIC simulations show static electric field contour plot illustrates the accelerating field for (a) d =0 mm, (b) $d = 2.5$ mm, (c) $d = 5$ mm, (d) $d = 7.5$ mm, and (e) $d = 10$ mm.

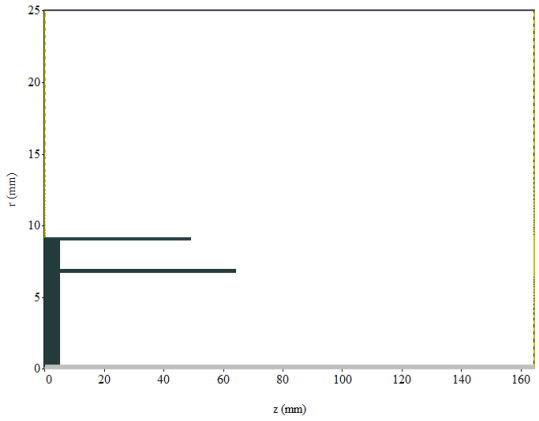

(a) Geometry for d=15 mm

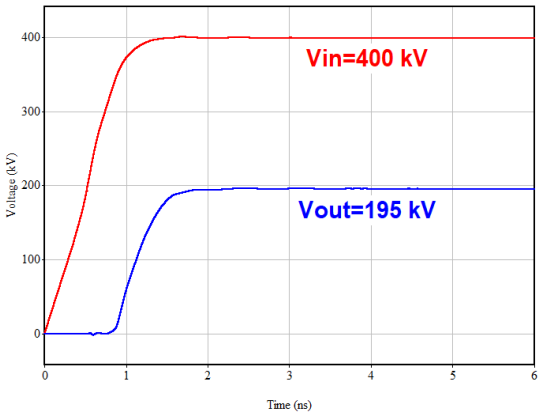

(b) V_{in}, V_{axial}

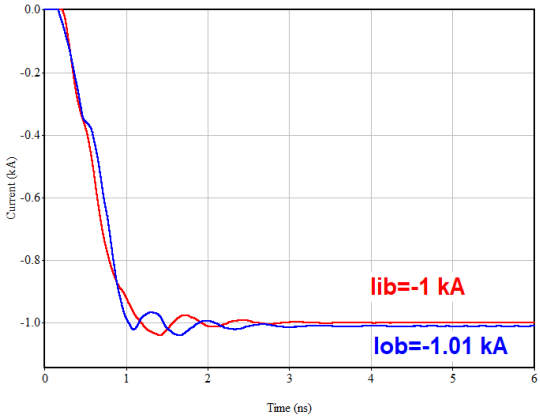

(c) I_{ib}, I_{ob}

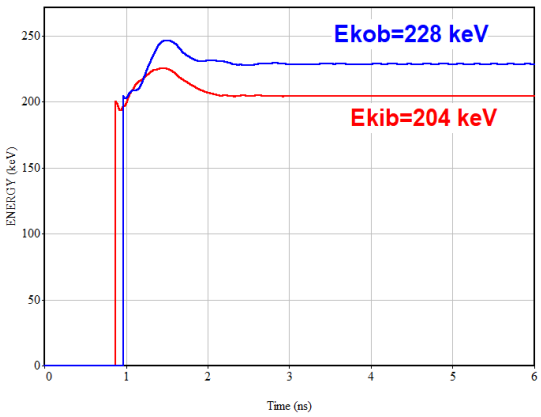

(d) Ek_{ib}, Ek_{ob}

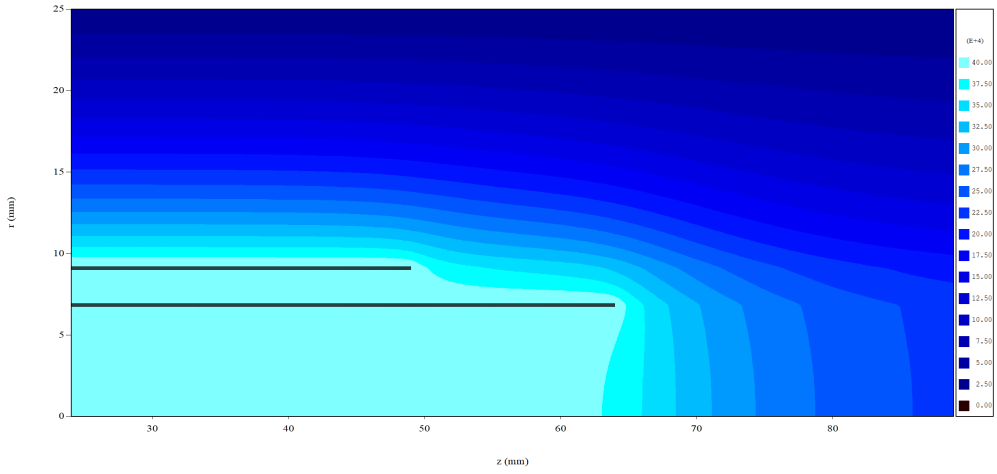

(e) Static electric field contour plot for $d = 15$ mm

Figure B.3: Simulation results of two nested MICDs (a) geometry of the problem, (b) applied (red) and axial (blue) voltages, (c) electron beam currents, (d) electron beam energies, (e) static electric field contour plot illustrates the accelerating field for the radial position of the inner cathode of $\frac{3}{4}$ of the outer cathode's radius and magnetic field strength 2 T.

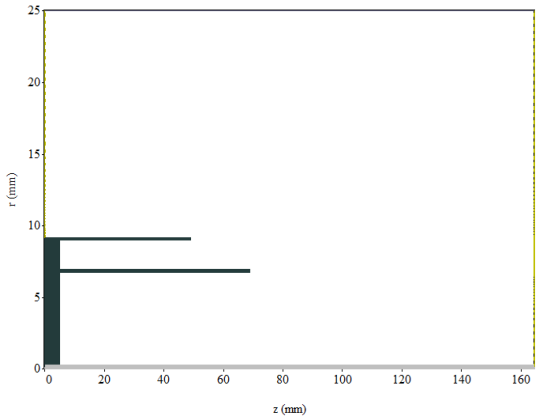

(a) Geometry for $d = 20$ mm

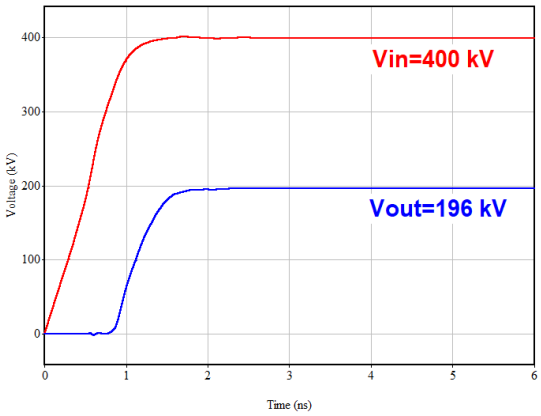

(b) V_{in}, V_{axial}

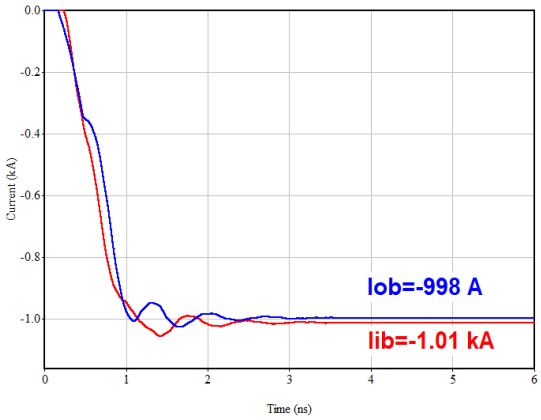

(c) I_{ib}, I_{ob}

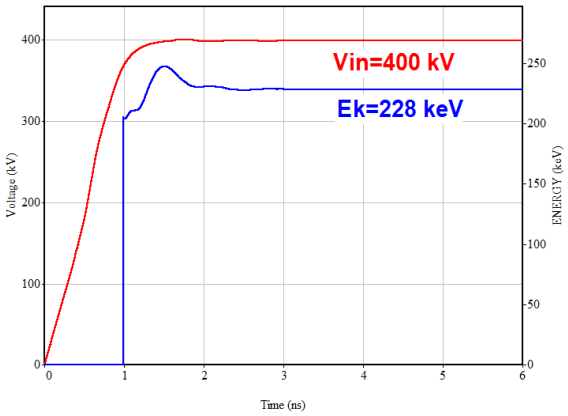

(d) Ek_{ib}, Ek_{ob}

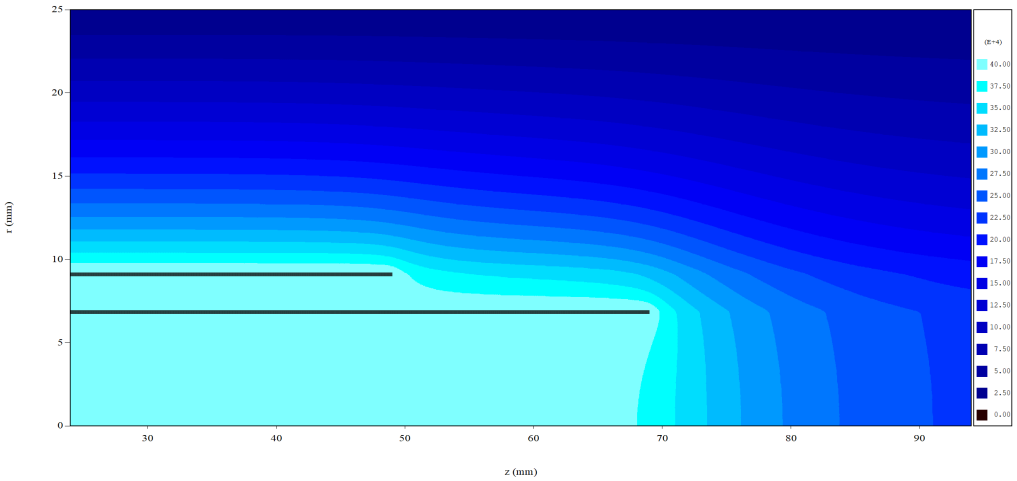

(e) Static electric field contour plot for $d = 20$ mm

Figure B.4: Simulation results of two nested MICDs (a) geometry of the problem, (b) applied (red) and axial (blue) voltages, (c) electron beam currents, (d) electron beam energies, (e) static electric field contour plot illustrates the accelerating field for the radial position of the inner cathode of $\frac{3}{4}$ of the outer cathode's radius and magnetic field strength 2 T.

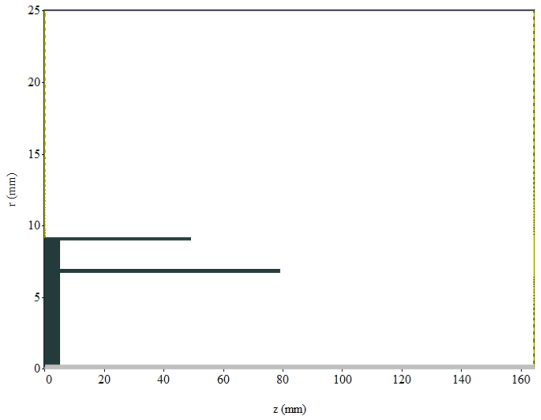

(a) Geometry for $d = 30$ mm

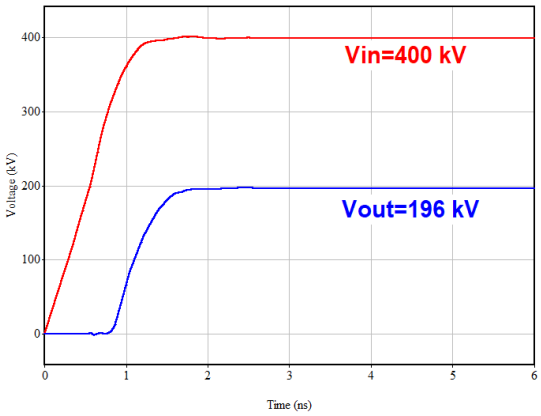

(b) V_{in}, V_{axial}

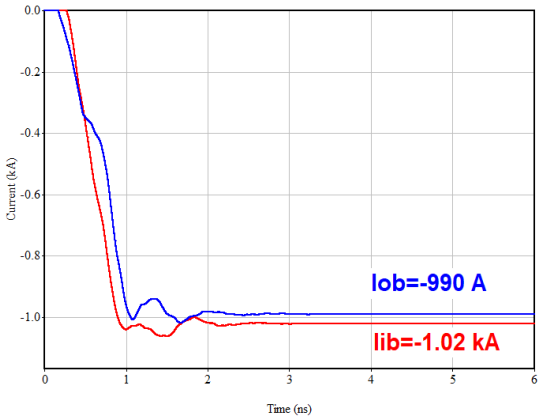

(c) I_{ib}, I_{ob}

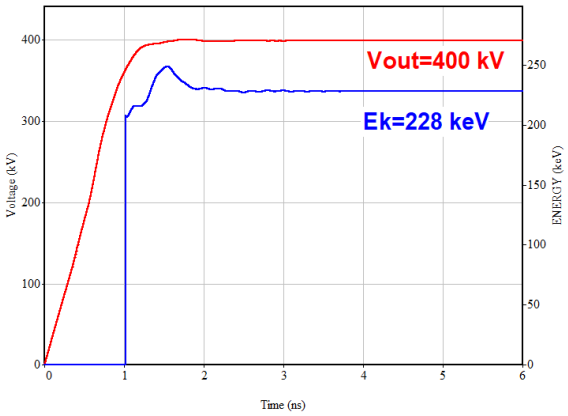

(d) Ek_{ib}, Ek_{ob}

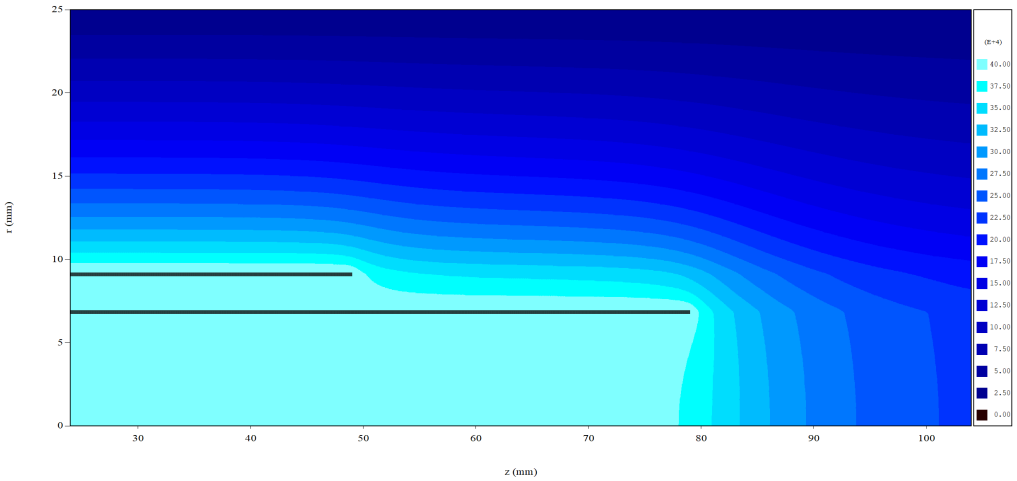

(e) Static electric field contour plot for $d = 30$ mm

Figure B.5: Simulation results of two nested MICDs (a) geometry of the problem, (b) applied (red) and axial (blue) voltages, (c) electron beam currents, (d) electron beam energies, (e) static electric field contour plot illustrates the accelerating field for the radial position of the inner cathode of $\frac{3}{4}$ of the outer cathode's radius and magnetic field strength 2 T.

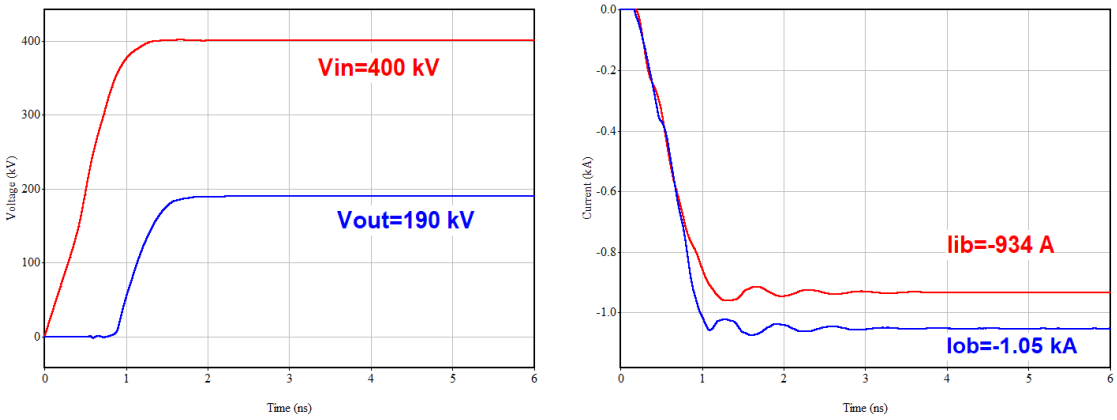

(a) V_{in}, V_{out} **(b)** I_{ib}, I_{ob}

(c) $E_{k_{ib}}, E_{k_{ob}}$ **(d)** Axial E-fields

Figure B.6: Simulation results show (a) input (V_{in}) and output (V_{out}) voltages, (b) output electron beam current for inner (I_{ib}) and outer (I_{ob}) beams, (c) output electron beam energy, (d) axial electric field at the edge of the inner and outer cathodes by applying a magnetic field strength of 300 T (basically infinite) in order to align with Fedosov's theory [79].

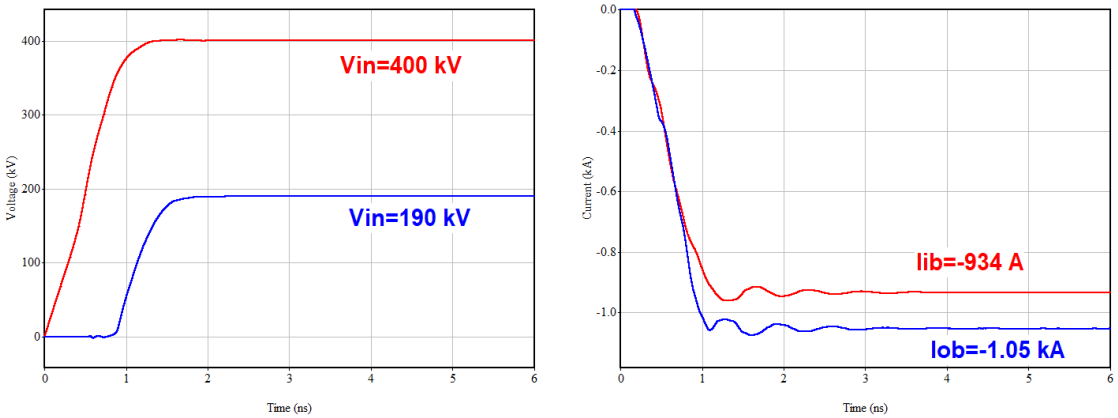

(a) V_{in}, V_{out} **(b)** I_{ib}, I_{ob}

(c) $E_{k_{ib}}, E_{k_{ob}}$ **(d)** Axial E-fields

Figure B.7: Simulation results show (a) input (V_{in}) and output (V_{out}) voltages, (b) output electron beam current for inner (I_{ib}) and outer (I_{ob}) beams, (c) output electron beam energy, (d) axial electric field at the edge of the inner and outer cathodes by applying a magnetic field strength of 3000 T (basically infinite) in order to align with Fedosov's theory [79].

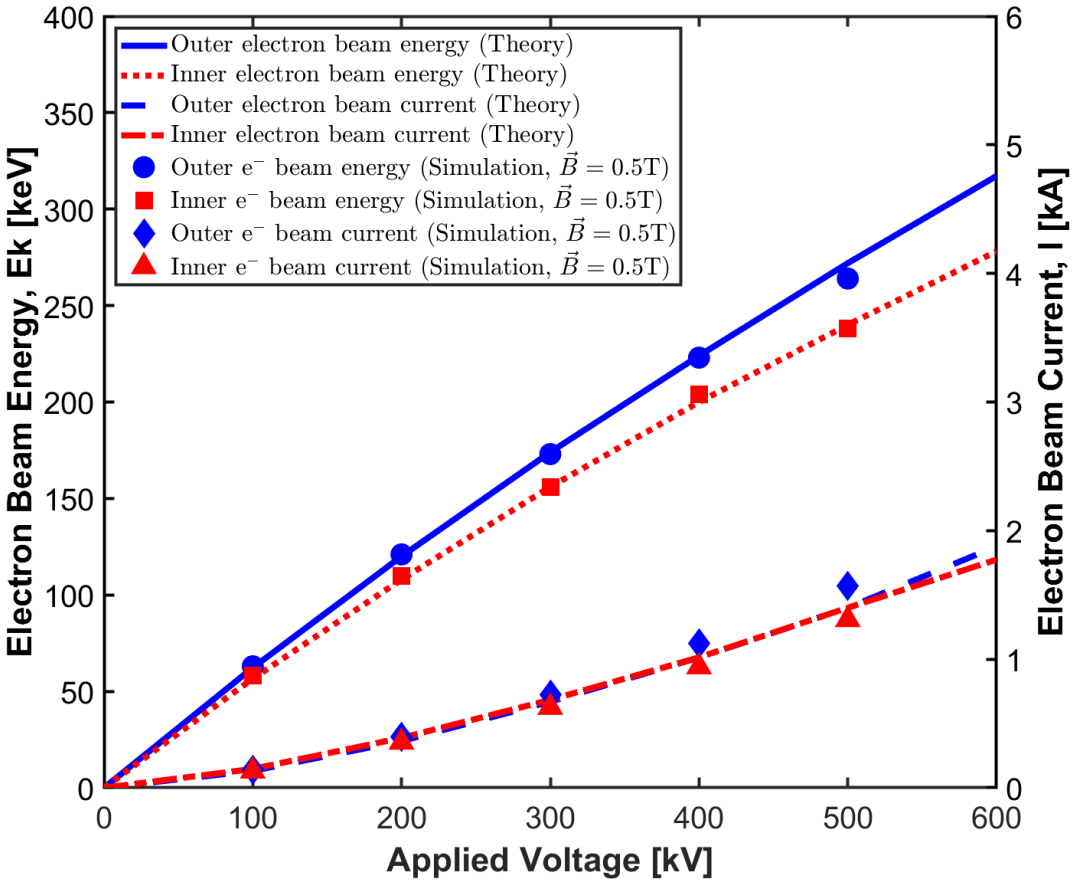

Figure B.8: Plot shows (i) analytically calculated electron beam energy and current from outer (solid blue, blue dash) and inner electron beam (red dot, red dash dot); (ii) MAGIC PIC simulated electron beam energy and current from outer (blue circle, blue diamond) and inner (red square, red triangle) electron beams as a function of applied voltages for $\vec{B} = 0.5$ T and $r_{ib} = \frac{3}{4} r_{ob}$.

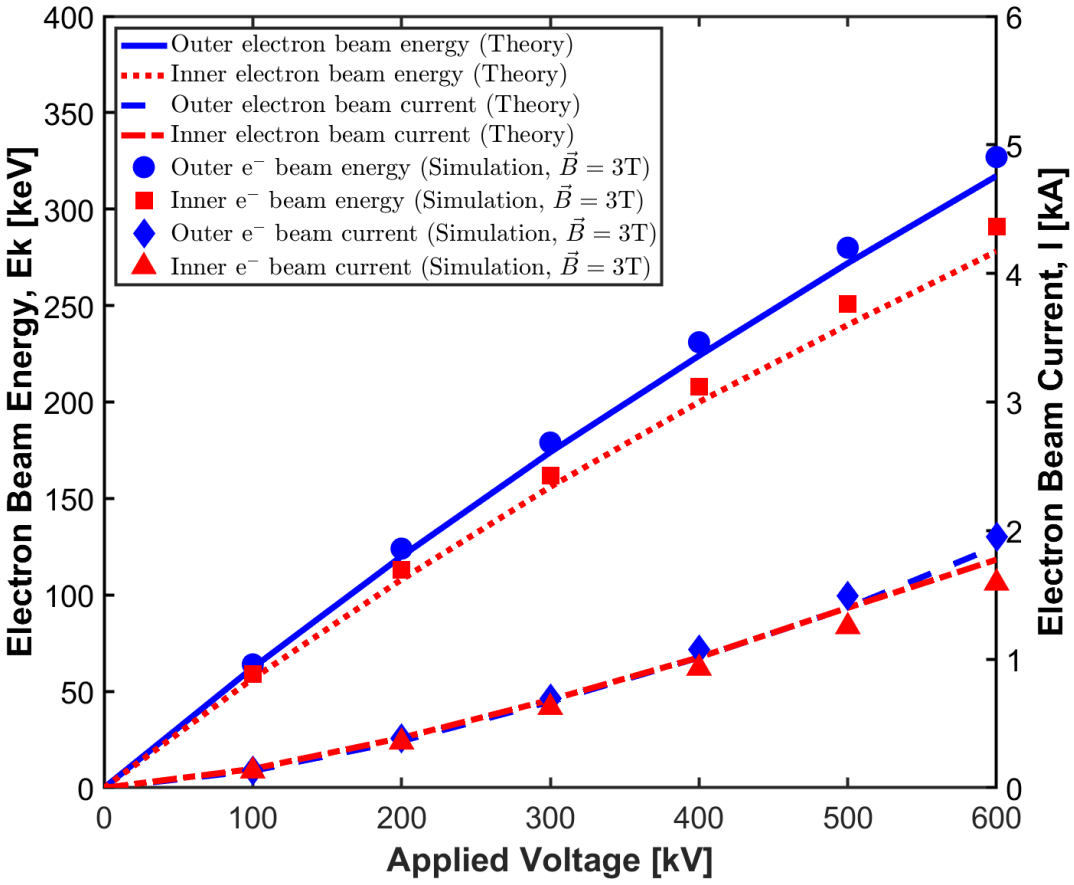

Figure B.9: Plot shows (i) analytically calculated electron beam energy and current from outer (solid blue, blue dash) and inner electron beams (red dot, red dash dot); (ii) MAGIC PIC simulated electron beam energy and current from outer (blue circle, blue diamond) and inner (red square, red triangle) electron beams as a function of applied voltages for $\vec{B} = 1$ T and $r_{ib} = \frac{3}{4} r_{ob}$.

Bibliography

[1] E. Schamiloglu, "High power microwave sources and applications," in *IEEE MTT-S Int. Microw. Symp. Dig. (IEEE Cat. No.04CH37535)*, vol. 2. IEEE, 2004, pp. 1001–1004. [Online]. Available: https://doi.org/10.1109/MWSYM.2004.1339150

[2] R. J. Barker and E. Schamiloglu, Eds., *High-Power Microwave Sources and Technologies*, 1st ed. New York, USA: IEEE Press, 2001. [Online]. Available: http://dx.doi.org/10.1109/9780470544877

[3] J. Benford, J. A. Swegle, and E. Schamiloglu, Eds., *High Power Microwaves*, 3rd ed. Taylor and Francis, Boca Raton, FL, USA: CRC Press, 2016.

[4] A. Figotin, *An Analytic Theory of Multi-stream Electron Beams in Traveling Wave Tubes*, 1st ed. Singapore, Singapore: World Scientific, 2020. [Online]. Available: https://doi.org/10.1142/11523

[5] J. H. Booske, R. J. Dobbs, C. D. Joye, C. L. Kory, G. R. Neil, G. Park, J. Park, and R. J. Temkin, "Vacuum electronic high power terahertz sources," *IEEE Trans. Terahertz Sci. Technol.*, vol. 1, no. 1, pp. 54–75, 2011. [Online]. Available: https://doi.org/10.1109/TTHZ.2011.2151610

[6] E. Schamiloglu, "High power microwave applications," in *High Power Microwaves*, J. Benford, J. A. Swegle, and E. Schamiloglu, Eds. Taylor and Francis, Boca Raton, FL, USA: CRC Press, 2016, ch. 3, pp. 41–87.

[7] D. A. Shiffler Jr., "High power traveling wave tubes powered by a relativistic electron beam," Ph.D. Dissertation, Cornell University, 1991.

[8] E. A. Nanni, "Cascaded particle accelerators reach new energy," *Nat. Photonics*, vol. 15, no. 5, pp. 405–406, 2021. [Online]. Available: https://doi.org/10.1038/s41566-021-00822-x

[9] K. N. Islam and E. Schamiloglu, "Multiple electron beam generation with different energies and comparable currents from a single cathode potential for high power traveling wave tubes (twts)," *J. Appl. Phys.*, vol. 131, no. 4, p. 044901, 2022. [Online]. Available: https://doi.org/10.1063/5.0072975

[10] K. N. Islam, L. D. Ludeking, A. D. Andreev, S. Portillo, A. M. N. Elfrgani, and E. Schamiloglu, "Modeling and simulation of relativistic multiple electron beam generation with different energies from a single-cathode potential for high-power microwave sources," *IEEE Trans. Electron Devices*, pp. 1–9, 2022. [Online]. Available: https://doi.org/10.1109/TED.2022.3140408

[11] L. Sivan, *Microwave Tube Transmitters*, 1st ed. NY, USA: Springer, 1994.

[12] A. S. Gilmour, *Klystrons, Traveling Wave Tubes, Magnetrons, Cross-Field Amplifiers, and Gyrotrons*, 1st ed. Boston, MA, USA: Artech House, 2011.

[13] J. R. Pierce, "My work with vacuum tubes at bell laboratories," *Vintage Electrics*, vol. 3, no. 1, 1991.

[14] R. J. Barker, J. H. Booske, N. C. L. Jr., and G. S. Nusinovich, Eds., *Modern Microwave and Millimeter-Wave Power Electronics*. Hoboken, NJ, USA: Wiley-IEEE Press, 2005.

[15] A. S. Gilmour, *Microwave Tubes*, ser. Artech House microwave library. University of Michigan, MI, USA: Artech House, 1986.

[16] J. H. Booske, D. R. Whaley, W. L. Menninger, R. S. Hollister, and C. M. Armstrong, "Traveling wave tubes (twts)," in *Modern Microwave and Millimeter-Wave Power Electronics*, R. J. Barker, J. H. Booske, N. C. L. Jr., and G. S. Nusinovich, Eds. Hoboken, NJ, USA: Wiley-IEEE Press, 2005, ch. 4, pp. 171–245.

[17] C. K. Chong, D. A. Layman, W. L. McGeary, W. L. Menninger, M. L. Ramay, and X. Zhai, "Q/v-band high-power uplink helix twt for future high-data-rate communications," *IEEE Trans. Electron Devices*, vol. 65, no. 6, pp. 2201–2205, 2018. [Online]. Available: https://doi.org/10.1109/TED.2018.2818619

[18] J. H. Booske and R. J. Barker, "Introduction and overview," in *Modern Microwave and Millimeter-Wave Power Electronics*, R. J. Barker, J. H. Booske, N. C. L. Jr., and G. S. Nusinovich, Eds. Hoboken, NJ, USA: Wiley-IEEE Press, 2005, ch. 1, pp. 1–33.

[19] G. Caryotakis, "Klystrons," in *Modern Microwave and Millimeter-Wave Power Electronics*, R. J. Barker, J. H. Booske, N. C. L. Jr., and G. S. Nusinovich, Eds. Hoboken, NJ, USA: Wiley-IEEE Press, 2005, ch. 3, pp. 107–170.

[20] C. Paoloni, D. Gamzina, R. Letizia, Y. Zheng, and N. C. L. Jr., "Millimeter wave traveling wave tubes for the 21st century," *J. Electromagn. Waves Appl.*, vol. 35, no. 5, pp. 567–603, 2021. [Online]. Available: https://doi.org/10.1080/09205071.2020.1848643

[21] W. Menninger, R. Benton, M. Choi, J. Feicht, U. Hallsten, H. Limburg, W. McGeary, and X. Zhai, "70% efficient ku-band and c-band twts for satellite downlinks," *IEEE Trans. Electron Devices*, vol. 52, no. 5, pp. 673–678, 2005.

[22] J. F. Skowron, "The continuous-cathode (emitting-sole) crossed-field amplifier," *Proc. IEEE*, vol. 61, no. 3, pp. 330–356, 1973.

[23] W. C. Brown, "Crossed-field amplifiers," in *Microwave Power Engineering*, ser. Electrical science series, E. C. Okress, Ed. New York, NY, USA: Academic Press, 1968, vol. 1, ch. 2, pp. 52–60.

[24] G. K. Farney and H. L. McDowell, "Crossed-field amplifiers," in *Microwave Power Engineering*, ser. Electrical science series, E. C. Okress, Ed. New York, NY, USA: Academic Press, 1968, vol. 1, ch. 2, pp. 52–60.

[25] G. S. Nusinovich, *Introduction to the Physics of Gyrotrons*. Baltimore, MD, USA: Johns Hopkins University Press, 2004, ch. 12. [Online]. Available: https://muse.jhu.edu/book/62236/pdf

[26] S. E. Tsimring, *Electron Beams and Microwave Vacuum Electronics*, ser. Wiley Series in Microwave and Optical Engineering. Hoboken, NJ, USA: Wiley, 2005.

[27] K. N. Islam, E. Schamiloglu, A. D. Andreev, F. Krawczyk, and B. Carlsten, "Simulations of a w-band circular twt," in *2019 International Vacuum Electronics Conference (IVEC)*, 2019, pp. 1–2. [Online]. Available: https://doi.org/10.1109/IVEC.2019.8744891

[28] M. P. Sulzer, "A radar technique for high range resolution incoherent scatter autocorrelation function measurements utilizing the full average power of klystron radars," *Radio Sci.*, vol. 21, no. 06, pp. 1033–1040, 1986. [Online]. Available: https://doi.org/10.1029/RS021i006p01033

[29] E. Schamiloglu and M. I. Fuks, "Relativistic magnetron using a virtual cathode," U.S. Patent 10192709B2, Jan. 2019.

[30] L. D. Ludeking, D. N. Smithe, R. Smith, and C. Chan, "Three dimensional simulation of cross-field devices and amplifiers," in *Abstracts. Int. Vacuum Electronics Conf. 2000 (Cat. No. 00EX392)*. IEEE, 2000, pp. 2–4. [Online]. Available: https://doi.org/10.1109/OVE:EC.2000.847408

[31] P. Ehret, H. Vogt, A. Peters, and E. Bosch, "L-band twtas for navigation satellites," *IEEE Trans. Electron Devices*, vol. 52, no. 5, pp. 679–684, 2005.

[32] M. I. Skolnik, *Introduction to Radar Systems*, ser. Electrical engineering series. McGraw-Hill, 2001. [Online]. Available: https://books.google.com/books?id=Y6-APwAACAAJ

[33] R. Kompfner, "The traveling-wave tube as amplifier at microwaves," *Pro. IRE.*, vol. 35, no. 2, pp. 124–127, 1947. [Online]. Available: https://doi.org/10.1109/JRPROC.1947.231238

[34] E. Schamiloglu, "Microwave fundamentals," in *High Power Microwaves*, J. Benford, J. A. Swegle, and E. Schamiloglu, Eds. Taylor and Francis, Boca Raton, FL, USA: CRC Press, 2016, ch. 4, pp. 93–146.

[35] K. L. Felch, B. G. Danly, H. R. Jory, K. E. Kreischer, W. Lawson, B. Levush, and R. Temkin, "Characteristics and applications of fast-wave gyrodevices," *Proc. IEEE*, vol. 87, no. 5, pp. 752–781, 1999. [Online]. Available: https://doi.org/10.1109/5.757254

[36] R. J. Barker and E. Schamiloglu, *HPM Sources: The DoD Perspective*. Wiley-IEEE Press, 2001, pp. 7–37. [Online]. Available: https://doi.org/10.1109/9780470544877.ch2

[37] E. Schamiloglu and R. J. Barker, "Special issue on pulsed power: Technology and applications," *Proc. IEEE*, vol. 92, no. 7, pp. 1011–1013, 2004. [Online]. Available: https://doi.org/10.1109/JPROC.2004.829064

[38] J. R. Pierce, "Double-stream amplifiers," *Proc. IRE*, vol. 37, no. 9, pp. 980–985, 1949. [Online]. Available: https://doi.org/10.1109/JRPROC.1949.230299

[39] A. V. Haeff, "The electron-wave tube-a novel method of generation and amplification of microwave energy," *Proc. IRE*, vol. 37, no. 1, pp. 4–10, 1949. [Online]. Available: https://doi.org/10.1109/JRPROC.1949.232968

[40] A. V. Haeff, "Space-charge effects in electron beams," *Proc. IRE*, vol. 27, no. 9, pp. 586–602, 1939. [Online]. Available: https://doi.org/10.1109/JRPROC.1939.228758

[41] A. V. Hollenberg, "Experimental observation of amplification by interaction between two electron streams," *Bell Syst. Tech. Jour.*, vol. 28, no. 1, pp. 52–58, 1949. [Online]. Available: https://doi.org/10.1002/j.1538-7305.1949.tb03623.x

[42] L. E. Neergard, "Analysis of a simple model of two-beam growing-wave tube," *RCA Rev.*, vol. 9, pp. 585–601, 1948. [Online]. Available: https://worldradiohistory.com/Archive-IRE/40s/IRE-1949-09.pdf

[43] B. E. Carlsten, K. A. Bishofberger, and R. J. Faehl, "Compact two-stream generator of millimeter- and submillimeter-wave radiation," *Phys. Plasmas*, vol. 15, no. 7, p. 073101, 2008. [Online]. Available: https://doi.org/10.1063/1.2938385

[44] D. Neben, K. Bishofberger, V. Pavlenko, and N. Yampolsky, "A co-axial electron gun to generate millimeter-wave RF using the two-stream instability," *Phys. Plasmas*, vol. 92, p. 053301, 2021. [Online]. Available: https://doi.org/10.1063/5.0038746

[45] Y. D. Mozgovoi, S. A. Khritkin, and Y. V. Evdokimov, "Microwave radiation of passing and counter electron beams in electrodynamic systems," in *2013 IEEE Int. Vac. Electron. Conf.*, 2013, pp. 1–2. [Online]. Available: https://doi.org/10.1109/IVEC.2013.6570988

[46] N. I. Zaitsev, N. F. Kovalev, B. D. Kolchugin, and M. I. Fuks, "Experimental investigation of a relativistic carcinotron," *Zh. Tekh. Fiz.*, vol. 52, pp. 1611–1617, Aug. 1982, provided by the SAO/NASA Astrophysics Data System. [Online]. Available: https://ui.adsabs.harvard.edu/abs/1982ZhTFi..52.1611Z

[47] V. E. Nechaev, E. I. Soluyanov, and M. I. Fuks, "Controlling the current of a hollow electron beam with a shielding beam in a magnetically insulated diode," *Pis'ma Zh. Tekh.*, vol. 5, pp. 113–117, Jan. 1979.

[48] S. H. Gold and G. S. Nusinovich, "Review of high-power microwave source research," *Rev. Sci. Instrum.*, vol. 68, no. 11, pp. 3945–3974, 1997. [Online]. Available: https://doi.org/10.1063/1.1148382

[49] L. D. Moreland, E. Schamiloglu, W. Lemke, S. D. Korovin, V. V. Rostov, A. M. Roitman, K. J. Hendricks, and T. A. Spencer, "Efficiency enhancement of high power vacuum bwo's using nonuniform slow wave structures," *IEEE Trans. Plasma Sci.*, vol. 22, no. 5, pp. 554–565, 1994. [Online]. Available: https://doi.org/10.1109/27.338268

[50] J. Fink, H. B. Schilling, and U. Schumacher, "Development and investigation of relativistic electron beams with finite energy spread and improved emittance," *J. Appl. Phys.*, vol. 51, no. 6, pp. 2995–3000, 1980. [Online]. Available: https://doi.org/10.1063/1.328111

[51] G. A. Mesyats, S. D. Korovin, A. V. Gunin, V. P. Gubanov, A. S. Stepchenko, D. M. Grishin, V. F. Landl, and P. I. Alekseenko, "Repetitively

pulsed high-current accelerators with transformer charging of forming lines," *Laser Part. Beams*, vol. 21, no. 2, p. 197, 2003. [Online]. Available: https://doi.org/10.1017/S0263034603212076

[52] K. N. Islam, A. D. Andreev, and E. Schamiloglu, "Experimental measurements of intense relativistic electron beam parameters on the sinus-6 high-current electron-beam accelerator," in *Proc. EAPPC-BEAMS-MG Conf.*, Biarritz, France, Feb. 2022, to be published.

[53] K. N. Islam, A. Andreev, and E. Schamiloglu, "Analytical calculations, numerical simulations of intense relativistic electron beam generation and transportation in cylindrical waveguide of the sinus-6 high-current electron-beam accelerator," in *Proc. EAPPC-BEAMS-MG Conf.*, Biarritz, France, Feb. 2022, to be published.

[54] A. D. Andreev, "Current-Voltage Characteristic of Nanosecond - Duration Relativistic Electron Beam," in *APS Division of Plasma Physics Meeting Abstracts*, ser. APS Meeting Abstracts, vol. 47, Oct. 2005, p. QP1.096.

[55] E. Schamiloglu, R. Barker, M. Gundersen, and A. Neuber, "Modern pulsed power: Charlie martin and beyond," *Proc. IEEE*, vol. 92, no. 7, pp. 1014–1020, 2004. [Online]. Available: http://dx.doi.org/10.1109/JPROC.2004.829058

[56] S. E. Graybill and S. V. Nablo, "The generation and diagnosis of pulsed relativistic electron beams above 10^{10} Watts," *IEEE Tran. Nucl. Sci.*, vol. 14, no. 3, pp. 782–788, 1967. [Online]. Available: https://doi.org/10.1109/TNS.1967.4324657

[57] R. B. Miller, *An Introduction to the Physics of Intense Charged Particle Beams*. Boston, MA, USA: Springer, 2012.

[58] J. A. Nation, "High-power electron and ion beam generation," *Part. Accel.*, vol. 10, pp. 1–30, 1979.

[59] Additively manufactured copper components for linear accelerators (ifast). Accessed on: November 2, 2021. [Online]. Available: https://ifast-project.eu/news/announcement/physics/additively-manufactured-copper-components-linear-accelerators

[60] J. Maenchen, G. Cooperstein, J. O'Malley, and I. Smith, "Advances in pulsed power-driven radiography systems," *Proc. IEEE*, vol. 92, no. 7, pp. 1021–1042, 2004.

[61] V. L. Granatstein and I. Alexeff, Eds., *High-Power Microwave Sources*. Boston, MA, USA: Artech House, 1987.

[62] B. V. Bunkin, A. V. Gaponov-Grekhov, A. S. El'Chaninov, F. I. Zagulov, S. D. Korovin, G. A. Mesiats, M. L. Osipov, E. A. Otlivanchik, M. I. Petelin, and A. M. Prokhorov, "Radar based on a microwave oscillator with a relativistic electron beam," *Pisma v Zh. Tekh. Fiz.*, vol. 18, no. 9, pp. 61–65, May 1992, provided by the SAO/NASA Astrophysics Data System. [Online]. Available: https://ui.adsabs.harvard.edu/abs/1992PZhTF..18...61B

[63] D. Andreev, A. Kuskov, and E. Schamiloglu, "Review of the relativistic magnetron," *Matter Radiat. Extrem.*, vol. 4, no. 6, p. 067201, 2019. [Online]. Available: https://doi.org/10.1063/1.5100028

[64] S. D. Korovin and V. V. Rostov, "High-current nanosecond pulse-periodic electron accelerators utilizing a tesla transformer," *Russ. Phys. J.*, vol. 39, pp. 1177–1185, Dec. 1996. [Online]. Available: https://ui.adsabs.harvard.edu/link_gateway/1996RuPhJ..39.1177K/doi:10.1007/BF02436160

[65] A. A. Kim, B. M. Kovalchuk, V. A. Kokshenev, A. V. Shishlov, N. A. Ratakhin, V. I. Oreshkin, V. V. Rostov, V. Koshelev, and V. F. Losev, "Review of high-power pulsed systems at the institute of high current electronics," *Matter Radiat. Extremes*, vol. 1, no. 4, pp. 201–206, 2016. [Online]. Available: https://doi.org/10.1016/j.mre.2016.08.001

[66] S. D. Korovin, V. V. Rostov, S. D. Polevin, I. V. Pegel, E. Schamiloglu, M. I. Fuks, and R. J. Barker, "Pulsed power-driven high-power microwave sources," *Proc. IEEE*, vol. 92, no. 7, pp. 1082–1095, 2004. [Online]. Available: https://doi.org/10.1109/JPROC.2004.829020

[67] E. Schamiloglu. Accessed on: November 20, 2021. [Online]. Available: http://http://ece-research.unm.edu/schamiloglu/

[68] G. A. Mesyats and D. I. Proskurovsky, Eds., *Pulsed Electrical Discharge in Vacuum*, 1st ed., ser. Springer Series on Atomic, Optical, and Plasma Physic. New York, NY, USA: Springer Berlin Heidelberg, 1989, vol. 5.

[69] G. A. Mesyats, *Pulsed Power*, 1st ed. Boston, MA, USA: Springer, 2005. [Online]. Available: https://doi.org/10.1007/b116932

[70] A. V. Gunin, V. F. Landl, S. D. Korovin, G. A. Mesyats, I. V. Pegel, and V. V. Rostov, "Experimental studies of long-lifetime cold cathodes for high-power microwave oscillators," *IEEE Trans. Plasma Sci.*, vol. 28, no. 3, pp. 537–541, 2000. [Online]. Available: https://doi.org/10.1109/27.887668

[71] S. P. Bugaev, E. A. Litvinov, G. A. Mesyats, and D. I. Proskurovski, "Explosive emission of electrons," *Sov. Phys. Usp.*, vol. 18, no. 1, p. 51, 1975.

[72] O. Loza, "Generation of high-current relativistic electron beams with stable (for a microsecond) parameters using explosive emission cathodes,"

Tech. Phys., vol. 53, no. 11, pp. 1479–1484, 2008. [Online]. Available: http://dx.doi.org/10.1134/S1063784208110133

[73] A. V. Gunin, S. D. Korovin, G. A. Mesyats, V. V. Rostov *et al.*, "Long-lived explosive-emission cathode for high-power microwave radiation generators," *Tech. Phys. Lett.*, vol. 25, no. 11, pp. 922–926, 1999. [Online]. Available: http://dx.doi.org/10.1134/1.1262685

[74] S. Y. Belomyttsev, I. V. Romanchenko, and V. V. Rostov, "Electric field strength at and near the cathode edge in a magnetically insulated coaxial diode," *Russ. Phys. J.*, vol. 51, no. 3, pp. 299–306, 2008. [Online]. Available: http://dx.doi.org/10.1007/s11182-008-9052-z

[75] D. Shiffler, M. Ruebush, D. Zagar, M. LaCour, M. Sena, K. Golby, M. Haworth, and R. Umstattd, "Cathode and anode plasmas in short-pulse explosive field emission cathodes," *J. Appl. Phys.*, vol. 91, no. 9, pp. 5599–5603, 2002. [Online]. Available: https://doi.org/10.1063/1.1457541

[76] R. K. Parker, "Explosive electron emission and the characteristics of high-current electron flow," Ph.D. Dissertation, University of New Mexico, Albuquerque, NM, USA, 1973.

[77] A. S. El'chaninov, F. Y. Zagulov, S. D. Korovin, and G. A. Mesyats, "Performance stability of vacuum diodes for heavy current relativistic electron beam accelerators," *J. Tech. Physics*, vol. 51, no. 5, pp. 1005–1007, 1981.

[78] R. J. Umstattd, D. Abe, J. Benford, D. Gallagher, R. M. Gilgenbach, D. Goebel, M. S. Litz, and J. Nation, "Cathodes and electron guns," in *High-Power Microwave Sources and Technologies*, R. J. Barker and E. Schamiloglu, Eds. New York, USA: CRC Press, 2001, ch. 9, pp. 284–324.

[79] A. I. Fedosov, E. A. Litvinov, S. Y. Belomytsev, and S. P. Bugaev, "Characteristics of electron beam formed in diodes with magnetic insulation," *Izv. Vyssh. Uchebn. Zavad. Fiz.*, vol. 10, pp. 134–135, Oct. 1977. [Online]. Available: https://doi.org/10.1007/BF00898924

[80] M. Friedman and M. Ury, "Production and focusing of a high power relativistic annular electron beam," *Rev. Sci. Instrum.*, vol. 41, no. 9, pp. 1334–1335, 1970. [Online]. Available: https://doi.org/10.1063/1.1684810

[81] S. I. Belomyttsev, E. A. Litvinov, G. A. Mesyats, and A. I. Fedosov, "Characteristics of the electron beam formed in a magnetic-insulation diode," *Fiz. Plazmy*, vol. 7, pp. 86–90, Jan. 1981.

[82] M. I. Fuks and E. Schamiloglu, "Two-dimensional single-stream electron motion in a coaxial diode with magnetic insulation," *Phys. Plasmas*, vol. 21, no. 5, p. 053102, 2014. [Online]. Available: https://doi.org/10.1063/1.4875749

[83] R. B. Miller, "Fundamentals of intense relativistic electron beams," *AIP Conf. Proc.*, vol. 184, no. 2, pp. 1729–1758, 1989. [Online]. Available: https://aip.scitation.org/doi/abs/10.1063/1.38024

[84] A. D. Andreev, L. Bi, A. M. Elfrgani, and E. Schamiloglu, "Computational study of an overmoded, with diameter to wavelength ratio ≈ 8, slow-wave structure (sws) of a relativistic backward-wave oscillator (bwo) operating in the e-band frequency range," in *14th UK-Europe-China Workshop on Millimetre-Waves and Terahertz Technologies (UCMMT)*, 2021, pp. 1–3.

[85] L. D. Moreland, E. Schamiloglu, R. W. Lemke, S. D. Korovin, and V. V. Rostov, "Enhanced frequency agility of high-power relativistic backward wave oscillators," *IEEE Trans. Plasma Sci.*, vol. 24, no. 3, pp. 852–858, Jun. 1996. [Online]. Available: https://doi.org/10.1109/27.533088

[86] A. M. Elfrgani, S. Prasad, M. I. Fuks, and E. Schamiloglu, "Relativistic bwo with linearly polarized gaussian radiation pattern," *IEEE Trans. Plasma Sci.*, vol. 42, no. 8, pp. 2135–2140, 2014. [Online]. Available: http://dx.doi.org/10.1109/TPS.2014.2331345

[87] K. Hahn, M. I. Fuks, and E. Schamiloglu, "Initial studies of a long-pulse relativistic backward-wave oscillator utilizing a disk cathode," *IEEE Trans. Plasma Sci.*, vol. 30, no. 3, pp. 1112–1119, 2002. [Online]. Available: https://doi.org/10.1109/TPS.2002.801628

[88] M. I. Fuks and E. Schamiloglu, "Amplification in a Resonant TWT Controlled by its Guide Magnetic Field," in *APS Division of Plasma Physics Meeting Abstracts*, ser. APS Meeting Abstracts, vol. 46, Nov. 2004, p. HP1.111.

[89] M. I. Fuks, E. Schamiloglu, and Y.-D. Li, "Rf priming for operation of relativistic twt with reflections near cyclotron resonance," *IEEE Trans. Plasma Sci.*, vol. 42, no. 1, pp. 38–41, 2014. [Online]. Available: https://doi.org/10.1109/TPS.2013.2288253

[90] E. Schamiloglu, "Bwos, mwcgs, and o-type cerenkov devices," in *High Power Microwaves*, J. Benford, J. A. Swegle, and E. Schamiloglu, Eds. Taylor and Francis, Boca Raton, FL, USA: CRC Press, 2016, ch. 8, pp. 281–321.

[91] K. N. Islam, A. D. Andreev, and E. Schamiloglu, "Two benchmark simulations of intense annular high-current electron beam generation, acceleration, and transport in a smooth cylindrical waveguide driven by the sinus-6 accelerator at unm," in *IEEE Int. Vacuum Electronics Conf. (IVEC)*, Montary, CA, USA, Apr. 2022, pp. 1–2, accepted.

[92] A. D. Andreev, K. N. Islam, and E. Schamiloglu, "Direct comparison of analyticaly derived fedosov solution with numerical simulations of intense relativis-

tic electron beam generation in magnetically-insulated coaxial diode of sinus-6 high-current electron-beam accelerator," in *IEEE Int. Vacuum Electronics Conf. (IVEC)*, Montary, CA, USA, Apr. 2022, pp. 1–2, accepted.

[93] H. C. Chen and P. J. Palmadesso, "Diocotron instability of a relativistic coaxial multi-ring hollow electron beam," *Phys. Fluids*, vol. 24, no. 2, pp. 357–362, 1981.

[94] B. E. Carlsten, "Microwave sources. [online]," Available at https://uspas.fnal.gov/programs/2019/newmexico/courses/microwave-sources.shtml, accessed on: June 17, 2019.

[95] M. Friedman, J. Krall, Y. Y. Lau, and V. Serlin, "Externally modulated intense relativistic electron beams," *J. Appl. Phys.*, vol. 64, no. 7, pp. 3353–3379, 1988. [Online]. Available: https://doi.org/10.1063/1.341521

[96] T. A. Spencer, K. J. Hendricks, J. W. Luginsland, and M. D. Stump, "Dynamics of the space-charge-limiting current in gyro-type devices," *IEEE Trans. Plasma Sci.*, vol. 26, no. 3, pp. 854–859, 1998. [Online]. Available: https://doi.org/10.1109/27.700853

[97] A. Rokhlenko, K. L. Jensen, and J. L. Lebowitz, "Space charge effects in field emission: One dimensional theory," *J. Appl. Phys.*, vol. 107, no. 1, p. 014904, 2010. [Online]. Available: https://doi.org/10.1063/1.3272690

[98] L. S. Bogdankevich and A. A. Rukhadze, "Stability of relativistic electron beams in a plasma and the problem of critical currents," *Sov. Phys. Usp.*, vol. 14, no. 2, p. 163, 1971.

[99] B. N. Brejzman and D. D. Ryutov, "Powerful relativistic electron beams in a plasma and in a vacuum (theory)," *Nucl. Fusion*, vol. 14, no. 6, pp. 873–907, dec 1974. [Online]. Available: https://doi.org/10.1088/0029-5515/14/6/012

[100] S. Y. Belomyttsev, V. V. Rostov, I. V. Romanchenko, S. A. Shunailov, M. Kolomiets, G. A. Mesyats, K. A. Sharypov, V. G. Shpak, M. R. Ulmaskulov, and M. I. Yalandin, "Magnetically insulated coaxial vacuum diode with partial space-charge-limited explosive emission from edge-type cathode," *J. Appl. Phys.*, vol. 119, no. 2, p. 023304, 2016. [Online]. Available: https://doi.org/10.1063/1.4938022

[101] T. Yatsenko, G. V. Sotnikov, S. Portillo, and K. Ilyenko, "Relativistic charged-particle beam space-charge limited current in finite length coaxial drift tube," *IEEE Trans. Plasma Sci.*, vol. 47, no. 5, pp. 2602–2608, 2019.

[102] T. Yatsenko, K. Ilyenko, and G. V. Sotnikov, "Limiting current of axisymmetric relativistic charged-particle beam propagating in strong axial magnetic field in coaxial drift tube," *Phys. Plasmas*, vol. 19, no. 6, p. 063107, 2012.

[103] ISO, "International organization for standardization," Feb. 1947, accessed on: October 5 , 2021. [Online]. Available: https://en.wikipedia.org/wiki/International_Organization_for_Standardization

[104] J. D. Huba, *NRL Plasma Formulary Supported by The Office of Naval Research*. Washington, DC, USA: Naval Research Laboratory, 2013. [Online]. Available: http://wwwppd.nrl.navy.mil/nrlformulary/

[105] C. D. Child, "Discharge from hot cao," *Phys. Rev.*, vol. 32, pp. 492–511, May 1911. [Online]. Available: https://link.aps.org/doi/10.1103/PhysRevSeriesI.32.492

[106] I. Langmuir, "The effect of space charge and residual gases on thermionic currents in high vacuum," *Phys. Rev.*, vol. 2, pp. 450–486, Dec 1913. [Online]. Available: https://link.aps.org/doi/10.1103/PhysRev.2.450

[107] H. F. Ivey, "Space charge and transit time considerations in planar diodes for relativistic velocities," *J. Appl. Phys.*, vol. 23, no. 2, pp. 208–211, 1952. [Online]. Available: https://ui.adsabs.harvard.edu/link_gateway/1952JAP...23..208I/doi:10.1063/1.1702175

[108] S. Y. Belomyttsev, S. D. Korovin, and I. V. Pegel, "Effect of the expanding explosive-emission centers plasma on the impedance of a high-current diode," *IEEE Trans. Plasma Sci.*, vol. 27, no. 6, pp. 1572–1577, 1999. [Online]. Available: https://doi.org/10.1109/27.808928

[109] T. C. Genoni and W. A. Proctor, "Upper bound for the space-charge limiting current of annular electron beams," *J. Plasma Phys.*, vol. 23, no. 1, pp. 129–139, 1980. [Online]. Available: https://doi.org/10.1063/1.874175

[110] L. D. Ludeking, A. J. Woods, and L. W. Cavey, "Magic tool suite user's manual, september 2015 edition, version 3.2.7, orbital atk, inc." [Online]. Available: http://www.MAGICtoolsuite.com

[111] K. L. Brown and G. W. Tautfest, "Faraday-cup monitors for high-energy electron beams," *Rev. Sci. Instrum.*, vol. 27, no. 9, pp. 696–702, 1956. [Online]. Available: https://doi.org/10.1063/1.1715674

[112] D. Pellinen and V. Staggs, "A technique to measure high-power electron beam currents," *Rev. Sci. Instrum.*, vol. 44, no. 1, pp. 46–49, 1973. [Online]. Available: https://doi.org/10.1063/1.1685953

[113] S. D. Korovin, E. A. Litvinov, G. A. Mesyats, A. M. Murzakaev, V. V. Rostov, V. G. Shpak, S. A. Shunailov, and M. I. Yalandin, "Experimental investigation of graphite explosive-emission cathodes operating in a periodic pulse regime," *Tech. Phys. Lett.*, vol. 30, no. 10, pp. 813–816, 2004. [Online]. Available: http://dx.doi.org/10.1134/1.1813718

[114] F. F. Chen, *Introduction to Plasma Physics and Controlled Fusion*, 3rd ed. New York, USA: Springer, 2016.

[115] S. Prasad, "Fast start of oscillations in a short-pulse relativistic magnetron driven by a transparent cathode," Ph.D. dissertation, University of New Mexico, Nov. 2011. [Online]. Available: https://digitalrepository.unm.edu/ece_etds/209

[116] A. D. Andreev, "Methods of produce short-pulse, high-power microwaves," Ph.D. dissertation, University of New Mexico, Nov. 2007.

[117] I. T&M Research Products. Accessed on: November 20, 2021. [Online]. Available: https://www.tandmresearch.com/

[118] N. Wax, "Some properties of tubular electron beams," *J. Appl. Phys.*, vol. 20, no. 3, pp. 242–247, 1949. [Online]. Available: https://doi.org/10.1063/1.1698349

[119] E. Schamiloglu, "Designing high power microwave systems," in *High Power Microwaves*, J. Benford, J. A. Swegle, and E. Schamiloglu, Eds. Taylor and Francis, Boca Raton, FL, USA: CRC Press, 2016, ch. 2, pp. 17–39.

[120] J. W. Luginsland, T. A. A. Jr., J. P. Verboncoeur, R. W. Lemke, L. Ludeking, P. M. Mardahl, A. T. Lin, Y. Y. Lau, and J. D. B. Jr., "Computational techniques," in *High-Power Microwave Sources and Technologies*, R. J. Barker and E. Schamiloglu, Eds. New York, USA: CRC Press, 2001, ch. 11, pp. 376–437.

[121] J. M. Creedon, "Relativistic brillouin flow in the high ν/γ diode," *J. Appl. Phys.*, vol. 46, no. 7, pp. 2946–2955, 1975. [Online]. Available: https://doi.org/10.1063/1.322034

[122] A. M. Ignatov and V. P. Tarakanov, "Squeezed state of high-current electron beam," *Phys. Plasmas*, vol. 1, no. 3, pp. 741–744, 1994. [Online]. Available: https://doi.org/10.1063/1.870819

[123] A. A. Grishkov and I. V. Pegel, "An annular high-current electron beam with an energy spread in a coaxial magnetically insulated diode," *Plasma Phys. Rep.*, vol. 39, no. 11, pp. 936–946, 2013. [Online]. Available: https://doi.org/10.1134/S1063780X13110056

[124] K. F. S. II, "Space-charge saturation and current limits in cylindrical drift tubes and planar sheaths," Ph.D. dissertation, University of North Texas, Aug. 2000, accessed on: October 17, 2021. [Online]. Available: https://digital.library.unt.edu/ark:/67531/metadc2598/m1/1/

[125] E. Schamiloglu, "Dispersion engineering for high power microwave amplifiers," in *Proc. of the 2012 EAPPC-Beams Conf.*, Karlsruhe, Germany, Sept 2012.